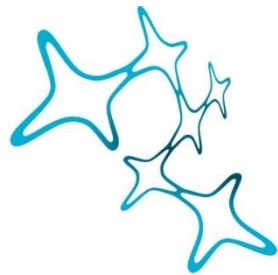

NEURAL ORGANISATION OF INNATE BEHAVIOUR IN ZEBRAFISH LARVAE

Duncan Stephen Mearns



Graduate School of
Systemic Neurosciences
LMU Munich



Dissertation der
Graduate School of Systemic Neurosciences der
Ludwig-Maximilians-Universität München

May 2021

Supervisor
Prof. Dr. Herwig Baier
Genes – Circuits – Behavior
Max Planck Institute of Neurobiology

First Reviewer: Prof. Dr. Herwig Baier
Second Reviewer: Prof. Dr. Alexander Borst

Date of Submission: 3rd May 2021
Date of Defense: 9th September 2021

To my family

SUMMARY

Animals' inner worlds are a hazy imitation of reality, shaped by evolution. Of the infinitude of stimuli that can arise in their natural environment, only a few will bear significance for an animal's survival and reproductive success. Thus, neural circuits have evolved to extract only these relevant stimuli from the background and connect them to downstream effectors. Sometimes, competing representations of the outside world arise in the brain, and these must be resolved to ensure adaptive behaviour. Through the study of an animal's behaviour, we can learn about its inner world: which stimuli it cares about; the desires these stimuli engender within it; and how its movements enact and extinguish those desires, allowing new stimuli to emerge that reorchestrate the inner world and refresh the cycle. Here, I present three studies that investigate the emergence of this world in the neural circuits of zebrafish larvae.

In the first study, I mapped the behavioural sequences of zebrafish larvae as they pursued and consumed prey. Manipulating their vision with genetic mutants, virtual reality, and lesion studies revealed the dynamic features of stimuli that drive switches in the behaviour. I showed that, by chaining kinematically varied swim types into regular sequences, larvae bring prey to a binocular zone in the near visual field. Here, the fused representation of the stimulus across hemispheres releases stereotyped strike manoeuvres, tuned to the distance to the prey.

In the second study, I helped investigate how visual circuits build representations of prey and predator stimuli. Measuring the responses of neurons to visual stimuli revealed how feature selectivity arises from the integration of upstream inputs. Features are unevenly represented across space, matching predicted changes in prey percepts as animals progress through their hunting sequences. When neurons tuned to specific features were ablated, I showed that the detection of prey was altered, no longer eliciting the usual hunting responses from animals.

In the third study, I contributed to the discovery of a circuit in the brain that coordinates behavioural responses to competing stimuli. When confronted with multiple threats, animals either ignore one and escape from the other, or average their locations and escape in an intermediate direction. I showed that these two strategies are mediated by distinct swims types. Inhibiting specific neurons in the brain reduced directional escapes, but not intermediate ones, revealing a circuit that contributes to a bottom-up attention mechanism.

Together, these three studies reveal the organisation of behaviour within neural circuits of the larval zebrafish brain. Finally, I consider the broader networks in the brain that might implement and modulate responses to salient visual stimuli, and how these circuits could serve as a substrate for behavioural evolution.

CONTENTS

1. Introduction	1
1.1 Organisation of behaviour	3
1.2 Competition in the brain	7
1.3 Zebrafish as a model in neuroethology	8
1.4 Organisation of zebrafish visuomotor circuits	11
1.5 Zebrafish as a genetically tractable system	15
2. Publications	20
2.1 Deconstructing hunting behaviour reveals a tightly coupled stimulus-response loop .	20
2.2 Retinotectal circuitry of larval zebrafish is adapted to detection and pursuit of prey ...	58
2.3 Neural circuitry for stimulus selection in the zebrafish visual system.....	105
3. Discussion	153
3.1 Mapping behaviour	154
3.2 Prey capture behaviour of the zebrafish larva	161
3.3 Neural circuits for prey capture	163
4. Outlook	173
Acknowledgements	187
Appendices	189

1. INTRODUCTION

“To move things is all mankind can do, for which the sole executant is the muscle, whether it be whispering a syllable or felling a forest.”

Charles Scott Sherrington

When nervous systems evolved more than half a billion years ago, the ability to sense and interact dynamically with their environments afforded those first animals a key adaptive advantage over their sessile counterparts. Brains evolved to perform behaviour and, consequently, as the adage goes, *nothing in neuroscience makes sense except in the light of behaviour*. The study of behaviour in both humans and non-humans has been invaluable for understanding the brain (Krakauer et al., 2017; Niv, 2020).

Early ethologists realised that animals do not perceive an unbiased view of the world. Rather, every animal’s internal experience is limited by the types and physiology of sensory receptors it possesses, the filters applied to these sensory inputs by layers of neural processing, its internal drives and desires, and the knowledge available to it through its behaviour. Jakob von Uexküll termed the limited worldview possessed by an animal the *Umwelt* (Uexküll, 1992). Von Uexküll divided this internal world of an animal into a perceptual field and a motor field, but realised the two were intricately linked (**Figure 1A**). In von Uexküll’s model, behaviour imbues objects in the world with meaning, and the perception of those objects compels animals to act. From a circuit neuroscience perspective, we might say that sensory circuits detect salient features in the environment; a sensorimotor transformation computes an optimal response given the current combination of features present; and motor circuits implement the response by coordinating the contraction of muscles. But von Uexküll’s model shows that this is more than a simple stimulus-response arc: the movements of the animal feed back into the environment, thereby changing it. Thus, a full understanding of the *Umwelt* comes only when we look at both the “inner world” of the subject (its brain), and the sensorimotor loops that play out in the environment (the behaviour).

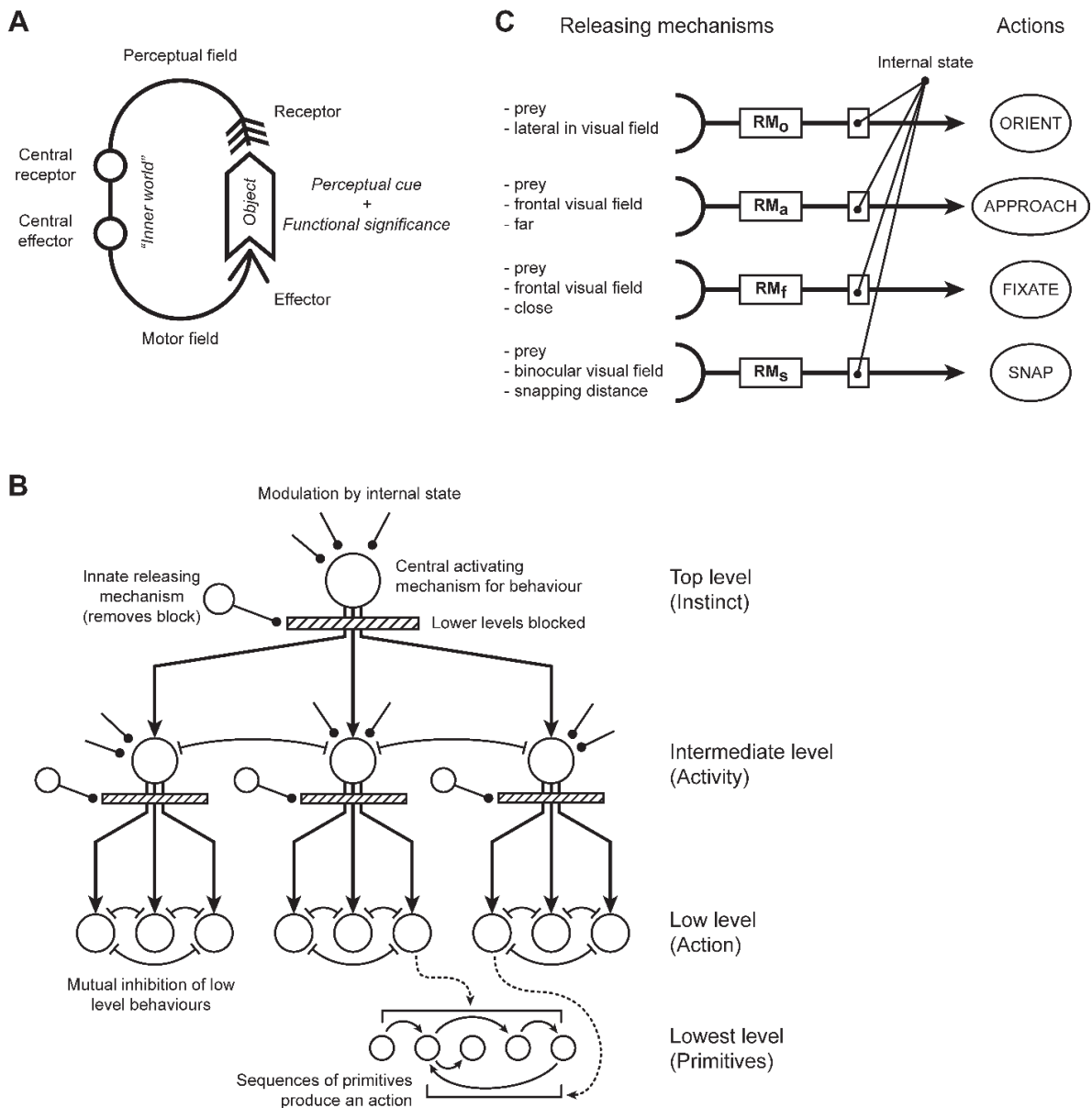


Figure 1. Classical models of behaviour

(A) Illustration of von Uexküll's *Umwelt* concept. Animals have a limited perception of the world, called their *Umwelt*. Animals only sense features of relevant objects, which release behaviours that feedback into the object, imparting it with a functional significance. Based on Uexküll (1992).

(B) Tinbergen's hierarchical model. Neuronal impulses try to flow down the hierarchy, but are blocked until an appropriate stimulus engages a releasing mechanism. Behaviours cross inhibit one another. Higher-level behaviours emerge from the sequencing of lower-level behaviours. Based on Tinbergen (1951), naming based on Anderson and Perona (2014).

(C) Ewert's model for the release of fixed action patterns for prey catching in toads. Sign stimuli drive actions via releasing mechanisms (RM). Based on Ewert (1987).

1.1 Organisation of behaviour

Behavioural hierarchies

Contemporaries of von Uexküll, including Niko Tinbergen, considered a founding father in the field of ethology, realised that behaviour could be measured, quantified, studied, and formalised into principles. In *The Study of Instinct*, Tinbergen proposed a hierarchical organisation of behaviour (Tinbergen, 1951). This model proposes that behaviour is composed of modules, organised over multiple levels and timescales (**Figure 1B**). At the highest level of the hierarchy, instincts are innate drives that directly promote an animal's survival and reproductive success, such as "feeding" or "reproduction". Next in the hierarchy comes activities, intermediate level behaviours that help to fulfil these drives, such as chasing down prey or courtship. Activities are composed of actions, which "consume" the instinct by fulfilling a specific goal of the animal. These behaviours do not occur randomly, and Tinbergen envisaged a neuronal "block" between levels of the hierarchy. This block is removed only if an appropriate stimulus, called the "sign stimulus", is present in the environment, which can unblock ("release") downstream behaviours via a releasing mechanism. At each level of the hierarchy, behaviours cross-inhibit each other to ensure animals pursue only a single goal at a time, and the "internal state" modulates the expression of behaviours, promoting some and suppressing others. In the absence of sign stimuli, animals engage in spontaneous "appetitive" behaviours that seek an appropriate stimulus to release downstream blocks.

The modular and hierarchical organisation of behaviour has invited comparisons to human language (Flash and Hochner, 2005). Actions might be considered the "syllables" of behaviour; activities the "sentences"; and the rules governing the sequencing of actions into broader activities a kind of "behavioural grammar" (Wiltschko et al., 2015). As such, the organisation of behaviour need not follow a strictly vertical hierarchy, and single actions can be reused between different activities (Egnor and Branson, 2016). Moreover, the action is not necessarily the lowest level of behavioural organisation, but rather can be further decomposed into motor primitives – or "movemes" as an analogy to "phonemes" (Del Vecchio et al., 2003) – the true "atoms" of behaviour (**Figure 1B**).

Experimental observations overwhelmingly confirm the usefulness of Tinbergen's model for understanding behaviour and the brain. Jörg-Peter Ewert's work on prey catching in toads identified distinct actions – orientating, approaching, fixating, snapping – that constitute the behaviour (Ewert, 1987) (**Figure 1C**). Psychophysical experiments identified sign stimuli, typically consisting of worm-shaped objects of a specific orientation, that release each action; and neural correlates of these stimuli and associated actions were identified in the brain.

More recently, computational modelling has confirmed a hierarchical organisation to the spontaneous, grooming, and odour-directed behaviours of flies (Berman et al., 2014; Seeds

et al., 2014; Tao et al., 2019); as well as behavioural sequences in worms, zebrafish larvae, and mice (Gomez-Marin et al., 2016; Marques et al., 2018; Wiltschko et al., 2015). Correspondences between specific sensory stimuli and motor actions have been identified for fly courtship (Coen et al., 2014), zebrafish prey capture (Semmelhack et al., 2014), and visually mediated escapes in insects, fish, and mammals (Klapoetke et al., 2017; Simmons et al., 2010; Temizer et al., 2015; Yilmaz and Meister, 2013). In many cases, the encoding of such sign stimuli was localised to specific neurons. Thus, identifying the building blocks of behaviour, how these building blocks are organised into sequences, and how these sequences are patterned by the stimuli impinging upon an animal's senses are integral to our understanding of the function of nervous systems.

Principles of behavioural organisation

Over recent decades, further principles underpinning the structure of animal behaviour have emerged (**Figure 2**). The existence of elementary building blocks for behaviour is rooted in biomechanics, muscle synergies, and the neural encoding of movement (Berman, 2018; Bizzi and Cheung, 2013; Brown and Bivort, 2018; Flash and Hochner, 2005). Collectively, these restrict the possible postures of an animal and force correlations between the relative positions of body parts. Consequently, posture is observed to be low-dimensional, and we might envisage behaviour as a trajectory through this low-dimensional postural space. Motor primitives or actions are typically short, recurring postural trajectories. The stereotypy and discreteness of behaviour – how similar the same actions are to each other and how different they are from other actions – are other important features to study. Stereotypy and discreteness are observed in the behaviour of flies, worms, and mice (Berman et al., 2014; Stephens et al., 2008; Wiltschko et al., 2015); although in other model systems such as the zebrafish larva it is less clear whether behaviours fall under discrete categories (Marques et al., 2018; Mirat et al., 2013), or exist as a continuum (Borla et al., 2002; Jouary and Sumbre, 2016; Patterson et al., 2013). Finally, researchers are still seeking frameworks for discussing and quantifying the hierarchical organisation of behaviour. Probabilistic models describing transitions between behaviours such as Hidden Markov Models (HMMs) (Katsov et al., 2017; Wiltschko et al., 2015), language-inspired dictionary-based approaches (Gomez-Marin et al., 2016), and dimensionality reduction via transition matrix decomposition (Berman et al., 2016) are among the promising tools deployed in recent years.

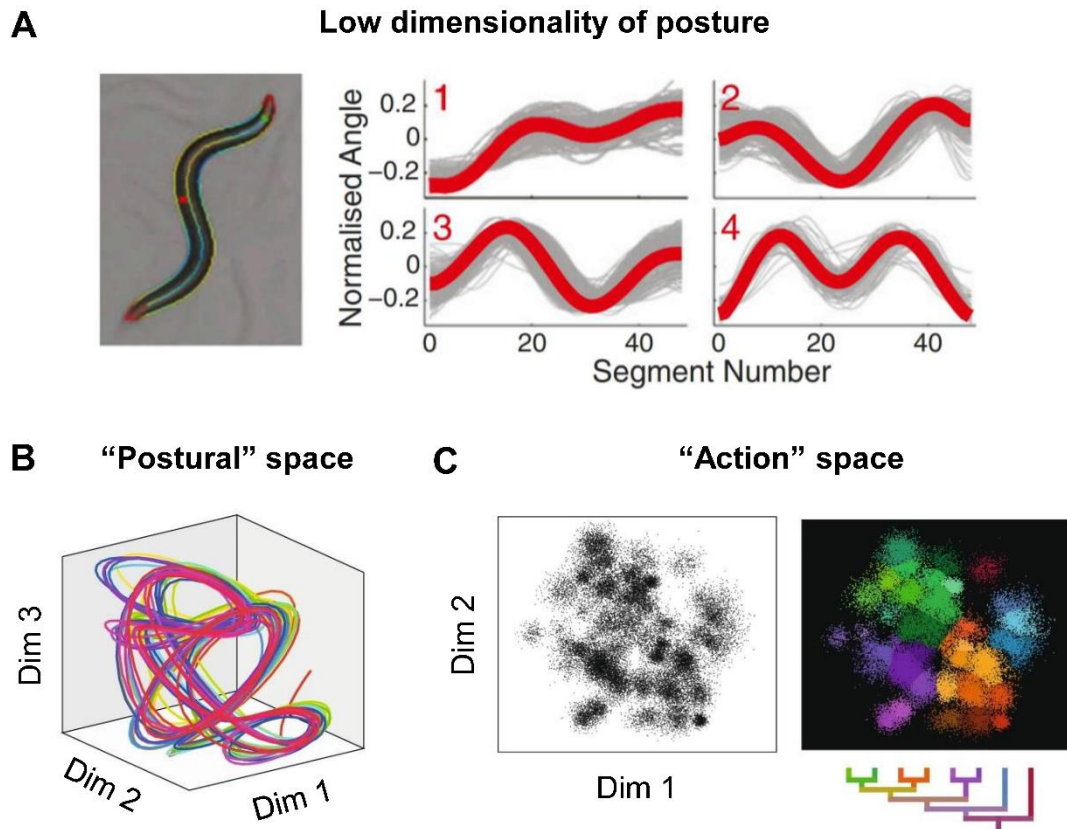


Figure 2. Principles of behavioural organisation

(A) Postural modes of the nematode worm. Correlations between angles along the central body axis as a worm moves allows its posture to be well described by the linear combination of only four shapes. Adapted from Brown et al. (2013).

(B) Illustration of behaviour as trajectories through a low-dimensional postural space. Dimensions in this space represent shapes that, when mixed together in different proportions, describe the posture of an animal. Paths through this space depict changes in posture over time, which recur as behaviours repeat. If new trajectories match past ones precisely, behaviour is stereotyped.

(C) Discreteness and hierarchy in behavioural maps. Points in the map represent entire movements (actions). Neighbouring points represent similar actions and clusters suggest discrete differentiable behaviours. Similar actions might be more likely to occur sequentially during behaviour, suggesting hierarchical organisation.

(B) & (C) adapted from Brown and Bivort (2018).

Prey capture and escape

Behavioural sequences emerge as animals respond to both external cues in the environment, and intrinsic brain activity representing an “internal state”. In the absence of classical “sign stimuli” to drive specific goal-directed movements, intrinsic neural activity predominantly patterns behaviour. Spontaneously generated behavioural sequences still obey a highly structured and hierarchical organisation in worms, flies, fish, and mice (Berman et al.,

2016; Dunn et al., 2016a; Katsov et al., 2017; Stephens et al., 2011; Wiltischko et al., 2015). The presence of salient stimuli in the environment, such as conspecifics, food, or predators, however, further shapes the structure and sequencing of behaviour (Coen et al., 2014; Ewert, 1987; Gomez-Marin et al., 2016; Han et al., 2017; Hinz and Polavieja, 2017; Marques et al., 2018; Tao et al., 2019). Two behaviours that have historically served as important models for the sensorimotor transformations underlying visual behaviour, and its neural circuit basis, are prey catching and escape.

Prey catching and escape are the manifestation of two of the most important drives that animals possess: eat, and don't get eaten. Starkly contrasting, prey capture represents an appetitive behaviour and escape a defensive one. Despite this, mounting evidence suggests that the two share common neuronal substrates. For example, in mammals, neurons in the periaqueductal gray (PAG) are involved in both prey capture and predator avoidance behaviours (Comoli et al., 2003). Similarly, the central amygdala is considered a hub for controlling both defensive and appetitive behaviours (Fadok et al., 2018). The optic tectum (superior colliculus) is implicated in both prey capture and escape in fish (Dunn et al., 2016b; Gahtan et al., 2005; Helmbrecht et al., 2018; Temizer et al., 2015), anurans (Ewert et al., 2001; Nakagawa and Hongjian, 2010), and rats (Sahibzada et al., 1986). In the case of the zebrafish larva, single neurons respond to both prey- and predator-like stimuli and population tuning changes depending on the internal state of the animal (Barker and Baier, 2015; Filosa et al., 2016), suggesting overlapping circuitry for the two behaviours. Remarkably, in some species there is evidence that escaping predators and hunting prey even deploy the same behavioural modules. For example, in the archerfish, high velocity darting swims towards prey are kinematically indistinguishable from escape responses (Wöhl and Schuster, 2007).

Many features of predator- and prey-like stimuli may allow – or necessitate – them to share common representations in the brain. First, an approaching predator will appear to loom on the retina of an animal. The motion of the predator, however, will similarly cause the prey to loom on its own retina. Thus, looming-detectors may respond to both predator and prey stimuli. The rate of this loom is determined by the size and speed of the approaching object. Thus, to disambiguate the two, animals must always be aware of their own motion and predict how it will cause the apparent size of objects in their visual field to change. Animals may also use independent cues to determine the size of objects in their visual field, allowing them to assess whether they are potential food, or potential threats.

Second, and crucial to both behaviours, is attention. Some stimuli, such as the sudden appearance of a predator, require an immediate response from the animal, and bottom-up attentional mechanisms exist to “alert” other circuits to these stimuli. Similarly, if an animal is hungry and actively searching for food, attention circuits might alert the brain to the presence of prey. These attentional mechanisms can suppress ongoing behaviours to promote a

response to the most salient stimulus at a given moment (Knudsen, 2018). Thus, a common attention circuit involved in both prey catching and predator avoidance might coordinate responses to salient stimuli in the environment, regardless of valence.

1.2 Competition in the brain

Feed-forward activation and global suppression

The visual scene can be cluttered with prey, predators, obstacles, conspecifics, and detritus. Somehow, the brain must resolve competing actions to the various sign stimuli that might be present in the visual field. This is particularly challenging for bilaterians (which includes all vertebrates), where each side of the brain might be receiving vastly different representations of the outside world.

In the grooming behaviour of fruit flies, currently active motor programs suppress others; ensuring only one behaviour in the grooming sequence occurs at a time (Seeds et al., 2014). A complementary feed-forward excitation chain exists in songbirds, allowing the orderly sequential execution of song syllables (Long et al., 2010). Global suppression of “weak” stimuli combined with enhancement of “strong” (i.e. salient) stimuli provides a general mechanism for selecting single objects in the visual field for a response (Knudsen, 2018). A feed-forward excitation, such as that found in birdsong production, could also help animals to keep track of salient objects in the visual field. Moreover, there is no reason why such mechanisms should be restricted to operating unilaterally, and could plausibly provide a mechanism for action selection across hemispheres.

However, overlap of the visual field between the two eyes can create duplicated responses to the same object on each side of the brain. In such circumstances, “suppressing” a response to one representation might cause maladaptive behaviour arising from the mislocalisation of objects in space. This creates a correspondence problem: how does the brain know that stimulus-evoked activity in each hemisphere represents the same object in space, or two different objects?

Stereopsis

Once the correspondence problem is solved, animals with binocular overlap in the visual field unlock access to a powerful computation: stereopsis. The distance between the eyes causes each to see a slightly different view of the world. This introduces a relative shift (disparity) between objects in the visual field at different distances, or an absolute shift relative to a reference point on each retina. While parallax, lens accommodation, and changes in angular size on the retina can also provide depth cues for animals, this information can only

be obtained from behaviour (i.e. by moving). Stereopsis allows animals to obtain depth perception “for free” from visual cues alone.

Disparity-detecting neurons are considered hallmarks of stereoscopic depth perception, and are found in the visual cortex of mammals with large overlapping visual fields (Barlow et al., 1967; Hubel and Wiesel, 1970; Ohzawa et al., 1990). However, stereoscopic depth perception also exists in insects such as the praying mantis (which do not have a cortex), and emerges via a different mechanism from mammals (Nityananda et al., 2016, 2018). Non-mammalian vertebrates, such as owls (Willigen, 2011) and toads (Collett, 1977), also use disparity to judge the depth of objects in the visual field. Interestingly, toads seem to use stereopsis to judge the distance to prey prior to snapping. These animals do not have a mammalian-like cortex, and hint that subcortical circuitry might also be able to generate stereoscopic depth perception. The tectum is a large centre of visual processing and a possible site for binocular integration, as is the pretectum, where binocular integration can resolve ambiguous whole-field motion stimuli in fish (Kubo et al., 2014).

1.3 Zebrafish as a model in neuroethology

Fish, representing approximately half of all vertebrate species, have long served as model systems for understanding animal behaviour and its neural basis. Tinbergen’s models of behaviour, for example, were inspired in part by his study of the courtship and territorial displays of sticklebacks. At the same time, neurophysiologists studied large neurons in the brains of fish (first identified in the 19th Century by Ludwig Mauthner) that are responsible for triggering escape responses (Korn and Faber, 2005; Wilson, 1959). Following pioneering work by George Streisinger and colleagues (Streisinger et al., 1981), in the latter half of the 20th Century the zebrafish larva became cemented as a model system for both developmental and behavioural genetics (Neuhauss et al., 1999; Nüsslein-Volhard, 2012), and neuroscience (Kimmel et al., 1982; Metcalfe et al., 1986).

Zebrafish larvae have many favourable characteristics that make them appealing for studying behaviour and its neural basis. First, zebrafish are tractable for large mutagenesis screens, which have identified hundreds of mutants with deficits in visual behaviours (Neuhauss et al., 1999). Large reverse genetic screens are now also possible with state-of-the-art genome engineering tools (Thyme et al., 2019). Thus, the zebrafish larva can help reveal the genetic basis of behaviour. Second, they embody a vertebrate with a limited yet interesting set of behaviours: behaviours that are simple enough to understand, study, map, and comprehend with available technology; and implemented by brains that share homology with other vertebrates. Finally, their small size, transparency, and a menagerie of genetic tools

allows the activity of single neurons throughout the brain to be studied and perturbed non-invasively in live behaving animals (Baier and Scott, 2009).

Zebrafish larvae have been demonstrated to be useful models for both prey capture and escape behaviours. The genetic toolbox has already revealed much of the visual circuitry underlying these behaviours, particularly in the retina, pretectum, and tectum. However, how representations of prey and predators emerge within these circuits, how attentional mechanisms in the brain select which representations an animal should act upon, and how the concatenation of these actions produce coherent, goal-directed behaviour remains less clear.

Zebrafish ethology

Zebrafish larvae swim in bouts, punctuated bursts of tail beating interspersed with periods of quiescence. These swim bouts last hundreds of milliseconds and typically occur with a frequency around once per second. Bouts are not homogeneous (**Figure 3**). The first bouts to be characterised were C-starts, a behavioural response to threatening stimuli widespread among fishes and amphibian larvae (Liu and Fetcho, 1999). From the early 2000's, researchers began investigating other bouts that zebrafish larvae produce. Budick & O'Malley distinguished between routine and escape turns, and distinct slow and fast swimming modes (Budick and O'Malley, 2000). The behavioural repertoire was later supplemented with additional swim types used during prey capture: J-turns, approach swims, and capture swims (Borla et al., 2002; McElligott and O'Malley, 2005; Patterson et al., 2013); delineation of different avoidance bouts such as the O-bend, S-startle and distinct short- and long-latency C-bends (Burgess and Granato, 2007a, 2007b; Liu et al., 2012); and the identification of distinct locomotor gaits (McLean et al., 2007; Müller and van Leeuwen, 2004; Severi et al., 2014). Marques et al. (2018) identified 13 distinct swim types in a comprehensive analysis of zebrafish larval bout diversity over a variety of behavioural contexts. These included the majority of previously identified bouts in addition to novel long- and short-duration strike responses, high-angle turns, and spot-avoidance turns.

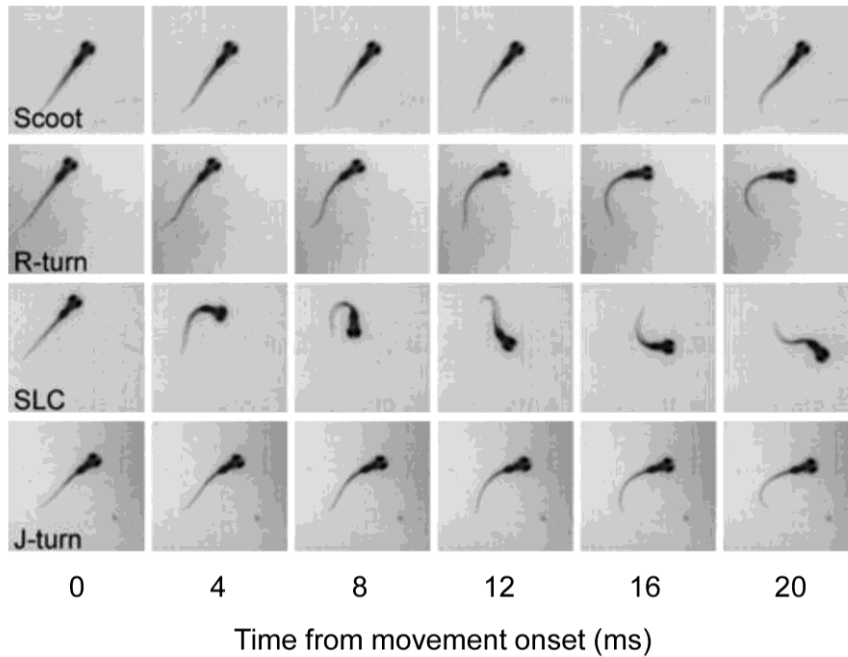


Figure 3. Diversity of zebrafish larval bouts

Examples of a forward swim (Scoot), routine turn (R-turn), short-latency escape response (SLC) and J-turn. Adapted from Fero et al. (2011).

While spontaneous swimming consists of kinematically distinct forward swims and turns (Girdhar et al., 2015; Mirat et al., 2013), such a clear delineation between types is not as obvious in the visually guided bouts that larvae deploy during prey capture (Borla et al., 2002; Jouary and Sumbre, 2016; Patterson et al., 2013). On the one hand, long-lasting large-amplitude J-turns are clearly different from short low-amplitude approach swims. However, whether these bouts belong to clusters of distinct behaviours or represent two extremes of a continuum remains contentious (see Marques et al., 2018). Resolving this will aid in understanding how sensorimotor transformations are realised by the brain (are actions released by unique sign stimuli, or guided by directing stimuli? – to use Tinbergen’s framework). The distinction can also inform hypotheses about how the brain represents these behaviours, with a continuum suggesting possible shared circuitry and discrete clusters opening the possibility for designated neural pathways controlling each behaviour.

Another open question about prey capture in the zebrafish larva is the nature of the final consummatory strike manoeuvre. It has long been clear that the capture does not constitute a single invariant behaviour. Zebrafish larvae, like other fishes, can perform either “ram” or “suction” captures, which involve consuming prey with or without an accompanying tail movement, respectively (Borla et al., 2002; Hernández et al., 2002; Patterson et al., 2013). However, the available evidence suggests that variation exists within the “ram” capture manoeuvre itself (Marques et al., 2018; McClenahan et al., 2012; Westphal and O’Malley,

2013). Again, it is not clear whether this variation reflects distinct modular behaviours or continuous modulation of a common swim pattern. Moreover, even less is known about what features of the stimulus determine which type of strike to perform, although it has been speculated that larvae might use binocular visual cues to determine distance to the prey, which in turn influences behavioural choice (Bianco et al., 2011; Patterson et al., 2013).

Together, these studies provide a strong foundation for mapping the diversity of bout types in zebrafish larvae. Less understood is how goal-directed and adaptive behaviours emerge from combining these bouts into sequences. During spontaneous swimming, larvae preferentially chain together turns in one direction then the other, producing meandering trajectories through the environment (Dunn et al., 2016a). In the natural environment, this exploratory swimming pattern is subject to interruption and modulation by external stimuli and changes in the internal state of the animal. While some bout types are typically only released in response to a limited set of stimuli, such as the O-bend (Burgess and Granato, 2007a), and C- and S-starts (Liu et al., 2012); others may be reused across multiple behaviours (Marques et al., 2018). Understanding the relation between specific stimuli and motor actions has implications for the organisation of sensorimotor circuits in the brain, suggesting one-to-one, one-to-many, or many-to-one mappings between sensory representations and downstream motor systems.

1.4 Organisation of zebrafish visuomotor circuits

Levitis et al. (2009) concisely define behaviour as *“the internally coordinated responses (actions and inactions) of whole living organisms (individuals or groups) to internal and/or external stimuli, excluding responses more easily understood as developmental changes”*. In this view, receptor neurons sense stimuli (internal and external), motor neurons mediate responses (the closing of von Uexküll’s loop), and intervening layers of interneurons coordinate internally. The majority of visually mediated behaviours in vertebrates, including zebrafish, start with photoreceptors in the retina. Retinal layers sequentially process visual information, which is then broadcast to multiple other brain regions exclusively via retinal ganglion cells (RGCs) (**Figure 4A**). These retinorecipient brain regions include the preoptic area, hypothalamus, thalamus, pretectum, and tectum (known as the superior colliculus in mammals). Following this massive divergence, information must eventually converge onto a finite set of motor neurons distributed between the ventral spinal cord and cranial nuclei. Motor neurons innervate muscles, whose coordinated contraction and relaxation effect postural changes in the animal, constituting the “response”.

Retina

Due to the camera-like structure of the vertebrate eye, each part of the retina processes a specific part of the visual field. The nasal retina (nearer to the nose) processes the lateral visual field, and the temporal retina (nearer to the ear) processes the frontal visual field. Similarly, the ventral and dorsal parts of the retina process the upper and lower halves of the visual field, respectively. The two eyes do not necessarily view entirely separate parts of the visual field, as regions of the temporal retinae may point towards the same points in space, creating a dynamic zone of binocular overlap. This zone is especially large when the eyes point forward.

The retina is a layered and heterogeneous structure (**Figure 4A**). At the level of the photoreceptors, visual information is split across four colour channels (fish have a UV cone in addition to the red, green and blue cones present in humans; rods are not functionally integrated into the circuit at the larval stage (Bilotta et al., 2001)). Information then flows vertically to bipolar cells, and then to RGCs. Wiring between the vertical layers as well as laterally acting horizontal and amacrine cells “tune” the responses of bipolar and ganglion cells to specific visual features. Thus within the ganglion cell layer of the retina there emerges multiple intermingled representations of the visual world. Moreover, these representations are not uniform across the retina, but rather features can be differentially processed over space (Baden et al., 2020). Thus, an animal’s perception of its *Umwelt* may vary across its visual field.

In zebrafish larvae, RGCs project to ten arborisation fields (AFs) (Burrill and Easter, 1994). The vast majority of RGCs terminate in AF10, the optic tectum, where they innervate one of nine layers. Many RGCs also project into one or multiple other AFs. The various combinations of retinal morphology and projection targets make for at least 50 morphological RGC types (Robles et al., 2014). Thus, each RGC transmits statistics about a part of visual space to one or multiple target regions, and each AF and tectal layer receives a mixture of representations from multiple RGC types (**Figure 4A**).

The tectum receives retinotopic input, meaning that the map of visual space on the retina is recapitulated spatially along the anatomical axes of the tectum. The temporal retina (frontal, potentially binocular visual field) innervates the anterior tectum, the nasal retina innervates the posterior tectum, the dorsal retina innervates the ventral tectum, and the ventral retina innervates the dorsal tectum (Stuermer, 1988). In other AFs, retinotopy is not necessarily conserved (e.g. AFs 2, 3, 5 and 9), or different parts of visual space may be over-represented (e.g. AF7 has its own retinotopic map but over-represents the temporal retina) (Robles et al., 2014). Moreover, in almost all fish species – zebrafish included – projections from the retina are fully crossed: the left side of the brain only receives input from the right retina and the right

side of the brain only receives inputs from the left retina. Thus, for binocular behaviour to be coordinated, visual information must cross between the hemispheres downstream of the retinal input.

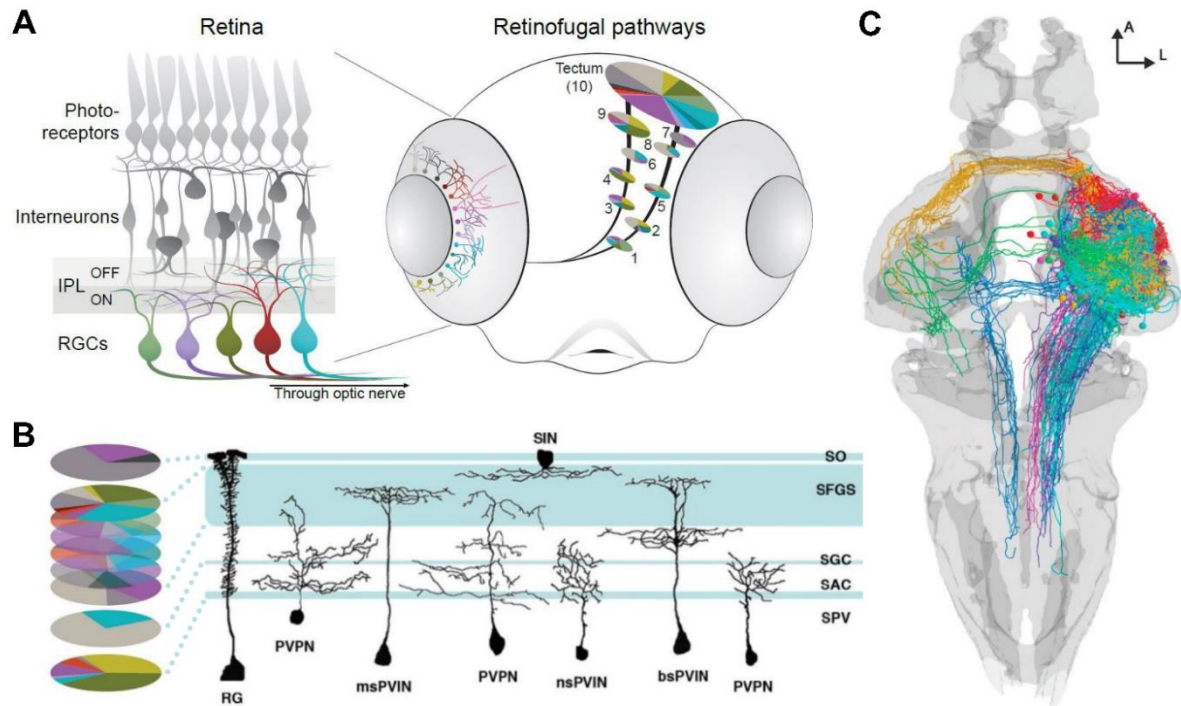


Figure 4. Organisation of the visual system in zebrafish larvae

(A) Encoding of visual features in the retina and brain. Retinal ganglion cells (RGCs) are feature detectors. Ten distinct brain regions receive input from RGCs, each from a specific combination of types, and a single type may transmit information to multiple brain regions. Adapted from Kölsch et al. (2021).

(B) Diversity of cell types in the tectum. Nine layers of the tectal neuropil receive retinal input, each from a different combination of RGC types. Periventricular (PV) neurons integrate and redistribute information across layers. Adapted from Nevin et al. (2010).

(C) Tectofugal projections in zebrafish larvae. Projection neurons transmit information from the tectum to other brain regions via specific anatomical pathways. Adapted from Helmbrecht et al. (2018).

Tectum

Most neurons in the tectum lie in the periventricular (PV) layer and extend neurites into the layered neuropil. These PV neurons exhibit impressive morphological diversity (Förster et al., 2017; Nevin et al., 2010; Robles et al., 2011), often spanning across multiple layers (**Figure 4B**). The primary output neurons of the tectum are periventricular projection neurons

(PVPNs), which represent at least seven distinct morphological types that target combinations of the pretectum, tegmentum, isthmic region, hindbrain, and contralateral tectum (Helmbrecht et al., 2018) (**Figure 4C**). In addition to the PV layer, some neuron somata lie within the tectal neuropil itself. These are the neuropil and superficial interneurons, or, rarely, projection neurons. Such an organisation suggests that the split visual features from the retina recombine across tectal layers. These recombined representations are then distributed to other executive and premotor brain regions.

Neurons in the tectum typically have small receptive fields, preserving the fine-grained topography inherited from the retina (Preuss et al., 2014; Zhang et al., 2011). These small receptive fields may allow larvae to localise small prey items in space (Gahtan et al., 2005), and indeed the superficial tectum receives inputs from RGCs tuned to prey like stimuli (Semmelhack et al., 2014), which appears to be conserved within PV cell populations (Bianco and Engert, 2015).

In addition to prey-like stimuli, the tectum also receives inputs from looming-selective RGCs (Temizer et al., 2015). Similarly, looming-selective responses are observed within tectal cells (Dunn et al., 2016b). Interestingly, some tectal neurons appear to be dually tuned to both small and large objects, suggesting potential overlap in the circuitry that processes prey and threats in the tectum (Barker and Baier, 2015). The majority of studies to date, however, have focussed on either RGC or tectal cell tuning, so it is less clear how the tectum integrates and transforms the visual information it receives from specific RGC channels.

Recently, tools have emerged that allow us to explore the relationship between form and function in tectal neurons (Förster et al., 2018). Moreover, since features are not uniformly encoded across the visual field, tectal microcircuits might similarly differ along visual axes. Helmbrecht et al. (2018) found topographic coding of prey- and predator-like stimuli in the outputs of the tectum, and there is some evidence that the anterior tectum is preferentially involved in processing prey stimuli (Muto et al., 2013). However, a systematic analysis of the functional processing of features by the tectum over the visual field is lacking.

Downstream circuits

The pretectum and tectum receive feature maps of space from the retina. While each pretectal nucleus appears to receive selective inputs from only a subset of RGC types, the tectum receives a less biased overview of the entire visual field. With the myriad of potentially competing and distracting stimuli in naturalistic environments, animals must select a single object for a response to ensure coherent behaviour. The midbrain attention network provides a possible neural substrate for such a computation (Knudsen, 2018).

In addition to encoding visual features, the tectum (superior colliculus) of many species also contains a “saliency map”, encoding the location of conspicuous features in the environment (Ben-Tov et al., 2015; Knudsen, 2018; Koch and Ullman, 1987; White et al., 2017). The formation of this saliency map is thought to consist of two components: focal enhancement of the most salient objects in the visual field, and the global inhibition of all others. Competition between salient stimuli could occur within the tectum itself (Kardamakis et al., 2015), or via a loop with a nucleus at the midbrain-hindbrain boundary known as the nucleus isthmi (Knudsen, 2018).

A saliency map such as that observed in lampreys and birds could implement a system known as “winner-take-all”, whereby a single stimulus is selected for a behavioural response at the expense of all others (Lee et al., 1999). In addition to winner-take-all, however, the superior colliculus (the mammalian homologue of the tectum) implements an integration of stimuli in the visual field, causing an average of competing behavioural outputs to emerge (Lisberger and Ferrera, 1997; Nummela and Krauzlis, 2011). While bottom-up attention is believed to be present in the tectum of fish (Ben-Tov et al., 2015), the mechanism by which fish resolve competing visual inputs to generate an appropriate behavioural response remains to be determined.

1.5 Zebrafish as a genetically tractable system

Behavioural studies can tell us how animals interact dynamically with their environments, and the kinds of computations they might use while doing so. Understanding the “inner world” of animals, however, requires us to measure and manipulate neural activity, ideally in a living, awake, behaving specimen. Measuring neural activity can tell us which neurons might be involved in the production of a behaviour, or perception of a stimulus. Removing those neurons from a circuit allows us to test whether the activity we observed was instructive for producing that behaviour or perception, merely coincidental, or perhaps performing a redundant computation in parallel with other circuits. We can also perturb activity dynamically – asking how an animal's behaviour might change if we temporarily excite or silence a population of neurons during our behavioural paradigms.

The transparency and genetic tractability of the zebrafish larva, along with a plethora of experimental tools, allows us to address such questions non-invasively. Particularly useful in zebrafish are optical methods that allow us to read out and perturb neural circuits with light (Baier and Scott, 2009) (**Figure 5A**). Many of these tools take the form of fluorescent proteins, light-gated ion channels, or enzymes that evolved in other species, and so must be introduced into neurons of interest via transgenesis.

Gal4/UAS

One way to introduce genetically encoded experimental tools into the brain is to take the promoter of a gene expressed in neurons, fuse it to the coding region of a transgene, and integrate the resulting construct into the genome (Higashijima et al., 2000). A more versatile approach involves splitting the expression system in two: having a population of *driver* lines that can drive expression of any tool in some neurons of interest, and a population of *reporter* lines whose genomes contain the tools themselves. Driver lines contain a transcription factor from another species, such as GAL4 from yeast, in their genome under control of a promoter (or enhancer) of interest. In yeast, GAL4 binds to an endogenous promoter element called the UAS and drives expression of downstream genes. Reporter lines contain a transgene under the control of a UAS. Crossing a driver line with a reporter line can produce double-transgenic animals that contain both the GAL4 *and* UAS. In these animals, our genetically encoded protein tools will only be present in the desired subset of cells (**Figure 5B**). One advantage of this system is that *any* driver can be combined with *any* reporter. Thus, when a new driver line is generated it immediately gains access to the complete pool of previously made reporters; similarly, new reporters can be readily combined with any pre-existing driver.

Functional imaging of neuronal activity

Calcium ions are a universal messenger in intracellular signalling pathways. In neurons, membrane depolarisation during action potentials causes calcium to enter the cytosol through voltage-gated channels, and thus intracellular calcium levels provide a proxy for neural activity (Grienberger and Konnerth, 2012). Calcium levels inside neurons can be visualised with the aid of fluorescent calcium indicators, whose fluorescence intensity changes depending on calcium concentration. While synthetic calcium sensors have existed since the 1980's (Tsien, 1980), protein-based sensors allow indicators to be expressed in specific cells using genetic tools (so-called genetically encoded calcium indicators, GECIs). GCaMP is a GECI created by the fusion of GFP with calmodulin (CaM, a calcium-binding protein) (Nakai et al., 2001). Subsequent improvements and modifications to the original GCaMP has provided an array of indicators varying in brightness, binding affinity, and decay rates (Akerboom et al., 2012; Tian et al., 2012).

Visualising neural activity at cellular resolution is further aided by two-photon laser scanning microscopy (Denk et al., 1990). Two-photon microscopy depends on the near simultaneous absorption of two photons to excite a fluorophore. Due to the rarity of the two-photon effect, excitation occurs within a much smaller volume of the imaging beam compared to one-photon methods, providing better optical sectioning. Moreover, the longer wavelength

light used for two-photon microscopy is scattered less by brain tissue, providing deeper penetration into the sample.

The transparency and small size of the zebrafish larva make it conducive to live imaging throughout its entire brain with two-photon microscopy. GCaMP's can be expressed in targeted neuronal populations using direct promoter fusions or bipartite systems like GAL4/UAS. Additionally, infrared light used for two-photon imaging is invisible to the larvae, allowing controlled visual stimuli to be presented (e.g. via a screen) to live behaving animals without interference from the imaging beam. This approach was used to identify AF7 as the target of prey-responsive RGCs (Semmelhack et al., 2014), map tectal responses to prey-like stimuli (Bianco and Engert, 2015), identify neural correlates of visually mediated escapes (Dunn et al., 2016b; Temizer et al., 2015), and identify different tectal output pathways for prey capture and predator avoidance (Helmbrecht et al., 2018). Two-photon calcium imaging can also readily be combined with other techniques, such as modelling of neuronal responses, single cell labelling, targeted ablations of specific populations, and optogenetics to investigate functional connectivity between brain regions and cell types (Orger and de Polavieja, 2017).

Targeted ablation of neurons

In addition to functional calcium imaging, two-photon microscopy provides a means to target single neurons in the brain for ablation (Muto and Kawakami, 2018; Orger et al., 2008). The two approaches can be applied sequentially within the same animal (**Figure 5C**). For example, larvae might be presented with a battery of visual stimuli and the tuning of single neurons measured. Then, functionally characterised neurons can be targeted for ablation with the two-photon laser (Vladimirov et al., 2018). An animal may be imaged again to determine how functional responses of other neurons in a circuit have changed, or freed from the embedding medium (typically agarose) and tested in behavioural assays.

Chemogenetics provides an alternative means to ablate neurons in zebrafish larvae. Nitroreductase (NTR) is a bacterial enzyme that metabolises the prodrug, metronidazole (MTZ). Since NTR is a protein, it can be introduced into specific cell populations via transgenesis, as described above. Upon bath application of MTZ, cells expressing NTR convert the prodrug into cytotoxic compounds, inducing cell death (**Figure 5D**). The approach is particularly useful for ablating a large number of cells, including entire brain regions, or genetically defined cell types. Larvae that have received NTR-mediated ablations are then viable for functional imaging studies, or testing in behavioural assays.

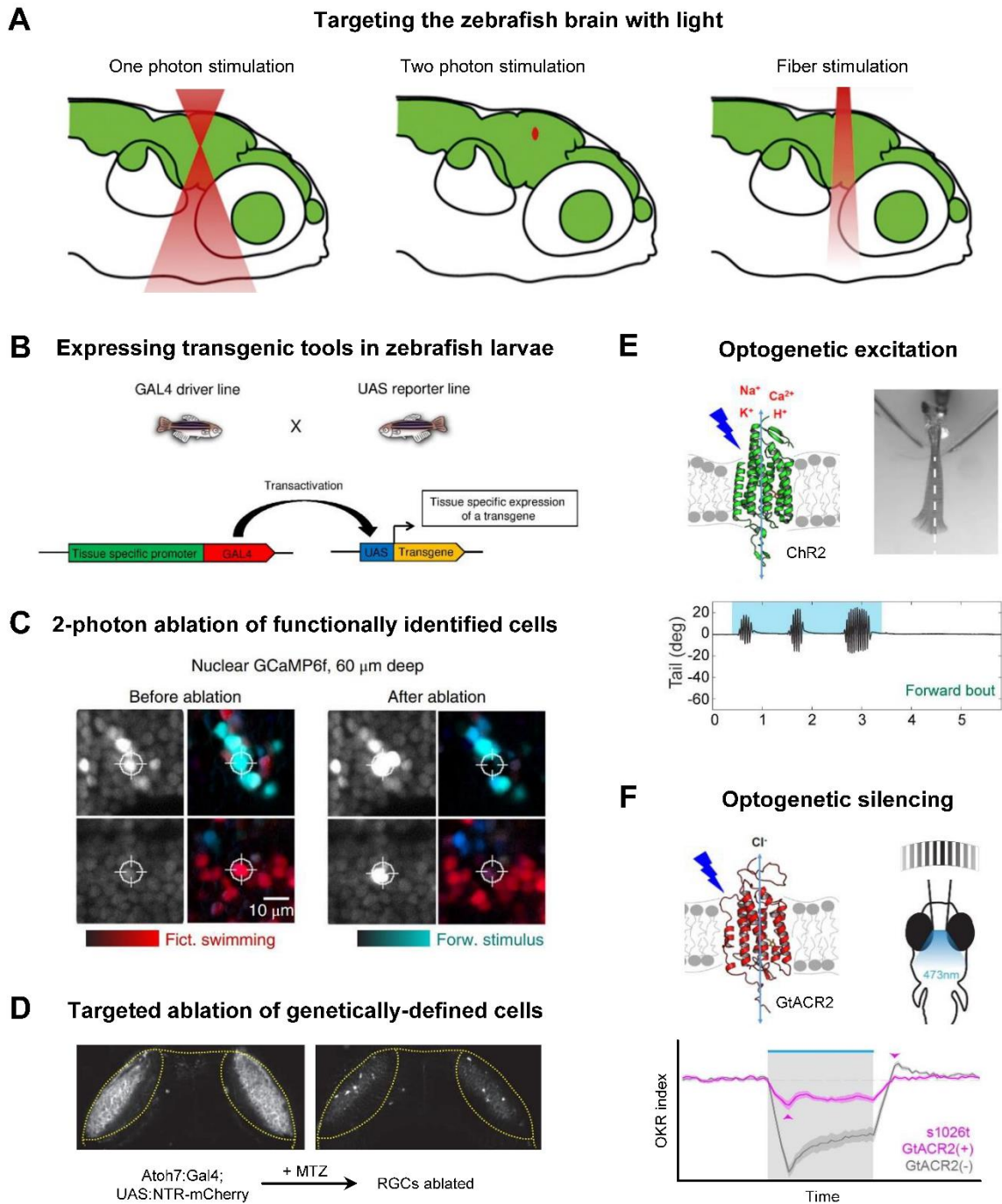


Figure 5. Tools for neural circuit analysis in zebrafish larvae

(A) Methods for targeted imaging and stimulation of the zebrafish larval brain. One photon scanning stimulates a cone through the brain. Two photon scanning stimulates a much smaller volume. An optic fibre will stimulate a column. Adapted from Baier and Scott (2009)

(B) The GAL/UAS system for transgenic expression in zebrafish. Decoupling promoters from transgenes using a bipartite expression system allows for the expression of the same transgenic tool in different cell types, and for the expression of different transgenic tools within the same cell type. Adapted from Sugano and Neuhauss (2013).

(C) Two-photon ablation of functionally identified cells. Imaging GCaMP6f in fish presented with different stimuli, followed by ablation of functionally identified cells. Adapted from Vladimirov et al. (2018).

(D) Targeted ablation of cells using nitroreductase (NTR). Application of the prodrug, MTZ, kills cells that expressing NTR, here tagged with a fluorescent molecule for visualisation, and expressed in RGCs using the GAL4/UAS system. Adapted from Barker and Baier (2015)

(E) Optogenetic elicitation of behaviour using ChR2. Top left: ChR2 is a membrane protein that conducts cations in the presence of blue light. Top right: a larva expressing ChR2 in its tectum was embedded in agarose. Stimulating the tectum with blue light delivered via an optic fibre induced forward swimming (bottom trace). Adapted from Helmbrecht et al. (2018).

(F) Optogenetic inhibition of behaviour using GtACR2. Top left: GtACR2 is membrane protein that conducts chloride in the presence of blue light. Top right: a larva expressing GtACR2 in its pretectum was embedded in agarose and shown a horizontally moving grating, which induces an optokinetic response (OKR). Stimulating the pretectum with blue light reduced the behavioural response to the grating (bottom trace). Adapted from Wu et al. (2020).

Channel schematics in (E) & (F) adapted from Jin et al. (2017).

Optogenetics

Targeted ablations provide a means to remove specific neuronal populations from a circuit, allowing their necessity for behaviour or the acquisition of functional responses in other neurons to be determined. However, these approaches permanently remove neurons from their circuits, and are not practicable for perturbing neural activity on short timescales. Optogenetics provides a means to reversibly and quickly excite or silence neurons non-invasively in live behaving animals.

Channelrhodopsin-2 (ChR2) is a light-gated cation channel found naturally in the green alga, *Chlamydomonas reinhardtii*. Stimulating the channel with blue light induces depolarising currents in cells (Nagel et al., 2003), including neurons (Boyden et al., 2005). In the genetically tractable optically transparent zebrafish larva, ChR2 can be introduced into specific neural populations using transgenesis. Neurons can then be stimulated broadly with, e.g., a blue LED, or in a spatially restricted manner with an optic fibre coupled to a laser, with fine temporal precision (**Figure 5E**) (Barker and Baier, 2015; dal Maschio et al., 2017; Thiele et al., 2014).

Optogenetic tools can also silence neurons with light. The first of these silencers to be developed was halorhodopsin from the archaea *Natronomonas pharaonis* (NpHR) (Zhang et al., 2007). NpHR is a light-activated chloride pump best stimulated with green light, which has successfully be used to investigate the neural basis of behaviour in zebrafish larvae (Arrenberg et al., 2009). However, the relative inefficiency and phototoxicity of halorhodopsin has driven researchers to seek alternative optogenetic silencers (Mahn et al., 2018). Promising among these new silencers are light-gated anion-conducting channels, such as GtACR's from *Guillardia theta* (Govorunova et al., 2015), which have been successfully proven in zebrafish (Antinucci et al., 2020; Mohamed et al., 2017; Wu et al., 2020) (**Figure 5F**).

2. PUBLICATIONS

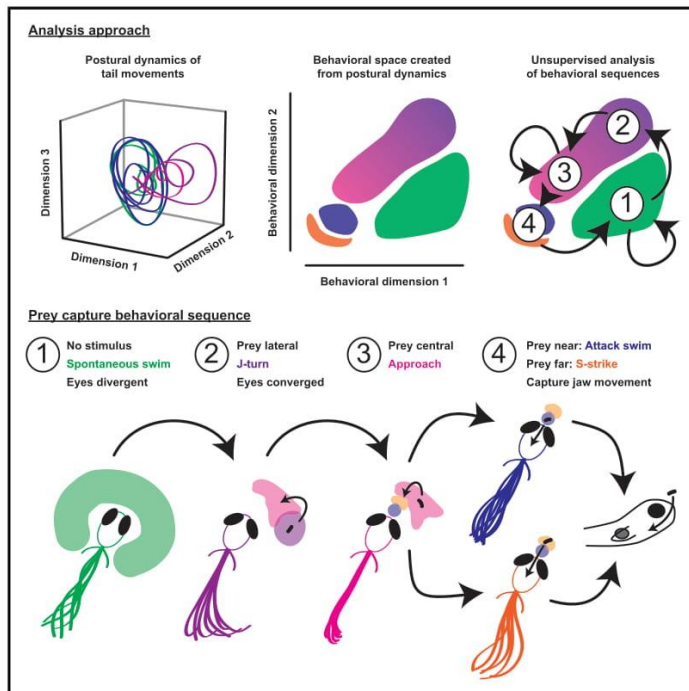
2.1 Deconstructing hunting behaviour reveals a tightly coupled stimulus-response loop

Duncan S. Mearns, Joseph C. Donovan, António M. Fernandes, Julia L. Semmelhack, and Herwig Baier

This article was published in *Current Biology* in January 2020 (Mearns et al., 2020).

Deconstructing Hunting Behavior Reveals a Tightly Coupled Stimulus-Response Loop

Graphical Abstract



Authors

Duncan S. Mearns,
Joseph C. Donovan,
António M. Fernandes,
Julia L. Semmelhack, Herwig Baier

Correspondence

hbaier@neuro.mpg.de

In Brief

Behavioral sequences are shaped by an animal's interaction with its environment. Mearns et al. find that, during hunting, zebrafish larvae adaptively interact with their prey through continuous integration of visual information. When prey reach a precise location in the binocular visual field, larvae perform a stereotyped strike maneuver.

Highlights

- Zebrafish hunting consists of stereotyped transitions in a behavioral continuum
- Chaining successive hunting bouts depends on short-term high-acuity visual cues
- Larvae capture prey from below with stereotyped jaw and tail movements
- Precise positioning of prey in the strike zone depends on binocular visual cues



Mearns et al., 2020, Current Biology 30, 54–69
January 6, 2020 © 2019 Elsevier Ltd.
<https://doi.org/10.1016/j.cub.2019.11.022>

CellPress

Deconstructing Hunting Behavior Reveals a Tightly Coupled Stimulus-Response Loop

Duncan S. Mearns,^{1,2} Joseph C. Donovan,¹ António M. Fernandes,¹ Julia L. Semmelhack,^{1,3} and Herwig Baier^{1,4,*}

¹Max Planck Institute of Neurobiology, Department of Genes – Circuits – Behavior, Am Klopferspitz 18, 82152 Martinsried, Germany

²Graduate School of Systemic Neurosciences, 82152 Martinsried, Germany

³Hong Kong University of Science and Technology, Division of Life Science, Clearwater Bay, Hong Kong, China

⁴Lead Contact

*Correspondence: hbaier@neuro.mpg.de

<https://doi.org/10.1016/j.cub.2019.11.022>

SUMMARY

Animal behavior often forms sequences, built from simple stereotyped actions and shaped by environmental cues. A comprehensive characterization of the interplay between an animal's movements and its environment is necessary to understand the sensorimotor transformations performed by the brain. Here, we use unsupervised methods to study behavioral sequences in zebrafish larvae. We generate a map of swim bouts, revealing that fish modulate their tail movements along a continuum. During prey capture, larvae produce stereotyped sequences using a subset of bouts from a broader behavioral repertoire. These sequences exhibit low-order transition dynamics and immediately respond to changes in visual cues. Chaining of prey capture bouts is disrupted in visually impaired (*lakritz* and *blumenkohl*) mutants, and removing the prey stimulus during ongoing behavior in closed-loop virtual reality causes larvae to immediately abort the hunting sequence. These results suggest that the continuous integration of sensory information is necessary to structure the behavior. This stimulus-response loop serves to bring prey into the anterior dorsal visual field of the larvae. Fish then release a capture strike maneuver comprising a stereotyped jaw movement and tail movements fine-tuned to the distance of the prey. Fish with only one intact eye fail to correctly position the prey in the strike zone, but are able to produce the strike itself. Our analysis shows that short-term integration of binocular visual cues shapes the behavioral dynamics of hunting, thus uncovering the temporal organization of a goal-directed behavior in a vertebrate.

INTRODUCTION

Quantitative descriptions of behavior are essential if we are to fully understand the brain [1]. Such descriptions have provided a framework for interrogating the genetic and neural basis of behavior in worms, flies, and mice [2–5]. It is believed that

complex, flexible behavior arises as a result of animals chaining together simpler, more stereotyped movements [6–8]. These movements have been termed motor primitives [9], synergies [10], movemes [11], or behavioral modules [5, 7, 12–14]. However, whether such modules truly constitute stereotyped, invariant movements or whether they merely reflect extremes in a behavioral continuum remains unclear [12, 14–17].

Animals chain their movements into sequences to achieve their desired goal. Such sequences may be stereotyped, with the behaviors chaining together in a similar way with each occurrence [18]. Alternatively, sequences may be flexible, with the ordering of modules different each time they appear. In such cases, sequences may be hierarchically organized, whereby switching between modules is stochastic but influenced by longer-term behavioral states or sensory stimuli [5, 19–21]. Classically, fixed-action patterns have described behaviors in which a single “releasing” stimulus is sufficient to drive an entire sequence of movements [8]. Alternatively, in a stimulus-response loop each movement generates a new sensory stimulus for the animal that, itself, serves as a trigger for the next movement in the chain [22].

Capturing prey is an innate and essential behavior for the survival of many animals. Zebrafish larvae hunt protists that float in the water column [23–25]. Both real and virtual prey presented to restrained animals can produce isolated orienting swim bouts and eye convergence, hallmarks of prey capture in zebrafish larvae [26–28]. Such movements could form a stimulus-response loop, whereby movements of the tail and eyes bring prey to the near-anterior visual field of the animals [16, 29]. However, it is not clear whether this would be implemented by gradual changes in the kinematics of bouts over the course of a hunting sequence [16,23], or as a result of discrete switches between more stereotyped motor patterns [14]. One possibility is that different stages of the behavior have a different organization. For example, animals might dynamically modulate their movements to adjust to the position of the prey during pursuit, but resort to more stereotyped motor patterns when consuming prey [22]. Studies of prey capture have predominantly focused only on tail, jaw, or fin movements, and it is not known how these movements are coordinated over the behavioral sequence [16, 23, 30, 31]. Moreover, it has been speculated that binocular overlap in the visual field produced during eye convergence is necessary to bring prey into a “strike zone” that triggers the final capture bout [16, 26, 32]. The necessity of binocular vision for hunting, however, has not been tested.



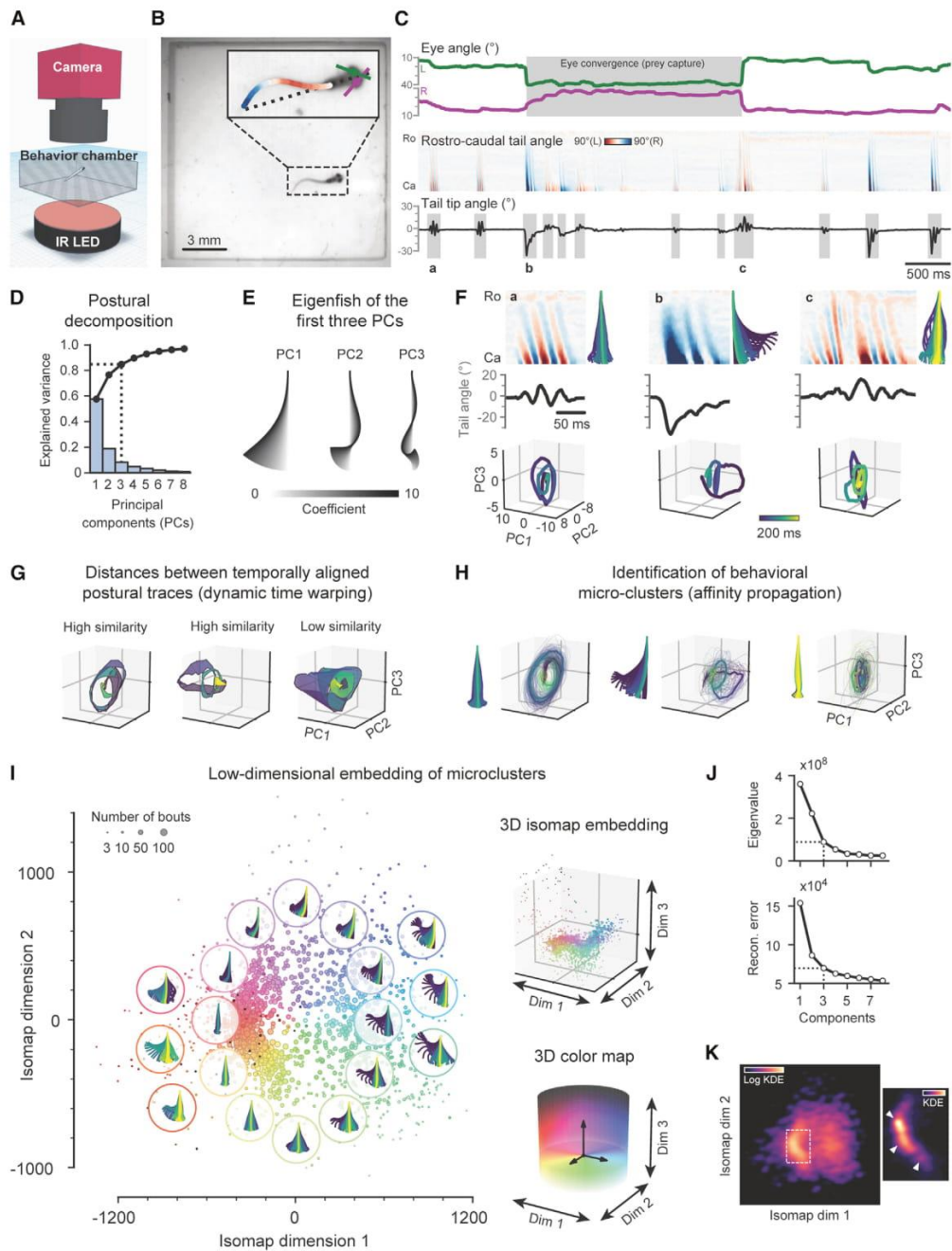


Figure 1. Zebrafish Larva Bouts Lie on a Behavioral Continuum

(A) Schematic of the setup used to record behavioral data.

(B) Example high-speed video frame. Inset overlaid with tail and eye tracking.

(C) Eye and tail kinematics extracted from 6 s of recording. Ro, rostral; Ca, caudal.

(D) Principal component analysis (PCA) of tail shapes. Explained variance (bars) and cumulative explained variance (points) of the first eight components. We retained three components (dotted line).

(E) “Eigenfish” of the first three PCs.

(legend continued on next page)

Here, we present a new computational framework for decomposing an animal's movements into kinematic and transition components. We apply our pipeline to the bouts of zebrafish larvae and find a continuum of behaviors. We use unsupervised analysis of behavioral transitions to reveal stereotyped chaining during prey capture through a subset of these bouts. These sequences emerge from a stimulus-response loop in which the fish's movements generate new stimuli that trigger subsequent bouts in the chain. Prey capture sequences are disrupted when we interfere with visual processing using genetic mutants or remove visual cues after the behavior is initiated. Further investigating the capture strike, we show discreteness in tail and jaw movements during this behavior. In addition, our approach reveals changes in the prey capture dynamics of monocularly blinded fish, impeding their ability to bring prey into the final "strike zone."

RESULTS

Zebrafish Swim Bouts Lie on a Low-Dimensional Behavioral Continuum

We sought a representation of zebrafish behavior that would reveal whether different bout types are truly stereotyped and discrete, or whether the kinematics are more graded. We recorded and tracked individual zebrafish larvae (7–8 days post-fertilization [dpf]; $n = 45$) hunting live prey (paramecia) in a custom-built behavioral arena (Figures 1A–1C; Video S1; STAR Methods). We analyzed 57,644 individual swim bouts with a pipeline involving four main steps. First, we reduced the dimensionality of our tracked data (Figures 1D–1F). Second, we computed the distance between each pair of bouts (Figure 1G). Third, we combined similar bouts into exemplars by micro-clustering (Figure 1H). Lastly, we performed non-linear embedding using the distances between these exemplars to generate the final behavioral space (Figures 1I–1K and S1).

Mechanical and neural constraints impose limits on the possible posture configurations for an animal; thus, movements are generally believed to lie on relatively low-dimensional manifolds [7, 12, 17, 33, 34]. As our tracking provides overly redundant measurements along the tail, we performed principal component analysis (PCA) on the sequence of all tail postures. Three PCs explained 85% of the variance in tail shape (Figure 1D). These PCs define postural modes and can be represented by a set of tail shapes known as "eigenfish" [17, 34, 35] (Figure 1E). As posture is dynamic over time, these shapes trace a trajectory in three-dimensional coordinate space (Figure 1F; Video S2). Retaining more than three postural modes did not

alter the final structure of the behavioral space (Figure S1A). Thus, the tail kinematics of zebrafish larva bouts can be accurately represented in this lower-dimensional space.

To measure the distance between different bouts of temporally varying postures, we used dynamic time warping (DTW), which handles temporal offsets and small variations better than Euclidean distance [36, 37] (Figure 1G). From these distances, we generated micro-clusters (each represented by a single exemplar) using affinity propagation [38] (Figure 1H). Micro-clustering serves numerous functions that aid with embedding and subsequent analysis. It robustly handles the non-metric distances obtained from DTW [38], removes rare or spurious events, and prevents common trajectories from dominating the embedding. Furthermore, we can conveniently embed data collected in different experiments by aligning to exemplars. Altering the number of exemplars did not strongly influence the structure of the final behavioral space (Figure S1B).

Next, we performed isomap embedding [39] using the DTW distances between exemplars (Figure 1I), which preserves global behavior structure preferentially to local structure. We could not discern any additional structure if we embedded all bouts, suggesting that we were not losing information about the structure of behavior by only embedding exemplars (Figure S1E). We found that three dimensions were sufficient to capture most of the variation in bout kinematics, as indicated by an elbow in both the eigenvalues and reconstruction error of the embedding (Figure 1J). Inspecting bouts that are represented in different regions of the behavioral space (Figure 1I), we found capture strikes (far left) [14, 40], forward scoots (lower left) [24, 41], routine turns (right) [24, 41], and J-turns characteristic of prey capture behavior (top) [25]. Our results suggest that turn angle, swimming speed, and tail laterality are the dominant kinematic features that define global bout structure (Figure S1F). Overall, we observed a high degree of continuity across bouts, consistent with earlier descriptions of zebrafish behavior [16, 23, 36].

To confirm that the apparent continuity in the behavior was not an artifact of the isomap embedding, we also performed t-SNE (Figure S1C) and UMAP (Figure S1D). While UMAP also revealed a more continuous behavioral space, t-SNE suggested a small degree of local clustering may be lost in our approach, mostly within the forward scoots (Figure S1C). Closer inspection of our isomap space, accounting for local structure preserved in the micro-clusters, recapitulated these local densities (Figure 1K). Thus, our results suggest a structure to zebrafish behavior that is largely continuous, with some local densities representing more stereotyped types of forward swim.

(F) Three example bouts, labeled a–c in (C). For each bout, we show curvature along rostral-caudal axis of the tail over time, trajectory through the first three PCs, and sequence of tail shapes reconstructed from PCs.

(G) Bout pairs aligned using dynamic time warping (DTW). High similarity, small sum of Euclidean distances between aligned points, represented by ribbon stretched between trajectories. Low similarity, large sum of distances.

(H) Bout micro-clusters identified with affinity propagation (thin lines). Thick line, exemplar. Left subpanels: tail movement represented by the exemplar.

(I) Isomap embedding of DTW distances between exemplars. Left: projection onto the first two dimensions. Right: projection onto first three dimensions. Points colored according to position within a hue-lightness cylinder centered on origin.

(J) Eigenvalues (top) and reconstruction errors (bottom) of the isomap embedding. We retained three components (dotted line).

(K) Kernel density estimation of bout density over first two isomap dimensions. Right: forward scoot region of the behavioral space (white dotted outline). Arrowheads: local densities.

See also Figure S1 and Videos S1 and S2.

Behavioral Sequences Are Built from a Small Number of Simple Chaining Rules

Next, we investigated the temporal organization of bout sequences for structure and stereotypy (Figure 2A). To this end, we decomposed the one-step transition frequency matrix between micro-clusters into a set of “transition modes,” each of which captures some feature of temporal behavioral dynamics (Figures 2B and S2B). Since the matrix is sparse, we first smoothed transitions using bout distances in behavioral space, as bouts with very similar kinematics likely share similar transitions (Figure S2A). We were particularly interested in three types of transition mode that can be obtained from this decomposition: the “common” mode, symmetric modes (S-modes), and anti-symmetric modes (A-modes). The common mode reflects the most commonly visited micro-clusters across all transitions. S-modes recover groups of bouts that contribute to a “sticky” behavioral state [42]. A-modes highlight dynamic transitions between groups of bouts. Each transition mode is associated with a singular value, which describes how much that mode contributes toward the overall transition structure.

The majority of transitions in our data were explained by a combination of the common mode, one S-mode, and one A-mode (Figure 2C, elbow in the singular values). To test whether the dynamics captured by these modes were consistent across animals, we tested our ability to predict the transitions performed by half of the animals using transition modes obtained from the other half (Figure 2D; STAR Methods). We found that the first S-mode (S1) improved our behavior prediction by 31% over a null model consisting only of the common mode (31.4 ± 4.5 , mean \pm SD), and the first A-mode (A1) improved our behavior prediction by 2% (2.0 ± 0.54 , mean \pm SD).

Next, we investigated which transitions were represented by each significant transition mode (Figures 2E–2G). We found that S1 separated approach swims from larger spontaneous swims and turns (Figure 2F). A1 appeared to represent transitions through J-turns, approach swims, and capture strikes, bouts classically associated with prey capture (Figure 2G). To confirm this, we used eye convergence as an independent measure of hunting behavior (Figure 2H) [26]. We identified bouts that occurred when the eyes were and were not converged (“prey capture” and “spontaneous,” respectively) and found that these correlated with S1 (Spearman’s $r = 0.71$) (Figures 2F and 2I). Furthermore, by studying changes in eye convergence, we could identify bouts that occurred at the beginning, middle, and end of a hunting sequence. This demonstrated that A1 accurately recovered behavioral sequences during prey capture ($r = 0.45, 0.41, 0.41$; A1 with early, mid, late prey capture) (Figures 2G and 2J). We then recorded fish swimming in the absence of prey and mapped their bouts into our behavioral space by alignment to the exemplars. Performing SVD of this spontaneous behavior revealed a dominant common mode and no significant A-modes (Figure S3). Thus, zebrafish larvae have a unique repertoire of bouts reserved for hunting and produce stereotyped and dynamic sequences using these bouts.

Seven Clusters in the Behavioral Space Correspond to Broad Bout Types

We next assigned labels to different parts of the behavioral space. This approach has three benefits. First, it allows us to

relate different regions of our space to bout types identified through other expert- and machine-annotated descriptions of behavior [14, 41] (Figures 3B and 3C). Second, larger clusters provide more robust states for Markov chain analysis than micro-clusters (Figures 3D–3G). Third, by integrating over many bouts, we can generate maps of stimuli that are associated with different regions of the behavioral space (Figure 3H).

To generate such labels, we generated a new behavioral space, accounting for both kinematic similarity and similarity in chaining structure (Figure 3A; STAR Methods). Kinematic similarity between exemplars was determined using DTW distances (Figure 1G). Chaining similarity was determined by finding exemplars that contributed similar weights to the transition modes (Figures 2F and 2G). We multiplied these numbers and proceeded with isomap embedding to generate the new space. Hierarchical clustering separated bouts into seven types (Figure S4A), corresponding to J-turns, approach swims, “slow 1” swims, capture strikes, “slow 2” swims, high-angle turns (HATs), and routine turns described in previous studies [14, 25, 41] (Figure 3B; Video S3). J-turns, approach swims, and capture strikes occupy the prey capture region of the behavioral space and predominantly occurred when the eyes were converged (Figures 3C and S4B). “Slow 2” swims, HATs, and routine turns were performed by fish during spontaneous swimming. “Slow 1” swims contributed to both prey capture and spontaneous behavior. Thus, taking transition dynamics into account, we could relate regions of our behavioral space to known bout types of zebrafish larvae and demonstrate the differential contributions of these swims to spontaneous and prey capture behavior.

Prey Capture Sequences Are Maintained through Tight Stimulus-Response Loops

Next, we wanted to test whether transition dynamics were shaped by short- or longer-term memory processes. We constructed a family of models using our behavioral clusters as states in a Markov chain and quantified how longer memories affected prediction of the next bout in a sequence (Figures 3D and 3E; STAR Methods). The default model contained no memory, and for all bout clusters (excluding capture strikes) prediction of the following bout could be improved by including knowledge of the previous bout label (J-turn, 43%; approach, 47%; slow 1, 8%; slow 2, 71%; HAT, 13%; routine turn, 118%). Our prediction of bouts following capture strikes was generally poor, possibly due to more variability within this cluster (Figure 3B). Further increasing the memory of previous bouts in a sequence did not improve prediction for bouts following J-turns, approach swims, or “slow 2” swims, though it did slightly improve performance for “slow 1” swims, HATs, and routine turns (7%, 5%, and 26%, respectively) (Figures 1E and S4C). This indicates that the preceding bout is a strong predictor of transition dynamics, which is compatible with “memoryless” behavior driven by a stimulus-response loop.

To investigate the most common transitions underlying predictable behavioral sequences, we visualized transitions as an ethogram (Figure 3F). The most likely transitions were from J-turns and approaches to another approach (>40%). Moreover, we found elevated transition probabilities between “slow 2” swims, HATs, and routine turns (11%–42%), and high probabilities of transitioning to “slow 1” swims from most other behaviors

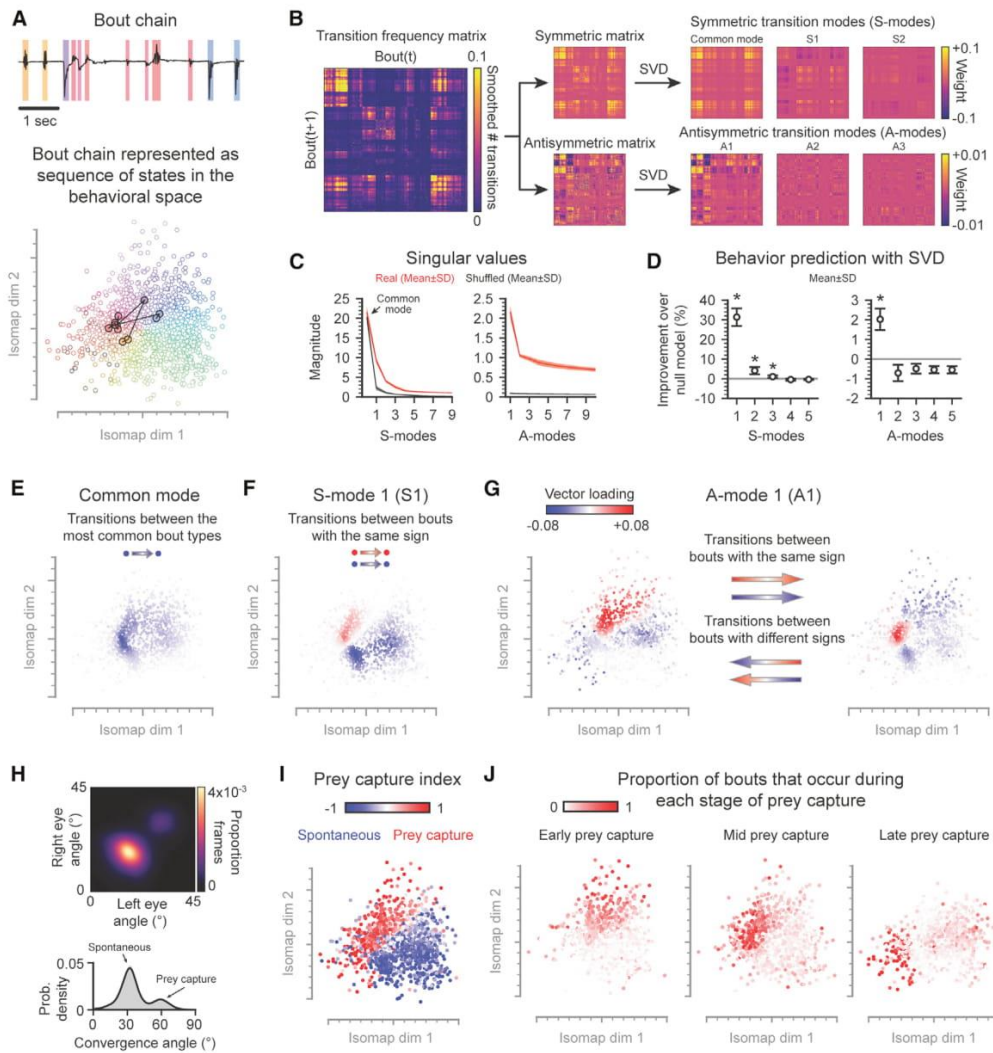
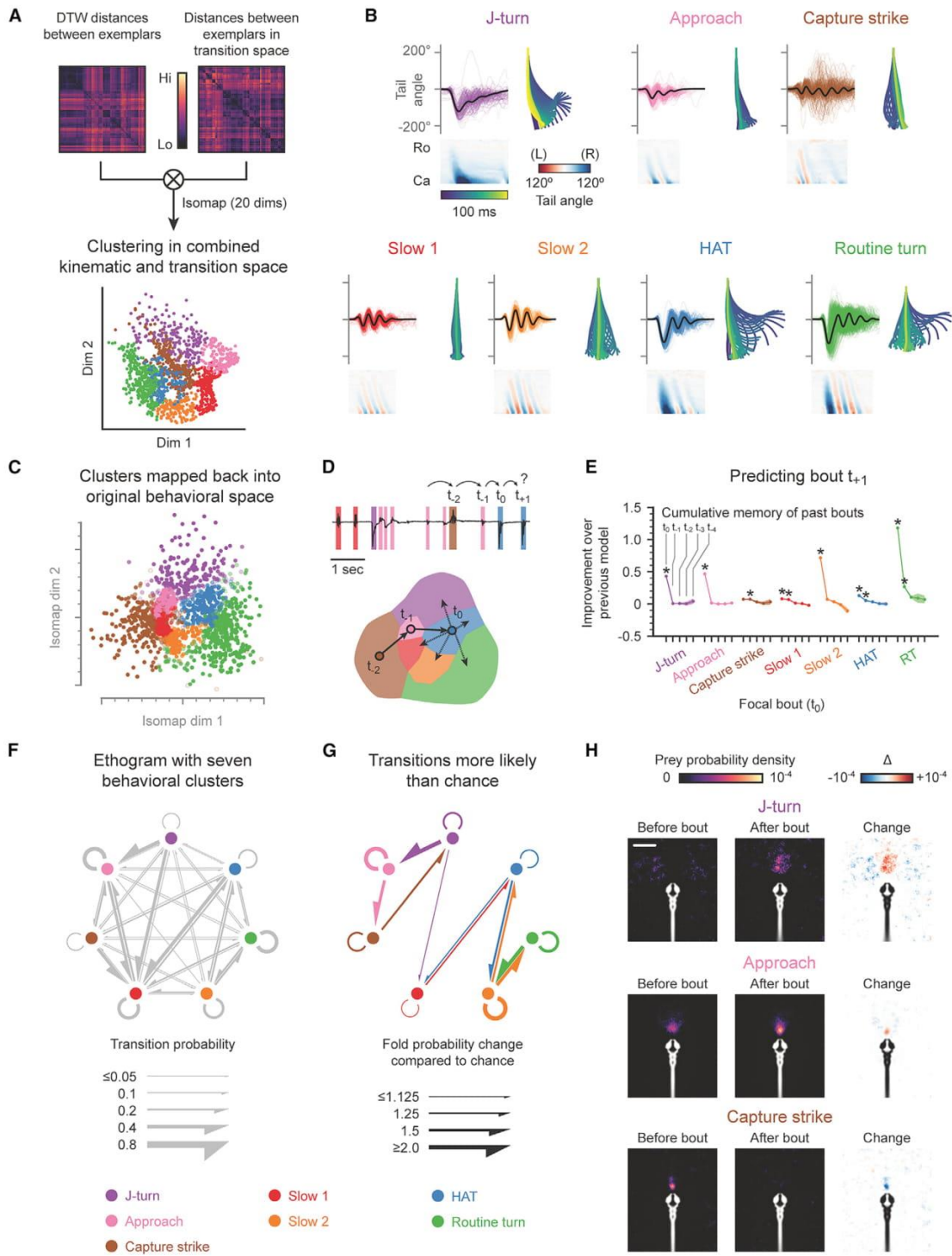


Figure 2. Singular-Value Decomposition Reveals Behavioral Dynamics

(A) Top: tail tip angle trace from Figure 1C. Bouts color-coded according to position in the behavioral space (bottom).
 (B) Decomposition of the transition frequency matrix (smoothed, obtained from all bouts) into transition modes by singular-value decomposition (SVD).
 (C) Singular values of the symmetric (left) and antisymmetric (right) components of the transition frequency matrix. Mean \pm SD over 10,000 partitions of the data (shaded area). Observed transitions (red), shuffled transitions (gray).
 (D) Improvement of behavioral prediction each transition mode offers over common mode. Mean \pm SD over 10,000 partitions. Left: S-modes. Right: A-modes. * $p < 0.001$, permutation test.
 (E–G) Contribution of each micro-cluster to selected transition modes.
 (E) Common mode. Color intensity reflects how often each position in space was visited.
 (F) S1, represented by a single vector. Transitions occur between bouts with the same sign (color).
 (G) A1, represented by a pair of vectors. Bouts with a given sign on the left transition to bouts with the same sign on the right. Bouts with a given sign on the right transition to bouts with the opposing sign on the left.
 (H) Top: 2D histogram of eye angles across all frames. Bottom: bimodal distribution of eye convergence angles across all frames. Local minimum in the eye convergence distribution provides a threshold for defining prey capture behavior.
 (I) Prey capture index of each micro-cluster. Index defined as (# prey capture bouts – # spontaneous bouts)/(# total bouts).
 (J) Proportion of bouts in each micro-cluster that occur during early (eyes converge during bout), middle (eyes are converged), or late (eyes de-converge during bout) prey capture.

See also Figures S2 and S3.



(legend on next page)

(15%–39%). To investigate which of these transitions were significant, we compared the observed probabilities to randomly shuffled bout sequences (Figure 3G). This corroborated the results of our SVD analysis, revealing unidirectional chaining through J-turns, approaches, and capture strikes that were >50% more likely than chance, as well as enriched transitions between spontaneous clusters (17%–127% increase).

We next calculated the probability density of a paramecium being within a certain area of the visual field before and after each type of bout (Figures 3H and S4D; STAR Methods). We found that J-turns were initiated when prey lie in the lateral visual field (~45° from midline) and served to center prey in the anterior visual field (~1° from midline) (Figure 3H, top). This new stimulus correlated with the onset of approach swims, which moved prey toward a stereotyped position in the near-anterior visual field (Figure 3H, middle). “Slow 1” swims occurred if prey were further away (Figure S4D). Prey in the near-anterior visual field (~0.4 mm from the fish) were associated with capture strikes (Figure 3H, bottom). Thus, the successive transformation of the visual scene as a result of the fish’s own motion could account for the stereotyped sequence through bouts we observed during prey capture. We do not find such stereotyped stimuli associated with spontaneous swims (Figure S4D), so bidirectional transitions between different types of forward swim and turn during this behavior are likely mediated by internal rather than external factors [43, 44].

Genetic Disruptions of Vision Do Not Change Bout Kinematics, but Alter Behavioral Dynamics

To explore how sensory cues orchestrate prey capture sequences, we tested fish larvae with perturbations of their visual system. *Lakritz* mutants (*lak^{th241}*) [45, 46] are blind due to a null mutation in *atonal homolog 7 (atoh7)*, a transcription factor necessary for RGC development (Figure 4A, middle). SVD revealed that key transition modes associated with prey capture were absent in *lak* mutants (absolute cosine similarity: 0.59, common; 0.13, S1; 0.06, A1) compared to wild-type sibling controls (similarity: 0.96, common; 0.88, S1; 0.72, A1) (Figures 4B and 4C, middle). We also performed pharmacogenetic ablation of RGCs after fish had already had prey capture experience [47] (Figure S5A). Ablated fish lacked normal prey capture

dynamics, which were present in sibling controls (similarity: 0.58, common; 0.13, S1; 0.12, A1) (Figures S5B–S5D). These results demonstrate that the stereotyped behavioral sequences that occur during prey capture are innate and, under normal light conditions, depend on vision.

We next investigated the effect of a more subtle mutant phenotype on the structure of prey capture behavior. *Blumenkohl* mutants (*blu^{tc257}*) [46] carry a mutation in *vglut2a*, a gene encoding one of the vesicular glutamate transporters expressed by RGCs. These mutants grow larger RGC axonal arbors in the tectum and show decreased visual acuity (Figure 4A, bottom) [48]. Mutants performed more spontaneous bouts than heterozygous sibling controls (similarity between common modes: 0.64) (Figure 4B, bottom). Controls exhibited normal prey capture dynamics (similarity compared to wild-types: 0.95, common; 0.93, S1; 0.87, A1), while mutants lacked the prey capture-associated transition modes (similarity compared to control: 0.64, common; 0.08, S1; 0.10, A1) (Figures 4C and S6A–S6C). Studying stimuli associated with different bout types in these animals revealed that mutants performed J-turns when prey were closer, consistent with reduced visual acuity and accounting for the observed reduction in their hunting activity (Figures 4D, S6D, and S6E).

Virtual Reality Experiment Reveals that Hunting Requires a Sustained Prey Stimulus

Fish larvae may make moment-to-moment decisions during hunting. Alternatively, a single releasing stimulus may be sufficient to drive the behavior to completion. We developed a free-swimming virtual prey capture assay that allowed us to control the visual cues presented to an animal (Figure 4E; STAR Methods). Projecting small white dots moving with paramecium-like kinetics on the surface of the water reliably triggered prey capture in 40% of animals tested (17/41, >5% time spent with eyes converged when stimulus present). We presented animals with “persisting” trials during which larvae were allowed to hunt virtual prey objects *ad libitum*, and “vanishing” trials during which prey disappeared as soon as eye convergence was detected online (Figure 4F). Hunting sequences were significantly shorter during vanishing trials, and this was significant across all responsive fish (mean 1.38 versus 0.82 s) (Figure 4G). Hunting sequences also consisted of fewer bouts during vanishing trials,

Figure 3. Prey Capture Dynamics Arise through a Stimulus-Response Loop

(A–C) Clustering bouts.

(A) Generating a combined kinematic-transition space. Seven behavioral clusters are defined using hierarchical clustering in 20 dimensions of this space (first two shown).

(B) Example bouts from seven behavioral clusters. Subpanels: individual tail angle traces in color with the average in black (top left); tail kinematics of a representative bout (bottom); tail reconstruction of the representative bout (right). HAT, high-angle turn.

(C) Isomap from Figure 11 showing location of behavioral clusters.

(D and E) Predicting the next bout in a behavioral sequence.

(D) Top: bout sequence from Figure 1C color-coded according to cluster. Bottom: schematic partitioning of the behavioral space into bout types, showing part of the above bout sequence.

(E) Incremental improvement over previous model prediction when successively adding memory of previous bouts in a sequence. Mean improvement ± SEM (*p < 0.01, Student’s t test, Bonferroni correction).

(F) Quantitative ethogram of zebrafish swimming behavior during prey capture. Colored circles represent behavioral clusters; gray arrows indicate probability of transitioning between clusters.

(G) Transition probabilities between clusters significantly higher than chance (*p < 0.05, permutation test, Holm-Bonferroni correction). Arrows show fold change in probability compared to shuffled data.

(H) Transformation of prey probability density in the visual scene during J-turns, approaches, and capture strikes in fish-centered coordinates. Images are thresholded using the 85th percentile. Average fish outline in white (left, center) or black (right). Scale bar, 1 mm.

See also Figure S4 and Video S3.

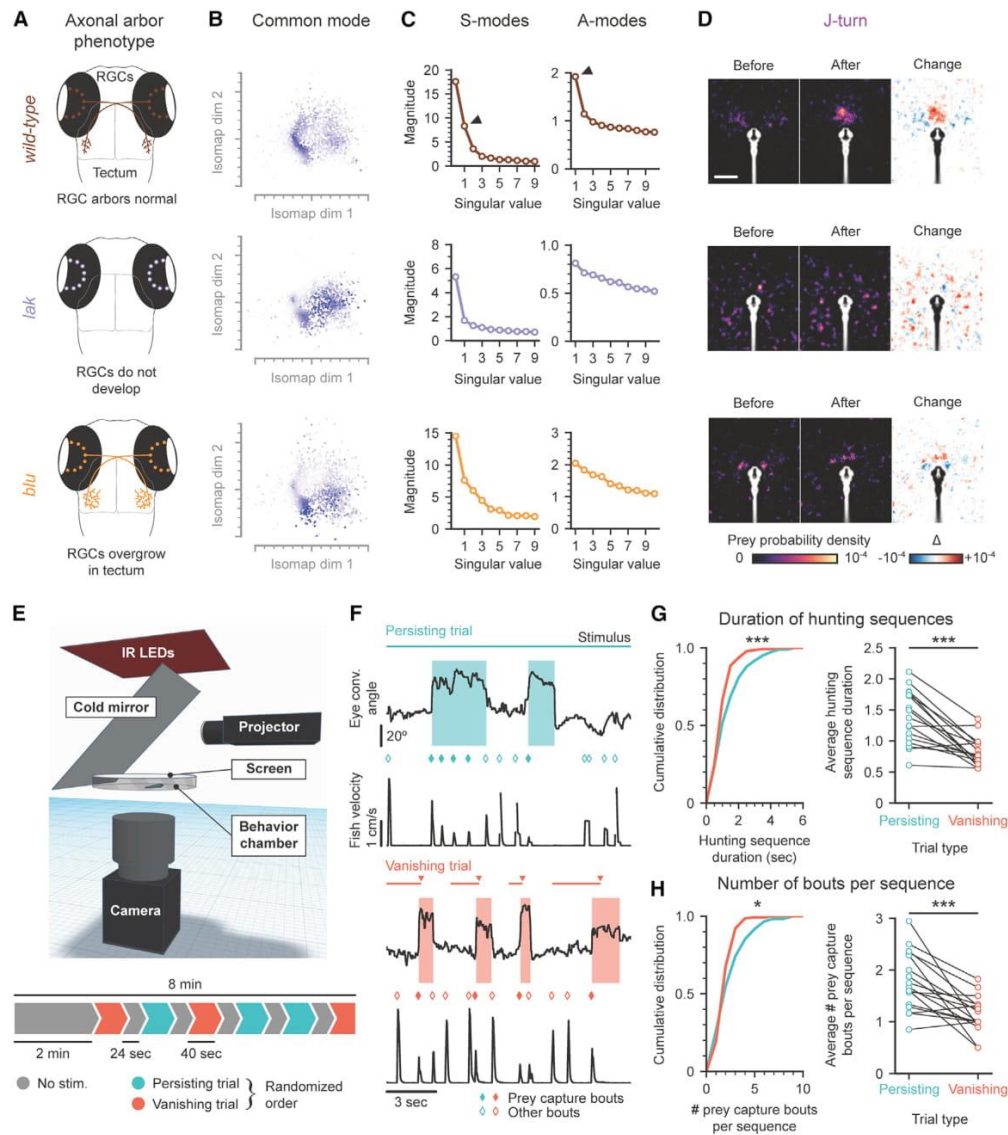


Figure 4. Chronic and Acute Disruption in Virtual Reality of Visual Cues Impairs Prey Capture

(A–D) Behavioral dynamics in mutants.

(A) Schematic anatomical phenotype of *lakritz* (*lak*) and *blumenkohl* (*blu*) mutants.

(B) Common mode obtained from the SVD of transition matrices after mapping bouts from wild-type sibling control (top), *lak* (middle), and *blu* (bottom) animals into the behavioral space from Figure 1.

(C) Singular values associated with S- and A-modes. Black arrowheads: prey capture-associated modes present in controls but absent or disrupted in mutants.

(D) Stimulus maps associated with J-turns.

(E–H) Acute disruption of visual cues during prey capture.

(E) Setup and experimental design for a virtual prey capture assay. Animals are presented with six 40 s stimulus trials, interspersed with intervals with no stimuli. Persisting trials: virtual prey are always present. Vanishing trials: virtual prey disappear as soon as eye convergence is detected.

(F) Example period from persisting (top) and vanishing (bottom) trials. Horizontal bars show when stimulus was present. Arrowheads indicate when eye convergence was detected online and the stimulus removed. Diamonds: automatic bout detection. Shaded regions: post hoc determination of eye convergence.

(G) Left: cumulative distribution of hunt durations ($***p < 0.001$, Kolmogorov-Smirnov test). Right: average prey capture sequence duration during persisting and vanishing trials ($***p < 0.001$, Wilcoxon signed-rank test).

(H) Left: cumulative distribution of bout chain lengths ($p < 0.05$, Kolmogorov-Smirnov test). Right: average number of bouts per hunting sequence ($***p < 0.001$, Wilcoxon signed-rank test).

See also Figures S5 and S6.

consistent across animals (median 1.7 versus 1.0 bouts per sequence) (Figure 4H).

Together, these results demonstrate that animals decide on the next bout in a sequence based on the available visual cues at a given moment. We conclude that prey capture is an example of a stimulus-response loop that serves to bring the prey to the near-anterior visual field of zebrafish, terminating with a capture strike.

Distance to the Prey Determines the Choice of Strike Type

We next analyzed the maneuvers that precede the capture of prey. Previously, strikes have been classified as ram or suction [16, 23], low or high velocity [40], and long or short duration [14]. We similarly found a bimodal distribution in capture strike duration, with one peak around 100 ms and a second peak around 200 ms (Figure 5A). Across all strike durations, however, we noticed that fish consumed prey after a stereotyped time (~50 ms), and that long-duration strikes resulted from a second, variable bout occurring immediately after the capture event. Re-embedding the first 50 ms of capture strike dynamics to produce a behavioral sub-space using our PCA-DTW-isomap pipeline revealed two clusters in the capture strike sub-space displaying markedly different postural dynamics (Figures 5B–5D; STAR Methods). We termed these maneuvers the attack swim and the S-strike (Figure 5E; Video S4). Almost all S-strikes were followed by a post-capture bout (“long duration”) whereas attack swims contributed to both long- and short-duration strikes (Figure 5A). This variation in strike dynamics suggests that the behavior does not represent a single stereotyped movement, but rather two possible capture strategies employed in different contexts.

To test whether different strikes might be selected in response to different stimuli, we investigated the prey probability density distribution in the visual field of animals prior to the two bout types. Both were triggered when prey was in the near-anterior visual field (Figure 5F); however, we noticed strong and characteristic fin abduction that only occurred prior to the onset of S-strikes [31]. This suggested that the animals were making preparatory movements before S-strikes, so we studied the evolution of the prey stimulus over time for hunting sequences ending in the two strike types (Video S5). We found prey position in the anterior visual field started to diverge approximately 250 ms prior to swim onset (Figures 5G and 5H). S-strikes occurred with a higher probability when prey was centered in the visual field 0.6 mm away. For attack swims, prey were less likely to be centered, and the behavior typically occurred once the prey was within 0.4 mm of the fish. These results indicate that larvae are sensitive to the distance of a prey item in the center of their visual field. Most commonly, larvae will perform an attack swim once prey reach a “strike zone.” If, however, the prey becomes centered in the visual field at a greater distance, larvae may resort to using their fins to keep the prey centered until it reaches the strike zone and then release an S-strike.

Larvae Perform Stereotyped Jaw Movements to Capture Prey in the Dorsal Visual Field

Animals exploit the three-dimensional water column during naturalistic behavior [49], and we wondered whether this was

also true during prey capture. Recording hunting behavior from the side revealed that larvae made full use of the vertical dimension and performed prominent cranial and jaw movements during this behavior (Video S6). To better quantify these movements, we modified our recording setup so that we could simultaneously track tail, jaw, and cranial movements with two views in a single camera (Figures 6A–6C; Video S7; STAR Methods). We found that the majority of jaw movements performed by larvae were initiated immediately after a swim bout (Figure 6D). We then applied our PCA-DTW-isomap pipeline to embed jaw movements in a new behavioral space, which revealed two distinct clusters (Figures 6E and 6F). The larger cluster corresponds to a relatively slow, low-amplitude depression of the jaw with little or no movement of the cranium and could relate to early buccal pumping in the larva or chemosensation (Figure 6G, left). The rarer jaw movement was highly stereotyped, comprising a rapid, large-amplitude depression of the jaw concurrent with cranial elevation (Figure 6G, right; Video S6). This movement was exclusively associated with capture events and was preceded by an attack swim or S-strike, or occurred in isolation as a “suction” capture [16, 30] (Figure 6H). Thus, different capture strategies in zebrafish larvae emerge by combining different stereotyped tail kinematics with stereotyped jaw kinematics.

Hunting episodes were associated with both changes in pitch and moving up and down in the water column (Figure 6C). Larvae had a mean preferred orientation of ~7° and rotated to ~12° prior to the onset of a capture (Figure 6I). Capture events occurred when prey were in the dorsal visual field (Figure 6J), which would correspond to a ventral position on the retina.

Larvae Use Binocular Vision to Position Prey in the Strike Zone

It has been proposed that larvae converge their eyes during prey capture in order to create an area of binocular overlap [16, 26]. To test the role of binocular vision in prey capture, we removed the lens from either one or both eyes (lensectomy or “delensing”) of 7-dpf larvae and tested their behavior the following day (Figure 7A; STAR Methods; sham = 16, unilateral = 18, bilateral = 16). Unilaterally delensed animals were able to converge their eyes to the same extent as controls, indicating that the procedure did not prevent eye movements; however, bilaterally delensed animals did not perform eye convergence, suggesting that lensectomy effectively blinded animals to prey items (Figure 7B). Unilaterally delensed animals spent less time engaged in prey capture than controls (median proportion of time: 0.25, sham, versus 0.15, unilateral) (Figure 7C) and detected prey only about half as often (median detection rate: 10 times per minute, sham, versus 6 times per minute, unilateral) (Figure 7D). Unilaterally delensed animals only initiated J-turns toward prey located on the same side as their intact eye (Figure 7E). Thus, binocular vision is not required to initiate hunting behavior.

We wanted to know how subsequent prey capture dynamics were affected in one-lensed animals. We used SVD to identify transition modes in control and unilaterally delensed groups and found a subtle but significant difference in A1 encoding prey capture sequence dynamics (similarity: 0.73)

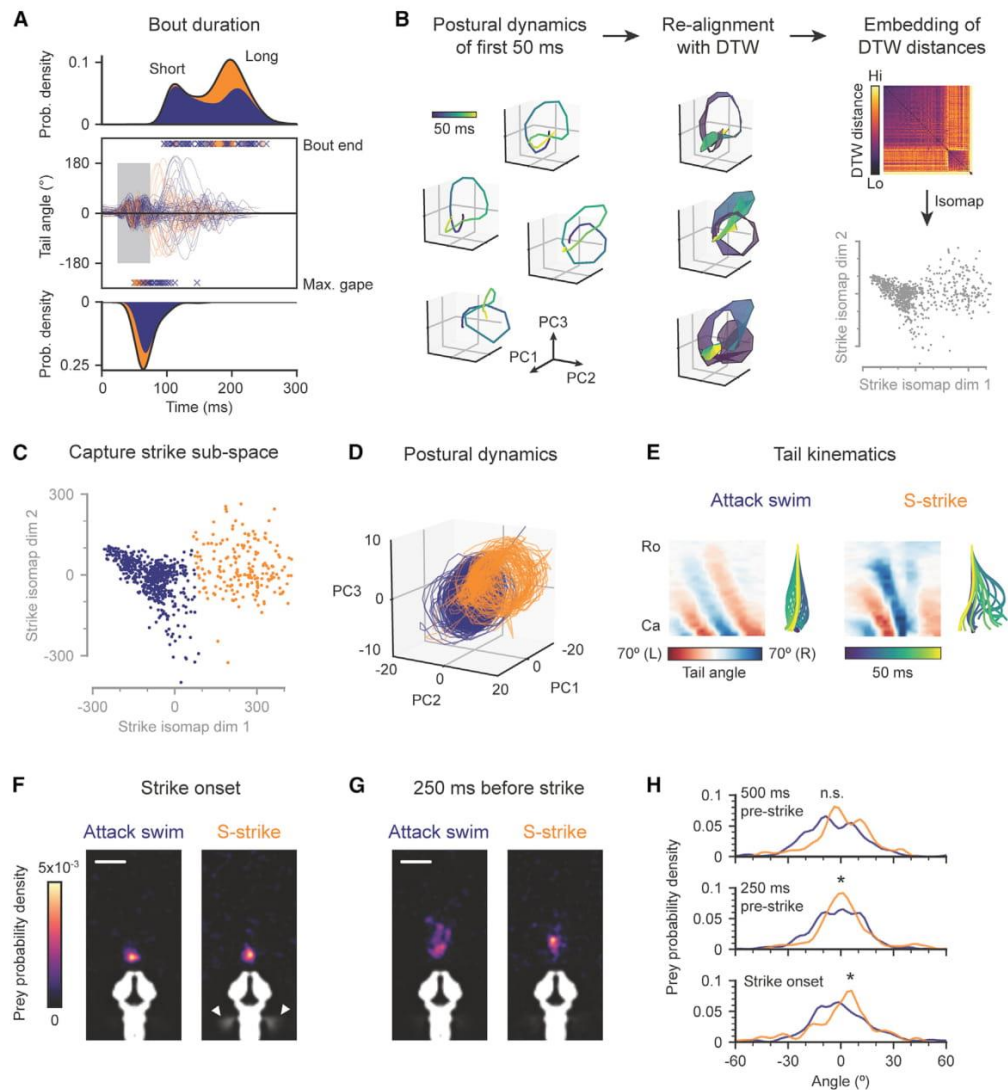


Figure 5. Prey Pursuit Concludes with Either of Two Distinct Capture Maneuvers

(A) Capture strikes consist of a capture phase and a variable post-capture phase. Top: stacked KDE of capture strike durations. Attack swims (blue) and S-strikes (orange). Middle: tail tip angle over time for capture strikes. Gray window: initial 50 ms capture phase. Bottom: KDE over jaw opening times.

(B) Pipeline for generating capture strike sub-space. Isomap embedding of DTW distances between initial capture phases of all strikes.

(C) K-means clustering (two clusters) in the capture strike sub-space. Blue, attack swims; orange, S-strikes.

(D) Trajectories through PCs for attack swims and S-strikes.

(E) Representative examples of an attack swim and an S-strike. Tail kinematics (left) and reconstructed bout (right).

(F) Prey probability density prior to attack swims (left) and S-strikes (right). White arrowheads: fin abduction.

(G) Prey probability density 250 ms prior to the onset of attack swims (left) and S-strikes (right). Scale bar in (F) and (G), 500 μm .

(H) Prey probability density as a function of azimuthal angle at different time points in hunting sequences resulting in attack swims (blue) or S-strikes (orange) ($*p < 0.05$, permutation test using energy statistics to compare distributions; n.s., not significant). See also Videos S4 and S5.

(Figure 7F). Specifically, transitions to capture strikes from approach swims were under-represented in the unilaterally delensed group (dotted outline). Unilaterally delensed animals

ended their hunting sequences with a capture strike only about half as often as controls (Figure 7G). We wanted to test whether this decrease in strike rate affected both attack

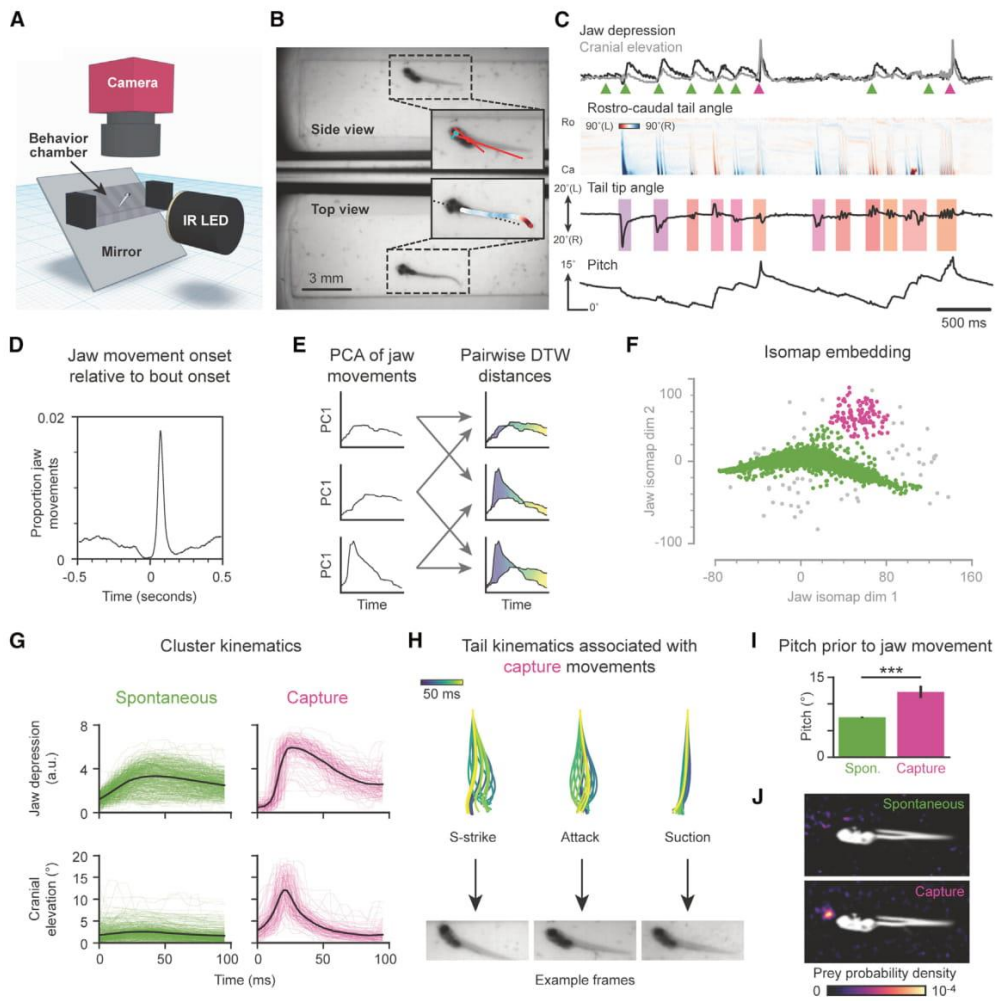


Figure 6. Larvae Capture Prey from Below with Stereotyped Jaw Kinematics

(A) Schematic of the setup used to record behavior simultaneously from above and from the side.
 (B) Example frame; insets are overlaid with tail and jaw tracking.
 (C) Jaw and tail kinematics from 4 s of behavioral recording. Top: depression of the jaw (black) and elevation of the cranium (gray). Arrowheads: jaw movement onsets. Spontaneous movements (green); capture strikes (magenta). Middle: tail tracking. Bouts color-coded according to nearest exemplar in behavioral space. Bottom: pitch of the fish.
 (D) Cross-correlation between bout onsets and jaw movement onsets.
 (E) Generating a jaw movement behavioral space. Jaw movements projected onto first PC followed by pairwise alignment and distance calculation with DTW.
 (F) Two-dimensional isomap embedding of DTW distances between jaw movements. Clustered using HDBSCAN into spontaneous jaw movements (green), capture jaw movements (magenta), and noise (gray).
 (G) Jaw depression (top) and cranial elevation (bottom) for spontaneous (left) and capture (right) jaw movements. Colored traces: individual movements. Black lines: average.
 (H) Example tail movements (top) preceding the shown capture jaw movement (bottom).
 (I) Pitch of fish prior to bouts containing spontaneous and capture jaw movements (**two-tailed $p < 0.001$, unpaired Student's t test). Mean \pm SEM.
 (J) Prey probability density prior to bouts containing spontaneous (top) and capture (bottom) jaw movements. White: average outline of fish. Anterior is left. See also [Videos S6](#) and [S7](#).

swims and S-strikes, so we again generated a capture strike sub-space (Figure 7H; cf. Figure 5B). We found that one-lensed animals performed only about a third as many attack swims (median number per animal: 14, sham; 4.5, unilateral)

and almost no S-strikes (median number per animal: 3.5, sham; 0, unilateral) (Figure 7I).

The reduction in capture strikes in unilaterally blinded animals suggested that larvae may be using binocular cues to

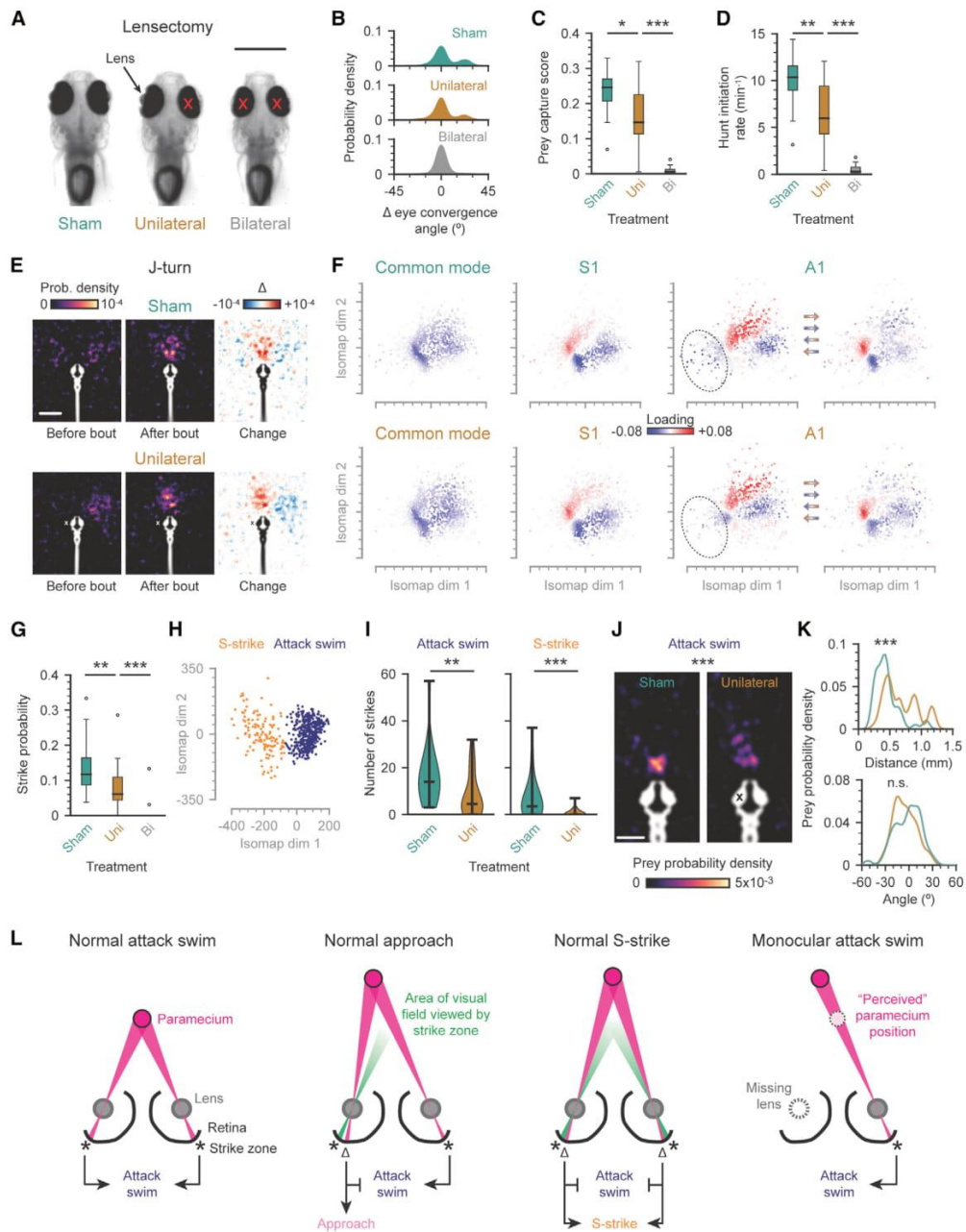


Figure 7. Larvae Use Binocular Cues to Position Prey on the Strike Zone

(A) Lensectomy. Lens dissected from one (unilateral) or both (bilateral) eyes (red crosses). Scale bar, 500 μ m.
 (B) Eye convergence distributions in sham, unilaterally, and bilaterally delensed larvae. Aligned to the resting eye convergence angle (0°).
 (C) Proportion of time spent engaged in prey capture (prey capture score) for each treatment group.
 (D) Number of times animals converged their eyes each minute (hunt initiation rate) for each treatment group.
 (E) Stimulus maps for sham and unilaterally delensed animals during J-turns. Animals that had their right lens removed are mirrored (white cross). Scale bar, 1 mm.
 (F) Transition modes of sham (top) and unilaterally delensed (bottom) animals. Differences between common modes not significant ($p > 0.05$). Differences between S1 and A1: $p < 0.05$, permutation test on absolute cosine similarity. Dotted outline: approximate location of capture strikes in the space.
 (G) Probability that hunting sequences terminate with a capture strike for animals in each treatment group.

(legend continued on next page)

judge distance to the prey. Studying the probability distribution in the visual field revealed that prey was less likely to fall in the strike zone of unilaterally delensed animals (Figure 7J; Video S8). These animals initiated attack swims when prey were further away (0.5 mm versus 0.4 mm) and skewed $\sim 10^{\circ}$ – 15° in the direction of their blinded eye (Figures 7J and 7K). Thus, it appears that larvae will typically perform the capture strike when prey fall on the temporal-ventral retina of both eyes (Figure 7L). If a fish brings the prey into the temporal-ventral retina of one eye, but is missing input from the other eye, it may trigger an attack swim prematurely. Furthermore, animals may use binocular cues to determine that prey is centered but too far from the strike zone, triggering an S-strike maneuver.

DISCUSSION

Our analysis reveals that zebrafish larvae capture prey through a stimulus-response loop relying on immediate binocular cues. We identify stereotyped bout sequences that emerge from low-order transition rules. Chronic “blurring” of the visual scene in genetic mutants impairs prey detection and removal of visual cues after initiation of behavior causes animals to abort the hunting sequence early. Bout sequences position the prey in the center of the proximal dorsal visual field, triggering a capture strike. Depending on the distance to the prey, animals will perform one of two possible strike maneuvers. Disrupting binocular vision impedes an animal’s ability to position the prey centrally in the visual field and causes premature release of a capture strike.

Different embedding approaches can highlight different structural aspects when visualizing behavior in lower dimensions. Previously, t-SNE has revealed local structure in the behavior of flies and fish [12, 14]. We found that isomap embedding performed well at separating distinct and rarer bout types such as J-turns and capture strikes (Figures 1I and 3C), but was less effective than t-SNE at separating different kinds of forward scoot (Figures 1I and S1C). Some of this local structure was, however, retained in an intermediate clustering step (Figures 1H and 1K). We also revealed distinct types of capture maneuvers and jaw movements using isomap embedding, and thus this approach may be complementary to t-SNE and UMAP when investigating the structure of behavior.

Previous studies of the temporal structure of behavior have employed Markov models [5, 19, 21]. We identified common transitions shared across different regions of our behavioral space,

and this aided the delineation of cluster boundaries subsequently used for Markov chain analysis (Figures 3A–3C). We did not find strong evidence of higher-order dynamics in our analysis of sequences built from these clusters (Figures 3D and 3E), suggesting that transition modes provide an accurate account of zebrafish larva prey capture behavior (Figures 3F and 3G). Recent work in this area has also found the preceding bout strongly influences the next, although longer-term dynamics, including satiety state, can have some subtle effects [50]. Future work may seek to generalize the analysis of transition modes to also account for behavioral changes over longer timescales.

We demonstrated that short-term visual cues on the order of 100s of milliseconds are necessary to maintain hunting behavior (Figures 4E–4H). Our new closed-loop virtual reality assay extends the possibilities for studying the visual cues necessary for the formation and maintenance of hunting behavior under more naturalistic free-swimming conditions, as previous analyses have been restricted to embedded preparations [26, 28, 29]. Short integration windows for deciding the next behavior have been observed in thermal navigation of larvae [51] and social affiliation of juvenile zebrafish [52]. Thus, stimulus-response loops driving behavioral chaining might not be specific to prey capture, but provide a more general mechanism underlying goal-directed behavior in zebrafish.

It has been proposed that a specialized UV-sensitive zone in the ventral retina could facilitate targeting prey from below [53–55]. We demonstrate that larvae do indeed orient themselves beneath the prey over the course of a hunting sequence (Figures 6I and 6J). Dedicated neural circuits in the retina and pretectum could mediate the initial formation of the stimulus-response loop [28, 55–58], subsequently maintained by the optic tectum [32, 59, 60] and the nucleus isthmi [61]. Future work may seek to identify and characterize the neural circuitry underlying prey capture strikes (Figure 5). When the eyes are converged, prey in the temporal-ventral retina is represented symmetrically in the anterior regions of both tecta. We posit the anterior tectum contains specialized circuitry for implementing the appropriate capture maneuver. The S-strike and attack swim may be driven by separate command-like neuronal populations [59], or alternatively by different activity patterns within a common population. These swims are performed in conjunction with a stereotyped jaw movement to capture prey (Figures 6F–6H; Videos S6 and S7). Producing invariant actions in response to stereotyped “releasing” stimuli has long been considered an efficient way to ensure reproducible outcomes in innate behaviors [8]. We speculate that by linking different releasing stimuli to stereotyped swims sharing a common jaw

(H) Capture strike sub-space, generated as outlined in Figure 5B. Capture strikes clustered into two types using K-means clustering. Attack swims (blue), S-strikes (orange).

(I) Number of strikes performed by animals split by strike type (attack swim versus S-strike) and treatment group (sham versus unilateral).

(J) Prey probability density at the onset of attack swims in sham (left) and unilaterally delensed (right) animals. Cross indicates eye with lens removed (right animals mirrored). Scale bar, 500 μ m.

(K) Prey probability densities prior to attack swims at various distances (top) and azimuthal angles (bottom) in the visual field for sham and unilaterally delensed animals. Positive angles signify azimuthal position toward the sighted eye.

(L) Model for the binocular control of capture strikes. Far left: a paramecium falling on the strike zone triggers an attack swim. Center left: a paramecium falling outside the strike zone triggers an approach. Center right: a paramecium centered in the visual field but outside the strike zone triggers an S-strike. Far right: a paramecium falling outside the strike zone in a larva with its left lens removed (gray dotted outline) triggers an inappropriate attack swim. Δ signifies offset between current prey position (magenta) and strike zone (asterisk/green cone).

(C), (D), (G), and (I): * $p < 0.05$, ** $p < 0.01$, *** $p < 0.001$; Mann-Whitney U test. (J) and (K): *** $p < 0.001$; n.s., not significant ($p = 0.15$), permutation test on energy distances between distributions. See also Video S8.

movement, the nervous system of the zebrafish larva has evolved an efficient means to produce reliable, yet flexible, behavior.

Since eye convergence was first identified as a hallmark of prey capture in zebrafish larvae, there has been speculation about a potential role of binocular vision in this behavior [16, 26]. We demonstrate that, in addition to reducing the rate of prey detection, loss of binocular vision reduces the probability to strike once a prey capture sequence has begun (Figures 7A–7G). One possible explanation is that the stimulus-response loop that brings prey to the near-anterior visual field is monocularly driven, with visual cues from each eye independently and stochastically releasing the next bout in the sequence. In this case, loss of vision in one eye would reduce the probability of a bout being generated, giving prey time to move out of the field of view of the intact eye. Alternatively, animals may integrate cues from both eyes to bring the prey optimally into the strike zone of both retinas. While we show that binocular cues are not required to release the capture strike behavior (Figures 7G–7I), they do appear to serve a role in the appropriate positioning of prey in the strike zone (Figures 7J–7L). These results suggest that binocular vision could be used as a mechanism to determine distance to prey in zebrafish larvae.

STAR★METHODS

Detailed methods are provided in the online version of this paper and include the following:

- **KEY RESOURCES TABLE**
- **LEAD CONTACT AND MATERIALS AVAILABILITY**
- **EXPERIMENTAL MODEL AND SUBJECT DETAILS**
 - Wild-type zebrafish larvae
 - Mutant zebrafish larvae
 - Genetic ablation of retinal ganglion cells (RGCs)
- **METHOD DETAILS**
 - Free-swimming behavioral assay with real prey
 - Tail and eye tracking
 - Generating a behavioral space
 - Mapping kinematic features and eye convergence into the behavioral space
 - Mapping bouts from other experiments into the behavioral space
 - Singular-value decomposition of behavioral transitions
 - Investigating transition modes with toy data
 - Eye convergence analysis
 - Clustering in a combined kinematic-transition space
 - Modeling transitions between clusters
 - Paramecium tracking
 - Generating stimulus maps
 - Free-swimming virtual prey capture assay
 - Capture strike analysis
 - Free-swimming behavioral assay in three dimensions
 - Jaw tracking
 - Generating a behavioral space of jaw movements
 - Paramecium tracking from the side
 - Lensectomy
- **QUANTIFICATION AND STATISTICAL ANALYSIS**
 - Identification of significant transition modes
 - Comparison of transition modes across experimental datasets
 - Simplex projection to test higher order behavioral dynamics
 - Identification of significant transitions in an ethogram
 - Statistical analysis of virtual prey experiments
 - Quantification of prey distance during capture strikes
 - Quantification of lensectomy experiments

● DATA AND CODE AVAILABILITY

SUPPLEMENTAL INFORMATION

Supplemental Information can be found online at <https://doi.org/10.1016/j.cub.2019.11.022>.

ACKNOWLEDGMENTS

The authors would like to thank all members of the Baier lab and colleagues at the Max Planck Institute of Neurobiology for discussions and helpful comments. In particular, we thank T. Helmbrecht, J. Larsch, S. Reinert, and D. Guggiana Nilo for constructive feedback on the manuscript. We thank M. Dal Maschio and N. Dolensek for especially helpful discussions. We thank V. Stih and L. Petrucco for help setting up and designing the virtual prey capture assay. We also thank K. Slanchev for providing *lakritz* and *blumenkohl* mutants. Schematics in Figures 4A and S5A were adapted with permission from unpublished work by Y. Kölsch. Funding was provided by the Max Planck Society.

AUTHOR CONTRIBUTIONS

Conceptualization, D.S.M., J.L.S., and H.B.; Methodology, D.S.M., J.C.D., A.M.F., and H.B.; Investigation, D.S.M.; Software, D.S.M. and J.C.D.; Formal Analysis, D.S.M.; Visualization, D.S.M.; Writing – Original Draft, D.S.M.; Writing – Review & Editing, J.C.D., A.M.F., J.L.S., and H.B.; Supervision, J.L.S. and H.B.; Funding Acquisition, H.B.

DECLARATION OF INTERESTS

The authors declare no competing interests.

Received: June 19, 2019

Revised: September 30, 2019

Accepted: November 6, 2019

Published: December 19, 2019

REFERENCES

1. Krakauer, J.W., Ghazanfar, A.A., Gomez-Marin, A., MacIver, M.A., and Poeppel, D. (2017). Neuroscience needs behavior: correcting a reductionist bias. *Neuron* 93, 480–490.
2. Cande, J., Namiki, S., Qiu, J., Korff, W., Card, G.M., Shaevitz, J.W., Stern, D.L., and Berman, G.J. (2018). Optogenetic dissection of descending behavioral control in *Drosophila*. *eLife* 7, e34275.
3. Kato, S., Kaplan, H.S., Schrödel, T., Skora, S., Lindsay, T.H., Yemini, E., Lockery, S., and Zimmer, M. (2015). Global brain dynamics embed the motor command sequence of *Caenorhabditis elegans*. *Cell* 163, 656–669.
4. Vogelstein, J.T., Park, Y., Ohyama, T., Kerr, R.A., Truman, J.W., Priebe, C.E., and Zlatic, M. (2014). Discovery of brainwide neural-behavioral maps via multiscale unsupervised structure learning. *Science* 344, 386–392.
5. Wiltschko, A.B., Johnson, M.J., Iurilli, G., Peterson, R.E., Katon, J.M., Pashkovski, S.L., Abaira, V.E., Adams, R.P., and Datta, S.R. (2015). Mapping sub-second structure in mouse behavior. *Neuron* 88, 1121–1135.
6. Anderson, D.J., and Perona, P. (2014). Toward a science of computational ethology. *Neuron* 84, 18–31.

7. Egnor, S.E.R., and Branson, K. (2016). Computational analysis of behavior. *Annu. Rev. Neurosci.* **39**, 217–236.
8. Tinbergen, N. (1951). *The Study of Instinct* (Oxford University Press).
9. Flash, T., and Hochner, B. (2005). Motor primitives in vertebrates and invertebrates. *Curr. Opin. Neurobiol.* **15**, 660–666.
10. Bizzi, E., and Cheung, V.C. (2013). The neural origin of muscle synergies. *Front. Comput. Neurosci.* **7**, 51.
11. Del Vecchio, D., Murray, R.M., and Perona, P. (2003). Decomposition of human motion into dynamics-based primitives with application to drawing tasks. *Automatica* **39**, 2085–2098.
12. Berman, G.J., Choi, D.M., Bialek, W., and Shaevitz, J.W. (2014). Mapping the stereotyped behaviour of freely moving fruit flies. *J. R. Soc. Interface* **11**, 20140672.
13. Brown, A.E.X., Yemini, E.I., Grundy, L.J., Jucikas, T., and Schafer, W.R. (2013). A dictionary of behavioral motifs reveals clusters of genes affecting *Caenorhabditis elegans* locomotion. *Proc. Natl. Acad. Sci. USA* **110**, 791–796.
14. Marques, J.C., Lackner, S., Félix, R., and Orger, M.B. (2018). Structure of the zebrafish locomotor repertoire revealed with unsupervised behavioral clustering. *Curr. Biol.* **28**, 181–195.e5.
15. Katsov, A.Y., Freifeld, L., Horowitz, M., Kuehn, S., and Clandinin, T.R. (2017). Dynamic structure of locomotor behavior in walking fruit flies. *eLife* **6**, e26410.
16. Patterson, B.W., Abraham, A.O., MacIver, M.A., and McLean, D.L. (2013). Visually guided gradation of prey capture movements in larval zebrafish. *J. Exp. Biol.* **216**, 3071–3083.
17. Szigeti, B., Deogade, A., and Webb, B. (2015). Searching for motifs in the behaviour of larval *Drosophila melanogaster* and *Caenorhabditis elegans* reveals continuity between behavioural states. *J. R. Soc. Interface* **12**, 20150899.
18. Long, M.A., Jin, D.Z., and Fee, M.S. (2010). Support for a synaptic chain model of neuronal sequence generation. *Nature* **468**, 394–399.
19. Berman, G.J., Bialek, W., and Shaevitz, J.W. (2016). Predictability and hierarchy in *Drosophila* behavior. *Proc. Natl. Acad. Sci. USA* **113**, 11943–11948.
20. Seeds, A.M., Ravbar, P., Chung, P., Hampel, S., Jr., Midgley, F.M., Jr., Mensh, B.D., and Simpson, J.H. (2014). A suppression hierarchy among competing motor programs drives sequential grooming in *Drosophila*. *eLife* **3**, e02951.
21. Tao, L., Ozarkar, S., Beck, J.M., and Bhandawat, V. (2019). Statistical structure of locomotion and its modulation by odors. *eLife* **8**, e41235.
22. Ewert, J.-P. (1987). Neuroethology of releasing mechanisms: prey-catching in toads. *Behav. Brain Sci.* **10**, 337–368.
23. Borla, M.A., Palecek, B., Budick, S., and O'Malley, D.M. (2002). Prey capture by larval zebrafish: evidence for fine axial motor control. *Brain Behav. Evol.* **60**, 207–229.
24. Budick, S.A., and O'Malley, D.M. (2000). Locomotor repertoire of the larval zebrafish: swimming, turning and prey capture. *J. Exp. Biol.* **203**, 2565–2579.
25. McElligott, M.B., and O'Malley, D.M. (2005). Prey tracking by larval zebrafish: axial kinematics and visual control. *Brain Behav. Evol.* **66**, 177–196.
26. Bianco, I.H., Kampff, A.R., and Engert, F. (2011). Prey capture behavior evoked by simple visual stimuli in larval zebrafish. *Front. Syst. Neurosci.* **5**, 101.
27. Muto, A., Ohkura, M., Abe, G., Nakai, J., and Kawakami, K. (2013). Real-time visualization of neuronal activity during perception. *Curr. Biol.* **23**, 307–311.
28. Semmelhack, J.L., Donovan, J.C., Thiele, T.R., Kuehn, E., Laurell, E., and Baier, H. (2014). A dedicated visual pathway for prey detection in larval zebrafish. *eLife* **3**, e04878.
29. Trivedi, C.A., and Bollmann, J.H. (2013). Visually driven chaining of elementary swim patterns into a goal-directed motor sequence: a virtual reality study of zebrafish prey capture. *Front. Neural Circuits* **7**, 86.
30. Hernández, L.P., Barresi, M.J.F., and Devoto, S.H. (2002). Functional morphology and developmental biology of zebrafish: reciprocal illumination from an unlikely couple. *Integr. Comp. Biol.* **42**, 222–231.
31. McClenahan, P., Troup, M., and Scott, E.K. (2012). Fin-tail coordination during escape and predatory behavior in larval zebrafish. *PLoS ONE* **7**, e32295.
32. Gahtan, E., Tanger, P., and Baier, H. (2005). Visual prey capture in larval zebrafish is controlled by identified reticulospinal neurons downstream of the tectum. *J. Neurosci.* **25**, 9294–9303.
33. Brown, A.E.X., and de Bivort, B. (2018). Ethology as a physical science. *Nat. Phys.* **14**, 653–657.
34. Stephens, G.J., Johnson-Kerner, B., Bialek, W., and Ryu, W.S. (2008). Dimensionality and dynamics in the behavior of *C. elegans*. *PLoS Comput. Biol.* **4**, e1000028.
35. Girdhar, K., Gruebele, M., and Chemla, Y.R. (2015). The behavioral space of zebrafish locomotion and its neural network analog. *PLoS ONE* **10**, e0128668.
36. Jouary, A., and Sumbre, G. (2016). Automatic classification of behavior in zebrafish larvae. *bioRxiv*. <https://doi.org/10.1101/052324>.
37. Sakoe, H., and Chiba, S. (1978). Dynamic programming algorithm optimization for spoken word recognition. *IEEE Trans. Acoust. Speech Signal Process.* **26**, 43–49.
38. Frey, B.J., and Dueck, D. (2007). Clustering by passing messages between data points. *Science* **315**, 972–976.
39. Tenenbaum, J.B., de Silva, V., and Langford, J.C. (2000). A global geometric framework for nonlinear dimensionality reduction. *Science* **290**, 2319–2323.
40. Westphal, R.E., and O'Malley, D.M. (2013). Fusion of locomotor maneuvers, and improving sensory capabilities, give rise to the flexible homing strikes of juvenile zebrafish. *Front. Neural Circuits* **7**, 108.
41. Mirat, O., Sternberg, J.R., Severi, K.E., and Wyart, C. (2013). ZebraZoom: an automated program for high-throughput behavioral analysis and categorization. *Front. Neural Circuits* **7**, 107.
42. Fritzsche, D., Virnik, E., Szyld, D.B., and Mehrmann, V. (2008). An SVD approach to identifying metastable states of Markov chains. *Electron. Trans. Numer. Anal.* **29**, 46–69.
43. Dunn, T.W., Mu, Y., Narayan, S., Randlett, O., Naumann, E.A., Yang, C.-T., Schier, A.F., Freeman, J., Engert, F., and Ahrens, M.B. (2016). Brain-wide mapping of neural activity controlling zebrafish exploratory locomotion. *eLife* **5**, e12741.
44. Wolf, S., Dubreuil, A.M., Bertoni, T., Böhm, U.L., Bormuth, V., Candelier, R., Karpenko, S., Hildebrand, D.G.C., Bianco, I.H., Monasson, R., and Debrégeas, G. (2017). Sensorimotor computation underlying phototaxis in zebrafish. *Nat. Commun.* **8**, 651.
45. Kay, J.N., Finger-Baier, K.C., Roeser, T., Staub, W., and Baier, H. (2001). Retinal ganglion cell genesis requires lakritz, a Zebrafish atonal Homolog. *Neuron* **30**, 725–736.
46. Neuhauss, S.C.F., Biehlmaier, O., Seeliger, M.W., Das, T., Kohler, K., Harris, W.A., and Baier, H. (1999). Genetic disorders of vision revealed by a behavioral screen of 400 essential loci in zebrafish. *J. Neurosci.* **19**, 8603–8615.
47. Fernandes, A.M., Larsch, J., Donovan, J.C., Helmbrecht, T.O., Mearns, D., Kölsch, Y., Maschio, M.D., and Baier, H. (2019). Neuronal circuitry for stimulus selection in the visual system. *bioRxiv*. <https://doi.org/10.1101/598383>.
48. Smear, M.C., Tao, H.W., Staub, W., Orger, M.B., Gosse, N.J., Liu, Y., Takahashi, K., Poo, M.M., and Baier, H. (2007). Vesicular glutamate transport at a central synapse limits the acuity of visual perception in zebrafish. *Neuron* **53**, 65–77.
49. Horstick, E.J., Bayley, Y., Sinclair, J.L., and Burgess, H.A. (2017). Search strategy is regulated by somatostatin signaling and deep brain photoreceptors in zebrafish. *BMC Biol.* **15**, 4.
50. Johnson, R.E., Linderman, S., Panier, T., Wee, C.L., Song, E., Herrera, K.J., Miller, A., and Engert, F. (2019). Probabilistic models of larval

- zebrafish behavior reveal structure on many scales. *Curr. Biol.* <https://doi.org/10.1016/j.cub.2019.11.026>.
51. Haesemeyer, M., Robson, D.N., Li, J.M., Schier, A.F., and Engert, F. (2015). The structure and timescales of heat perception in larval zebrafish. *Cell Syst.* *7*, 338–348.
 52. Larsch, J., and Baier, H. (2018). Biological motion as an innate perceptual mechanism driving social affiliation. *Curr. Biol.* *28*, 3523–3532.e4.
 53. Schmitt, E.A., and Dowling, J.E. (1999). Early retinal development in the zebrafish, *Danio rerio*: light and electron microscopic analyses. *J. Comp. Neurol.* *404*, 515–536.
 54. Zimmermann, M.J.Y., Nevala, N.E., Yoshimatsu, T., Osorio, D., Nilsson, D.-E., Berens, P., and Baden, T. (2018). Zebrafish differentially process color across visual space to match natural scenes. *Curr. Biol.* *28*, 2018–2032.e5.
 55. Yoshimatsu, T., Schröder, C., Berens, P., and Baden, T. (2019). Cellular and molecular mechanisms of photoreceptor tuning for prey capture in larval zebrafish. *bioRxiv*. <https://doi.org/10.1101/744615>.
 56. Antinucci, P., Folgueira, M., and Bianco, I.H. (2019). Pretectal neurons control hunting behaviour. *eLife* *8*, e48114.
 57. Muto, A., Lal, P., Ailani, D., Abe, G., Itoh, M., and Kawakami, K. (2017). Activation of the hypothalamic feeding centre upon visual prey detection. *Nat. Commun.* *8*, 15029.
 58. Wee, C.L., Song, E.Y., Johnson, R.E., Ailani, D., Randlett, O., Kim, J.Y., Nikitchenko, M., Bahl, A., Yang, C.T., Ahrens, M.B., et al. (2019). A bidirectional network for appetite control in larval zebrafish. *eLife* *8*, e43775.
 59. Helmbrecht, T.O., Dal Maschio, M., Donovan, J.C., Koutsouli, S., and Baier, H. (2018). Topography of a visuomotor transformation. *Neuron* *100*, 1429–1445.e4.
 60. Bianco, I.H., and Engert, F. (2015). Visuomotor transformations underlying hunting behavior in zebrafish. *Curr. Biol.* *25*, 831–846.
 61. Henriques, P.M., Rahman, N., Jackson, S.E., and Bianco, I.H. (2019). Nucleus isthmi is required to sustain target pursuit during visually guided prey-catching. *Curr. Biol.* *29*, 1771–1786.e5.
 62. Štíh, V., Petrucco, L., Kist, A.M., and Portugues, R. (2019). Stytra: an open-source, integrated system for stimulation, tracking and closed-loop behavioral experiments. *PLoS Comput. Biol.* *15*, e1006699.
 63. van der Maaten, L., and Hinton, G. (2008). Visualizing data using t-SNE. *J. Mach. Learn. Res.* *9*, 2579–2605.
 64. McInnes, L., Healy, J., and Melville, J. (2018). UMAP: uniform manifold approximation and projection for dimension reduction. *arXiv*, arXiv:1802.03426. <https://arxiv.org/abs/1802.03426>.

STAR★METHODS

KEY RESOURCES TABLE

REAGENT or RESOURCE	SOURCE	IDENTIFIER
Chemicals, Peptides, and Recombinant Proteins		
Metronidazole	Sigma-Aldrich	M3761
Tricaine (MS-222)	Sigma-Aldrich	A5040
Deposited Data		
Processed behavioral data	This paper	https://doi.org/10.17632/mw2mmpdz3g.1
Experimental Models: Organisms/Strains		
Tg(ath5:QF2)mpn405	[47]	N/A
Tg(QUAS:epNTR-tagRFP)mpn165	[47]	N/A
<i>lakritz</i>	[46]	<i>th241</i>
<i>blumenkohl</i>	[46]	<i>tz257</i>
Software and Algorithms		
Custom tracking and behavior analysis code	This paper	https://bitbucket.org/mpinbaierlab/mearns_et_al_2019
StreamPix 5	Norpix	https://www.norpix.com/
Python 2.7	Anaconda2	https://www.anaconda.com/
Python 3.4	Anaconda3	https://www.anaconda.com/
Stytra	[62]	http://www.portugueslab.com/stytra/
OpenCV	OpenCV	https://opencv.org/
VirtualDub	VirtualDub	http://www.virtualdub.org/
Tinkercad	Tinkercad	https://www.tinkercad.com/

LEAD CONTACT AND MATERIALS AVAILABILITY

Further information and requests for reagents should be directed to and will be fulfilled by the Lead Contact, Herwig Baier (hbaier@neuro.mpg.de). This study did not generate new unique reagents.

EXPERIMENTAL MODEL AND SUBJECT DETAILS

All animal procedures conformed to the institutional guidelines set by the Max Planck Society and were approved under licenses from the regional government of Upper Bavaria (Regierung von Oberbayern).

Wild-type zebrafish larvae

For all experiments, unless noted otherwise, we obtained TLN (nacre) embryos from an outcross of TLN homozygous to TL/TLN heterozygous adults. Until 3 days post fertilization (dpf) embryos were raised in Danieau's solution (17 mM NaCl, 2 mM KCl, 0.12 mM MgSO₂, 1.8 mM Ca(NO₃)₂, 1.5 mM HEPES) at a density of 60 embryos per 50 mL at 28°C with a 14 h-10 h light-dark cycle. Thereafter, embryos were transferred to new dishes containing fish system water and raised at a density of 30 larvae per 50 mL until behavioral testing at 7 dpf or 8 dpf. At 5 dpf and 6 dpf, a few drops of dense paramecia culture (*Paramecium multimicronucleatum*, Carolina Biological Supply Company, Burlington, NC) were added to each dish and larvae were allowed to feed *ad libitum*.

Mutant zebrafish larvae

For experiments with mutants, we used *lakritz* (*lak^{th241}*) and *blumenkohl* (*blu^{tz257}*) mutants [46] in a TL background. *Lak* mutants were obtained from a heterozygous in-cross. Homozygous mutants could be clearly identified by their dark color compared to sibling controls (mixture of heterozygotes and wild types) in a visual background adaptation (VBA) assay. *Blu* mutants were obtained by outcrossing heterozygous females to homozygous males. Similar to *lak*, mutants could be identified unambiguously with a VBA assay. Larvae were raised as described above, except they were not fed at 5 and 6 dpf, and thus their naive prey capture ability was assayed at 7 dpf. This was to minimize potential confounding effects of experience-dependent improvement in prey capture efficacy between groups.

Genetic ablation of retinal ganglion cells (RGCs)

Chemogenetic ablation of RGCs was performed using the Q-system driving the expression of an enhanced version of nitroreductase (epNTR). Double transgenic larvae (*Tg(ath5:QF2)mpn405*; *Tg(QUAS:epNTR-tagRFP)mpn165*) [47] were fed at 5dpf and 6dpf with

paramecia and then incubated with 5mM metronidazole (MTZ, Sigma Aldrich) in fish water containing 0.2% DMSO, for 24 h. The MTZ solution was washed out and larvae were allowed to recover overnight before behavioral experiments were performed at 8dpf. Controls were siblings only expressing *QUAS:epNTR-tagRFP* and treated similarly with MTZ.

METHOD DETAILS

Free-swimming behavioral assay with real prey

Experiments with real prey were conducted using a custom-built behavioral setup. Behavior arenas were produced by flooding a 35 mm Petri dish with 2% agarose (Biozym, Germany), with an acrylic square (15 × 15 mm, 5 mm deep) placed in the center. Once the agarose had set, the acrylic square was removed producing a hollow chamber with transparent walls. Single larvae were introduced to the chamber along with a drop of culture containing approximately 50-100 paramecia. The chamber was filled to the top with fish system water and a glass coverslip was placed over the chamber to flatten the meniscus. This provided a clean, transparent chamber where behavior could be observed and tracked.

Behavior experiments were performed in a climate-controlled box kept at $28 \pm 1^\circ\text{C}$ between 3 and 12 h after lights on. Each larva was recorded for 20 min using a high speed camera (PhotonFocus, MV1-D1312-160-CL, Switzerland), fitted with an objective (Sigma 50 mm f/2.8 ex DG Macro, Japan), connected to a frame grabber (Teledyne DALSA X64-CL Express, Ontario, Canada). The camera was positioned over the behavior arena, which was lit from below with a custom-built near infrared LED array (LEDs from OSRAM Licht AG). Behavior was filmed at 500 frames per second (fps) with a frame size of 500×500 pixels covering an area slightly larger than the arena (Figure 1B), providing a final resolution of approximately 0.03 mm/pixel. The aperture of the camera objective was adjusted such that the fish was in focus throughout the entire depth of the arena. Recording was performed using StreamPix 5 software (NorPix, Quebec, Canada) and individual trials were initiated through a custom written Python script. Each 20 min session was split into 20x 1 min recording trials, with < 1 s between the end of one trial and the beginning of the next, to keep video files to a manageable size. If frames were dropped during a trial, the recording was stopped to prevent problems in subsequent analyses. Videos were compressed offline in VirtualDub with Xvid compression before tracking was performed.

Tail and eye tracking

Tracking was performed using custom-written Python scripts. Each frame was tracked independently. Each frame was divided by a background image, calculated as the median of every 100th frame over all trials from a given animal. The frames were then thresholded and contours extracted using OpenCV. The largest contour in the image was taken as the outline of the fish and all other pixels were discarded. Then, the histogram of pixel values of the fish was normalized and a second threshold was applied to find the three largest contours within the fish, corresponding to the two eyes and swim bladder. The eyes were identified automatically as the two contours with the nearest centroids and left and right identities were assigned using the sign of the vector product between lines connecting the swim bladder to these two points. The heading of the fish was defined by a vector starting in the center of the swim bladder and passing through the midpoint between the eye centroids. The angle of each eye was calculated from the image moments of their contours and was defined as:

$$\frac{1}{2} * \arctan\left(\frac{2 * u_{11}}{u_{20} - u_{02}}\right),$$

where u_{ij} is the corresponding central moment. The eye angles in an egocentric reference were calculated as the difference between the heading angle and absolute orientation of the eyes, and eye convergence defined as the difference between the eye angles. A 100 ms median filter was applied to smooth the traces obtained from each eye while preserving edges. The two thresholds used for tracking were set manually for each fish. In frames where the eye contours could not be detected through thresholding, we instead applied a watershed algorithm to obtain contours and then proceeded as above.

Due to the dark pigmentation of *lak* and *blu* mutants, there was insufficient contrast to segment the eyes from the surrounding skin using either thresholding or watershed analysis. For this reason, eye tracking could not be performed in these animals. To calculate the heading in this case, we used the second threshold to segment the head and body of the fish from the tail, for which we identified the minimum enclosing triangle using OpenCV. The heading was then defined as a vector passing through the apex and centroid of this triangle, and the position of the swim bladder was estimated as lying midway between these two points.

To track the tail of the fish, we skeletonized the contour obtained after applying the first threshold described above. We started the tracking from the point on this skeleton nearest to the swim bladder. We used a custom-written algorithm to identify the longest path through the skeletonized image that started at this point, ended at the tip of a branch, and began in the opposite direction of the heading vector. We then linearly interpolated 51 equally spaced points along this path to obtain the final tail points.

The tail tip angle was defined as the angle between the midline of the fish (provided by the heading vector) and a vector between the center of the swim bladder and the last point of the tail. This angle is used to help visualize the sinusoidal oscillation of the tail, but was not used as the basis of any analysis in the paper.

We vectorized the tracked tail points for kinematic analysis in a similar manner to what has been previously described [34, 35]. Briefly, we calculated the angle between the midline (defined by the heading vector) and a vector drawn between each adjacent pair of tail points, providing a 50 dimensional representation of the tail in each frame. A three frame median filter was applied to the heading angle and tail kinematics to remove single frame noise.

The mean tail tip curvature was computed as the mean of the last ten points of the tail angle vector, and was used for bout segmentation. Bouts were detected by applying a threshold to the smoothed absolute value of the first derivative of this mean tail tip curvature. Uncharacteristically long bouts detected with this method were further split by finding inflection points in the smoothed absolute value of the mean tail tip curvature convolved with a cosine kernel.

Generating a behavioral space

To generate our behavioral space, we excluded any bouts during which the tail of the fish hit the wall of the behavior chamber. This was to ensure that only the fish's self-generated motion – and not motion artifacts introduced from distortion of the tail by the wall – was considered when mapping the behavioral space. Consequently, not all the bouts we observed could be mapped into the space.

To describe bouts in terms of their postural dynamics, we performed principal component analysis (PCA) on the tail kinematics across all bout frames. Data were normalized before applying PCA by subtracting the mean tail shape and dividing by the standard deviation.

The next step in generating the behavioral space involved computing the distance between every pair of bouts with dynamic time warping (DTW) [37]. DTW finds an alignment between two time series that minimizes a cost function, which is the sum of the Euclidean distances between each pair of aligned points. In our analysis, we only allowed trajectories to be warped within a 10 ms time window. For bouts of different lengths, we padded the end of the shorter bout with zeros until it was the same length as the longer bout. We performed each alignment twice, reversing the sign of all the values for one of the trajectories the second time, and considered the distance between two bouts to be: $\min(DTW(t_1, t_2), DTW(t_1, -t_2))$, thus effectively ignoring the left/right polarity of the bouts.

To generate the behavioral space, we performed a round of affinity propagation [38] prior to embedding, using the negative DTW distance between a given pair of bouts as a measure of their similarity. We varied the affinity parameter in this step, testing values ranging from 400 to 4000 (number of clusters ranging from 1634 to 179), and found it did not have a strong impact on the structure of the final behavioral space (Figure S1B). Therefore, we used the median similarity between bouts as the preference for the clustering (~400). Doing so provided 2,802 clusters, of which we excluded any clusters containing fewer than three bouts, thus ensuring that only repeatedly observable motor patterns were used for generating the behavioral space. As a final quality check, we manually inspected every cluster exemplar and removed incorrectly identified bouts, which usually was the result of tracking artifacts from a paramecium crossing the tail of the fish. The final number of clusters that we kept for embedded was 1,744.

Since affinity propagation identifies an exemplar to represent each cluster, we produced our final behavioral space by performing isomap embedding [39] of these exemplars. For the isomap embedding, we constructed a nearest-neighbors graph of the exemplars using their DTW distances, and calculated the minimum distance between each pair of points in this graph. The isomap components correspond to the eigenvectors of this graph distance matrix.

In addition to isomap, we also performed t-SNE [63] and UMAP [64] of the data. As with isomap, we performed the embedding using the precomputed DTW distances between the 1,744 exemplars. For t-SNE, we systematically varied the perplexity (10, 20, 50) and learning rate (10, 100, 1000) of the embedding to see whether this significantly changed the visualization of the behavioral space (Figure S1C). Similarly with UMAP, we systematically varied the nearest neighbors parameter trying values between 5 and 50 (Figure S1D).

Isomap, t-SNE and UMAP embeddings in Figure S1E were obtained using the precomputed DTW distances between all bouts in the dataset. We used 20 nearest neighbors (or 20 perplexity, in the case of t-SNE) to generate these spaces.

Mapping kinematic features and eye convergence into the behavioral space

With our PCA-DTW-isomap approach, each point in the behavioral space represents a small cluster of bouts. For each bout, we calculated the mean speed, angle through which the fish turned, maximum angular velocity of the fish, and the time at which the maximum angular velocity occurred (turn onset). In Figure S1F, we show the median of each of these features over a cluster. Similarly, we could calculate the proportion of bouts in each cluster that occurred during spontaneous, early, mid, or late prey capture as defined below (see Eye convergence analysis). The prey capture index was defined as:

$$\frac{\# \text{prey capture bouts in cluster} - \# \text{spontaneous bouts in cluster}}{\# \text{bouts in cluster}}$$

Mapping bouts from other experiments into the behavioral space

To map bouts from new experiments into the behavioral space, we extracted tail kinematics and identified bouts as described above (see Tail and eye tracking). The postural dynamics of each new bout was projected onto the first three principal components obtained from the main dataset to bring it into the same space as bouts from that dataset. Then, each bout was mapped to one of the 1,744 exemplars identified in “Generating a behavioral space” using dynamic time warping (DTW), with the nearest exemplar having the smallest DTW distance to the bout. In this way, each new bout could be projected into the three dimensional behavioral space defined by the 1,744 exemplars.

Singular-value decomposition of behavioral transitions

To identify transition modes, we generated a transition frequency matrix, M , where M_{ij} contains the number of transitions from micro-cluster j to micro-cluster i , where each micro-cluster is a small cluster of bouts in the behavioral space identified with affinity propagation (see Generating a behavioral space). This matrix included all the transitions from all animals for a given experiment.

Since there are more than 3 million ($1,744^2$) possible transitions between motifs, and only 44,154 transitions in our largest dataset, the matrix M is necessarily sparse. This would hinder the identification of common dynamical motifs, and so we performed smoothing on matrix M by blurring similar transitions into each other. To achieve this, we took advantage of the fact that nearby points in our behavioral space encode bouts with similar postural dynamics. We computed a weighting matrix, W , where $W_{ij} \equiv e^{-a \cdot d(p_i, p_j)}$. $d(p_i, p_j)$ is the Euclidean distance between a pair of points in the three-dimensional behavioral space, and a is a smoothing factor (see Figure S2A).

We normalized matrix W so that the columns summed to one and then smoothed the transitions in matrix M with the transformation: $M_{smooth} = WMW^T$.

To distinguish between symmetric transitions (i.e., those that occur in both direction), and antisymmetric transitions (i.e., those in which transitions in one direction outweigh those in the other), we decomposed the smoothed matrix, M_{smooth} , into its symmetric and antisymmetric parts, where:

$$M_{smooth} = M_{symmetric} + M_{antisymmetric}$$

$$M_{symmetric} = 1/2 (M_{smooth} + M_{smooth}^T)$$

$$M_{antisymmetric} = 1/2 (M_{smooth} - M_{smooth}^T)$$

The symmetric and antisymmetric transition modes were found by taking the SVD of these two matrices respectively.

Every real or complex matrix, A , can be factorized using the singular-value decomposition (SVD) into three matrices such that:

$$A = USV^T$$

The columns of U and rows of V^T define two sets of orthonormal basis vectors and S is a diagonal matrix containing the singular values, ordered from largest to smallest. The SVD describes the transformation performed by matrix, A . Under this transformation, each row of the matrix, V^T , is mapped to the corresponding column of U and scaled by the associated singular value. Therefore, this decomposition provides an unbiased description of the most common transitions between micro-clusters.

A symmetric matrix, such as $M_{symmetric}$, geometrically defines a scaling transformation. Consequently, its singular-value decomposition is the same as its eigendecomposition: spaces U and V are the same and S contains the eigenvalues. As such, the n^{th} transition mode of $M_{symmetric}$ can be written:

$$\vec{v}_n \cdot \sigma_n \cdot \vec{v}_n^T$$

where \vec{v}_n is the singular vector with corresponding singular value, σ_n . To visualize symmetric transition modes (S-modes), we found the contribution of each micro-cluster to the singular vector defining that transition mode and show this in the behavioral space.

An antisymmetric matrix, such as $M_{antisymmetric}$, describes a set of orthogonal rotations. As such, spaces U and V are related by a 90° rotation and each transition mode can be written:

$$\begin{pmatrix} \vec{v}_1 & \vec{v}_2 \end{pmatrix} \begin{pmatrix} 0 & -\sigma_n \\ \sigma_n & 0 \end{pmatrix} \begin{pmatrix} \vec{v}_1 & \vec{v}_2 \end{pmatrix}^T$$

where \vec{v}_1 and \vec{v}_2 are orthonormal, and σ_n is the corresponding singular value. Positive values in \vec{v}_1 map to positive values in \vec{v}_2 , positive values in \vec{v}_2 map to negative values in \vec{v}_1 , negative values in \vec{v}_1 map to negative values in \vec{v}_2 and negative values in \vec{v}_2 map to positive values in \vec{v}_1 :

$$\begin{array}{ccc} v_1^+ & \rightarrow & v_2^+ \\ \uparrow & & \downarrow \\ v_2^- & \leftarrow & v_1^- \end{array}$$

These are the transitions we represent with arrows in figures displaying A-modes.

Investigating transition modes with toy data

To generate a toy behavioral space, we generated nine clusters with a 2D Gaussian distribution of points (SD = 0.06) and cluster centers drawn randomly from a 2D uniform distribution between 0 and 1. Each cluster contained a random number of points (drawn from a normal distribution; mean = 50, SD = 5). We selected a random seed that produced significant overlap between clusters in the 2D hypothetical behavioral space. Each point in this space was considered analogous to a micro-cluster in our isomap space.

We manually distributed the nine clusters between three hypothetical “states.” For “separated behavioral states,” each state consisted of three clusters and each of the nine clusters belonged to only a single state. For “overlapping behavioral states,” each state consisted of four clusters and three of the clusters were shared between two states.

To generate symmetric transition structure between the three states, we used a left stochastic matrix, P_S , with values:

$$P_S = \begin{pmatrix} 0.7 & 0.2 & 0.1 \\ 0.2 & 0.7 & 0.1 \\ 0.1 & 0.1 & 0.8 \end{pmatrix}$$

To generate antisymmetric transition structure between the three states, we used a left stochastic matrix, P_A , with values:

$$P_A = \begin{pmatrix} 0.3 & 0.1 & 0.7 \\ 0.5 & 0.1 & 0.1 \\ 0.2 & 0.8 & 0.2 \end{pmatrix}$$

To generate transition frequency matrices, we performed Monte Carlo simulation with 2000 transitions (separated behavioral states) or 10,000 transitions (overlapping states) using one of the stochastic matrices above. For each transition, we randomly selected a “micro-cluster” from the next state in the sequence. After the simulation was complete, we added random transitions to the matrix for a final total of 2500 transition (separated states) or 12,500 transition (overlapping states).

We then proceeded to perform smoothing of the transition matrices obtained in our simulations, split matrices into symmetric and antisymmetric components, performed SVD on each of these matrices, and performed hierarchical clustering in the space defined by transition modes (first two S-modes for symmetric, first A-mode for antisymmetric). For separated behavioral states we generated three clusters and for overlapping behavioral states we generated six clusters (three regions of the behavioral space that contribute to a single state, three regions of the behavioral space that contribute to multiple states). We then computed a confusion matrix, C , where C_{ij} is the number of points assigned cluster label i by our hierarchical clustering and whose ground-truth label is j .

Eye convergence analysis

To identify periods of eye convergence, we calculated a kernel density estimation (Gaussian kernel, bandwidth = 2.0) of the eye convergence angles across all frames for a given fish. This distribution was bimodal (eyes converged or unconverged) and therefore we defined the eye convergence threshold as the antimode (least frequent value between the two modes). To identify spontaneous, early, mid, and late prey capture bouts, we calculated the mean eye convergence angle over the first and last 20 ms of a bout, and concluded the eyes were converged if this number was above the threshold. Bouts were classified as spontaneous if the eyes were unconverged at the beginning and end of a bout; early prey capture if the eyes were unconverged at the beginning and converged at the end of the bout; mid prey capture if the eyes were converged at the beginning and end of the bout; and late prey capture if the eyes were converged at the beginning and unconverged at the end of the bout.

Clustering in a combined kinematic-transition space

To define behavioral clusters, we combined information about bouts’ kinematics and transitions to generate a new combined kinematic-transition space. Kinematic similarity between exemplars was computed from DTW distances as described above. We constructed a transition space by combining the first two non-common symmetric transition modes, S1, and S2, and the pair of vectors defining the first antisymmetric transition mode, A1, and then calculating an orthogonal basis (using the Gram-Schmidt process).

We multiplied the kinematic DTW distances between exemplars by the distance between exemplars in transition space (generated by combining singular vectors as described above). Each exemplar was then represented by a feature vector, with each feature being the similarity to every other exemplar. We performed dimensionality reduction on this new feature space (using isomap), retaining 20 components. We then performed ward hierarchical clustering in this reduced space. We calculated the silhouette score associated with different thresholds for defining cluster boundaries, and identified a local maximum at seven. The bouts belonging to each cluster were inspected and confirmed to align well with previous annotations of zebrafish behavior.

In Figure 3C, we colored points in the original behavioral space based on the cluster they were assigned in the combined kinematic-transition space. The transparency value in that graph was determined by the number of nearest neighbors that were assigned the same cluster label.

To produce average traces for the tail tip angle in Figure 3B, we aligned all exemplars belonging to a given cluster using dynamic time warping and took the average of the aligned traces. The representative examples we show are real bouts with a similar tail angle trace to the average.

Modeling transitions between clusters

For this analysis, we first identified every uninterrupted chain containing at least two bouts in our data which could be assigned a behavioral cluster, i.e., only chains of bouts from within a single recording trial (see *Free-swimming behavioral assay with real prey*) and that could be embedded in the behavioral space (see [Generating a behavioral space](#)). We then tested the ability of a series of Markov models – ranging from zeroth to fifth order – to predict each subsequent bout. For this purpose, we modeled each cluster as a state in a Markov process (allowing transitions to the same state, since fish can perform the same type of bout twice in a row). Each of our models contained seven states (from our behavioral clusters), s_1, s_2, \dots, s_7 , and we denote the current state, t_0 , the next state t_{+1} , the previous state t_{-1} , etc.

A zeroth order Markov model does not know the current state and therefore guesses the next state based simply on the distribution of bouts across all states:

$$P(t_{+1} = s_j | t_0 = s_j) = P(s_j)$$

In a first order Markov model, the current state is known. To predict the next state, we considered all other times the current state was visited (t_n) and observed which bout occurred next in the sequence:

$$P(t_{+1} = s_j | t_0 = s_j) = P(t_{n+1} = s_j | t_n = s_j)$$

For the second-order Markov model, we took into account the last two states in a chain when predicting the next state:

$$P(t_{+1} = s_j | t_0 = s_j, t_{-1} = s_k) = P(t_{n+1} = s_j | t_n = s_j, t_{n-1} = s_k)$$

Similarly, for Markov models up to order, m , we predicted the next state:

$$P(t_{+1} = s_j | t_0 = s_j, t_{-1} = s_k, \dots, t_{1-m} = s_n) = P(t_{n+1} = s_j | t_n = s_j, t_{n-1} = s_k, \dots, t_{n+1-m} = s_n)$$

Paramecium tracking

To track paramecia within frames, we performed background division (see [Tail and eye tracking](#)) followed by Gaussian blurring (using a 3×3 pixel kernel) over the image. Next, we applied an adaptive threshold to the image and rotated and centered the fish in the frame using the midpoint between the eyes and the heading obtained from tracking. To identify paramecia, we applied a median filter over the image (5×5 pixels), then performed gray erosion (3×3 flat structuring element) and thresholding. We counted contours with an area > 3 pixels as paramecia, and used the centroids of these contours to determine prey position in the visual field.

Generating stimulus maps

To obtain maps of prey probability density, we performed paramecium tracking as described above for all bouts belonging to a given behavioral cluster (depending on the figure, using either the first and last frame as defined by bout segmentation, or defined time points). Normalized histograms of prey density were obtained after overlaying paramecium positions in all images and masking out the area of the image containing the fish (identified through thresholding of an average image). These histograms were then smoothed with a Gaussian kernel. To identify regions of the visual field with a higher paramecium density, we applied the same process to $\sim 90,000$ randomly chosen frames from all videos and subtracted this baseline density from the image. We then threshold the resulting density plot using the 85th percentile, setting all pixels below this value to zero, and overlaid the average image of the fish.

We obtained time series of paramecium density by aligning video sequences to the onset of the capture strike and proceeded to analyze frames as described above.

Free-swimming virtual prey capture assay

We designed a setup to present virtual prey stimuli to individual zebrafish larvae via a screen on the surface of the water. We adapted a previously described virtual reality setup (Stytra) which allows real-time tracking and presentation of visual stimuli [62]. Behavior arenas were produced by flooding a 55 mm Petri dish with 2% agarose (Biozym, Germany), with a circle mold (18×18 mm, 5 mm deep) placed in the center. Once the agarose had set, the mold was removed producing a hollow chamber with transparent walls. Individual animals are placed in the arena with fish water and a projection filter (3008 - Tough Frost, Rosco) was placed on top. Visual prey-like stimuli were projected onto this filter via a cold mirror (45° AOI, 101×127 mm, Edmund optics).

Animals were recorded at 300 fps with a Ximea MQ013MG-ON camera placed below the arena using a 25 mm lens (Edmund Optics Nr. 59-872). Diffuse infrared illumination for imaging was provided from the top using an IR LED array (RAYMAX 25, 120°). A white light source was also provided from the top. Stimuli were presented to the fish via the projector (DLP LightCrafter 4500, 912×1140 pixels) but blocked before the camera by an IR band-pass filter. Three lenses were combined together to reduce the size of the projected stimuli on the screen (one 150 mm lens, AC508-150-A and two 75 mm lenses, AC508-075-A-ML). Image acquisition, real-time processing and stimulus generation were performed on a Desktop PC running Stytra [62]. Briefly, the background was modeled using a mean image from several previous frames. The difference between the current frame and the thresholded background was computed. The eyes and swim bladder were identified as the largest contours in the thresholded image. The heading of the fish and the angle of each eye were computed using the vector starting in the center of the swim bladder and passing through the midpoint between the eye centroids (see [Tail and eye tracking](#)). Each experiment started with a two minute pre-trial period (no stimulus) in order for the fish adapt to the arena. This period was used to compute a distribution of spontaneous eye convergence angles. The 98th percentile of the data was computed from this distribution and subsequently used during virtual prey presentation as a threshold to detect eye convergence (prey capture). Virtual prey stimuli consisted of gray dots of a single pixel moving linearly with a speed matching real paramecia. For each experiment, 50 virtual prey items were presented on each trial. We presented animals with six trials, lasting 40 s each. In three of the trials virtual prey disappeared for 2 s each time eye convergence was detected online (“vanishing” trials). In the other three trials, prey remained visible the whole time (“persisting” trials). The order of persisting and vanishing trials was randomized for each fish. Five periods of no stimulus presentation lasting 24 s each were interspersed in between each trial. Analysis was performed with custom-written Python scripts.

Capture strike analysis

We defined capture strikes as bouts that belonged to a micro-cluster containing > 50% late prey capture bouts. To determine the moment of capture in [Figure 5A](#), we selected 100 random capture strikes and manually annotated the frames where the jaw was maximally extended.

For subsequent analysis, we only considered the 50 ms time window shown in [Figure 5A](#) (24–74 ms after the bout onset as determined by our bout segmentation algorithm) and proceeded with our general DTW-isomap embedding algorithm as described above (see [Generating a behavioral space](#)). To generate the capture strike subspace, we computed the DTW distance between each pair of strikes, only allowing warping within a 6 ms (3 frames) time window. We used the resulting pairwise distance matrix directly for isomap embedding, keeping the first two dimensions. Note we did not need to perform an intermediate affinity propagation micro-clustering step, due to the small size of this dataset. We then performed k-means clustering ($k = 2$) to classify strikes.

Free-swimming behavioral assay in three dimensions

To record behavior simultaneously from above and from the side, we designed a new chamber. A 3 mL transparent, unfrosted plastic cuvette was with flooded with 2% agarose. An acrylic rod ($20 \times 5 \times 5$ mm) was inserted into the liquid agarose, which was allowed to set, after which the rod was removed leaving behind a hollow chamber. As before, individual larvae were introduced into the chamber with a drop of paramecia culture topped up with fish system water. The opening was plugged with a small piece of acrylic cut to match the cross section of the chamber (5×5 mm). The cuvette was placed on its side on top of a glass coverslip suspended above a mirror angled at 45° . The high speed camera was positioned above this setup in such a way as to allow the fish in the chamber as seen from above as well as the reflected side view from the mirror to be visible within the field of view of the camera. The IR LED array was rotated by 90° , allowing the chamber to be illuminated from the side and from below (via the mirror) with a single light source. We reduced the aperture of the camera objective so that the entire arena was in focus in both views and offset the decrease in luminance by increasing the exposure time of each frame. Consequently, for this experiment we achieved a frame rate of 400 fps. As described above, data from each fish was split into 20x 1 min recording trials.

To record jaw movements during prey capture with higher spatial resolution in [Video S6](#), we used two cameras (PhotonFocus, MV1-D1312-160-CL, Switzerland) and two light sources and filmed a number of fish swimming in a custom-built transparent chamber. We waited for one of the fish to start hunting a paramecium in the field of view of both cameras and manually triggered the recording. Frame acquisition was synchronized using StreamPix 5 and a dual camera frame grabber.

Jaw tracking

As for the single view setup, each frame was tracked independently offline using custom-written Python scripts. Each frame was divided by a background image, calculated as the median of every 100th frame over a recording trial. The upper and lower halves of the frame were tracked separately. The lower half of the frame, containing the image of the fish as seen from above, was tracked as described above. Fish were only tracked from the side when their heading was within $\pm 45^\circ$ of the imaging plane to minimize artifacts arising as a result of foreshortening. Frames were thresholded and contours extracted using OpenCV. The largest contour in the image was taken as the outline of the fish and all other pixels were discarded. Then, the histogram of pixel values of the fish was normalized and a second threshold was applied to find a contour enclosing the head and body of the fish. The pitch and angle of the cranium were calculated using image moments of these two contours respectively, with cranial elevation defined as the difference between them.

To find the point of the base of the jaw, we first identified the centroid of the head-body contour and the vector defined by the cranium angle (i.e., orientation of this contour in the frame). We extended this vector from the centroid until it intersected the fish contour. Next, we found the midpoint between the centroid and this intersection point. From this midpoint, we extended a vector orthogonal to cranium angle vector until it intersected the fish contour at the base of the jaw. Jaw depression was defined as the Euclidean distance between the midpoint and this intersection point.

The cranial elevation angle and jaw depression were smoothed with an edge-preserving five-frame median filter. Then, we applied a high-pass filter by subtracting the baseline of these two kinematic features over a recording. To compute this baseline, we first calculated a 250 ms rolling minimum, and then computed the one-second rolling mean of this rolling minimum. This provided a relatively stable baseline for identifying jaw movements, despite changes in pitch and azimuth of the fish over a recording. To segment jaw movements, we identified periods when the baseline-adjusted jaw depression, smoothed with a 50 ms rolling average, was above a predetermined threshold and defined movement onset and offset as inflection points in this smoothed trace.

Generating a behavioral space of jaw movements

To generate the jaw movement behavioral space in [Figure 6F](#), we performed PCA on the jaw depression and cranial elevation traces across movement frames (see [Jaw tracking](#)). We calculated the DTW distance (warping bandwidth = 10 ms) between each pair of movements projected onto the first principal component ([Figure 6E](#)), and performed isomap embedding using the resulting distance matrix. To identify clusters, we used Hierarchical Density-Based Spatial Clustering of Applications with Noise (HDBSCAN) (hdbscan library, Python).

Paramecium tracking from the side

We tracked paramecium and generated stimulus maps from the side in a similar manner as described above (see [Paramecium tracking](#) and [Generating stimulus maps](#)). To generate stimulus maps, we aligned frames using the centroid of the contour outlining the head and the pitch of the fish in the water. Baseline paramecium density was calculated from ~18,000 randomly selected frames.

Lensectomy

For lensectomy experiments, larvae were allowed to feed on paramecia *ad libitum* between 5 and 6 dpf. At 7 dpf, larvae were anaesthetized in 0.02% tricaine (MS-222, Sigma-Aldrich) and then embedded in 2% low melting point agarose (Invitrogen). Larvae were kept anaesthetized for the entire surgery. Some of the agarose was removed from around the eyes using a scalpel to facilitate access. Animals undergoing sham, unilateral, or bilateral lensectomy were all treated in the same way up to this point and mounted alongside each other to ensure as similar treatment conditions as possible. Lensectomies were performed with borosilicate glass needles pulled to a sharp point. A single horizontal incision was made in the transparent cuticle of the eye and the lens was removed, taking care not to damage other parts of the eye such as the retinal pigment epithelium. This was performed on either one or both eyes. Unilateral lensectomies included animals that had either the left or right lens removed. Animals were freed from the agarose and allowed to recover overnight in fish system water. Immediately prior to behavioral testing at 8 dpf, animals were inspected for swelling or other aberrations to the eye, and excluded from the experiment if this was seen. Animals were tested in the 2D prey capture assay as described above. After behavioral testing, each larva was re-embedded in agarose and a snapshot of its head obtained with a camera mounted to a stereomicroscope to confirm that the lens had not regenerated.

QUANTIFICATION AND STATISTICAL ANALYSIS

Statistical tests were performed using the SciPy library in Python, or, if appropriate tests were not available in this library, we wrote new code to perform statistical tests. For plots, the type of error bar and p values are indicated in the figure legends.

Identification of significant transition modes

Significant transition modes in [Figure 2D](#) were identified by permutation testing and cross validation. Animals were split into training and test groups (50% animals in each group). Transition matrices were constructed for these two groups and SVD was used to identify transition modes of the training group. For each mode we constructed a transition model by adding the common transition mode to it. We compared these training models with the test group's transition matrix by computing the sum of squares error between them. This was repeated across 10,000 splits into training and test datasets. We tested the significance of each mode with a one-sided t test on the distribution of sum-of-square errors across all partitions of the data (significance level = 0.01), for modes that provided a better prediction than the common-mode model alone.

Comparison of transition modes across experimental datasets

To compare transition modes across datasets and treatment groups, we calculated the absolute value of the cosine similarity between the first four symmetric modes (S-modes) or first four antisymmetric mode pairs (A-modes). To test significance, we performed a permutation test. We permuted the labels between the two groups 1000 times (or if an exact test required less than 1000 comparisons, used that) and calculated the pairwise similarity of equivalent modes. This generated a null distribution of similarities against which we could calculate a p value for the observed similarity between unshuffled groups. For calculating the similarity between antisymmetric modes, we compared both left and right singular vectors to account for rotations and took the maximum. In the [Results](#) section, we report the similarity between like transition modes (i.e., always comparing S1 to S1 and A1 to A1 etc.). In [Figures S3C](#), [S5D](#), and [S6C](#) we show pairwise similarities between different transition modes.

Simplex projection to test higher order behavioral dynamics

To test whether higher-order behavioral dynamics were present in behavioral data ([Figure 3E](#)), we took each focal bout and inspected the preceding bouts in the chain. We identified all other occasions that this sequence of states occurred in the rest of the data and calculated which state was most likely to occur next. We calculated the probability of predicting the next bout correctly across all instances of a given behavioral cluster to obtain a distribution. We compared the probability distributions obtained by considering the past n-1 bouts in a chain with those obtained comparing the past n bouts in the chain using a one-tailed Student's t test and corrected for multiple comparisons with a Bonferroni correction (significance level = 0.01).

Identification of significant transitions in an ethogram

To identify which first-order transitions between behavioral clusters were significant ([Figure 3F](#)), we used a permutation test. We shuffled the order of bouts *within* each fish 1000 times and recomputed the first-order Markovian transition probability matrices. This gave a reference distribution of transition probabilities between each pair of modules from which we could calculate one-tailed p values. We considered significant transitions as those that had a p value < 0.05 after applying a Holm-Bonferroni correction ($7^2 = 49$ comparisons).

Statistical analysis of virtual prey experiments

We compared the cumulative distributions of bout duration and number of prey capture bouts per sequence across all trials with a Kolmogorov-Smirnov test. To compare averages for these two metrics, we calculated the mean per fish and then compared control and test trials with a Wilcoxon signed rank test.

Quantification of prey distance during capture strikes

We tracked paramecia in the front central visual field of the larvae and calculated the probability density as described above. We compared groups with a permutation test on energy distances. We shuffled labels between groups (attack swim versus S-strike or unilateral versus sham) 1,000,000 times to calculate a null distribution of energy distances. We calculated the one-tailed p value by comparing the observed energy distance to this null distribution. We calculated the energy statistic in two dimensions to compare 2D stimulus maps, or one dimension to compare distances and angles.

Quantification of lensectomy experiments

In [Figure 7](#), we tested time spent in prey capture (prey capture score), hunt initiation rate, strike probability, and number of capture strikes of each type between sham and unilateral, or unilateral and bilateral conditions with a Mann-Whitney U-test.

DATA AND CODE AVAILABILITY

The code generated during this study and sample data are available on Bitbucket (https://bitbucket.org/mpinbaierlab/mearns_et_al_2019). Processed data generated during this study are available at Mendeley data (<https://doi.org/10.17632/mw2mmpdz3g.1>). The full dataset generated during this study has not been deposited in a public repository due to its large size but is available from the corresponding author on request.

Current Biology, Volume 30

Supplemental Information

Deconstructing Hunting Behavior Reveals a Tightly Coupled Stimulus-Response Loop

Duncan S. Mearns, Joseph C. Donovan, António M. Fernandes, Julia L. Semmelhack, and Herwig Baier

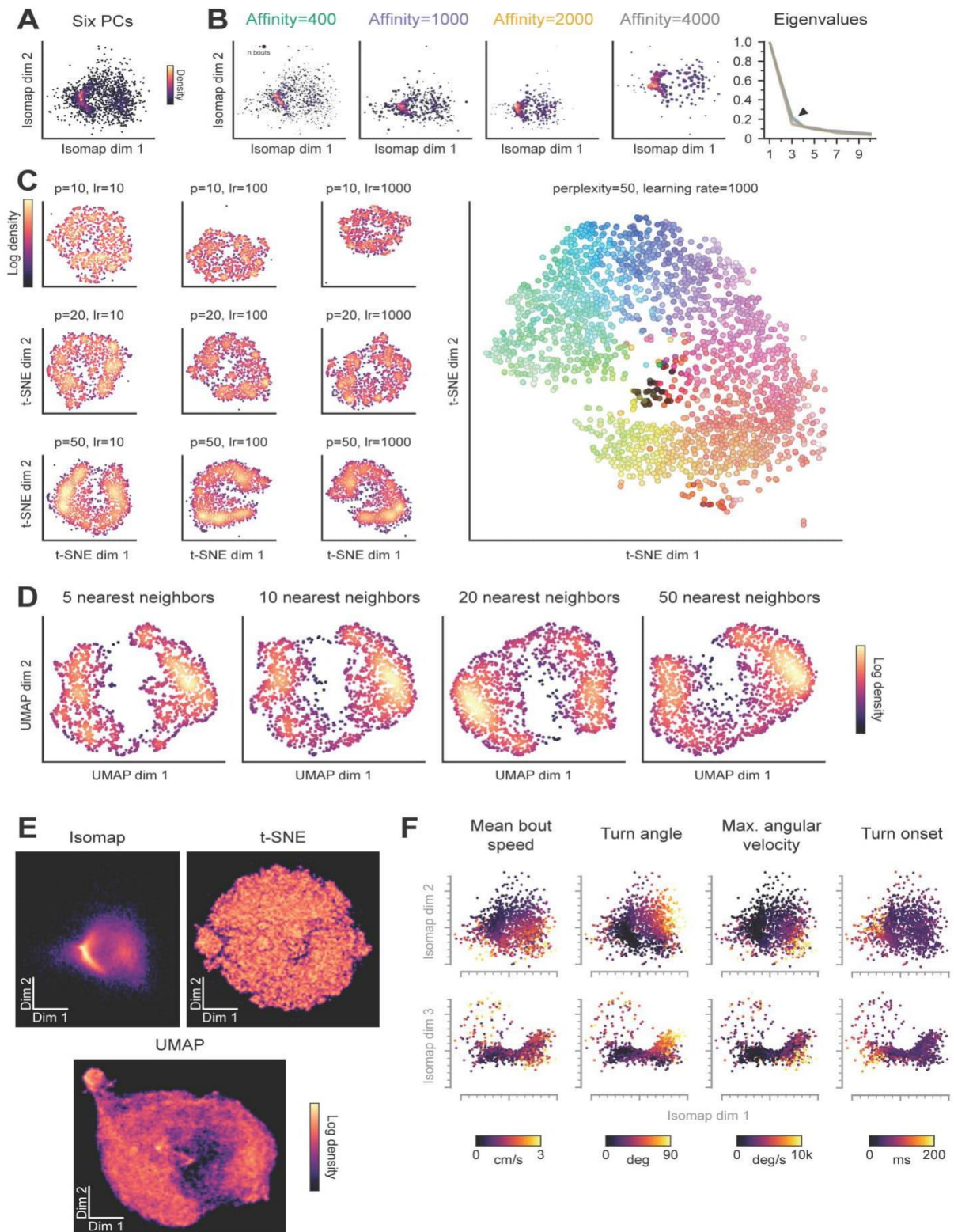


Figure S1. Validation of the behavioral embedding, Related to Figure 1.

(A) First two dimensions of behavioral space obtained by calculating the DTW distances using six principal components of postural space, which collectively explain 95% of the variance in tail shape (compare **Figure 1I,K**). (B) First two dimensions of the behavioral spaces obtained by embedding with different affinities. Across all affinity values there is a clear elbow in the third eigenvalue of the embedding (black arrowhead on right). Eigenvalues are normalized such that the first has a value of one. (C) Behavioral spaces obtained through t-SNE of the DTW distances between exemplars with different embedding parameters (p: perplexity, lr: learning rate). Right: behavioral space obtained through t-SNE, color coded according to the position of bouts in the space shown in **Figure 1I** for comparison. (D) Behavioral spaces obtained through UMAP of the DTW distances between exemplars, with different numbers of nearest neighbors used for the embedding. (E) Isomap, t-SNE, and UMAP embeddings obtained from the DTW distances between all bouts (not only exemplars). (F) Mean speed, turn angle, maximum angular velocity, and time of turn onset mapped into the behavioral space. Values represent median across each micro-cluster.

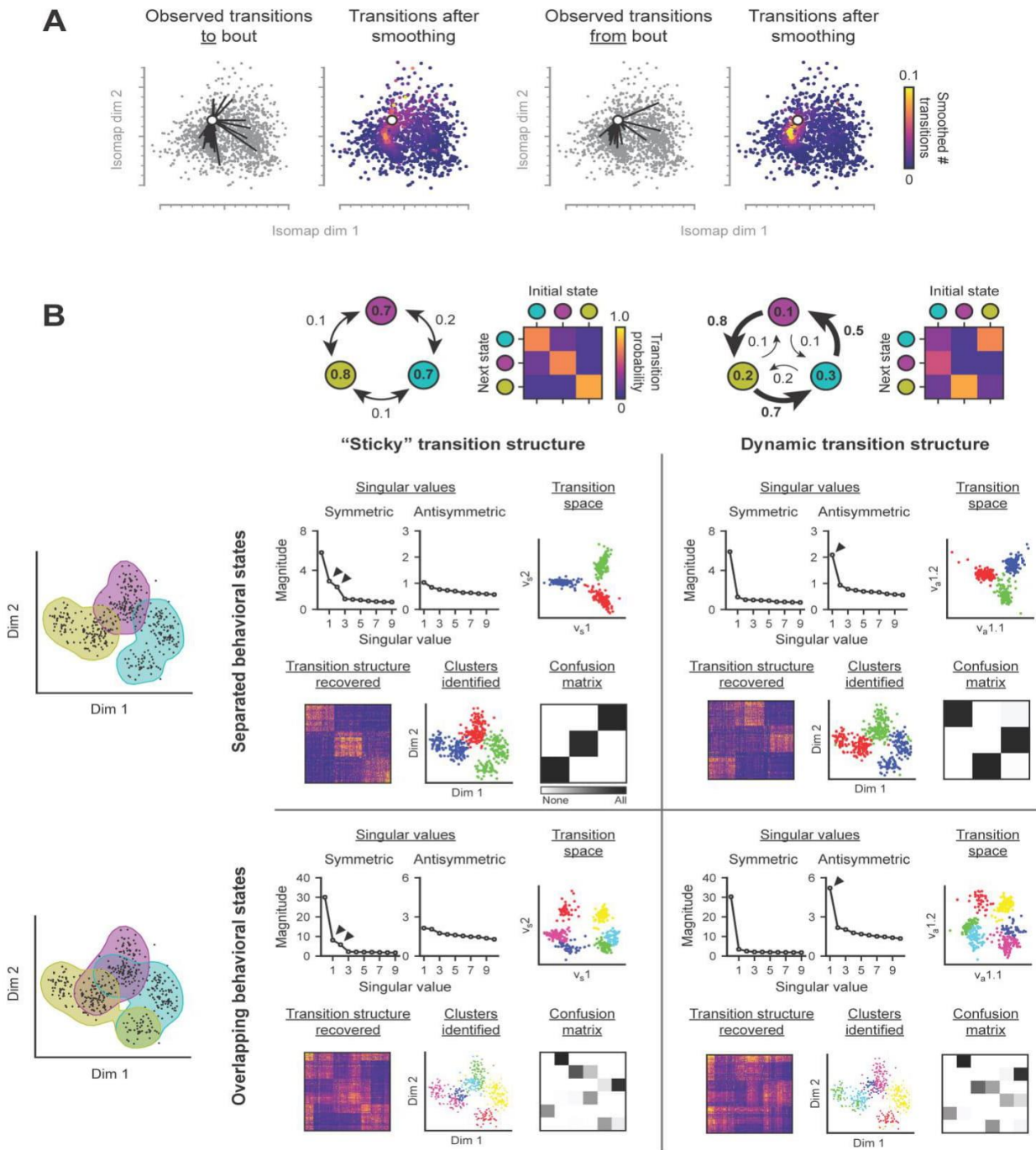


Figure S2. Example transition structures revealed through singular-value decomposition, Related to Figure 2.

(A) Smoothing transitions in the behavioral space. Note, that only the first two dimensions of the behavioral space are shown, although transitions are smoothed in three dimensions. (B) Singular-value decomposition (SVD) to identify transition modes in toy data. Top: for demonstration, two different hypothetical transition structures between three behavioral states represented by an ethogram and a transition probability matrix. Left,

structure dominated by symmetric transitions: behavioral states are “sticky”, and animals have an equal probability of transitioning in either direction between a pair of states. Right, structure dominated by antisymmetric transitions: behavioral states are dynamic, and animals are more likely to transition through states according to a specific sequence. Left: two different hypothetical distributions for the behavioral states in an arbitrary kinematic space. Each black point represents a hypothetical behavioral micro-cluster, analogous to points in the isomap space (see **Figure 1I**). Shaded regions show kernel density estimation over micro-clusters belonging to a given behavioral state. Top, separated behavioral states: each micro-cluster in the kinematic space only belongs to a single behavioral state. Bottom, overlapping states: micro-clusters in the kinematic space may contribute to multiple behavioral states. Center: behavioral sequences modelled using each combination of transition structure and behavioral state organization, and then analyzed using the SVD approach outlined in **Figure 2B** (including smoothing). Transition matrices are generated through a Monte-Carlo simulation using the Markov transition probabilities shown in top row, with stochastic (noisy) transitions contributing 20% of the total transitions. Singular values: singular values obtained from the symmetric and antisymmetric components of the modelled transition frequency matrix. Black arrowheads show higher singular values indicative of a given transition structure being present in the data. Transition space: behavior micro-clusters mapped onto the singular vectors and clustered with ward hierarchical clustering (colors). Behaviors modelled with symmetric transition structure are mapped onto the first two symmetric transition modes (v_s1 and v_s2 , respectively). Behaviors modelled with antisymmetric transition structure are mapped onto the pair of vectors representing the first antisymmetric transition mode ($v_a1.1$ and $v_a1.2$). Transition structure recovered: smoothed transitions between each pair of micro-clusters, matrix ordered using hierarchical distances in the transition space. Clusters identified: clusters identified by hierarchical clustering in the transition space mapped into the hypothetical behavioral space. Confusion matrix: ground truth cluster labels compared to cluster labels obtained from the SVD. When states overlap in behavioral space, ground truth cluster labels are defined by intersections.

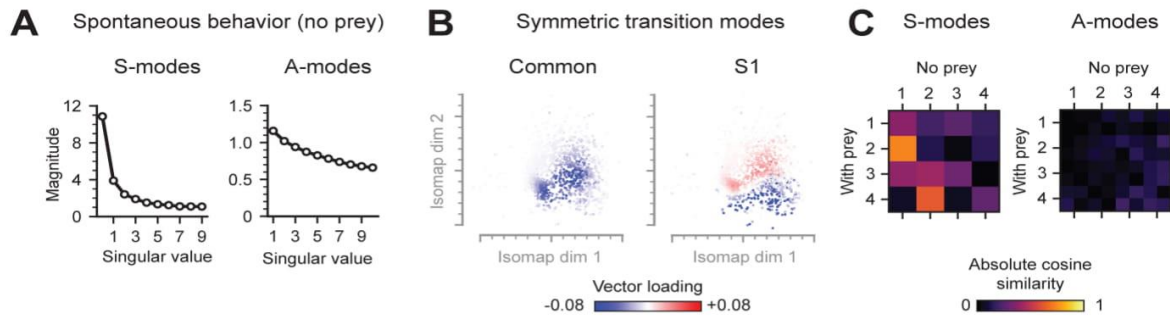


Figure S3. Behavioral dynamics in the absence of prey, Related to Figure 2.

(A) Singular values of the symmetric (S-modes) and antisymmetric (A-modes) transition modes acquired from fish swimming in the absence of prey. (B) Common mode and first S- mode (S1) of fish swimming in the absence of prey. Behavioral dynamics are shifted towards the spontaneous region of the behavioral space (compare Figure 2E,F). (C) Comparison of the transition modes acquired from fish swimming in the absence and presence of prey. Pairwise absolute cosine similarities between vectors representing each transition mode. If transition modes were exactly identical, the matrix would show a strong diagonal stripe.

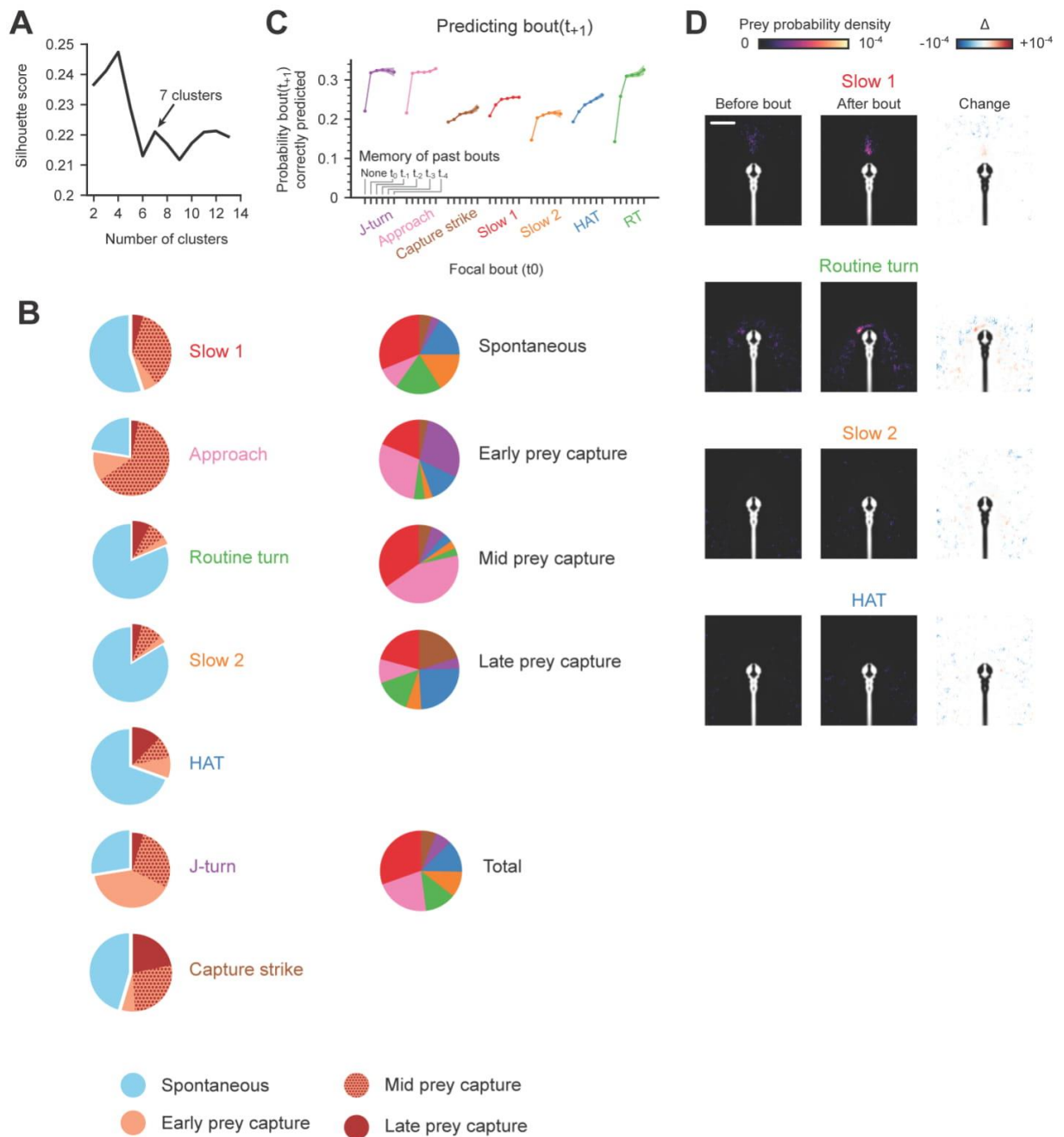


Figure S4. Behavioral clusters, Related to Figure 3.

(A) Silhouette score for different numbers of clusters in the combined kinematic-transition space. A small peak in the silhouette score at seven motivated the use of this number of clusters, though behavior in space isn't distinctly modular, so variations in silhouette score are small. The slightly better silhouette score at four clusters is less biologically plausible and results in excessive over-clustering. (B) Left: proportion of bouts in each cluster that occur during spontaneous swimming (blue), early prey capture when the eyes first converge (pink), mid prey capture when the eyes are converged (pink with red dots), or late prey capture when the eyes de-converge (red),

where prey capture state is determined by eye convergence criteria. Approach swims, J-turns and capture strikes predominantly occur during prey capture while other clusters are more associated with spontaneous swimming. Right: breakdown of spontaneous swimming and prey capture stages showing proportion of bouts belonging to each cluster. Chart colors correspond to labels on the left (and are consistent with other parts of the paper). J-turns are over-represented during early prey capture, approach swims are over-represented during early and mid prey capture, and capture strikes are over-represented during late prey capture. Lower right: proportion of all bouts belonging to each cluster. **(D)** Stimulus maps associated with slow 1 swims, routine turns, slow 2 swims and high amplitude turns (HATs). Slow 1 swims are associated with some density in the anterior visual field, suggesting their use to pursue more distant prey during prey capture. High density around the head of the fish during routine turns is likely a result of errors in particle tracking when animals are near a wall. Average image of the fish is shown in white (left, center) or black (right). Scale bar: 1 mm.

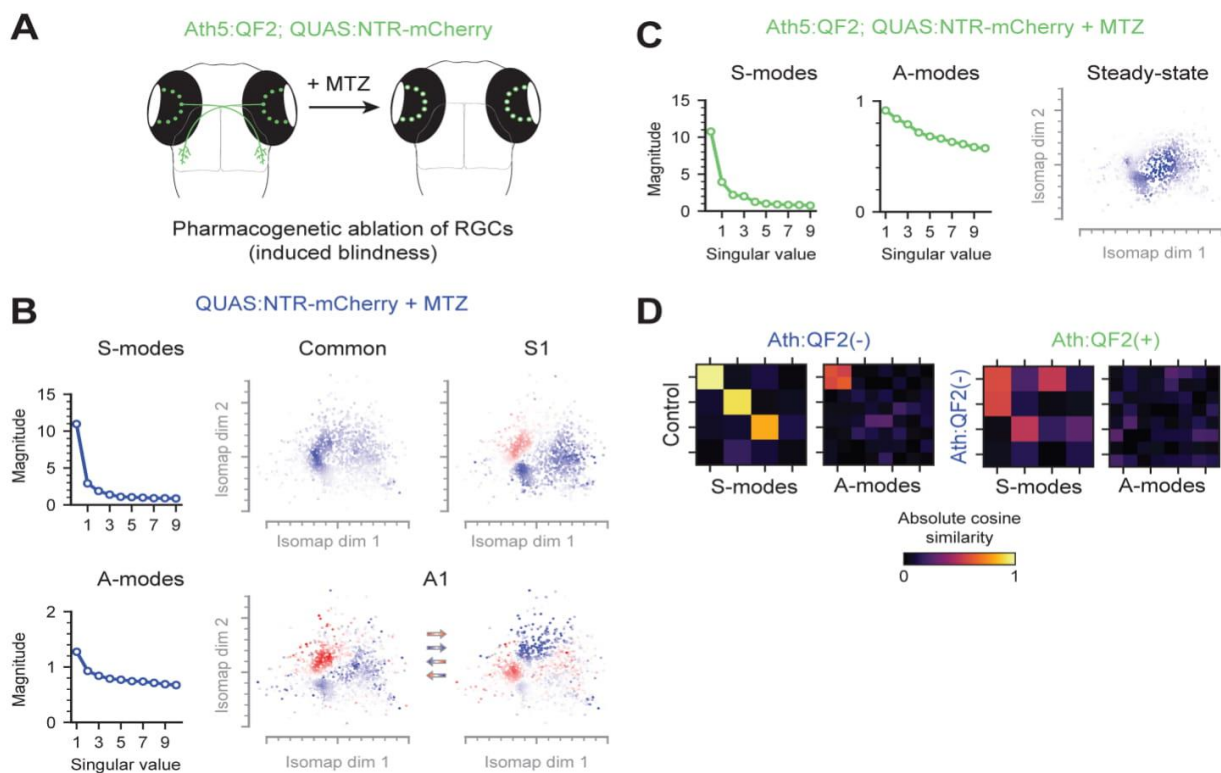


Figure S5. Behavioral dynamics in RGC-ablated fish, Related to Figure 4.

(A) Schematic showing induced blindness in double transgenic larvae. Nitroreductase (NTR) induces apoptosis in the presence of the drug, metronidazole (MTZ). We use the QF2/QUAS bipartite genetic expression system to drive NTR in retinal ganglion cells (RGCs). At 6 dpf animals are treated with MTZ, causing loss of RGCs. (B) Behavioral dynamics in MTZ-treated *Ath5:QF2(-)* (control) animals. Top: symmetric transition modes (S-modes). The common mode shows that these animals make full use of their behavioral space and the first S-mode (S1) shows separation of prey capture and spontaneous bouts. Bottom: antisymmetric transition modes (A-modes). The first A-mode (A1) contains normal prey capture dynamics. (C) Behavioral dynamics in ablated animals. Ablated animals display only a single elevated transition mode – the common mode – which shows their behavior is skewed towards the spontaneous region of the behavioral space. (D) Comparison of transition modes across groups. Left: transition modes obtained from non-ablated *Ath:QF2(-)* animals compared to canonical modes (control) obtained from original dataset (see **Figure 2**). The vectors representing the A1 are rotated by about 45° in the transition space relative to the canonical mode. Right: ablated modes compared to *Ath:QF2(-)* controls.

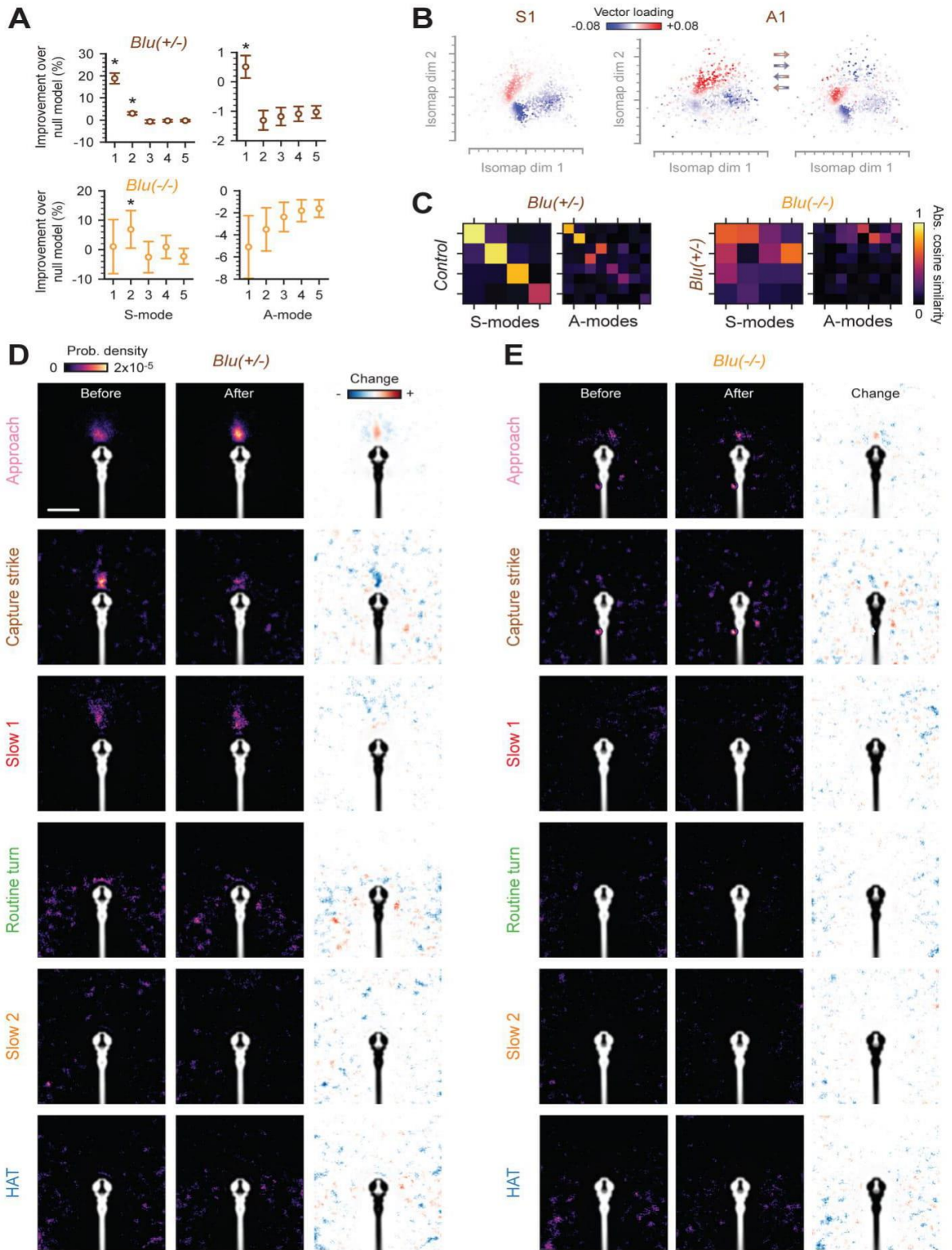


Figure S6. Behavioral dynamics in *blumenkohl* mutants, Related to Figure 4.

(A) Predicting behavior from transition modes in heterozygous sibling controls (*blu*(+/-), top) and *blu*(-/-) mutants (bottom). (B) First symmetric (S1) and antisymmetric (A1) transition modes of control animals, showing normal prey capture dynamics. (C) Comparison of transition modes across groups. Color intensity indicates absolute value of the dot product between singular vectors for the first four S- and A-modes. Left: *blu* heterozygous sibling control modes compared to canonical modes obtained from original dataset (see **Figure 2**). Right: *blu* mutant modes compared to controls. (D) Stimuli associated with different bout types in *blu*(+/-) control animals. Approach swims, capture strikes and slow 1 swims associated with prey capture behavior are triggered by similar stimuli as in wild-types (compare **Figure 3H**). (E) Stimuli associated with different bout types in *blu* mutants. Note the lower prey probability density in the anterior visual field prior to approach swims, capture strikes and slow 1 swims, indicating that these bouts are not as reliably triggered by specific releasing stimuli compared with controls. Scale bar in (D): 1 mm, applies to all sub-panels in (D) and (E).

2.2 Retinotectal circuitry of larval zebrafish is adapted to detection and pursuit of prey

Dominique Förster[†], Thomas O. Helmbrecht[†], **Duncan S. Mearns**, Linda Jordan, Nouwar Mokayes, and Herwig Baier

[†]These authors contributed equally to this work.

This article was published in *eLIFE* in October 2020 (Förster et al., 2020).

Retinotectal circuitry of larval zebrafish is adapted to detection and pursuit of prey

Dominique Förster^{1†}, Thomas O Helmbrecht^{1,2†}, Duncan S Mearns^{1,2}, Linda Jordan¹, Nouwar Mokayes¹, Herwig Baier^{1*}

¹Max Planck Institute of Neurobiology, Department Genes – Circuits – Behavior, Martinsried, Germany; ²Graduate School of Systemic Neurosciences, LMU BioCenter, Martinsried, Germany

Abstract Retinal axon projections form a map of the visual environment in the tectum. A zebrafish larva typically detects a prey object in its peripheral visual field. As it turns and swims towards the prey, the stimulus enters the central, binocular area, and seemingly expands in size. By volumetric calcium imaging, we show that posterior tectal neurons, which serve to detect prey at a distance, tend to respond to small objects and intrinsically compute their direction of movement. Neurons in anterior tectum, where the prey image is represented shortly before the capture strike, are tuned to larger object sizes and are frequently not direction-selective, indicating that mainly interocular comparisons serve to compute an object's movement at close range. The tectal feature map originates from a linear combination of diverse, functionally specialized, lamina-specific, and topographically ordered retinal ganglion cell synaptic inputs. We conclude that local cell-type composition and connectivity across the tectum are adapted to the processing of location-dependent, behaviorally relevant object features.

Introduction

Theories of efficient sensory coding (*Barlow, 1961*) often make the implicit assumption that the goal of sensory processing is a veridical representation of the external world. However, it is clear that the ultimate arbiter of efficiency is natural selection and that genetic information, developmental time, space, and material impose constraints on the design of the nervous system. Each of these evolutionary constraints has contributed to the neural implementations as we witness them in today's animal brains, making the ultimate goal of calculating an optimization function difficult to achieve (*Chalk et al., 2018; Dan et al., 1996; Machens et al., 2005; Simoncelli, 2003*). To understand why circuits are organized as they are and develop as they do, it is of paramount importance to identify constant and pervasive selective pressures that arise from the species-specific lifestyle of the animal. This study provides experimental support for the notion that the local statistics of the sensory environment, which changes dynamically as the animal interacts with the outside world, shape the topographic specializations of higher-order sensory and sensorimotor circuitry.

For many decades the retinotectal projection of zebrafish has served as a paradigmatic example for a visual map. Retinal inputs to the tectum are ordered retinotopically such that the position of an object in the visual field matches a corresponding focus of activity in tectal space (e.g., *Muto et al., 2013*). Neighborhood relationships in the environment, as they are projected onto the two-dimensional sheet of photoreceptors in the retina, are represented by neural activity in neighboring regions of the tectum. Visual stimuli in the front of the larva are detected by temporal regions of the retina, which transmit pre-processed information via the axons of retinal ganglion cells (RGCs) to anterior regions of the tectum. Similarly, stimuli in the peripheral visual field behind the animal activate nasal retina and posterior tectum, respectively (*Figure 1A*). The tectum then ultimately transforms visual information into behavioral commands (e.g., *Helmbrecht et al., 2018*).

*For correspondence: hbaier@neuro.mpg.de

†These authors contributed equally to this work

Competing interests: The authors declare that no competing interests exist.

Funding: See page 23

Received: 05 May 2020

Accepted: 07 September 2020

Published: 12 October 2020

Reviewing editor: Koichi Kawakami, National Institute of Genetics, Japan

© Copyright Förster et al. This article is distributed under the terms of the [Creative Commons Attribution License](https://creativecommons.org/licenses/by/4.0/), which permits unrestricted use and redistribution provided that the original author and source are credited.

eLife digest The retina is the thin layer of tissue in the eye that can receive light stimuli and convert them into electric signals to be transmitted to the brain. The cells that sense fine detail cluster at the center of the retina while the motion-sensing cells that keep track of movement lie at the periphery.

When zebrafish larvae hunt, their motion-sensing cells are triggered as a prey crosses their peripheral field of view. They then turn and swim towards it. As they approach, the prey image moves to the detail-sensing part of the retina and appears larger, filling more of the field of view at close range. The signals are then processed in defined parts of the brain, in particular in a region called the optic tectum. How this area is organized in response to the organization of the eye and the requirements of the hunt is still unclear.

Förster et al. set out to explore how the hunting routine of zebrafish larvae shapes the arrangement of neurons in the optic tectum. The larvae were exposed to different images representing the various aspects of the prey capture process: small moving dots represented passing prey at a distance, while large moving dots stood for prey just before capture. Measuring activity in the neurons of the optic tectum revealed that, like the eye, different areas specialize in different tasks. The back of the tectum was frequently activated by small dots and worked out which direction they were moving in during the first hunting steps. The front of the tectum responded best to large dots, often ignoring their direction, and helped the larvae to track their prey straight ahead. To test these findings, Förster et al. destroyed the large object-responsive cells with a laser and watched the larvae hunting real prey. Without the cells, the fish found it much harder to track and catch their targets.

These results shed light on the link between behavior and how neurons are arranged in the brain. Future work could explore how the different neurons in the optic tectum are connected, and the behaviors they trigger in the fish. This could help to reveal general principles about how sensory information guides behavior and how evolution has shaped the layout of the brain.

The neuropil of the larval zebrafish tectum is spatially organized along the superficial-to-deep axis into layers, ten of which are receiving input from dedicated subsets of RGCs (Robles et al., 2013; Robles et al., 2014). The remaining layers are innervated by axons from the somatosensory lateral line (Thompson et al., 2016) or contain dendrites and axons of interneurons and projection neurons (Helmbrecht et al., 2018). The tectal neuropil layers are schematically depicted in Figure 1B. Recent work has revealed an enormous functional and morphological diversity of RGC types, which serve as local feature detectors for specific aspects of the visual scene, such as direction of motion, onset or offset of light, object size or chromaticity. Earlier studies have shown that individual RGCs select one layer each, in which they arborize and make synapses onto tectal dendrites (Xiao and Baier, 2007). Thus, each retinorecipient layer contains a complete, yet feature-selective, map of visual space. RGCs that respond to visual features resembling the speed and size of prey project to the most superficial layer (SO; Semmelhack et al., 2014; see Figure 1B), whereas RGCs that are specifically tuned to a rapidly expanding (looming) dark object, simulating an approaching predator or an obstacle on a collision course, terminate in deeper layers (SFGS5/6; Temizer et al., 2015; see Figure 1B).

Asymmetries in visual feature processing have been recognized across the retina of several vertebrates (for a recent review, see Baden et al., 2020). Prime examples for such functional specializations are the fovea of primates (Sinha et al., 2017), the asymmetric distributions of RGC types and photoreceptors in mice (Baden et al., 2016; Bleckert et al., 2014; Szatko et al., 2020; Warwick et al., 2018) and of bipolar cells, photoreceptors and RGCs in zebrafish (Yoshimatsu et al., 2020; Zhou et al., 2020; Zimmermann et al., 2018). The two retinotopic dimensions of the tectum, the anterior-posterior and the dorsal-ventral axis, have so far received little attention in this regard. Zebrafish larvae do not possess a *prima facie* fovea, although they have evolved a high-acuity subarea in the temporal-ventral quadrant of the retina in which RGCs are more densely packed than in the periphery (Schmitt and Dowling, 1999; Zhou et al., 2020). This region holds the image of prey in the final phase of hunting behavior and, similar to the mammalian fovea,

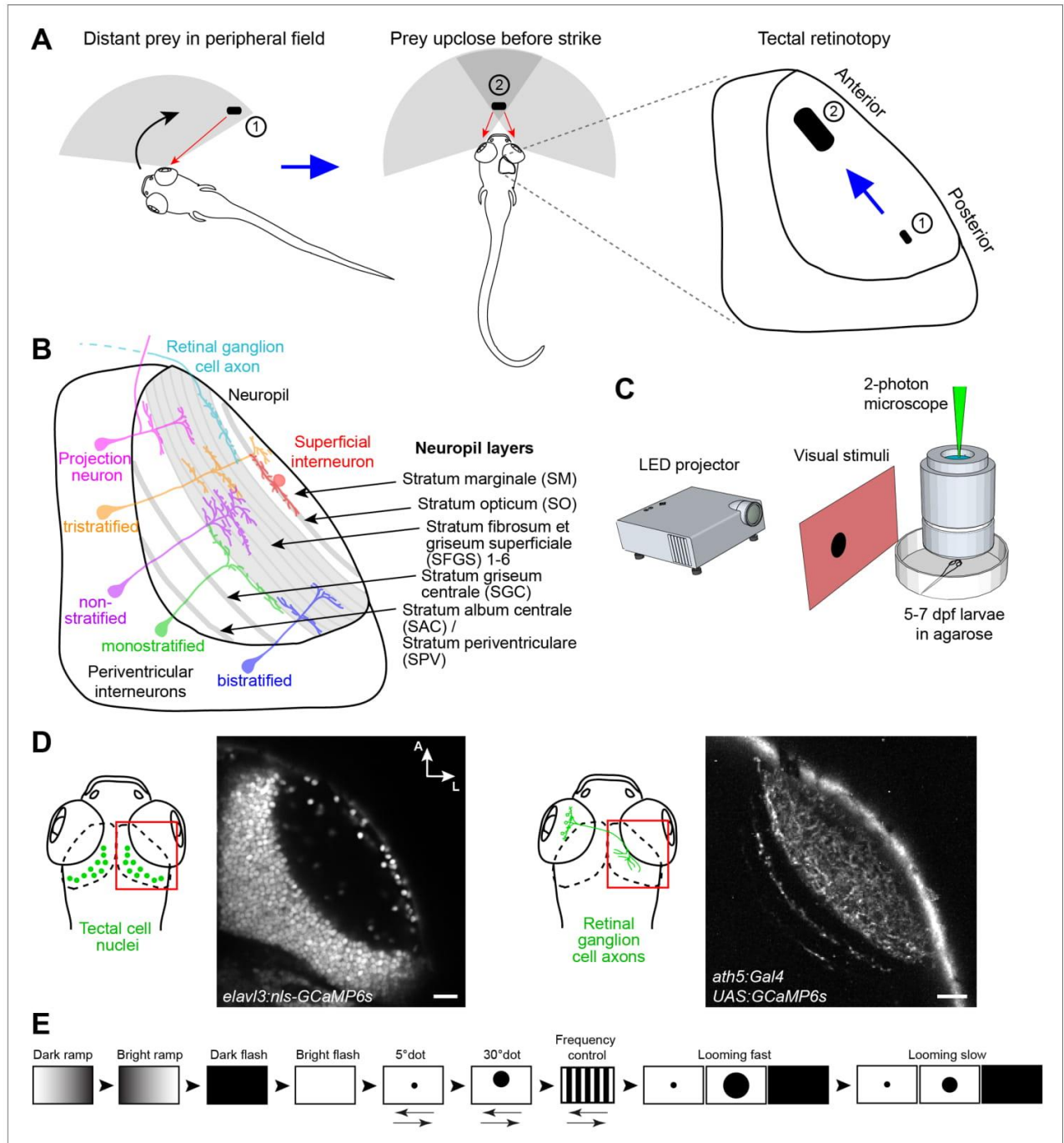


Figure 1. Experimental paradigm for studying location-specific processing in the tectum. (A) In a typical hunting sequence, the fish detects prey in its peripheral visual field (1), ultimately turns and approaches to bring the prey image into its central binocular field (2). Hypothetically, the retinotectal map might be adapted to this location- and size-specific representation of the prey object. (B) Sketch of the tectum showing previously described cell types and neuropil layers. (C) Schematic for functional imaging setup. (D) On the left: Region of interest (ROI) for imaging tectal cell responses and exemplary expression of nuclear-localized GCaMP6s. On the right: ROI for RGC imaging and expression of GCaMP6s in RGC axons under control of *ath5:Gal4*. (E) Figure 1 continued on next page

Figure 1 continued

Stimulus protocol. Arrows below stimulus representation indicate object movement, first in nasal, then in temporal direction. See Materials and methods for details. Scale bar in (D): 20 μm .

occupies a disproportionately large area of the visual map in the tectum. Despite a wealth of data on tectal neuron morphologies (see *Figure 1B*; Förster et al., 2017; Nevin et al., 2010; Robles et al., 2011; Scott and Baier, 2009), systematic changes in cell-type composition or connectivity along the anterior-posterior or dorsal-ventral axes of the tectum, resulting in gradients or other asymmetries of feature selectivity, have just begun to be revealed (Wang et al., 2020).

Here, we ask if such asymmetries can be predicted from first principles and related to the behavioral ecology of the zebrafish larva. As the animal interacts with a visual object through its own movements, relevant stimulus features continually change within the retinotopic coordinate frame. For example, in a typical hunting cycle, a zebrafish larva detects a prey item at a distance in its peripheral, monocular visual field (Mearns et al., 2020; Patterson et al., 2013). Posterior tectal circuits might therefore have evolved to respond to small-sized objects of ca. 5° and to locally compute their direction of movement. As the fish turns toward and approaches the prey, the stimulus enters the central, binocular visual field and expands to ca. 30° in visual angle (*Figure 1A*). Activation of the anterior tectum has previously been described during this late hunting phase (Muto et al., 2013). Neurons in the anterior tectum should therefore be tuned to larger object sizes and may rely on interocular comparisons to compute the object's displacement from the midline. At all positions, the tectum should be able to distinguish between prey and looming threats and process them separately (Barker and Baier, 2015). The laminar segregation of functional channels, which are established by RGC inputs, is therefore expected to be maintained by tectal circuits independent of retinotopic location.

Using volumetric two-photon calcium imaging to map out the feature space along the anterior-posterior retinotopic axis and across the layers of the tectum, we discovered a neural substrate for each of above predictions. Moreover, we show that the broad range of tectal responses originate to a large extent, but not exclusively, from a linear combination of functionally diverse RGC inputs. The dendrites of tectal cells are positioned in layers that predict their stimulus selectivity. We conclude that the cellular architecture underlying local processing in the tectum is adapted to the expected features of a prey object as it moves across the visual field during a hunting pursuit.

Results

Tectal neurons respond to a broad range of visual features

To broadly sample responses to object features, we designed a battery of simplified visual stimuli and controls. We employed two-photon calcium imaging of 5 to 7 dpf old larvae, which received monocular visual stimulation (*Figure 1C*). At this larval stage, panneuronal expression of the nuclear-localized calcium indicator GCaMP6s (driven by the *elav/3* promoter) labels on average 5793 ± 202 cells per tectum ($n = 10$ fish; mean \pm SEM) (*Figure 1D*). The stimulus set consisted of a moving dot of 5° ("small"), which approximates the size of prey at the onset of hunting behavior (Bianco and Engert, 2015; Patterson et al., 2013; Semmelhack et al., 2014), a moving dot of 30° ("large"), which is the approximate size of prey directly before the capture strike, and an expanding disc at different velocities, which simulates an approaching object and is able to evoke escape responses (Bhattacharyya et al., 2017; Dunn et al., 2016; Temizer et al., 2015). We further added controls for global luminance changes (dark and bright ramps and flashes), as well moving gratings with high spatial (5°) and temporal frequency as a negative control for small-dot responses (*Figure 1E*; see Materials and methods). With this battery of visual stimuli, we obtained reproducible calcium responses in up to 30% of all tectal cells per imaging plane. We created 15 regressors for the different stimulus variants and calculated a score value for each tectal cell (*Figure 2A*). To classify functional response types, we performed hierarchical clustering of representative response vectors obtained by affinity propagation (see Materials and methods). This resulted in a dendrogram for 76 exemplars, which are representative of the 1759 sampled tectal cells in total (*Figure 2B–D*, and *Figure 2—figure supplement 1A*). A silhouette analysis to validate the clustering showed that a

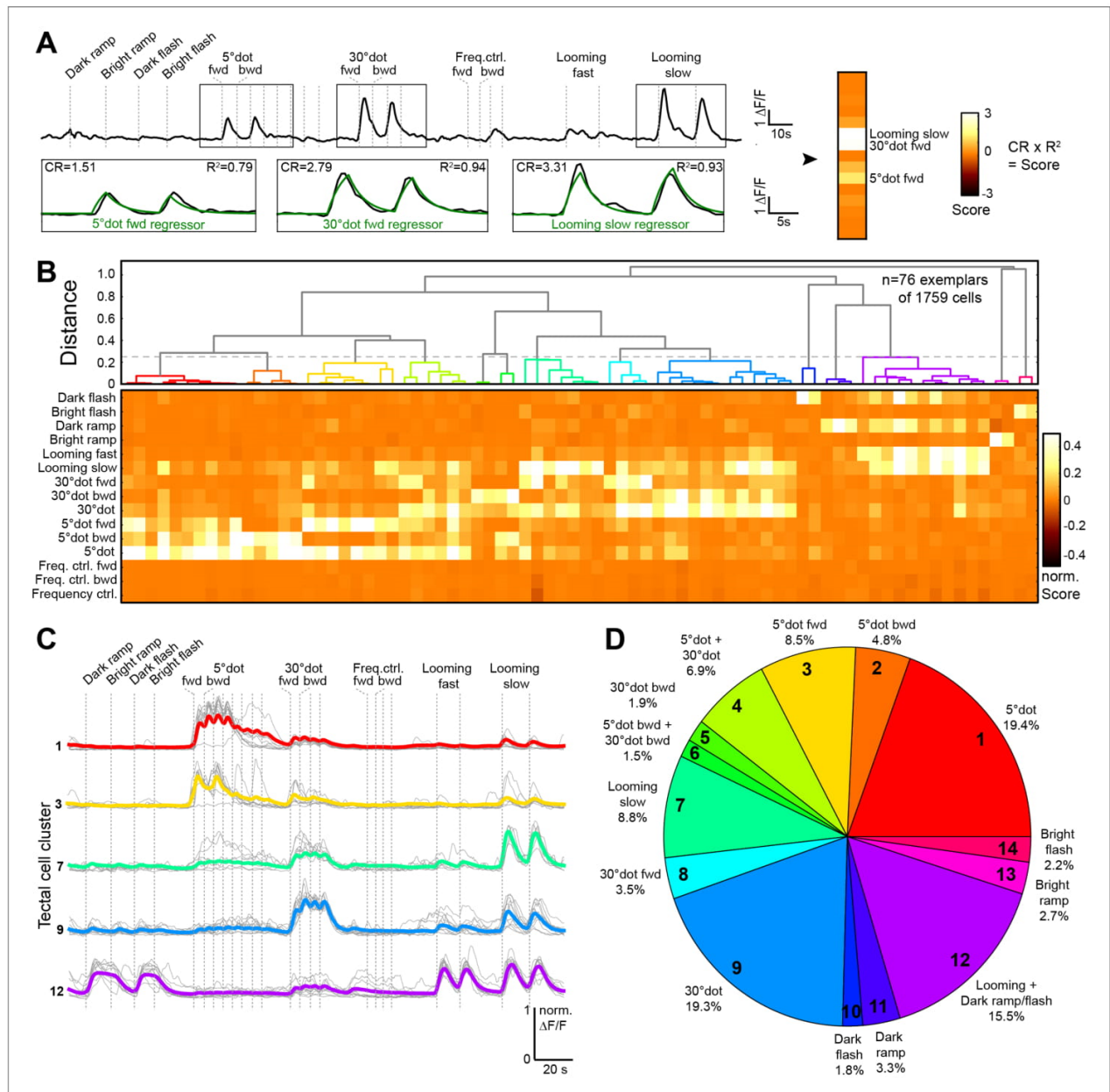


Figure 2. Behaviorally relevant response clusters in the tectum. (A) Analysis of calcium imaging data. Within selected response windows (black rectangles), the $\Delta F/F$ traces were correlated to the corresponding regressor and 15 score values were calculated for each cell (CR: coefficient of regression, R²: correlation, response: black trace, model: green trace). (B) Hierarchical clustering of functional cell types in the tectum. Normalized scores for 76 exemplars, obtained by affinity propagation of 1759 cells (of three larvae) in total are shown. Dashed line indicates a chosen distance threshold of 0.25, which results in 14 functional clusters. (C) Normalized calcium transients of all exemplars (gray) and average traces of all cells (colored) for the five largest clusters. (D) Functional cluster distribution. Tectal cluster numbers are indicated. The online version of this article includes the following figure supplement(s) for figure 2:

Figure supplement 1. Functional clustering of tectal cells.

minimal number of 14 clusters yielded an optimal classification of the data (*Figure 2—figure supplement 1B*; see Materials and methods).

To investigate the dimensional structure of the different response profiles, we performed principal component analysis on the scores for all tectal cells. Plotting the three main principal components (PCs), which could explain 74.9% of the variance in the dataset, aligned the scores along three axes for small-dot, large-dot, and looming/luminance- (OFF-) responding cells (*Figure 2—figure supplement 1C and D*). To show that the measured tectal cell responses were significantly different from chance, we shuffled the scores for each regressor 1000 times and calculated the PCs. Taking the average of the explained variance per shuffling, we consistently found a lower average explained variance, that is 57.6% for the three main PCs (*Figure 2—figure supplement 1D*), indicating that tectal cells do not respond randomly to our set of stimuli.

Responses of tectal neurons are enriched for various forms of object motion

Overall, we found a broad spectrum of different response types in the tectum. Few cells responded to only one of the presented stimuli; most cells we imaged were multi-responsive (*Figure 2B*). 43.6% of all cells responded to a looming stimulus (with a score >0.2), 41.1% responded to a small dot, and 33.1% responded to a large dot (*Figure 2D*). Only a small number of cells responded to a bright ramp (2.7%) or a bright flash (2.2%), and these cells were rarely sensitive to other stimuli. Responses to dark ramp and dark flash often coincided with each other and with responses to looming stimuli (fast and slow), but rarely overlapped with responses to small or large moving dots. Responses to a slow-looming stimulus showed a gradual overlap with moving-dot responses; more than half of all cells that were sensitive to a large dot also responded to a slow-looming stimulus. The 5° grating did not trigger significant responses in the tectum, suggesting a selectivity to individual objects rather than to high spatial frequency.

Next, we characterized the tuning properties of tectal cells whose somata reside inside the tectal neuropil. Superficial interneurons (SINs), with cell bodies in the SO to SFGS1 neuropil layers, have previously been reported to receive size-tuned retinal inputs (*Del Bene et al., 2010; Preuss et al., 2014*). The largest fraction of SINs was mapped to our large-dot responsive cluster (~45%; *Figure 2—figure supplement 1E*), whereas only a small number of SINs (~6%) were sensitive to a 5° dot. Neuropil interneurons (NINs), residing within deeper layers of the neuropil, predominantly belong to the looming/dark ramp-responsive cluster (~30%), with about 20% of NINs responding to large dots (*Figure 2—figure supplement 1E*).

Taken together, the majority of tectal cells, both in the periventricular layer and embedded in the neuropil, respond to object motion, that is small, or large, or looming dots, sometimes in combination. A substantial fraction of cells responds to global dimming or looming (OFF cells). Very few cells respond to global brightening (ON cells). OFF and ON cells are largely non-overlapping with object-detecting cells.

Tectal responses originate from diverse, feature-specific RGC inputs

We next asked to what extent the feature selectivity of tectal neurons is inherited from retinal inputs. In our imaging setup, we applied the same battery of visual stimuli to larvae expressing cytoplasmic GCaMP6s in RGCs (*Figure 1D*). A pixel-wise regressor and cluster analysis resulted in a dendrogram for 1157 exemplars, which were grouped into ten functional clusters (although four RGC clusters resulted in the highest silhouette coefficient, we chose 10 clusters, for a significantly higher modeling correlation score, as shown below) (*Figure 3A–C*, and *Figure 3—figure supplement 1*; see Materials and methods).

Overall, RGC responses were similar to tectal responses, but less specialized, with only few pixels responding exclusively to a single stimulus. Two thirds (67.2%) of the pixels responded to a large dot with a score greater than 0.2 (*Figure 3A* and *Figure 3—figure supplement 1A*). Generalized OFF responses to a dark ramp and a looming stimulus were similarly prominent. Non-intuitively, ON responses were sometimes combined with dark looming stimuli (RGC cluster no. 2 and 9; *Figure 3A* and *Figure 3—figure supplement 1A*), a tuning profile we did not observe in tectal cells. Interestingly, direction-selective responses to forward- (nasalward-) moving stimuli, especially to a large dot, were more abundant than for the opposite direction (*Figure 3A*). These units are expected to be

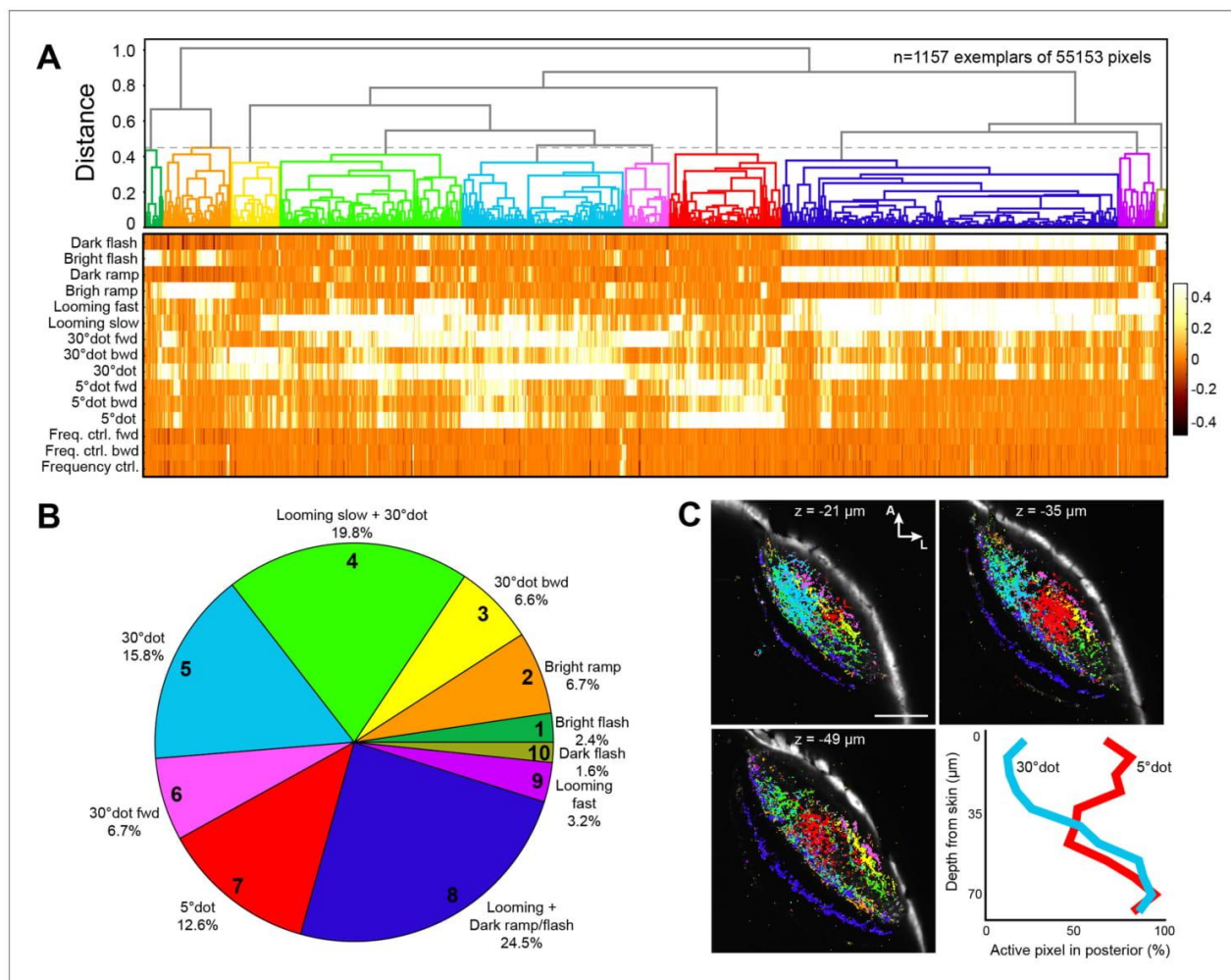


Figure 3. Clustering of functional RGC responses in the tectum. (A) Hierarchical clustering of functional RGC pixels. Normalized scores for 1157 exemplars, obtained by affinity propagation of 55,153 pixels in total are shown. Dashed line indicates a chosen distance threshold of 0.45, which results in 10 functional clusters. (B) Functional cluster distribution of all analyzed RGC pixels. Cluster numbers are indicated. (C) Spatial distribution of functional RGC pixels in the tectal neuropil. Pixels were cluster-color-coded and overlaid onto single planes of the *ath5:Gal4 UAS:GCaMP6s* expression pattern. Z indicates plane position as the distance from dorsal skin ($z = 0 \mu\text{m}$). Last panel in (C) shows quantification of 30° dot-responsive (blue) and 5° dot-responsive (red) pixels in the posterior tectum along different z-planes. Scale bar: 50 μm .

The online version of this article includes the following figure supplement(s) for figure 3:

Figure supplement 1. Functional clustering of RGC types.

Figure supplement 2. Figure panels showing the active RGC pixels of three imaging planes from **Figure 3C** separately for the three relevant clusters (30° dot, 5° dot, looming+dark ramp/flash).

activated when an object approaches from behind or when the fish turns toward an object in its peripheral visual field.

Tectal neurons linearly combine retinal inputs, but also compute de novo additional features

We asked to what extent we could quantitatively explain the sampled tectal responses by using ganglion cell input. This analysis can distinguish between two extreme scenarios: The tectum may either be a passive relay station for RGC inputs. Or, alternatively, it may 're-compute' the image based on

unrelated RGC inputs. We used a simple feed-forward, linear modeling approach (L1-regularized, Lasso) with non-negative constraints to predict tectal cell responses by a sum of weighted RGC inputs (Figure 4A; see Materials and methods). Modeling the scores for each of the 1759 tectal cells resulted in a high prediction quality (median correlation $R^2_{\text{score}} = 0.68$, median RMSE = 0.06; Figure 4B and Figure 4—figure supplement 1). Similarly, we modeled the calcium transients for all tectal cells and calculated the correlation R_{trace} between measured and predicted values (Figure 4C and D). We also tested how a varying score threshold for the RGC responses, and thus a different number of RGC clusters would change the modeling prediction quality. We found that the best prediction of tectal calcium transients (R_{trace}) can already be achieved by linear modeling of only four RGC clusters. Correlation for the tectal score values (R^2_{score}), however, increases significantly with ten RGC clusters (Figure 4—figure supplement 1).

Most tectal cell responses could be well explained by a linear combination of on average two RGC input clusters (Figure 4D); ~36% of all responses could even be predicted by a single RGC input weight. However, specific tectal response features were modeled poorly: First, nearly all modeled tectal calcium traces showed responses to a large dot, owing to the high abundance of RGC responses to this stimulus (Figure 4D). Second, the weak RGC responses to a moving small dot resulted in a poor prediction of the DS tectal clusters no. 2 and 6 (Figure 4D). Third, modeling tectal calcium responses that are exclusive to ON or OFF stimuli was generally imperfect, and the worst correlation R^2_{score} was found for the tectal gradual OFF-selective cluster no. 11. Our modeling results suggest that most visual representations in the tectum are directly inherited from RGC inputs. In addition, non-retinal, presumably intratectal computations add feature specificities, such as information on the direction of small moving objects, and sharpen both object-size and luminance selectivities of tectal neurons.

Tectal layers process different object features according to their retinal inputs

We asked if tectal layers are distinct with respect to their feature selectivity. Along the superficial-to-deep axis, in line with previous publications, we found that RGC axons sensitive to small dots enter the tectum in superficial layers (SO in SFGS4) with a peak in SFGS1/2 (Figure 3—figure supplement 1D; Preuss et al., 2014). DS pixels were located most superficially in the posterior half of SFGS1 (Figure 3C; Nikolaou et al., 2012). OFF-responsive axons, on the other hand, arborized in deep SFGS layers, SGC and SAC/SPV, and most extensively in SFGS5/6 (Figure 3—figure supplement 1D; Temizer et al., 2015). To investigate if the dendrite morphologies of functionally identified tectal neurons matched these input layers, we carried out function-guided inducible morphological analysis (FuGIMA) of single tectal neurons (Förster et al., 2018). We used nuclear-localized GCaMP6f (nls-GCaMP6f) and regressor-based analysis to identify tectal cells that belong to the three largest clusters: small-dot responsive, large-dot responsive, and OFF cells. Co-expressed photoactivatable GFP (paGFP) was then used to fluorescently label a cell of interest with a two-photon laser pulse directed at the soma (Figure 5A and B). After allowing some time for diffusion of the activated GFP into the neurites, single cells were traced and registered to a standard brain together with RGC reference markers. This allowed us to quantify the extent of neurite arborization in each layer of the tectum (Figure 5C–E).

We compared our FuGIMA dataset ($n = 91$ cells) to a random collection of single tectal cells ($n = 188$; Figure 5—figure supplement 1), which were stochastically labeled with the BGUG method (Xiao and Baier, 2007). This analysis revealed that the three functional classes sampled branched preferentially in SFGS5/6. In addition, we found that small- and large-dot responsive cells showed significantly denser arborizations in SO, SFGS1/2, and SFGS3/4 compared to OFF cells. OFF cells, on the other hand, were biased to extend neurites in the SGC, the SAC, SAC/SPV and the SM (Figure 5E). SM is a layer at the surface of the tectum, which is innervated by the torus longitudinalis, a higher-order visual area with strong OFF responses (Northmore, 1984; Robles et al., 2020). SGC is a neuropil area abutting SFGS, in which multisensory information is processed. SAC is close to RGC axons that terminate in SAC/SPV and carry ambient luminance information to the tectum (Kölsch et al., 2020). A comprehensive catalog of all identified tectal interneuron morphotypes is shown in Figure 5—figure supplement 2.

We further investigated the extent of tectal cell arborizations by measuring the arbor areas in each layer (Figure 5—figure supplement 3A). We found that single cell arbors were generally small

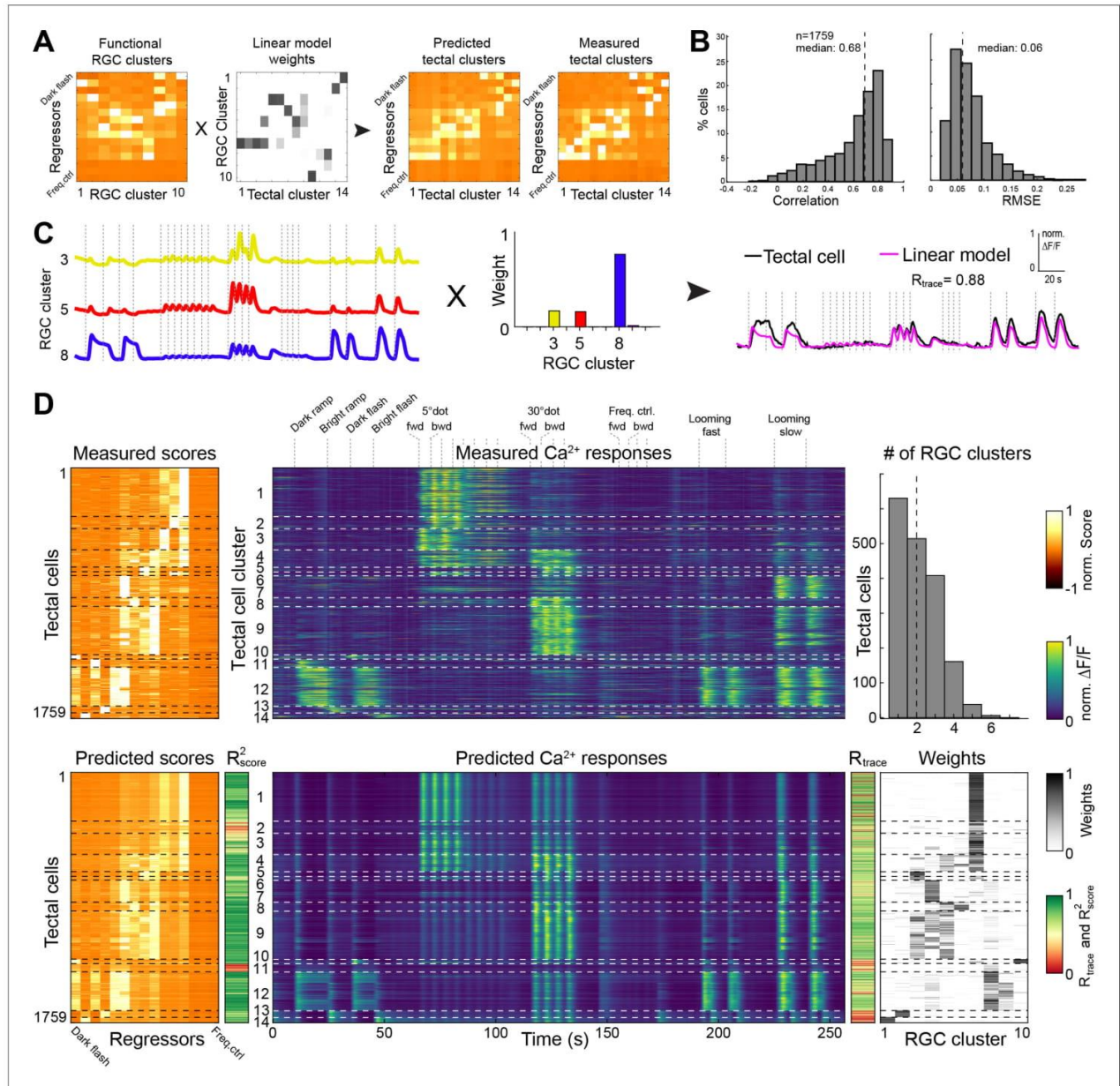


Figure 4. Modeling of tectal responses by linear combinations of RGC inputs. (A) Modeling workflow. Tectal cluster scores were predicted by a linear combination of weighted RGC cluster scores and finally compared to previously measured tectal scores. For color scale, see (D). (B) Prediction quality for modeling the scores of each sampled tectal cell ($n = 1759$). Left graph shows the correlation between predicted and measured scores. Right graph shows distribution of root mean squared errors of the cross-validated model (see Materials and methods for details). (C) Example for modeling the calcium response of a single tectal cell from weighted average responses of three RGC clusters. (D) Summary of modeling scores (left), calcium responses (middle), and weights (lower right) for all tectal cells ($n = 1759$). Functional tectal clusters are indicated by dashed horizontal lines. Color scales are shown on the right. Upper graph on the right shows the distribution of the number of RGC clusters used for modeling tectal responses. Dashed vertical line indicates a median of two RGC clusters.

The online version of this article includes the following figure supplement(s) for figure 4:

Figure supplement 1. Linear modeling parameters.

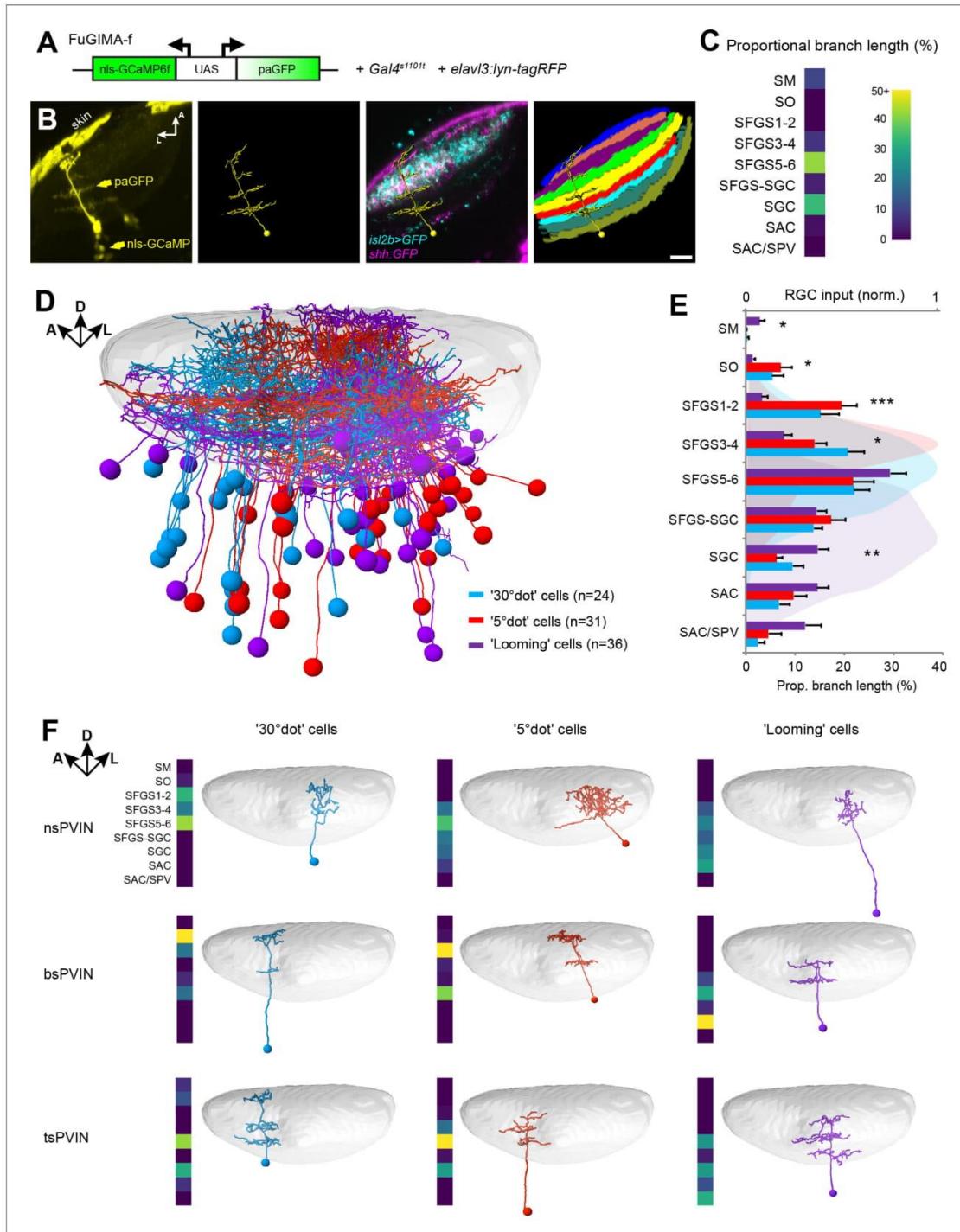


Figure 5. Dendrite morphologies of functionally identified tectal neurons match input layers. (A) The FuGIMA-f construct, which allows coexpression of nuclear-localized GCaMP6f and photoactivatable GFP (paGFP), was combined with *Gal4s1101t* for panneuronal expression and *elavl3:lyn-tagRFP* for image registrations. (B) Workflow of single-cell photoactivation, cell tracing, landmark registrations and layer quantifications (see Materials and methods for details). (C) Morphological barcode for the cell in (B). (D) Sideview of registered FuGIMA cells in the tectum of a standard brain. Tectal neuropil is Figure 5 continued on next page

Figure 5 continued

shaded in gray. (E) Average proportional branch length of neurites in the respective tectal layers, quantified for 30° dot- (blue), 5° dot- (red), and looming- (purple) responsive cells. Statistically significant differences between 5° dot- and looming-responsive cells are indicated by stars. For comparison, the quantification of RGC input in the respective layers is shown in the back (see **Figure 3—figure supplement 1D**). Error bars are SEM. ***: $p < 0.001$, **: $p < 0.01$, and *: $p < 0.05$. (F) Exemplary tectal cell morphotypes identified for the response groups described above. PVIN: periventricular interneuron; ns: non-stratified; bs: bistratified; ts: tristratified. Scale bar in (B): 20 μm . The online version of this article includes the following figure supplement(s) for figure 5:

Figure supplement 1. Comparison and quantification of tectal cell morphologies.

Figure supplement 2. Tectal interneuron catalog.

Figure supplement 3. Quantification of tectal cell arbor size.

in superficial layers (SM to SFGS3-4) and largest in deeper layers (SFGS5-6 to SAC/SPV; **Figure 5—figure supplement 3B**). When comparing the ratio of deep vs. superficial arbor size of multi-stratified cells, we found morphological differences between object-motion responsive and OFF cells. While on average, small-dot responsive cells have a columnar shape, OFF cells have extended arbors in deeper layers, rendering them cone-shaped (**Figure 5—figure supplement 3C and D**). We did not detect a systematic morphological difference between small- and large-dot responsive cells (**Figure 5F**). Object-motion responsive and OFF cells thus target layers that match their corresponding retinal and, in the case of SM, non-retinal inputs and also differ in more subtle morphological features.

Retinotectal circuits are differentially tuned for object size and direction along the anterior-posterior axis

Along the anterior-posterior (A-P) axis, we found a separation of size-selective RGC terminals. RGC axons responding to a large dot were mainly located in the anterior-dorsal quadrant of the tectal neuropil, whereas small-dot responsive pixels were found in the medial to posterior part (**Figure 3C**). This compartmentalization is inherited by the corresponding tectal populations (**Figure 6A**). Compared to all sampled cells, the large-dot response cluster was shifted to the anterior tectum, while cell bodies responding to small dots were biased to the posterior region. The strongest posterior bias was found for direction-selective cell bodies, responsive to a small, forward moving dot (**Figure 6A**). We extended this analysis to our FuGIMA dataset, to quantify the extent of neurite arborizations in the neuropil. We found the same effect, that is large-dot responsive cells arborize more extensively in the anterior neuropil, compared to all sampled interneurons, while ~90% of neurites from DS small-dot responsive cells were found in the posterior half (**Figure 6B and C**). These findings indicate a spatial gradient of sensitivity to object size, which is introduced by the topographic order of RGC inputs and inherited by the retinotopic array of tectal cells.

Ablation of small size-tuned RGC inputs removes tectal responses to small objects

To directly demonstrate that RGCs impose their feature selectivity onto postsynaptic tectal cells, we carried out an ablation experiment. From a previous study, we knew that small-dot responsive RGCs project specifically into SO after forming a collateral arbor in AF7, the neuropil of the parvocellular superficial pretectal nucleus (**Semmelhack et al., 2014**). By laser ablation of the RGC axon bundle that leaves AF7, we achieved selective disruption of small-object input to the SO layer (**Figure 7A–C**). Functional calcium imaging before and after the ablations revealed that small-dot responses were significantly diminished in tectal cells (**Figure 7D, E and G**). In contrast, the number of looming-responsive cells in the affected tectum was not reduced, but even increased in some animals, possibly due to the loss of inhibition by the small-object-processing circuit (see **Barker and Baier, 2015; Figure 7D, F and G**). These results indicate that RGC projections to SO are essential for tectal cells to assume their tuning to small-object motion.

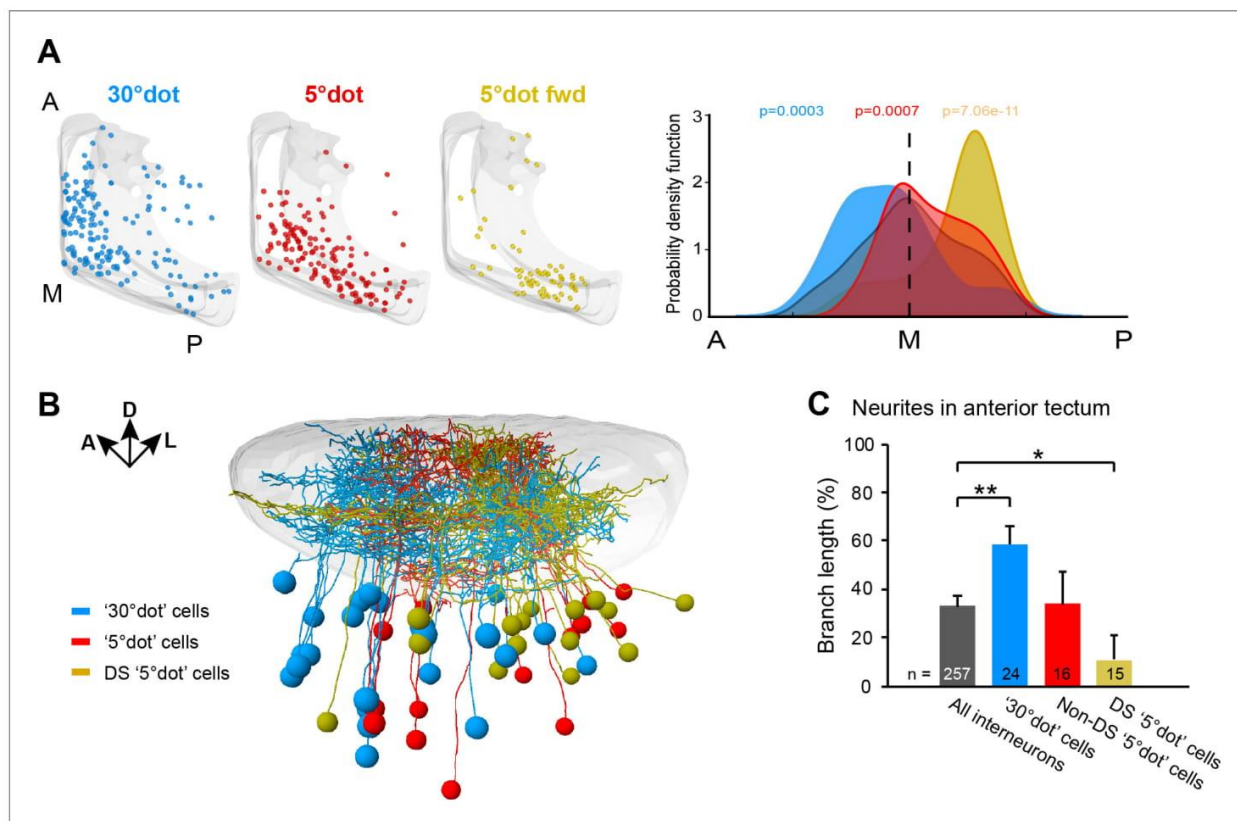


Figure 6. Functional compartmentalization of the tectum along the anterior-posterior axis. (A) Distribution of tectal cell bodies from 30°-dot (blue), 5°-dot (red) and 5°-dot-forward (yellow) response clusters. Anterior (A), medial (M) and posterior (P) positions of the tectum are indicated. Graph shows probability density function for cell body distribution. Integrals are colored according to their functional cluster with p-values characterizing the difference from the distribution of all sampled cells (gray integral). (B) Tectal sideview of registered FuGIMA neurons showing the distribution of 30°-dot (blue), 5°-dot non-DS (red) and 5°-dot-DS (yellow) cells. (C) Quantification of proportional neurite branch length of tectal cells in the anterior tectum. N equals number of cells. **: $p = 0.006$; *: $p = 0.014$.

Tectal representation of large (close) objects in frontal visual field is required for hunting

As the fish larva approaches a prey item, such as a paramecium or a rotifer, object size on the retina increases in visual angle. During hunting, the eyes converge and create an area of binocular overlap in the temporal retina. Convergent eye movements are accompanied by specialized turns, known as J-turns, that serve to center the prey in the visual field. Converged eyes and J-turns are characteristic of hunting episodes. We hypothesized that the large-dot responsive cells in the anterior tectum might be relevant for tracking prey at close range. To test this, we ablated between 3 and 15 single cells, which had been classified as large-dot responsive, in the right tectum (Figure 8A). Prey capture behavior was then analyzed in free-swimming larvae (Mearns et al., 2020).

Following removal of large-dot responsive cells, animals spent less time with their eyes converged, indicating less time spent engaged in hunting behavior (Figure 8B). In addition, their J-turns were biased to the right side, indicating defective prey detection by the left eye or right (ablated) tectum, respectively (Figure 8C and D). Control fish, in which entirely non-responsive cells were ablated, showed no effect on prey capture behavior and were indistinguishable from untreated or agarose-embedded larvae (Figure 8A–D and Figure 8—figure supplement 1A–C). Likewise, ablation of small-dot responsive cells, either in the anterior or posterior tectum did not result in

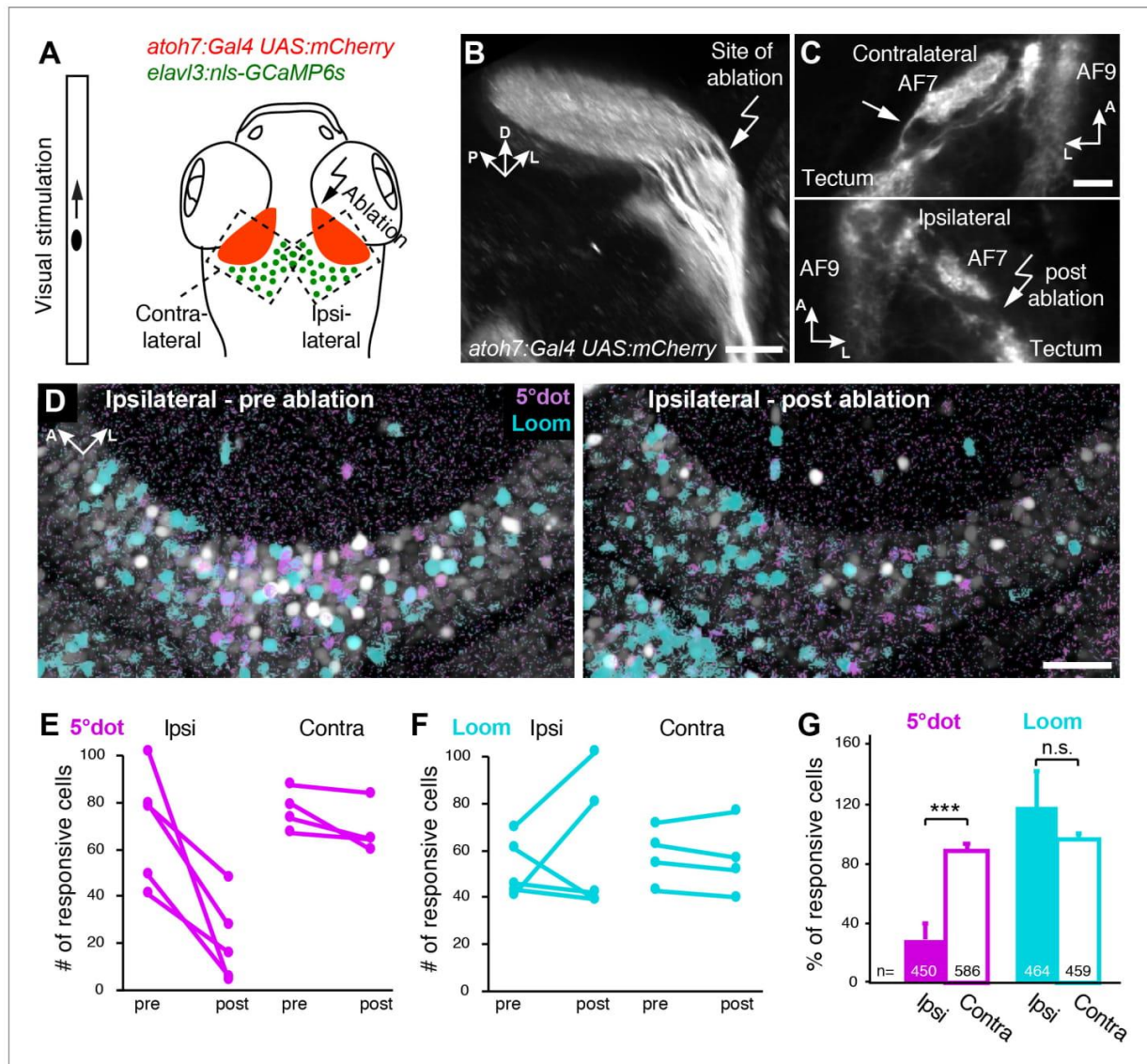


Figure 7. Small size-tuned RGC inputs are essential for small-object processing in the tectum. (A) Experimental setup for RGC axon ablations. Larvae are expressing mCherry in RGCs and nuclear GCaMP6s panneuronally. The eye contralateral to the ablation site is visually stimulated and the ipsilateral tectal cells are functionally imaged before and after the ablations. As a control, the eye ipsilateral to the ablation site is stimulated and the contralateral tectal cells are imaged in the same fish. (B) Sideview of mCherry expression in RGCs at 6 dpf shows the most lateral axon bundle, which leaves AF7 for the SO layer (arrow). (C) Dorsal view of single image planes showing the axon fibers of interest in the contralateral (control, upper panel) and ipsilateral (ablated, lower panel) pretectum of the same fish. (D) Single functional image planes, projected over time, showing nuclear GCaMP6s expression in the ipsilateral tectum, before (6 dpf, left) and after (7 dpf, right) ablation. Pixels are color-coded by preference for 5° dot (magenta) or looming (cyan) stimuli. (E) Number of cells per image plane (out of two fish), which are responsive to a 5° dot stimulus, before and after ablations in the ipsilateral and the contralateral tectum. (F) Same as (E), showing the number of cells responsive to a looming stimulus. (G) Fraction of 5°-dot- and looming-responsive cells after ablations in the ipsilateral and contralateral tectum. Error bars are SEM. ***: $p = 0.0006$; n.s.: $p = 0.46$. N equals number of cells from two independent fish. Scale bars in (B): 30 μm , (C): 20 μm , and (D): 50 μm .

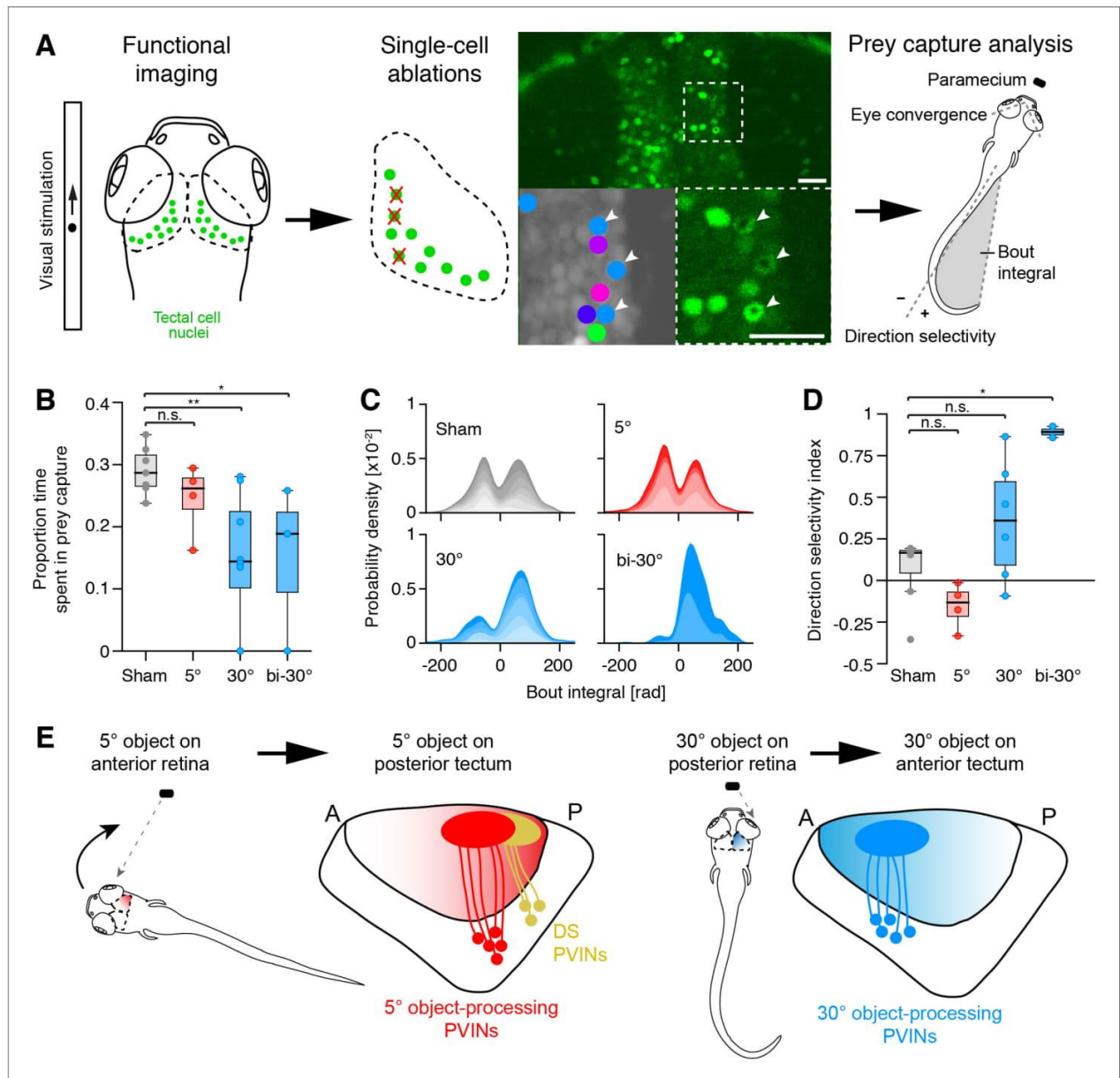


Figure 8. Large-object processing cells are required for hunting behavior. (A) 7 dpf old fish panneuronally expressing nuclear-localized GCaMP6s (green) were visually stimulated and imaged. Tectal cells were functionally identified (cluster-colored circles) and selected for ablations (arrowheads). At dpf, hunting behavior was analyzed in free-swimming larvae. (B) Proportion of time larvae spent engaged in hunting behavior, having their eyes converged. Single data points represent individual fish. ‘Sham’ (gray): control larvae with ablations of non-responsive cells, ‘5°’ (red): unilateral ablations of 5°-dot-responsive cells in the right tectum, ‘30°’ (blue): unilateral ablations of 30°-dot-responsive cells in the right tectum, ‘bi-30°’: bilateral ablations of 30°-dot-responsive cells. *: $p = 0.02$, **: $p = 0.006$, n.s.: $p = 0.15$. (C) Probability density plots of bout integrals for the initial J-turns, with positive values indicating a rightward and negative values indicating a leftward turn. Color shading indicates accumulated data for individual fish. (D) Direction selectivity index for initial J-turns of individual fish. *: $p = 0.029$, n.s.: $p > 0.05$. (E) Ethological relevance for A-P distribution of functionally distinct tectal cells. Before initiation of prey capture behavior, small moving objects are likely spotted in the temporal, monocular visual field. Precise recognition and processing of object movement by posterior DS cells avoids losing the object and enables adapted orientation turns towards the object. During prey pursuit, prey size seemingly increases and is detected by large-dot-responsive cells in the anterior tectum. Eye convergence allows binocular processing of object size and movement.

Figure 8 continued on next page

Figure 8 continued

The online version of this article includes the following figure supplement(s) for figure 8:

Figure supplement 1. Tectal cell ablation controls and enucleation experiments.

significant behavioral changes (**Figure 8B–D**). This suggests that for cells, which tile the visual field by only 5°, the ablated cell numbers were not sufficient to observe an effect on behavior.

Both tectal hemispheres cooperate in guiding capture of prey in the frontal visual field

Intriguingly, we observed in our imaging experiments, that a substantial number of cells in the left tectum were responsive to prey-like stimuli presented to the left (ipsilateral) eye (**Figure 8—figure supplement 1D**). These cells are probably activated by the right (contralateral) tectum via an intertectal commissure. We hypothesized that these cells help to sharpen responses across both tecta by suppressing background activity in the tectum that is not directly stimulated by RGC inputs. To test this hypothesis, we laser-ablated large-dot responsive cells in the anterior tectum on both sides (**Figure 8B–D**). (Note that these cells were identified by imaging responses in both tecta to stimulation of only the left eye.) In bilaterally ablated animals, the tendency to increase right J-turns and reduce left J-turns in response to prey was even more pronounced than in right-tectum-only ablated larvae, supporting our hypothesis.

Background suppression of the tectal activity ipsilateral to the stimulated eye might enhance activity in the contralateral, visually stimulated tectum. To investigate this possibility, we imaged the tectum of fish in which the right eye was removed (**Figure 8—figure supplement 1E**). In these animals, we observed a significant increase in the number of large-dot responsive cells in the right, visually stimulated tectum, that is ipsilateral to the enucleated side. This result suggests that stimulus-evoked activity is normally dampened by background activity in the contralateral tectum by intertectal inhibitory connections. This background activity is suppressed, either physiologically by strong unilateral, stimulus-evoked activation of the other tectum (**Figure 8C and D**), or experimentally by removal of its own retinal inputs (**Figure 8—figure supplement 1E**). Taken together, our ablation results begin to reveal the logic of intertectal coordination of responses to prey in the frontal visual field.

Discussion

In this study, we have discovered how the topographic layout of retinotectal circuitry is adapted to demands of the zebrafish larva's behavioral ecology. We postulate that natural selection has favored the evolution of position-dependent specializations in the neural architecture underlying the processing of object motion as it is caused by both the prey's and the fish's movements. The tectum is critically involved in identification, localization, pursuit, and capture of prey (**Gahtan et al., 2005; Semmelhack et al., 2014**). In the following, we will go through circuit adaptations to each of these functions.

Identifying prey, and distinguishing it from a potential predator, is critical for the larva's survival. In previous studies, we discovered that this distinction is made by size and movement characteristics of the perceived object (**Barker and Baier, 2015**). Small, sideways-moving dots are readily approached (**Semmelhack et al., 2014**), whereas expanding (looming) dots, displayed to the side of the fish while it is immobilized, are categorized as threatening and avoided by vigorous escape attempts (**Bhattacharyya et al., 2017; Temizer et al., 2015**). Here, we show that the RGC axon populations that respond to these two categories terminate in different layers of the tectum. Retinal inputs carrying prey-like signals mainly enter the tectum in layers SO and SFGS1-4, and looming-sensitive RGC axons are largely restricted to SFGS5/6 and SGC. In addition, broadly-tuned OFF signals are transmitted to the deep retinorecipient layers SGC and SAC/SPV. These include sudden and gradual transitions from light to dark.

The tectal cells that respond to these stimulus categories exhibit morphologies that match their predicted input channels, as previously shown for direction-selective RGC inputs and tectal cell dendritic arborizations (**Gabriel et al., 2012**). Prey-selective neurons extend dendrite branches into the

superficial layers of the tectum, while looming-sensitive neurons tend to arborize in middle to deep layers. As a general principle, most of the feature selectivities of tectal neurons are inherited from their functionally diverse RGC inputs. A simple excitation-only, feed-forward model showed that more than a third of the tectal response classes match a single RGC input class. The vast majority of the remaining responses were explained by a linear combination of two, or sometimes more, RGC inputs. In one experimentally accessible case, we could directly show that RGCs pass their small-dot responsive tuning on to downstream tectal cells. A similar modeling approach was recently performed to study functional connectivity between RGCs and the dorsolateral geniculate nucleus (dLGN) in the mouse thalamus (Román Rosón *et al.*, 2019). Analogous to our findings, the authors described a high correlation between functional dLGN in- and output, and thus a low level of signal convergence.

The zebrafish tectum, however, is not merely a passive relay station for retinal inputs. First, we found that responses to large objects are markedly reduced in the tectum compared to RGCs. Second, direction selectivity to backward-moving objects is calculated *de novo* in the tectum. This was especially striking for the 5° dot stimulus. A circuit involving feed-forward inhibition by SINs, which suppresses tectal responses to non-preferred directions, could account for this computation (Abbas *et al.*, 2017). Third, a substantial number of tectal cells selectively respond to a dark ramp stimulus; such cells were not observed in our RGC dataset. Thus, tectum-intrinsic circuitry adds direction selectivity to a subset of channels and generally refines and sharpens the responses.

The anatomical separation of small-dot responsive and looming-sensitive circuits probably reflects functional segregation of the two processing streams. Barker and Baier, 2015 postulated a circuit motif that implements balanced, reciprocal inhibition of the two systems driving approach vs. avoidance. Such a circuit could generate a winner-take-all mechanism capable of coordinating behavioral responses to stimuli of opposite valence. The visual system needs to rapidly distinguish between prey and threat across the entire visual field. A specialization of tectal layers for the processing of key features orthogonal to the two retinotopic axes, as reported here, seems to be an adaptive solution for that challenge. Moreover, bundling in space the visual processing of object valence, global patterns and luminance levels by laminar separation may also serve to minimize wiring lengths of the corresponding neural elements in the tectal neuropil (Baier, 2013; Chklovskii *et al.*, 2002).

By sampling feature-selective responses along the anterior-posterior axis of the tectum, we uncovered functional specializations of tectal regions, which probably reflect systematic changes in cell-type composition and connectivity. Object translation across the visual field is caused by a combination of both the prey's movement and the fish's own swimming, the latter often in response to position of the prey. Larval zebrafish are able to detect a prey item at a distance of several millimeters. A typical prey object, such as a paramecium or a rotifer, of 250 μm length, which is 3 mm away, subtends a visual angle of approximately 5°. Previously, we and others had detected responses of head-fixed larvae, embedded in agarose, to virtual, high-contrast objects of 2–6° diameter (Bianco *et al.*, 2011; Semmelhack *et al.*, 2014). Moving dots of 1° rarely elicited a response. This seems to be the resolution limit of the larval fish's visual system and is in agreement with the physical limit posed by photoreceptor spacing in the retina (Haug *et al.*, 2010). As the fish turns toward and approaches the prey, the prey 'image' slides from nasal to temporal zones of the retina and from posterior to anterior regions of the tectum (Figure 8E). At the same time, the visual angle covered by the prey gradually increases. This might explain a shared sensitivity to slow-looming stimuli, which is featured by more than half of all large dot-responsive cells. Interestingly, this overlap is negligible for fast looming stimuli, what might indicate a separation of approach and avoidance circuits. The fish executes a capture strike when the prey is in the upper central field of both eyes at a distance range of 0.3–0.7 mm (Mearns *et al.*, 2020). This corresponds to 20–40° of visual angle. Two tasks of successful hunting, the detection of distant prey in the peripheral visual field and the fixation of prey at close range in front of the animal shortly before the capture strike, informed our choice of 5° ('small') and 30° ('large') virtual objects for our imaging experiments. We discovered two asymmetries in the retinotectal map that appear to support these two different phases of hunting behavior.

First, an overrepresentation of small-dot responsive, direction-selective cells in the posterior tectum appears to be an adaptation to the preponderance of small prey objects in the peripheral field of view, whose movement is, at least initially, independent of the fish's own. These tectal cells acquire their direction selectivity by *de novo* computations from size-tuned, non-DS RGC inputs (Figure 8E). Determining the direction of prey by a local mechanism is particularly important for the

lateral field of view, which is entirely monocular. The further away from the midline the prey's location is the greater the turning angle that is needed to steer the fish toward its food. Fish will preferentially orient towards prey in their lateral visual field, because it gives them more time to move their body into the right position for a successful strike. Moreover, turning is energetically costly and may alert nearby predators and prey alike. For a prey object that already moves from back to front and whose image therefore slides from the nasal to the temporal retina, the turn angle will be smaller: the food may swim right in front of the fish, from where it might even be sucked into the mouth without extensive pursuit. Zebrafish larvae have been observed to use such a sit-and-wait mode of hunting (*Patterson et al., 2013*).

Second, the anterior tectum is enriched for large-dot responsive tectal cells (*Figure 8E*), which appear to facilitate the initiation of prey capture-associated J-turns, as shown here by laser ablation. J-turns are fine adjustments of body posture characteristic of hunting. These cells are frequently not direction-selective and communicate via commissural connections with the contralateral tectum. Initial imaging and behavioral experiments following ablations suggest that activation of large-dot selective cells suppresses responses in the contralateral tectum. We propose that such an intertectal inhibitory mechanism helps to correct slight displacements of the prey from the midline (see also *Gebhardt et al., 2019*). This signal may be transformed into fine orienting tail movements by one of the tectorecipient premotor areas in the hindbrain (*Helmbrecht et al., 2018*).

In conclusion, this work has revealed a neural architecture of the tectum that is well adapted to the demands of the animal's behavioral ecology. More generally, we demonstrate that the well-studied retinotectal map is spatially organized by function along both its retinotopic and laminar axes. The visual map in the tectum is thus not a veridical, unbiased representation of all positions in visible space, but rather warped by location-dependent feature statistics. Future work will undoubtedly uncover additional adaptations and will shed light on both the proximate, developmental mechanisms and the ultimate, evolutionary forces that are shaping this important visuomotor hub in the vertebrate brain.

Materials and methods

Key resources table

Reagent type (species) or resource	Designation	Source or reference	Identifiers	Additional information
Chemical compound, drug	Alpha-Bungarotoxin	Invitrogen	Invitrogen:B1601	
Chemical compound, drug	Tricaine	Sigma-Aldrich	Sigma-Aldrich:MS-222	
Genetic reagent (<i>Danio rerio</i>)	<i>Tg(elavl3:nls-GCaMP6s)mpn400</i>	<i>Förster et al., 2017</i>	ZFIN ID: ZDB-ALT-170731-37	
Genetic reagent (<i>Danio rerio</i>)	<i>Tg(ato7:Gal4-VP16)s1992t (ath5:Gal4)</i>	<i>Del Bene et al., 2010</i>	ZFIN ID: ZDB-FISH-150901-27082	
Genetic reagent (<i>Danio rerio</i>)	<i>Tg(UAS:GCaMP6s)mpn101</i>	<i>Thiele et al., 2014</i>	ZFIN ID: ZDB-FISH-150901-22562	
Genetic reagent (<i>Danio rerio</i>)	<i>Et(E1b:Gal4-VP16)s1101t</i>	<i>Scott et al., 2007</i>	ZFIN ID: ZDB-FISH-150901-5255	
Genetic reagent (<i>Danio rerio</i>)	<i>Tg(elavl3:lyn-tagRFP)mpn404</i>	<i>Dal Maschio et al., 2017</i>	ZFIN ID: ZDB-ALT-170731-38	
Genetic reagent (<i>Danio rerio</i>)	<i>Tg(isl2b:Gal4-VP16, myl7:TagRFP)zc65</i>	<i>Fujimoto et al., 2011</i>	ZFIN ID: ZDB-FISH-150901-13523	
Genetic reagent (<i>Danio rerio</i>)	<i>Tg(14xUAS:EGFP)mpn100</i>	<i>Thiele et al., 2014</i>	ZFIN ID: ZDB-GENO-140812-1	
Genetic reagent (<i>Danio rerio</i>)	<i>Tg(Shha:GFP)t10</i>	<i>Neumann and Nüsslein-Volhard, 2000</i>	ZFIN ID: ZDB-GENO-060207-1	
Genetic reagent (<i>Danio rerio</i>)	<i>Tg(UAS:mCherry)s1984t</i>	<i>Heap et al., 2013</i>	ZFIN ID: ZDB-FISH-150901-14417	

Continued on next page

Continued

Reagent type (species) or resource	Designation	Source or reference	Identifiers	Additional information
Genetic reagent (<i>Danio rerio</i>)	<i>Tg(brn3c:GAL4, UAS:gap43-GFP)s318t (BGUG)</i>	<i>Xiao and Baier, 2007</i>	ZFIN ID: ZDB-ALT-070423-6	
Genetic reagent (<i>Danio rerio</i>)	<i>Tg(UAS:paGFP,nlsGCaMP6f)mpn104 (UAS:FuGIMA-f)</i>	This paper		Tol2-mediated transgenesis
Software, algorithm	Imaris	Bitplane		http://www.bitplane.com
Software, algorithm	ImageJ/Fiji	<i>Schindelin et al., 2012</i>		http://fiji.sc
Software, algorithm	MorphoLibJ (ImageJ plugin)	<i>Legland et al., 2016</i>		http://imagej.net/morpholibj
Software, algorithm	PsychoPy2	<i>Peirce, 2007</i>		http://www.psychopy.org
Software, algorithm	Python 2.7	Python.org		http://www.python.org
Software, algorithm	Python 3	Python.org		http://www.python.org
Software, algorithm	CalmAn (Calcium Imaging Analysis toolbox)	<i>Giovannucci et al., 2017</i>		http://github.com/flatironinstitute/CalmAn
Software, algorithm	NeuTube	<i>Feng et al., 2015</i>		http://www.neutracing.com
Software, algorithm	Advanced Normalization Tools (ANTs)	<i>Avants et al., 2010</i>		http://stnava.github.io/ANTs
Software, algorithm	RStudio Version 1.0.136	RStudio		http://www.rstudio.com
Software, algorithm	R package nat (NeuroAnatomy Toolbox)	<i>Bates et al., 2020</i>		http://jefferis.github.io/nat/
Software, algorithm	3DSlicer	<i>Fedorov et al., 2012</i>		http://www.slicer.org
Software, algorithm	Plotly Chart Studio	Plotly.com		http://www.plotly.com
Software, algorithm	Custom tracking and behavior analysis code	<i>Mearns et al., 2020</i>		http://bitbucket.org/mpinbaierlab/mearns_et_al_2019

Experimental model and subject details

All animal procedures conformed to the institutional guidelines set by the Max Planck Society, and were approved by the regional government of Upper Bavaria (Regierung von Oberbayern; approved protocols: ROB-55.2-1-54-2532-101-2012 and ROB-55.2-2532.Vet_02-19-16).

Transgenic constructs

To generate *UAS:FuGIMA-f*, paGFP (gift from K. Svoboda, addgene no. 18697) and nls-GCaMP6f (*Förster et al., 2017*) were cloned on either side of a bidirectional 14xUAS in a Tol2 vector, featuring a transgenesis marker ('bleeding heart', *cmlc2:mCherry*). Transgenic fish were generated using the standard Tol2 transposon system, and the highly variegated line *Tg(UAS:paGFP,nlsGCaMP6f)mpn104* was used for experiments.

Transgenic zebrafish lines

For all experiments, we used 5–7 days post fertilization (dpf) larvae carrying mutations in the *mitfa* gene (*nacre*), which were raised on a 14 hr light/10 hr dark cycle at 28°C. To record functional responses to visual stimuli of tectal cells, we used *Tg(elavl3:nls-GCaMP6s)mpn400* fish and similarly for RGCs, we used *Tg(ato7:Gal4-VP16)s1992t*; *Tg(UAS:GCaMP6s)mpn101* fish. RGC axon ablation experiments were performed in *Tg(ato7:Gal4-VP16)s1992t*; *Tg(UAS:mCherry)s1984t*; *Tg(elavl3:nls-GCaMP6s)mpn400* fish, and tectal cells were ablated in *Tg(elavl3:nls-GCaMP6s)mpn400* fish.

FuGIMA experiments were performed in incrossed *Et(E1b:Gal4-VP16)*s*1101t (=Gal4^{s1101t}); Tg(UAS:paGFP,nlsGCaMP6f)*mpn*104 (=FuGIMA-f); Tg(*elavl3:lyn-tagRFP*)*mpn*404* fish. Other single-cell reconstructions were generated using *Et(E1b:Gal4-VP16)*s*1013t (=Gal4^{s1013t}); Tg(*brn3c:Gal4, UAS:gap43-GFP*)*s*318t (=BGUG)* fish. To define tectal layers, RGC expression in *Tg(*isl2b:Gal4-VP16*)*z*c65; Tg(14xUAS:EGFP)*mpn*100* fish and in *Tg(*Shha:GFP*)*t*10* fish was used. To allow registrations to a standard brain, all fish were crossed to the line *Tg(*elavl3:lyn-tagRFP*)*mpn*404*.

Tectal cell counts

5–7 dpf larvae expressing *elavl3:nls-GCaMP6s* were embedded in 2% low-melting-point agarose and a lethal dose of tricaine methanesulfonate (MS-222) was applied. After 15 min, the tectal brain regions were imaged on a Zeiss LSM780 microscope (voxel size: $0.27 \times 0.27 \times 1.5 \mu\text{m}^3$). Images were manually segmented in Imaris (v8.0, Bitplane) by setting pixel intensities outside of the tectum to 0. Using ImageJ (v1.52n), pixel intensities were inverted, images were Gaussian filtered and a classic watershed segmentation was applied (MorphoLibJ plugin). ROIs smaller than 400 voxels were removed and the number of ROIs was analyzed in 3D.

Functional imaging and visual stimulation

In vivo calcium imaging was performed on a previously described two-photon microscope (Förster *et al.*, 2017) on 5–7 dpf transgenic zebrafish larvae expressing either cytoplasmic GCaMP6s in RGCs or nuclear-localized GCaMP6s panneuronally. Larvae were mounted in 2% low-melting-point agarose. The stimulus was projected onto a white diffusive screen using the red channel of a LED projector, in a distance of 4 cm from the larva. The projection was presented monocularly and covered $\sim 120^\circ$ of the larva's field of view. GCaMP6 signals were recorded by scanning at 920 nm, at ~ 2 Hz, at a resolution of $\sim 0.6 \mu\text{m}/\text{pixel}$. The tectum was covered in depth by acquiring z-planes with a distance of $\sim 7 \mu\text{m}$.

Visual stimulation was designed using PsychoPy2 and consisted of a dark ramp (red to black, 3 s), a bright ramp (black to red, 3 s), a dark flash (red to black), and a bright flash (black to red). This was followed by a small horizontally moving dot (5° , $90^\circ/\text{s}$) in forward (temporal to nasal) and backward (nasal to temporal) directions (two repetitions each), and at two elevations of the screen, first at equatorial plane and then elevated by $\sim 20^\circ$ (two repetitions each). We chose dark dots on a bright (red) background. Published (Antinucci *et al.*, 2019) and our own unpublished results have shown that these stimuli are efficient at eliciting hunting-like behavior in a dark 2P microscope environment, in the absence of UV stimulation (Yoshimatsu *et al.*, 2020). Subsequently, a big dot was moving horizontally (30° , $90^\circ/\text{s}$) in forward and backward directions (repeated twice), at an elevation of $\sim 10^\circ$, thus covering the two horizontal planes of the small dot. The frequency control consisted of black gratings with a spatial frequency of 5° and a temporal frequency of $90^\circ/\text{s}$, moving in forward and backward directions (repeated twice). The looming stimuli consisted of a fast ($\sim 60^\circ/\text{s}$, linear expansion) and a slow-looming disc ($\sim 20^\circ/\text{s}$, linear expansion), both ending with a black screen (two repetitions each). This stimulus protocol was repeated twice with a total acquisition length of 515 s.

Analysis of imaging data

Recorded imaging data were pre-processed as described previously (Helmbrecht *et al.*, 2018). In brief, images were motion-corrected using the CalmAn package, uniformly filtered over three frames and the dF/F was calculated using the 5th percentile of the traces. In total 15 regressors for all stimulus components were created and convolved with a corresponding GCaMP6 kernel. Neuronal activity was analyzed pixel-wise for RGC and ROI-wise for tectal imaging data, by calculating a score of all regressors to the calcium responses of each pixel using a linear regression model of the selected response window with the regressor (Python scikit-learn). For the score, the coefficient of the regression (CR; corresponding to the dF/F) was multiplied by the correlation value R^2 . All pixels and ROIs were imaged twice using the same stimulus and the final score was calculated via a weighted average of the scores by the corresponding R^2 .

Clustering of functional responses

To determine overall response types, the scores were normalized per fish to the 99th percentile of all pixels/ROIs recorded.

For the functional clustering of the responsive tectal ROIs, three fish (7594 ROIs) expressing *elavl3:nls-GCaMP6s* were analyzed by first removing ROIs with maximum scores smaller than 0.2 (1908 ROIs remaining). Next, to reduce noise and to find local structure in the dataset, affinity propagation clustering (scikit learn – preference: median of similarities) was performed (151 clusters). Keeping clusters with at least 5 ROIs, yielded in total 80 clusters with chosen exemplars. To extract the global cluster structure, these 80 exemplars were further clustered using hierarchical clustering (scipy.cluster) using correlation as distance metric. Clusters with less than 20 ROIs were removed. We calculated a silhouette coefficient to validate the clustering. A distance threshold of 0.25 was chosen, which yielded a minimal number of clusters (14) with the highest silhouette coefficient. This finally resulted in 14 tectal cell clusters with a total of 76 exemplars and 1759 ROIs (92.2%). Principal component analysis (PCA) was performed on the score values of each stimulus for all tectal cells.

Similarly to the clustering of tectal neurons, the responsive RGC pixels of one fish (14 planes; each 297×303 pixel) expressing *ath5:Gal4 UAS:GCaMP6s* were analyzed by again removing pixels with maximum scores smaller than 0.4 (remaining 58,910 pixel) and performing affinity propagation clustering (scikit learn – preference: median of similarities). Keeping clusters with at least five pixels (0.01% of all pixels), yielded in total 1243 clusters with chosen exemplars. These 1243 exemplars were further ordered by hierarchical clustering (scipy.cluster) using correlation as distance metric. Cluster with less than 589 pixels (1% of all pixels) were removed. After silhouette analysis, a distance threshold of 0.45 was chosen, which yielded ten clusters with a total of 1157 exemplars and 55,153 pixels (93.6%). Although four RGC clusters yielded a higher silhouette coefficient, we chose ten clusters, which resulted in a significantly higher correlation value (R^2_{score}) for the following linear modeling analysis (see **Figure 4—figure supplement 1A**).

To quantify the number of pixels per RGC cluster in tectal compartments and layers (**Figure 3C** and **Figure 3—figure supplement 1D**), we used ImageJ to manually draw ROIs and to count pixels for each compartment/lamina in each image plane.

Mapping of functional responses from independent experiments onto our clustered datasets

To map response types of SINS, NINs and enucleated fish, functional imaging was performed as described. ROIs were defined semi-automatically to segment only single, separated tectal cell bodies in the tectal neuropil and/or the periventricular layer. Several fish per experiment were analyzed to calculate the scores, and again pixels with maximum scores smaller than 0.2 were removed. A k-nearest neighbor classifier (`sklearn.neighbors.KNeighborsClassifier`) was trained on the *elavl3:nls-GCaMP6s* clustered ROIs (1759 ROIs with cluster labels, $k = 10$) and the scores of every mapped fish were assigned to the cluster dataset using either predicted labels for the ROIs distribution or probability estimates for the population distributions. The classification was cross-validated by splitting the *elavl3:nls-GCaMP6s* dataset into 70% training and 30% test data, which evaluated to an accuracy of 92%. A similar, pixel-wise approach was used to map the functional RGC data of two additional *ath5:Gal4; UAS:GCaMP6s* fish onto the ten RGC clusters by choosing $k = 100$ (**Figure 3—figure supplement 1C**).

Modeling of tectal responses using RGC inputs

To predict the tectal responses using RGC information, we applied a linear modeling approach using L1-regularized regression (Lasso) (`sklearn.linear_model.Lasso`) with non-negative constraint. The cost function of the Lasso is defined by:

$$\text{Cost} = \sum_{i=0}^n \left(y_i - \sum_{j=0}^m w_j x_{ij} \right)^2 + \lambda \sum_{j=0}^m |w_j|$$

The regularization parameter (λ) helps to reduce the impact of multicollinearities between the average scores of RGC classes, and the optimal λ was found by minimizing the mean squared error of a grid search on a log scale between $1e^{-5}$ and $1e^{-1}$ (**Figure 4—figure supplement 1B**). The modeling of the scores of every single tectal neuron (total 1759) was performed using the 15-dimensional average scores of the 10 defined RGC clusters, so that:

$$PredScore\ Tectal\ Neuron = b + \sum_{j=0}^{m(RGC)} w_j \text{AvgScore}RGC_j$$

The *PredScore* was evaluated by calculating the R^2_{score} of the regression. To predict the calcium traces of the tectal cells, we used the resulting weights of the regression and calculated the dot product of the average RGC responses with the corresponding weights (w) and bias (b) and evaluated the result via the Pearson correlation (R_{trace}) between the predicted and measured calcium responses.

The model was tested by comparing the resulted distribution of response correlations to the distribution of a random model, by choosing for every cell 1000 times random weights (**Figure 4—figure supplement 1C**). In addition, the model was cross-validated by splitting the data into a training and test set using one of the two trials per cell, and a corresponding RMSE (root mean squared error) of the test dataset was calculated (**Figure 4B**).

FuGIMA and other single-cell labeling experiments

Tectal responses in fish expressing *elavl3:lyn-tagRFP* and *UAS:FuGIMA-f* under control of *Gal4s1101t* were functionally imaged as described above. After image acquisition, a custom-written, regressor-based python script was used to overlay a color map of correlated pixels on the mean $\Delta F/F$ image to identify cells of functional interest. Single-cell photoactivation of paGFP was performed as previously described (**Förster et al., 2018**). Typically, 2–3 photoactivation cycles were sufficient to reach the maximal fluorescence intensity in tectal interneurons. After allowing paGFP to diffuse into all neurites of the photoactivated cell for about 30–45 min, a high-resolution z-stack of the whole tectum, including both paGFP and lyn-tagRFP channels, was acquired at a confocal microscope (LSM700 or LSM780, Zeiss; 20x/1.0 NA water-dipping objective).

Other single-cell reconstructions (randomly-labeled tectal neurons) were performed using the BGUG method as previously published (**Helmbrecht et al., 2018**). In brief, fish expressing a highly variegated Gap43-GFP under control of the tectal *Gal4s1013t* line were crossed to *elavl3:lyn-tagRFP* fish and offspring were screened for sparse GFP expression in tectal interneurons.

All individual neurons were traced semi-automatically using the software neuTube (Build1.0z) and SWC files were generated for each cell.

Image registration

All image registrations were performed using the Advanced Normalization Tools (ANTs) software (**Avants et al., 2010**), and live expression of *elavl3:lyn-tagRFP* served as a reference channel. First, a FuGIMA standard brain was generated by mirroring all FuGIMA cells to one brain half and by subsequent registration to one exemplary lyn-tagRFP channel, which served as a template. ANTs parameters recently determined for live samples were applied (**Marquart et al., 2017**). Second, this FuGIMA standard brain was registered to the zebrafish single-neuron atlas (**Kunst et al., 2019**) in three steps: (1) registration of the FuGIMA template to a tectal subvolume of the live lyn-tagRFP standard brain from the atlas, (2) extension to the full live standard brain volume, (3) registration of the live standard brain to the fixed standard brain of the atlas. Similarly, the BGUG dataset was first registered to its own standard brain, which was subsequently registered to the single-neuron atlas. Finally, single-neuron tracings (SWC files) were aligned using the `antsApplyTransformToPoints` function contained in the ANTsR package. For visualizations and 3D renderings, we used the web interface of the single-neuron atlas (<http://fishatlas.neuro.mpg.de/>). All single-neuron data from this study are publicly available through this atlas.

Morphological quantifications

To add landmarks for the tectal laminae, we co-registered the expression patterns of *isl2b:Gal4 UAS:GFP* and *shh:GFP* into the FuGIMA standard brain. We then used these anatomical labels, together with the software 3D slicer (<http://www.slicer.org/>), to manually segment the individual tectal layers. For every cell, we measured the fiber lengths in each layer and calculated the percentage of the cell's total neurite length (proportional branch length) using a custom-written python script. Single-cell morphological barcodes (heatmaps) were generated using Plotly Chart Studio (<https://plot.ly/>).

To quantify the neurite arbor size of tectal cells, we used the 'Oblique slicer' and 'Measurement points' tools in Imaris (v8.02; Bitplane) to define and extract planar coordinates for each laminar stratification (Figure 5—figure supplement 3A). The areas in μm^2 were quantified using a custom-written python script.

Ablation and enucleation experiments

For RGC axon ablations, 6 dpf old larvae expressing mCherry in RGCs and nuclear GCaMP6s panneuronally were mounted in agarose and were intraspinaly injected with alpha-bungarotoxin (2 mg/ml, Invitrogen, B1601). Tectal cell responses were functionally imaged as described above. Subsequently, the axon bundle, which leaves AF7 for the tectal SO layer was cut at the same 2P microscope by scanning a 10 μm line (0.01 $\mu\text{m}/\text{pixel}$) at 760 nm for 500 ms transverse to the fascicle. The laser intensity at the objective focal plane was ~ 30 mW. Afterwards, fish were released from agarose to recover overnight in Danieau's solution. At 7 dpf, fish were re-embedded and functional imaging of tectal cell responses was repeated. Somata signals in the tectal neuropil served as landmarks for approximate reidentification of the same imaging planes obtained at 6 dpf. Regressor analysis was described as above and cluster-color-coded responsive tectal cells were counted manually.

For tectal cell ablations, 7 dpf old larvae expressing nuclear GCaMP6s panneuronally were embedded in agarose and functionally imaged at the 2P microscope. Up to 3–5 tectal cells per imaging plane (max. 15 cells per fish) were selected for their response type, and were ablated by 30 ms two-photon laser pulses (800 nm, ~ 35 mW), pointed at the nucleus.

For enucleation experiments, 4 dpf old fish expressing *elavl3:nls-GCaMP6s* were placed in 2% low-melting agarose with 0.02% tricaine methanesulfonate (MS-222). The right eye was removed using custom-made micro-scalpels. Fish were allowed to recover for two days in Danieau's solution until functional imaging was performed at 6 dpf.

Free-swimming prey capture assay

Prior to testing prey capture behavior, larvae were allowed to feed ad libitum on paramecia from 5 to 6 dpf. At 7 dpf, larvae were embedded in agarose and cells in the tectum were ablated (see above). Larvae were freed from agarose and allowed to recover overnight. Prey capture behavior was tested the following day at 8 dpf. Controls groups were unembedded siblings, siblings embedded but not subject to the ablation protocol, and 'sham' ablated siblings.

The free-swimming prey capture assay was performed as described previously (Mearns et al., 2020). Briefly, larvae were introduced individually into an arena (15 \times 15 \times 5 mm) with 50–100 paramecia (*Paramecium multimicronucleatum*). Each larva was allowed to feed for 20–30 min while being recorded from above at 500 frames per second using a high-speed camera (PhotonFocus, MV1-D1312-160-CL, Switzerland). In each frame of the recordings, the eyes and tail of the fish were tracked offline using custom-written Python software (https://bitbucket.org/mpinbaierlab/mearns_et_al_2019). Tail tracking was performed using background subtraction and thresholding followed by skeletonization of the largest contour in the image. Swim bouts were identified using a change point algorithm on the derivative of the tail angle with respect to time. Eye tracking was performed similarly using background subtraction, thresholding and contour detection. For each animal independently, we calculated the distribution of eye convergence angles over the experiment and used the local minimum in the resulting bimodal distribution as the prey capture threshold. Since eye convergence is a reliable indicator of prey capture in zebrafish larvae (Bianco et al., 2011; Patterson et al., 2013; Mearns et al., 2020), we defined hunting events as any time the eye convergence angle was above this threshold. Initial orienting J-turns were defined as any bout where the eyes were unconverged before and converged after the bout. The bout integral was calculated by summing the tail tip angle values over the duration of the bout, with positive values indicating a rightward turn and negative values indicating a leftward turn. The direction of the turn was defined by the sign of the bout integral (positive for right, negative for left). The direction selectivity index was computed as [(# right J-turns - # left J-turns) / (total # J-turns)] for each fish, with a value of 1 indicating all J-turns were to the right, -1 indicating all J-turns were to the left, and 0 indicating no overall bias in J-turn direction.

Statistical analysis

Statistical tests were two-tailed t-tests, if not stated otherwise. For the quantification of prey capture behavior, statistics were performed using the scipy library in Python 3. The proportion of time larvae spent engaged in hunting behavior was compared between treatment groups using a Mann-Whitney U test. Similarly, the direction selectivity index of initial J-turns was compared between treatment groups using a Mann-Whitney U test.

Acknowledgements

We thank Irene Arnold-Ammer for help with molecular biology, Krasimir Slanchev for support during fish maintenance and husbandry, Michael Kunst for advice on image registration and the entire Baier lab for constructive feedback and discussions throughout the project. This study made use of the high-performance application services at the Max Planck Computing and Data Facility for processing image registrations. Funding was provided by the Max Planck Society (all authors).

Additional information

Funding

Funder	Author
Max Planck Society	Dominique Förster Thomas O Helmbrecht Duncan S Mearns Linda Jordan Nouwar Mokayes Herwig Baier

The funders had no role in study design, data collection and interpretation, or the decision to submit the work for publication.

Author contributions

Dominique Förster, Conceptualization, Data curation, Formal analysis, Methodology, Writing - original draft, Project administration, Designed the experiments. Performed the experiments with support from LJ; Thomas O Helmbrecht, Conceptualization, Data curation, Software, Formal analysis, Writing - review and editing, Designed the experiments, Analyzed the data; Duncan S Mearns, Data curation, Software, Methodology, Writing - review and editing, Performed and analyzed prey capture experiments; Linda Jordan, Data curation, Methodology; Nouwar Mokayes, Data curation, Software, Wrote the code for morphological quantifications; Herwig Baier, Conceptualization, Supervision, Funding acquisition, Writing - review and editing

Author ORCIDs

Dominique Förster  <https://orcid.org/0000-0002-7821-6755>

Herwig Baier  <https://orcid.org/0000-0002-7268-0469>

Ethics

Animal experimentation: All animal procedures conformed to the institutional guidelines set by the Max Planck Society, and were approved by the regional government of Upper Bavaria (Regierung von Oberbayern; approved protocols: ROB-55.2-1-54-2532-101-2012 and ROB-55.2-2532.Vet_02-19-16).

Decision letter and Author response

Decision letter <https://doi.org/10.7554/eLife.58596.sa1>

Author response <https://doi.org/10.7554/eLife.58596.sa2>

Additional files

Supplementary files

- Transparent reporting form

Data availability

All data generated or analysed during this study are included in the manuscript and supporting files. Single cell reconstructions are available through our zebrafish atlas at <http://fishatlas.neuro.mpg.de/>.

The following datasets were generated:

References

- Abbas F, Triplett MA, Goodhill GJ, Meyer MP. 2017. A Three-Layer network model of direction selective circuits in the optic tectum. *Frontiers in Neural Circuits* **11**:88. DOI: <https://doi.org/10.3389/fncir.2017.00088>, PMID: 29209178
- Antinucci P, Folgueira M, Bianco IH. 2019. Pretectal neurons control hunting behaviour. *eLife* **8**:191. DOI: <https://doi.org/10.7554/eLife.48114>
- Avants BB, Yushkevich P, Pluta J, Minkoff D, Korczykowski M, Detre J, Gee JC. 2010. The optimal template effect in Hippocampus studies of diseased populations. *NeuroImage* **49**:2457–2466. DOI: <https://doi.org/10.1016/j.neuroimage.2009.09.062>, PMID: 19818860
- Baden T, Berens P, Franke K, Román Rosón M, Bethge M, Euler T. 2016. The functional diversity of retinal ganglion cells in the mouse. *Nature* **529**:345–350. DOI: <https://doi.org/10.1038/nature16468>, PMID: 26735013
- Baden T, Euler T, Berens P. 2020. Understanding the retinal basis of vision across species. *Nature Reviews Neuroscience* **21**:5–20. DOI: <https://doi.org/10.1038/s41583-019-0242-1>, PMID: 31780820
- Baier H. 2013. Synaptic laminae in the visual system: molecular mechanisms forming layers of perception. *Annual Review of Cell and Developmental Biology* **29**:385–416. DOI: <https://doi.org/10.1146/annurev-cellbio-101011-155748>, PMID: 24099086
- Barker AJ, Baier H. 2015. Sensorimotor decision making in the zebrafish tectum. *Current Biology* **25**:2804–2814. DOI: <https://doi.org/10.1016/j.cub.2015.09.055>, PMID: 26592341
- Barlow HB. 1961. *Possible Principles Underlying the Transformation of Sensory Messages*. MIT Press. DOI: <https://doi.org/10.7551/mitpress/9780262518420.003.0013>
- Bates AS, Manton JD, Jagannathan SR, Costa M, Schlegel P, Rohlfing T, Jefferis GS. 2020. The Natverse, a versatile toolbox for combining and analysing neuroanatomical data. *eLife* **9**:e53350. DOI: <https://doi.org/10.7554/eLife.53350>, PMID: 32286229
- Bhattacharyya K, McLean DL, MacIver MA. 2017. Visual threat assessment and reticulospinal encoding of calibrated responses in larval zebrafish. *Current Biology* **27**:2751–2762. DOI: <https://doi.org/10.1016/j.cub.2017.08.012>, PMID: 28889979
- Bianco IH, Kampff AR, Engert F. 2011. Prey capture behavior evoked by simple visual stimuli in larval zebrafish. *Frontiers in Systems Neuroscience* **5**:101. DOI: <https://doi.org/10.3389/fnsys.2011.00101>, PMID: 22203793
- Bianco IH, Engert F. 2015. Visuomotor transformations underlying hunting behavior in zebrafish. *Current Biology* **25**:831–846. DOI: <https://doi.org/10.1016/j.cub.2015.01.042>, PMID: 25754638
- Bleckert A, Schwartz GW, Turner MH, Rieke F, Wong RO. 2014. Visual space is represented by nonmatching topographies of distinct mouse retinal ganglion cell types. *Current Biology* **24**:310–315. DOI: <https://doi.org/10.1016/j.cub.2013.12.020>, PMID: 24440397
- Chalk M, Marre O, Tkačik G. 2018. Toward a unified theory of efficient, predictive, and sparse coding. *PNAS* **115**:186–191. DOI: <https://doi.org/10.1073/pnas.1711114115>, PMID: 29259111
- Chklovskii DB, Schikorski T, Stevens CF. 2002. Wiring optimization in cortical circuits. *Neuron* **34**:341–347. DOI: [https://doi.org/10.1016/S0896-6273\(02\)00679-7](https://doi.org/10.1016/S0896-6273(02)00679-7), PMID: 11988166
- Dal Maschio M, Donovan JC, Helmbrecht TO, Baier H. 2017. Linking neurons to network function and behavior by Two-Photon holographic optogenetics and volumetric imaging. *Neuron* **94**:774–789. DOI: <https://doi.org/10.1016/j.neuron.2017.04.034>, PMID: 28521132
- Dan Y, Atick JJ, Reid RC. 1996. Efficient coding of natural scenes in the lateral geniculate nucleus: experimental test of a computational theory. *The Journal of Neuroscience* **16**:3351–3362. DOI: <https://doi.org/10.1523/JNEUROSCI.16-10-03351.1996>, PMID: 8627371
- Del Bene F, Wyart C, Robles E, Tran A, Looger L, Scott EK, Isacoff EY, Baier H. 2010. Filtering of visual information in the tectum by an identified neural circuit. *Science* **330**:669–673. DOI: <https://doi.org/10.1126/science.1192949>, PMID: 21030657
- Dunn TW, Gebhardt C, Naumann EA, Riegler C, Ahrens MB, Engert F, Del Bene F. 2016. Neural circuits underlying visually evoked escapes in larval zebrafish. *Neuron* **89**:613–628. DOI: <https://doi.org/10.1016/j.neuron.2015.12.021>, PMID: 26804997
- Fedorov A, Beichel R, Kalpathy-Cramer J, Finet J, Fillion-Robin JC, Pujol S, Bauer C, Jennings D, Fennessy F, Sonka M, Buatti J, Aylward S, Miller JV, Pieper S, Kikinis R. 2012. 3D slicer as an image computing platform for the quantitative imaging network. *Magnetic Resonance Imaging* **30**:1323–1341. DOI: <https://doi.org/10.1016/j.mri.2012.05.001>, PMID: 22770690

- Feng L, Zhao T, Kim J. 2015. neuTube 1.0: a new design for efficient neuron reconstruction software based on the SWC format. *Eneuro* **2**:ENEURO.0049-14.2014. DOI: <https://doi.org/10.1523/ENEURO.0049-14.2014>, PMID: 26464967
- Förster D, Dal Maschio M, Laurell E, Baier H. 2017. An optogenetic toolbox for unbiased discovery of functionally connected cells in neural circuits. *Nature Communications* **8**:116. DOI: <https://doi.org/10.1038/s41467-017-00160-z>, PMID: 28740141
- Förster D, Kramer A, Baier H, Kubo F. 2018. Optogenetic precision toolkit to reveal form, function and connectivity of single neurons. *Methods* **150**:42–48. DOI: <https://doi.org/10.1016/j.ymeth.2018.08.012>
- Fujimoto E, Gaynes B, Brimley CJ, Chien CB, Bonkowsky JL. 2011. Gal80 intersectional regulation of cell-type specific expression in vertebrates. *Developmental Dynamics* **240**:2324–2334. DOI: <https://doi.org/10.1002/dvdy.22734>, PMID: 21905164
- Gabriel JP, Trivedi CA, Maurer CM, Ryu S, Bollmann JH. 2012. Layer-Specific Targeting of Direction-Selective Neurons in the Zebrafish Optic Tectum. *Neuron* **76**:1147–1160. DOI: <https://doi.org/10.1016/j.neuron.2012.12.003>
- Gahtan E, Tanger P, Baier H. 2005. Visual prey capture in larval zebrafish is controlled by identified reticulospinal neurons downstream of the tectum. *Journal of Neuroscience* **25**:9294–9303. DOI: <https://doi.org/10.1523/JNEUROSCI.2678-05.2005>, PMID: 16207889
- Gebhardt C, Auer TO, Henriques PM, Rajan G, Duroure K, Bianco IH, Del Bene F. 2019. An interhemispheric neural circuit allowing binocular integration in the optic tectum. *Nature Communications* **10**:5471. DOI: <https://doi.org/10.1038/s41467-019-13484-9>, PMID: 31784529
- Giovannucci A, Friedrich J, Kaufman M, Churchland AK, Chklovskii D, Paninski L, Pnevmatikakis EA. 2017. OnACID: online analysis of calcium imaging data in real time. *bioRxiv*. DOI: <https://doi.org/10.1101/193383>
- Haug MF, Biehlmair O, Mueller KP, Neuhaus SCF. 2010. Visual acuity in larval zebrafish: behavior and histology. *Frontiers in Zoology* **7**:8. DOI: <https://doi.org/10.1186/1742-9994-7-8>
- Heap LA, Goh CC, Kassahn KS, Scott EK. 2013. Cerebellar output in zebrafish: an analysis of spatial patterns and topography in eurydendroid cell projections. *Frontiers in Neural Circuits* **7**:53. DOI: <https://doi.org/10.3389/fncir.2013.00053>, PMID: 23554587
- Helmbrecht TO, Dal Maschio M, Donovan JC, Koutsouli S, Baier H. 2018. Topography of a visuomotor transformation. *Neuron* **100**:1429–1445. DOI: <https://doi.org/10.1016/j.neuron.2018.10.021>, PMID: 30392799
- Kölsch Y, Hahn J, Sappington A, Stemmer M, Fernandes AM, Helmbrecht TO, Lele S, Butrus S, Laurell E, Arnold-Ammer I, Shekhar K, Sanes JR, Baier H. 2020. Molecular classification of zebrafish retinal ganglion cells links genes to cell types to behavior. *bioRxiv*. DOI: <https://doi.org/10.1101/2020.07.29.226050>
- Kunst M, Laurell E, Mokayes N, Kramer A, Kubo F, Fernandes AM, Förster D, Dal Maschio M, Baier H. 2019. A Cellular-Resolution atlas of the larval zebrafish brain. *Neuron* **103**:21–38. DOI: <https://doi.org/10.1016/j.neuron.2019.04.034>, PMID: 31147152
- Legland D, Arganda-Carreras I, Andrey P. 2016. MorphoLibJ: integrated library and plugins for mathematical morphology with ImageJ. *Bioinformatics* **32**:btw413. DOI: <https://doi.org/10.1093/bioinformatics/btw413>
- Machens CK, Gollisch T, Kolesnikova O, Herz AV. 2005. Testing the efficiency of sensory coding with optimal stimulus ensembles. *Neuron* **47**:447–456. DOI: <https://doi.org/10.1016/j.neuron.2005.06.015>, PMID: 16055067
- Marquart GD, Tabor KM, Horstick EJ, Brown M, Geoca AK, Polys NF, Nogare DD, Burgess HA. 2017. High-precision registration between zebrafish brain atlases using symmetric diffeomorphic normalization. *GigaScience* **6**:1–15. DOI: <https://doi.org/10.1093/gigascience/gix056>, PMID: 28873968
- Mearns DS, Donovan JC, Fernandes AM, Semmelhack JL, Baier H. 2020. Deconstructing hunting behavior reveals a tightly coupled Stimulus-Response loop. *Current Biology* **30**:54–69. DOI: <https://doi.org/10.1016/j.cub.2019.11.022>, PMID: 31866365
- Muto A, Ohkura M, Abe G, Nakai J, Kawakami K. 2013. Real-time visualization of neuronal activity during perception. *Current Biology* **23**:307–311. DOI: <https://doi.org/10.1016/j.cub.2012.12.040>, PMID: 23375894
- Neumann CJ, Nusslein-Volhard C. 2000. Patterning of the zebrafish retina by a wave of sonic hedgehog activity. *Science* **289**:2137–2139. DOI: <https://doi.org/10.1126/science.289.5487.2137>, PMID: 11000118
- Nevin LM, Robles E, Baier H, Scott EK. 2010. Focusing on optic tectum circuitry through the Lens of genetics. *BMC Biology* **8**:126. DOI: <https://doi.org/10.1186/1741-7007-8-126>, PMID: 20920150
- Nikolaou N, Lowe AS, Walker AS, Abbas F, Hunter PR, Thompson ID, Meyer MP. 2012. Parametric functional maps of visual inputs to the tectum. *Neuron* **76**:317–324. DOI: <https://doi.org/10.1016/j.neuron.2012.08.040>, PMID: 23083735
- Northmore DPM. 1984. Visual and saccadic activity in the goldfish torus Longitudinalis. *Journal of Comparative Physiology A* **155**:333–340. DOI: <https://doi.org/10.1007/BF00610587>
- Patterson BW, Abraham AO, MacIver MA, McLean DL. 2013. Visually guided gradation of prey capture movements in larval zebrafish. *Journal of Experimental Biology* **216**:3071–3083. DOI: <https://doi.org/10.1242/jeb.087742>, PMID: 23619412
- Peirce JW. 2007. PsychoPy—psychophysics software in python. *Journal of Neuroscience Methods* **162**:8–13. DOI: <https://doi.org/10.1016/j.jneumeth.2006.11.017>, PMID: 17254636
- Preuss SJ, Trivedi CA, vom Berg-Maurer CM, Ryu S, Bollmann JH. 2014. Classification of object size in retinotectal microcircuits. *Current Biology* **24**:2376–2385. DOI: <https://doi.org/10.1016/j.cub.2014.09.012>, PMID: 25242030
- Robles E, Smith SJ, Baier H. 2011. Characterization of genetically targeted neuron types in the zebrafish optic tectum. *Frontiers in Neural Circuits* **5**:1. DOI: <https://doi.org/10.3389/fncir.2011.00001>, PMID: 21390291

- Robles E, Filosa A, Baier H. 2013. Precise lamination of retinal axons generates multiple parallel input pathways in the tectum. *Journal of Neuroscience* **33**:5027–5039. DOI: <https://doi.org/10.1523/JNEUROSCI.4990-12.2013>, PMID: 23486973
- Robles E, Laurell E, Baier H. 2014. The retinal projectome reveals brain-area-specific visual representations generated by ganglion cell diversity. *Current Biology* **24**:2085–2096. DOI: <https://doi.org/10.1016/j.cub.2014.07.080>, PMID: 25155513
- Robles E, Fields NP, Baier H. 2020. The zebrafish visual system transmits dimming information via multiple segregated pathways. *Journal of Comparative Neurology* **1**:24964. DOI: <https://doi.org/10.1002/cne.24964>
- Román Rosón M, Bauer Y, Kotkat AH, Berens P, Euler T, Busse L. 2019. Mouse dLGN receives functional input from a diverse population of retinal ganglion cells with limited convergence. *Neuron* **102**:462–476. DOI: <https://doi.org/10.1016/j.neuron.2019.01.040>, PMID: 30799020
- Schindelin J, Arganda-Carreras I, Frise E, Kaynig V, Longair M, Pietzsch T, Preibisch S, Rueden C, Saalfeld S, Schmid B, Tinevez JY, White DJ, Hartenstein V, Eliceiri K, Tomancak P, Cardona A. 2012. Fiji: an open-source platform for biological-image analysis. *Nature Methods* **9**:676–682. DOI: <https://doi.org/10.1038/nmeth.2019>, PMID: 22743772
- Schmitt EA, Dowling JE. 1999. Early retinal development in the zebrafish, *Danio rerio*: light and electron microscopic analyses. *The Journal of Comparative Neurology* **404**:515–536. DOI: [https://doi.org/10.1002/\(SICI\)1096-9861\(19990222\)404:4<515::AID-CNE8>3.0.CO;2-A](https://doi.org/10.1002/(SICI)1096-9861(19990222)404:4<515::AID-CNE8>3.0.CO;2-A), PMID: 9987995
- Scott EK, Mason L, Arrenberg AB, Ziv L, Gosse NJ, Xiao T, Chi NC, Asakawa K, Kawakami K, Baier H. 2007. Targeting neural circuitry in zebrafish using GAL4 enhancer trapping. *Nature Methods* **4**:323–326. DOI: <https://doi.org/10.1038/nmeth1033>, PMID: 17369834
- Scott EK, Baier H. 2009. The cellular architecture of the larval zebrafish tectum, as revealed by Gal4 enhancer trap lines. *Frontiers in Neural Circuits* **3**:13. DOI: <https://doi.org/10.3389/neuro.04.013.2009>
- Semmelhack JL, Donovan JC, Thiele TR, Kuehn E, Laurell E, Baier H. 2014. A dedicated visual pathway for prey detection in larval zebrafish. *eLife* **3**:e04878. DOI: <https://doi.org/10.7554/eLife.04878>
- Simoncelli EP. 2003. Vision and the statistics of the visual environment. *Current Opinion in Neurobiology* **13**: 144–149. DOI: [https://doi.org/10.1016/S0959-4388\(03\)00047-3](https://doi.org/10.1016/S0959-4388(03)00047-3), PMID: 12744966
- Sinha R, Hoon M, Baudin J, Okawa H, Wong ROL, Rieke F. 2017. Cellular and circuit mechanisms shaping the perceptual properties of the primate fovea. *Cell* **168**:413–426. DOI: <https://doi.org/10.1016/j.cell.2017.01.005>, PMID: 28129540
- Szatko KP, Korympidou MM, Ran Y, Berens P, Dalkara D, Schubert T, Euler T, Franke K. 2020. Neural circuits in the mouse retina support color vision in the upper visual field. *Nature Communications* **11**:1–14. DOI: <https://doi.org/10.1038/s41467-020-17113-8>, PMID: 32661226
- Temizer I, Donovan JC, Baier H, Semmelhack JL. 2015. A visual pathway for Looming-Evoked escape in larval zebrafish. *Current Biology* **25**:1823–1834. DOI: <https://doi.org/10.1016/j.cub.2015.06.002>, PMID: 26119746
- Thiele TR, Donovan JC, Baier H. 2014. Descending control of swim posture by a midbrain nucleus in zebrafish. *Neuron* **83**:679–691. DOI: <https://doi.org/10.1016/j.neuron.2014.04.018>, PMID: 25066082
- Thompson AW, Vanwalleghem GC, Heap LA, Scott EK. 2016. Functional profiles of visual-, Auditory-, and water Flow-Responsive neurons in the zebrafish tectum. *Current Biology* **26**:743–754. DOI: <https://doi.org/10.1016/j.cub.2016.01.041>, PMID: 26923787
- Wang K, Hinz J, Zhang Y, Thiele TR, Arrenberg AB. 2020. Parallel channels for motion feature extraction in the pretectum and tectum of larval zebrafish. *Cell Reports* **30**:442–453. DOI: <https://doi.org/10.1016/j.celrep.2019.12.031>
- Warwick RA, Kaushansky N, Sarid N, Golan A, Rivlin-Etzion M. 2018. Inhomogeneous encoding of the visual field in the mouse retina. *Current Biology* **28**:655–665. DOI: <https://doi.org/10.1016/j.cub.2018.01.016>, PMID: 29456141
- Xiao T, Baier H. 2007. Lamina-specific axonal projections in the zebrafish tectum require the type IV collagen dragnet. *Nature Neuroscience* **10**:1529–1537. DOI: <https://doi.org/10.1038/nn2002>, PMID: 17982451
- Yoshimatsu T, Schröder C, Nevala NE, Berens P, Baden T. 2020. Fovea-like photoreceptor specializations underlie single UV cone driven Prey-Capture behavior in zebrafish. *Neuron* **107**:320–337. DOI: <https://doi.org/10.1016/j.neuron.2020.04.021>, PMID: 32473094
- Zhou M, Bear JE, Roberts PA, Janiak F, Semmelhack JL, Yoshimatsu T, Baden T. 2020. What the zebrafish's Eye Tells the Zebrafish's Brain: Retinal Ganglion Cells for Prey Capture and Colour Vision. *bioRxiv*. DOI: <https://doi.org/10.1101/2020.01.31.927087>
- Zimmermann MJY, Nevala NE, Yoshimatsu T, Osorio D, Nilsson DE, Berens P, Baden T. 2018. Zebrafish differentially process color across visual space to match natural scenes. *Current Biology* **28**:2018–2032. DOI: <https://doi.org/10.1016/j.cub.2018.04.075>, PMID: 29937350



Figures and figure supplements

Retinotectal circuitry of larval zebrafish is adapted to detection and pursuit of prey

Dominique Förster et al

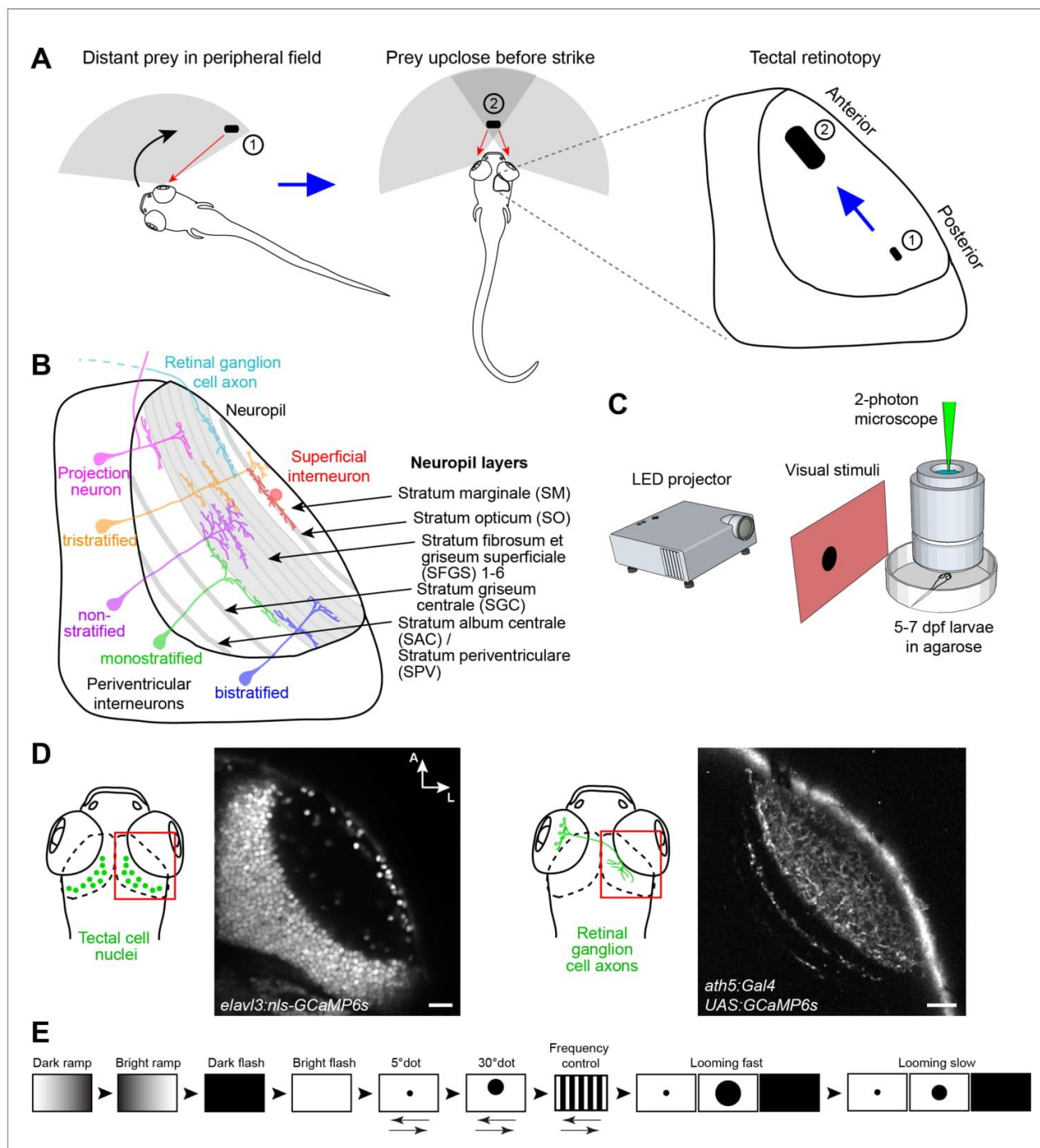


Figure 1. Experimental paradigm for studying location-specific processing in the tectum. (A) In a typical hunting sequence, the fish detects prey in its peripheral visual field (1), ultimately turns and approaches to bring the prey image into its central binocular field (2). Hypothetically, the retinotectal map might be adapted to this location- and size-specific representation of the prey object. (B) Sketch of the tectum showing previously described cell types and neuroepil layers. (C) Schematic for functional imaging setup. (D) On the left: Region of interest (ROI) for imaging tectal cell responses and exemplary expression of nuclear-localized GCaMP6s. On the right: ROI for RGC imaging and expression of GCaMP6s in RGC axons under control of *ath5:Gal4*. (E) Figure 1 continued on next page

Figure 1 continued

Stimulus protocol. Arrows below stimulus representation indicate object movement, first in nasal, then in temporal direction. See Materials and methods for details. Scale bar in (D): 20 μm .

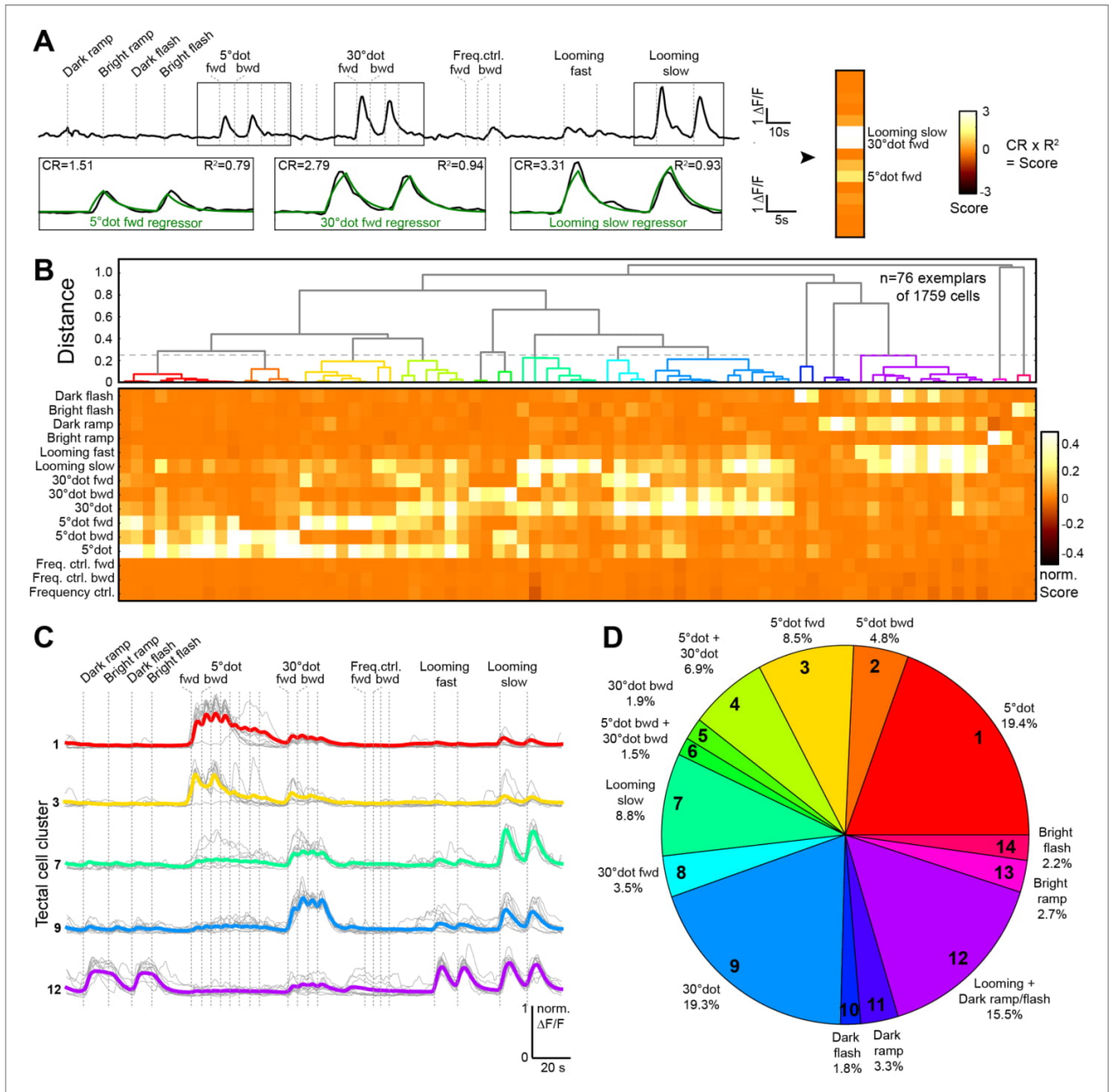


Figure 2. Behaviorally relevant response clusters in the tectum. (A) Analysis of calcium imaging data. Within selected response windows (black rectangles), the $\Delta F/F$ traces were correlated to the corresponding regressor and 15 score values were calculated for each cell (CR: coefficient of regression, R^2 : correlation, response: black trace, model: green trace). (B) Hierarchical clustering of functional cell types in the tectum. Normalized scores for 76 exemplars, obtained by affinity propagation of 1759 cells (of three larvae) in total are shown. Dashed line indicates a chosen distance threshold of 0.25, which results in 14 functional clusters. (C) Normalized calcium transients of all exemplars (gray) and average traces of all cells (colored) for the five largest clusters. (D) Functional cluster distribution. Tectal cluster numbers are indicated.

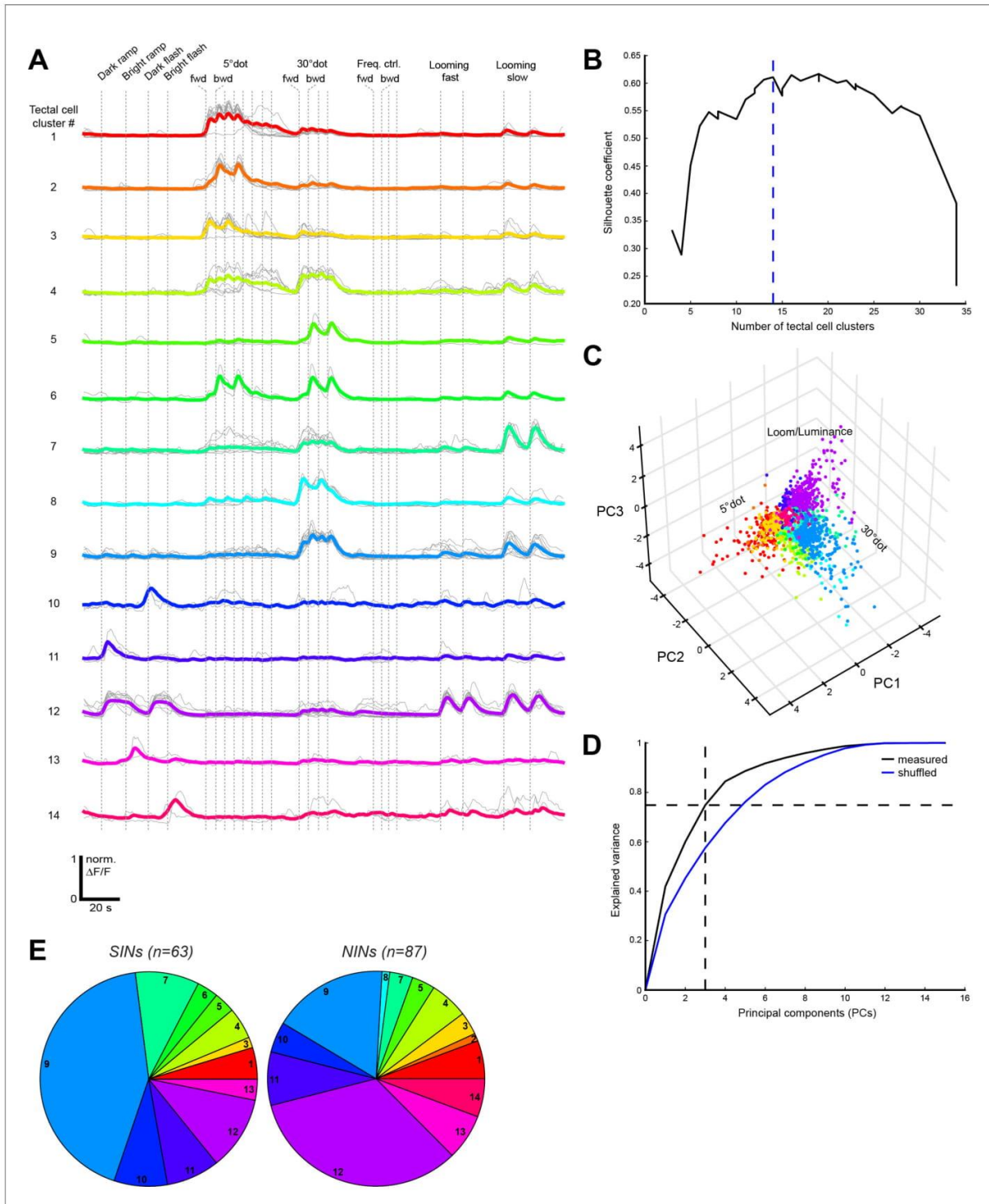


Figure 2—figure supplement 1. Functional clustering of tectal cells. (A) Normalized calcium transients of all exemplars (gray) and average transients of all cells (colored) for the 14 tectal clusters. (B) Validation of cluster number by the silhouette coefficient. A minimal number of 14 clusters was chosen
 Figure 2—figure supplement 1 continued on next page

Figure 2—figure supplement 1 continued

(dashed blue line). (C) 3D representation of the three main principal components (PCs) for all tectal cells. Data points are colored by their corresponding cluster. (D) The chosen number of three PCs explains 74.9% of the variance in the measured data (black curve). Shuffled data (blue curve) resulted in a lower average explained variance (57.6% for the three main PCs). (E) Functional cluster distribution of superficial interneurons (SINs) and neuropil interneurons (NINs), imaged in the *elavl3:nls-GCaMP6s* line (n = number of cells from three fish). Cluster numbers are indicated.

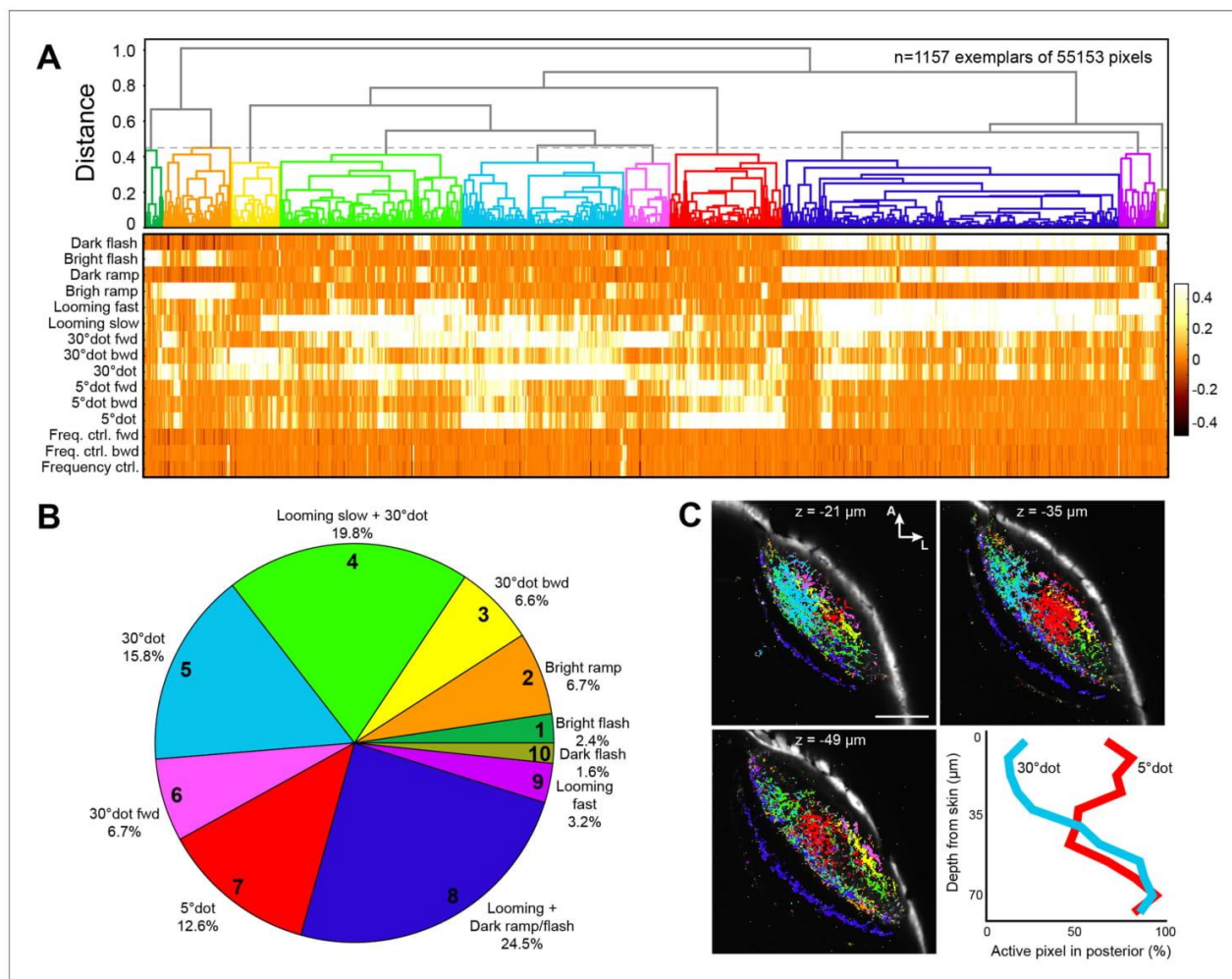


Figure 3. Clustering of functional RGC responses in the tectum. (A) Hierarchical clustering of functional RGC pixels. Normalized scores for 1157 exemplars, obtained by affinity propagation of 55,153 pixels in total are shown. Dashed line indicates a chosen distance threshold of 0.45, which results in 10 functional clusters. (B) Functional cluster distribution of all analyzed RGC pixels. Cluster numbers are indicated. (C) Spatial distribution of functional RGC pixels in the tectal neuropil. Pixels were cluster-color-coded and overlaid onto single planes of the *ath5:Gal4 UAS:GCaMP6s* expression pattern. Z indicates plane position as the distance from dorsal skin ($z = 0 \mu\text{m}$). Last panel in (C) shows quantification of 30° dot-responsive (blue) and 5° dot-responsive (red) pixels in the posterior tectum along different z-planes. Scale bar: 50 μm .

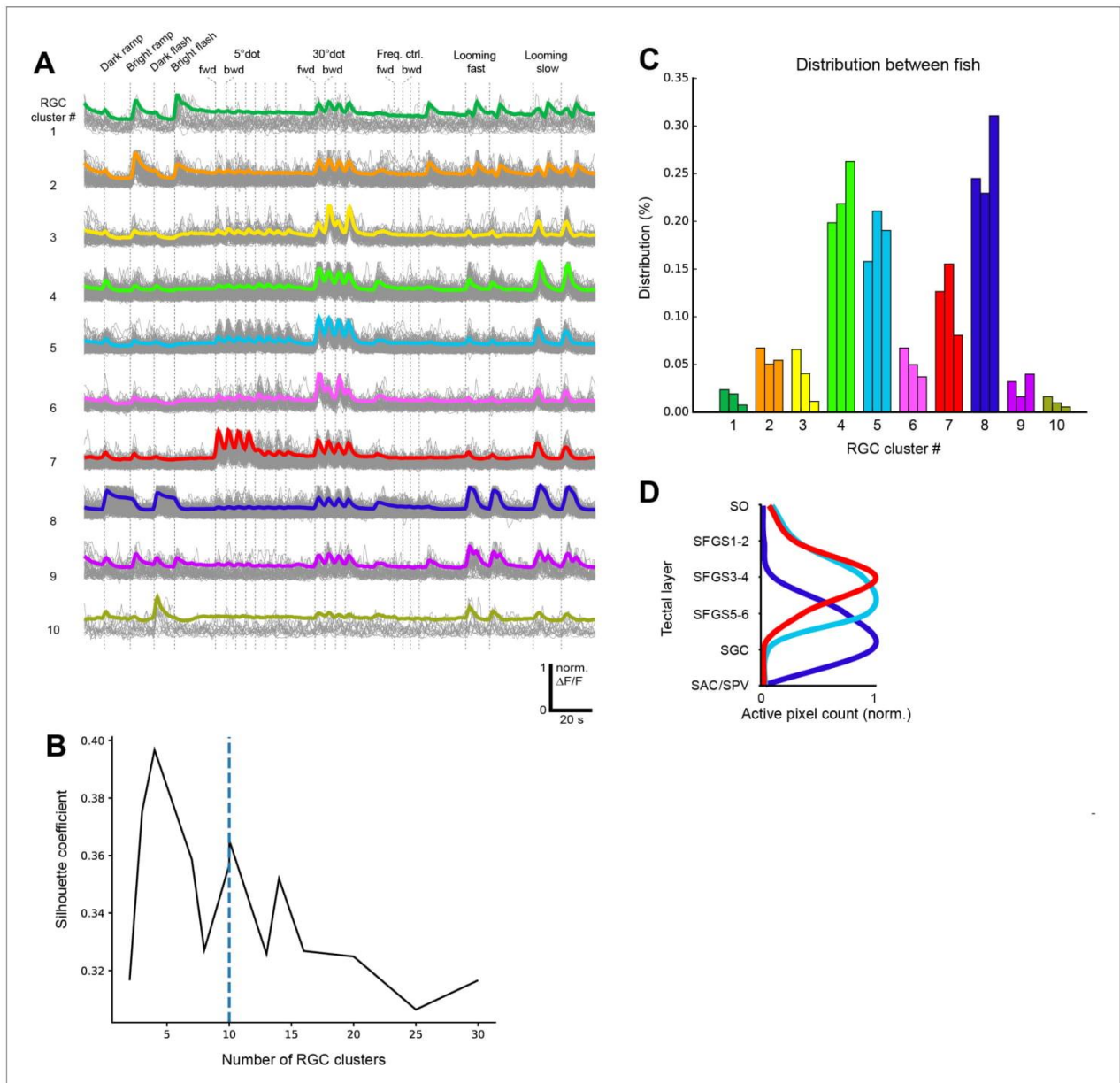


Figure 3—figure supplement 1. Functional clustering of RGC types. (A) Normalized calcium transients of all exemplars (gray) and average transients of all pixels (colored) for the 10 RGC clusters. (B) Silhouette plot for cluster validation. A number of 10 RGC clusters was chosen (dashed blue line) as it significantly improves the modeling correlation compared to four clusters (see **Figure 4—figure supplement 1A**). (C) Comparison of RGC cluster distribution for three independent larvae. Data from the first larva (first bars) are shown in **Figure 2** and were used for modeling. (D) Quantification of 30° dot- (light blue), 5° dot- (red), and looming+dark ramp/flash-responsive (dark blue) pixels in the segmented tectal layers, throughout the whole image stack shown in **Figure 3C**.

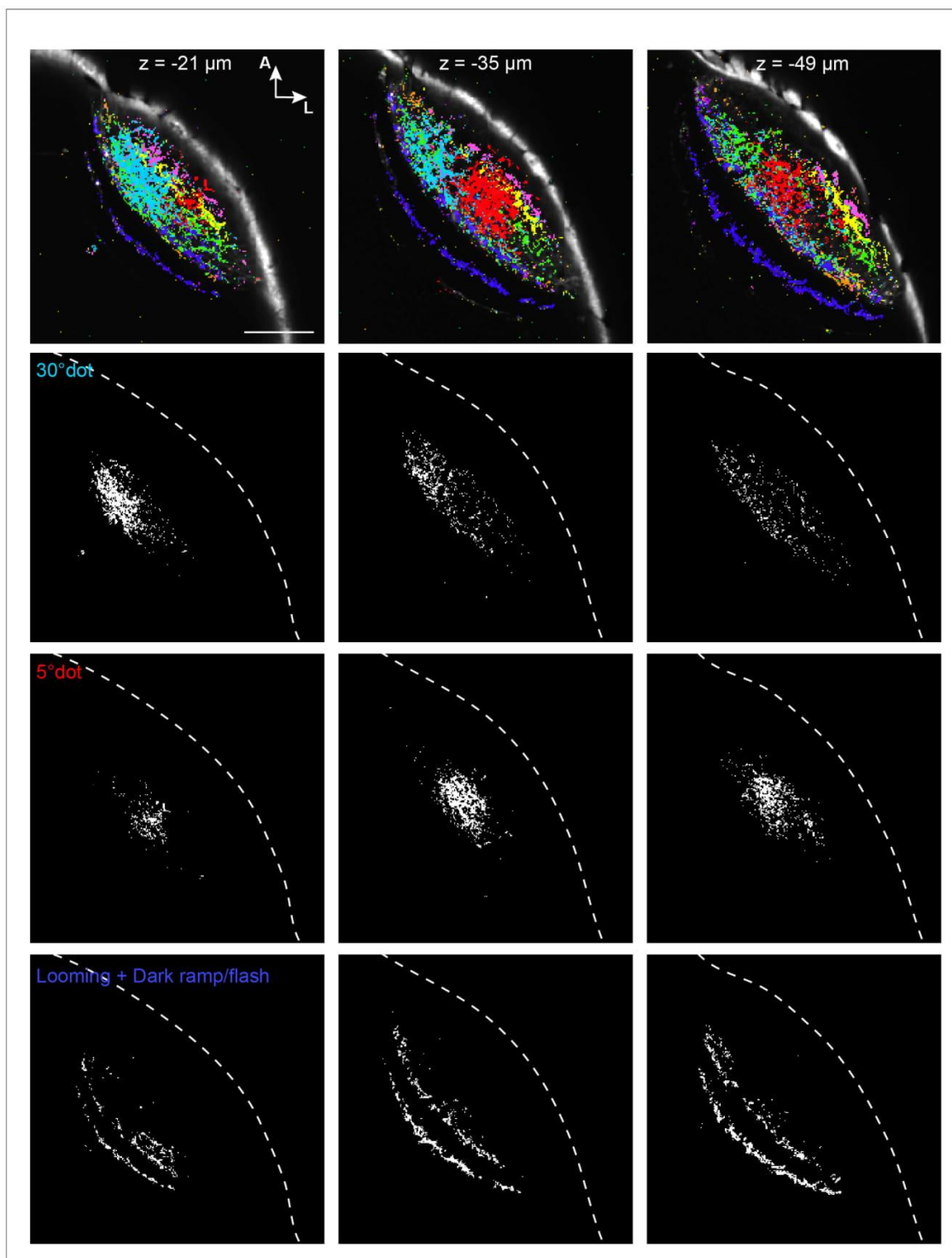


Figure 3—figure supplement 2. Figure panels showing the active RGC pixels of three imaging planes from *Figure 3C* separately for the three relevant clusters (30° dot, 5° dot, looming+dark ramp/flash). Skin is outlined by white-dashed line. Scale bar: 50 μm .

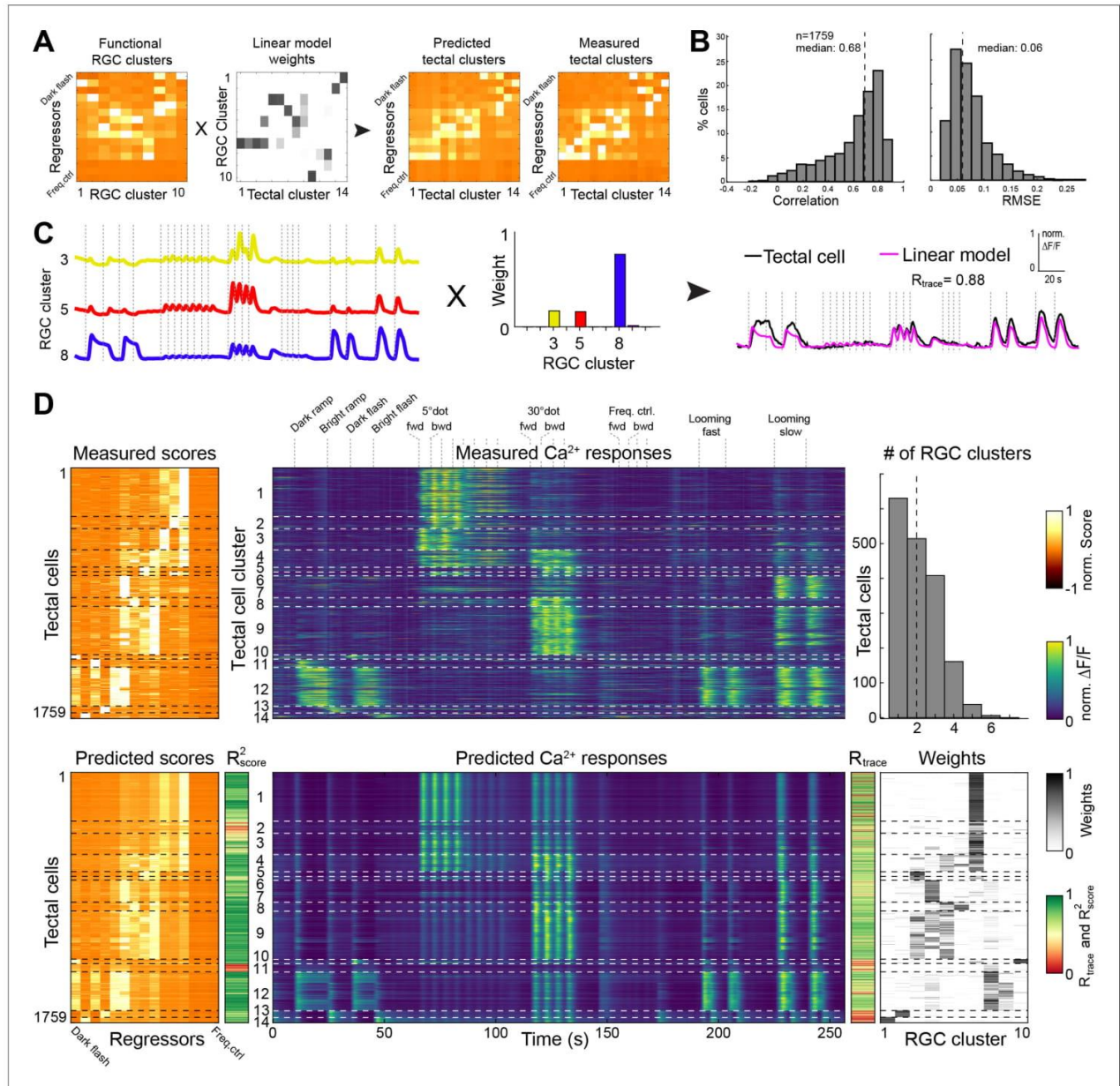


Figure 4. Modeling of tectal responses by linear combinations of RGC inputs. (A) Modeling workflow. Tectal cluster scores were predicted by a linear combination of weighted RGC cluster scores and finally compared to previously measured tectal scores. For color scale, see (D). (B) Prediction quality for modeling the scores of each sampled tectal cell ($n = 1759$). Left graph shows the correlation between predicted and measured scores. Right graph shows distribution of root mean squared errors of the cross-validated model (see Materials and methods for details). (C) Example for modeling the calcium response of a single tectal cell from weighted average responses of three RGC clusters. (D) Summary of modeling scores (left), calcium responses (middle), and weights (lower right) for all tectal cells ($n = 1759$). Functional tectal clusters are indicated by dashed horizontal lines. Color scales are shown on the right. Upper graph on the right shows the distribution of the number of RGC clusters used for modeling tectal responses. Dashed vertical line indicates a median of two RGC clusters.

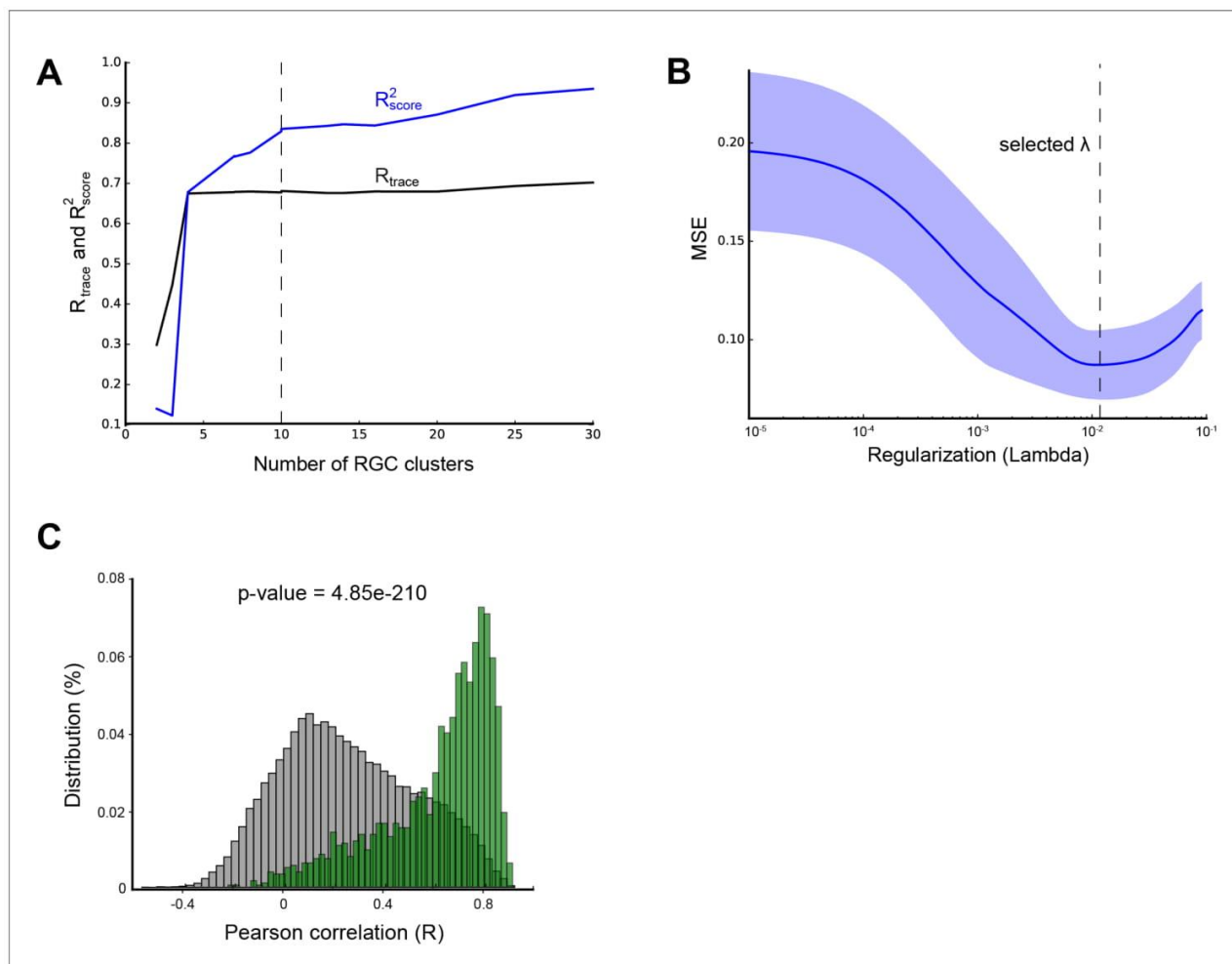


Figure 4—figure supplement 1. Linear modeling parameters. (A) Modeling prediction quality shown as correlation values R_{score}^2 and R_{trace} , as a function of RGC cluster number. (B) Mean squared error (MSE) of modeling prediction as a function of the regularization parameter λ . See Materials and methods for details. (C) Correlation (R) between predicted and measured scores for modeling data (green) compared to a randomized model (gray). See Materials and methods for details.

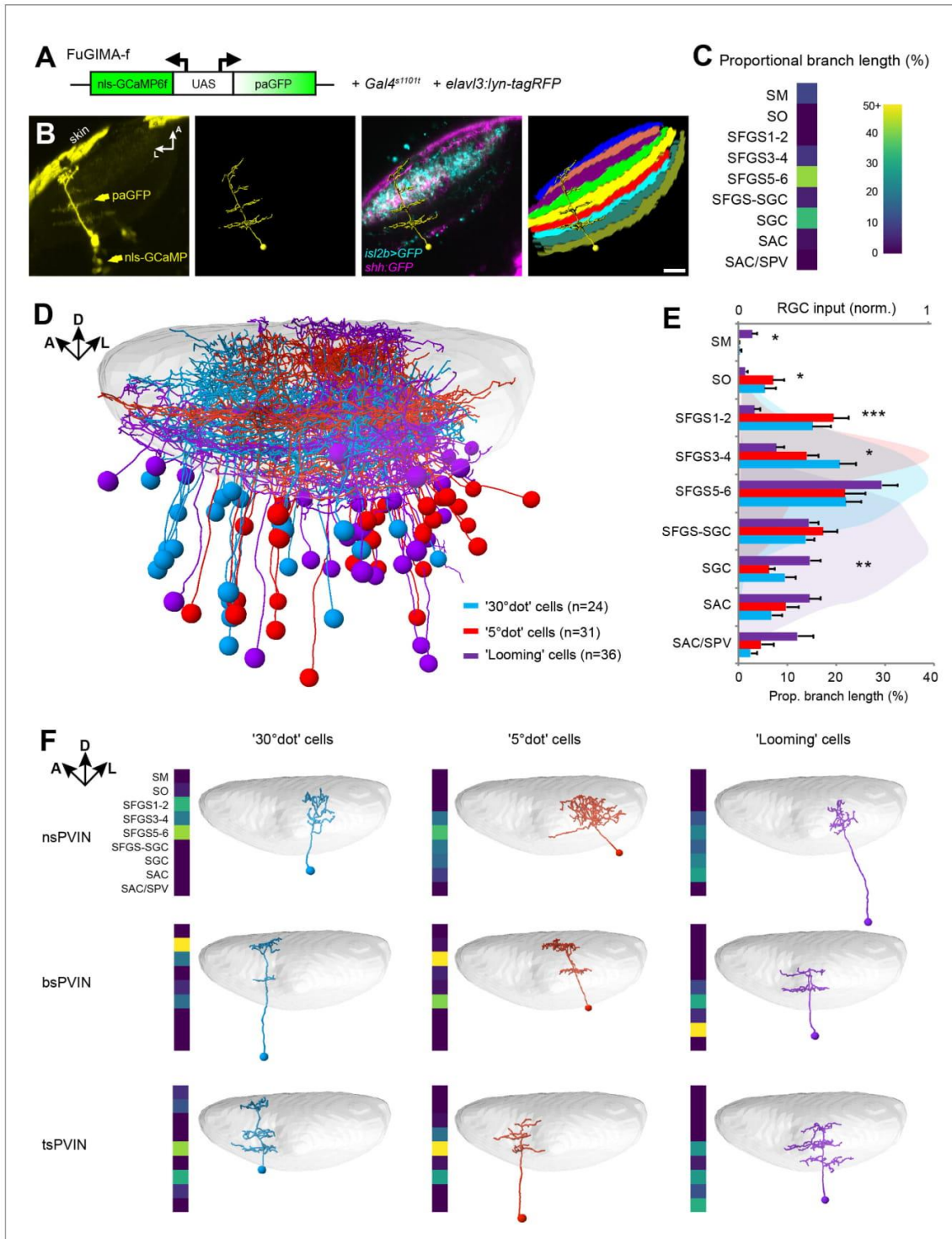


Figure 5. Dendrite morphologies of functionally identified tectal neurons match input layers. (A) The FuGIMA-f construct, which allows coexpression of nuclear-localized GCaMP6f and photoactivatable GFP (paGFP), was combined with *Gal4s1101t* for panneuronal expression and *elav13:lyn-tagRFP* for Figure 5 continued on next page

Figure 5 continued

image registrations. (B) Workflow of single-cell photoactivation, cell tracing, landmark registrations and layer quantifications (see Materials and methods for details). (C) Morphological barcode for the cell in (B). (D) Sideview of registered FuGIMA cells in the tectum of a standard brain. Tectal neuropil is shaded in gray. (E) Average proportional branch length of neurites in the respective tectal layers, quantified for 30° dot- (blue), 5° dot- (red), and looming- (purple) responsive cells. Statistically significant differences between 5° dot- and looming-responsive cells are indicated by stars. For comparison, the quantification of RGC input in the respective layers is shown in the back (see **Figure 3—figure supplement 1D**). Error bars are SEM. ***: $p < 0.001$, **: $p < 0.01$, and *: $p < 0.05$. (F) Exemplary tectal cell morphotypes identified for the response groups described above. PVIN: periventricular interneuron; ns: non-stratified; bs: bistratified; ts: tristratified. Scale bar in (B): 20 μm .

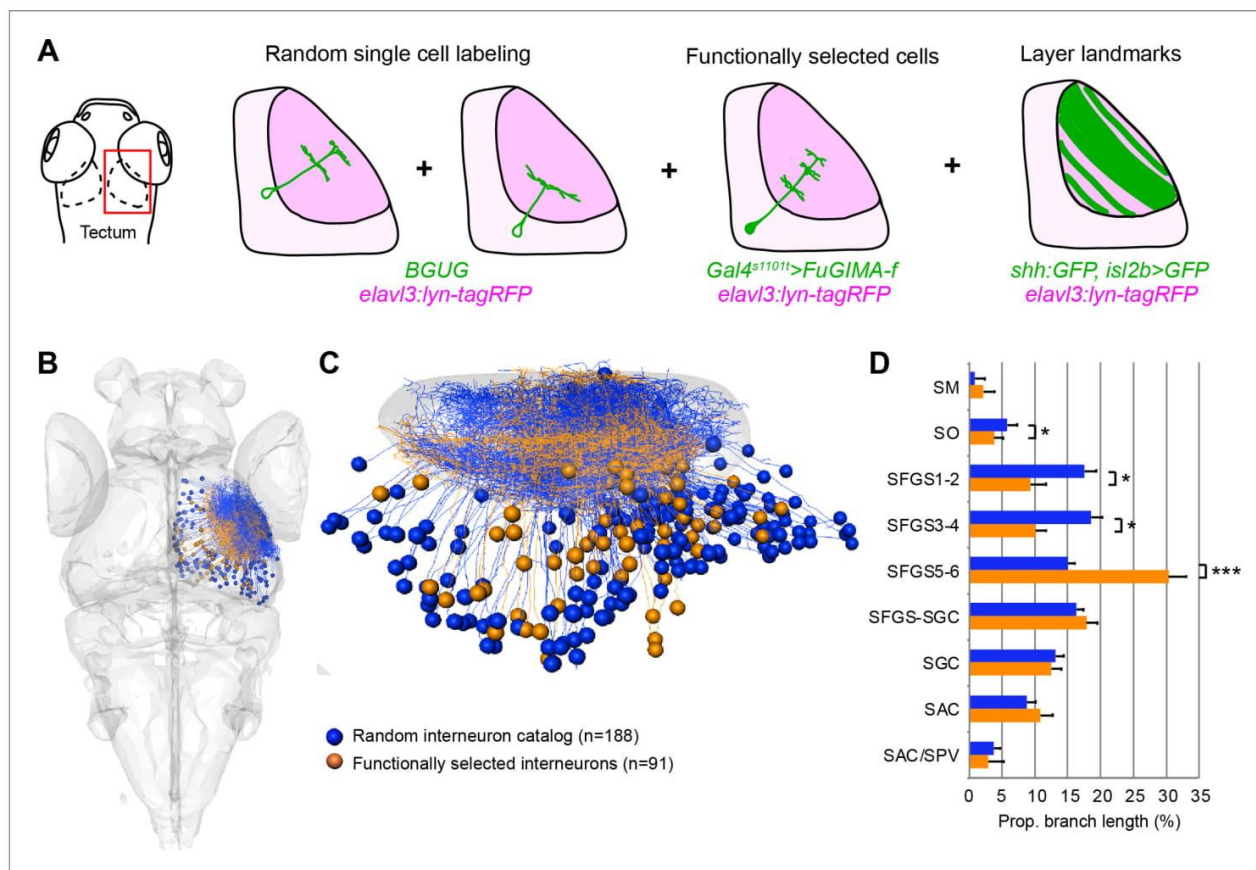


Figure 5—figure supplement 1. Comparison and quantification of tectal cell morphologies. (A) Workflow for combining single-cell data. A common reference marker (*elavl3:lyn-tagRFP*) allowed co-registration of randomly labeled single cells (BGUG method), functionally selected single cells (FuGIMA method), and RGC expression patterns as landmarks for tectal laminae. (B) Dorsal overview of collected tectal interneurons from BGUG dataset (blue) and FuGIMA dataset (orange). (C) Tectal sideview. Dorsal is up and anterior is left. (D) Average proportional branch length of tectal cell neurites in the respective layers, for randomly labeled (blue) and functionally selected cells (orange). Error bars are SEM. ***: $p < 0.001$, and *: $p < 0.05$.

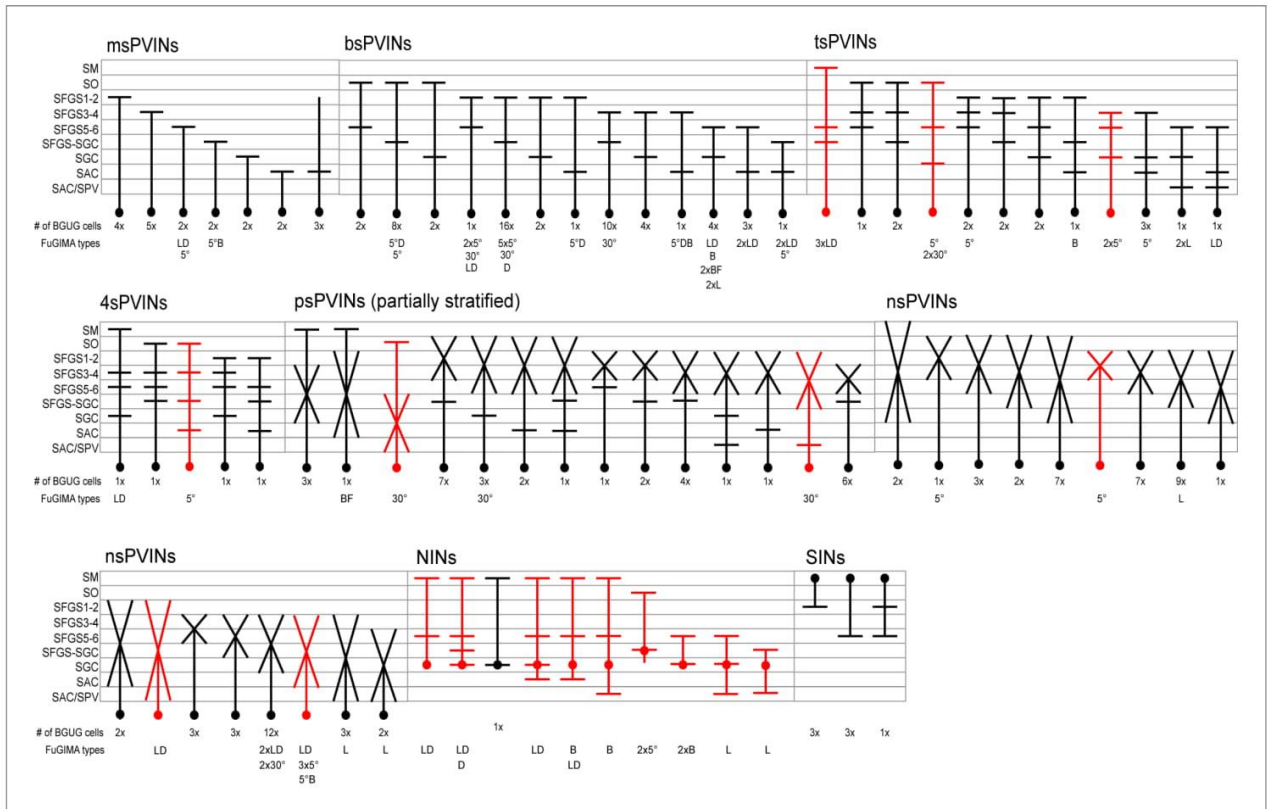


Figure 5—figure supplement 2. Tectal interneuron catalog. Schematic representation of all identified morphotypes for tectal interneurons. The number of collected BGUG cells for each type is presented below. Red morphotypes have only been identified by the FuGIMA method. Identified functional types are indicated below. L: looming, D: dark ramp, B: bright ramp, 5°: small dot, 30°: big dot, BF: bright flash. PVIN: periventricular interneuron, NIN: neuropil interneuron, SIN: superficial interneuron, ms: monostratified, bs: bistratified, ts: tristratified, 4 s: tetrastratified, ps: partially stratified, ns: non-stratified/diffuse.

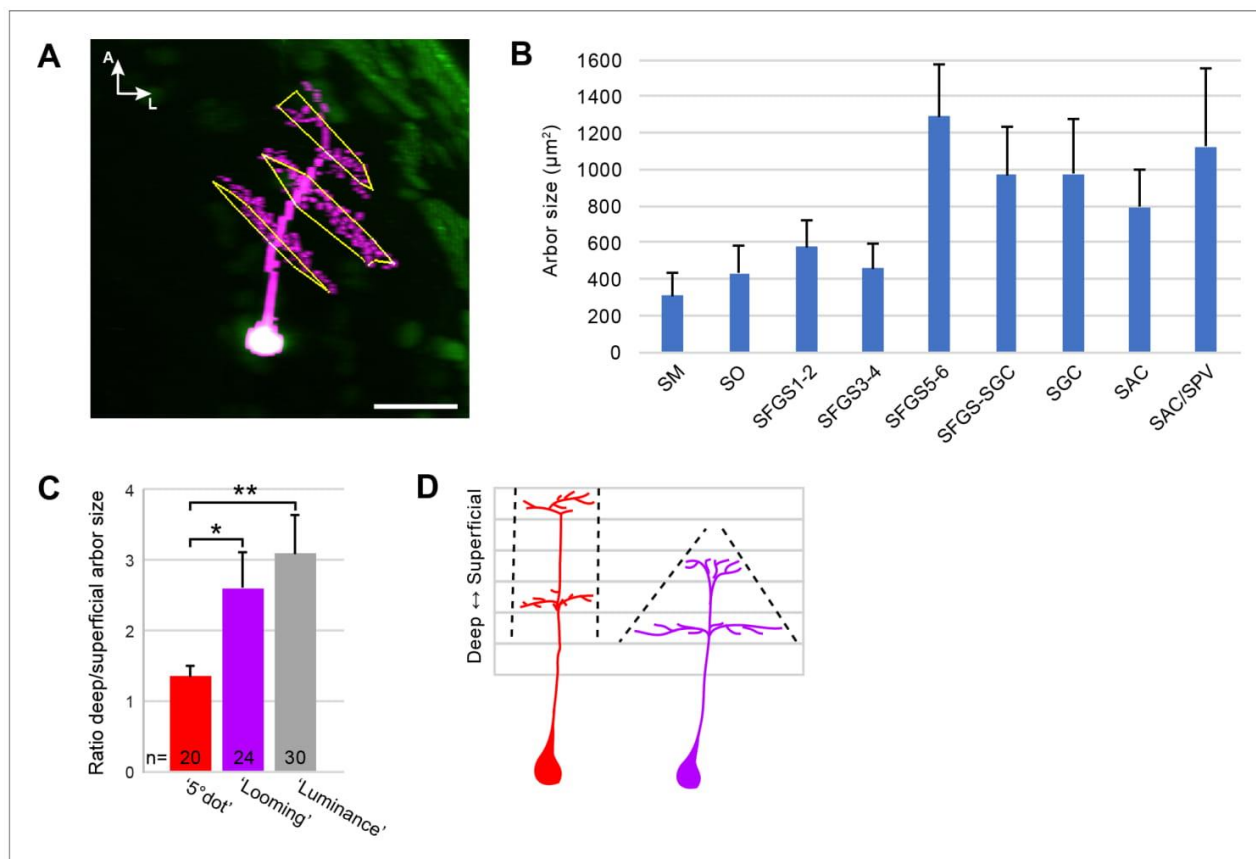


Figure 5—figure supplement 3. Quantification of tectal cell arbor size. (A) Illustration of arbor quantification for a tristratified tectal cell. (B) Average arbor area in different tectal laminae. Error bars are SEM. (C) Ratio of deep vs. superficial arbor area within the same cells, for 5° dot-, Looming-, and Luminance-responsive cell types. Error bars are SEM. **: $p < 0.01$, and *: $p < 0.05$. (D) Illustration of columnar-shaped, 5° dot-responsive cells (red) and cone-shaped, looming-responsive cells (purple).

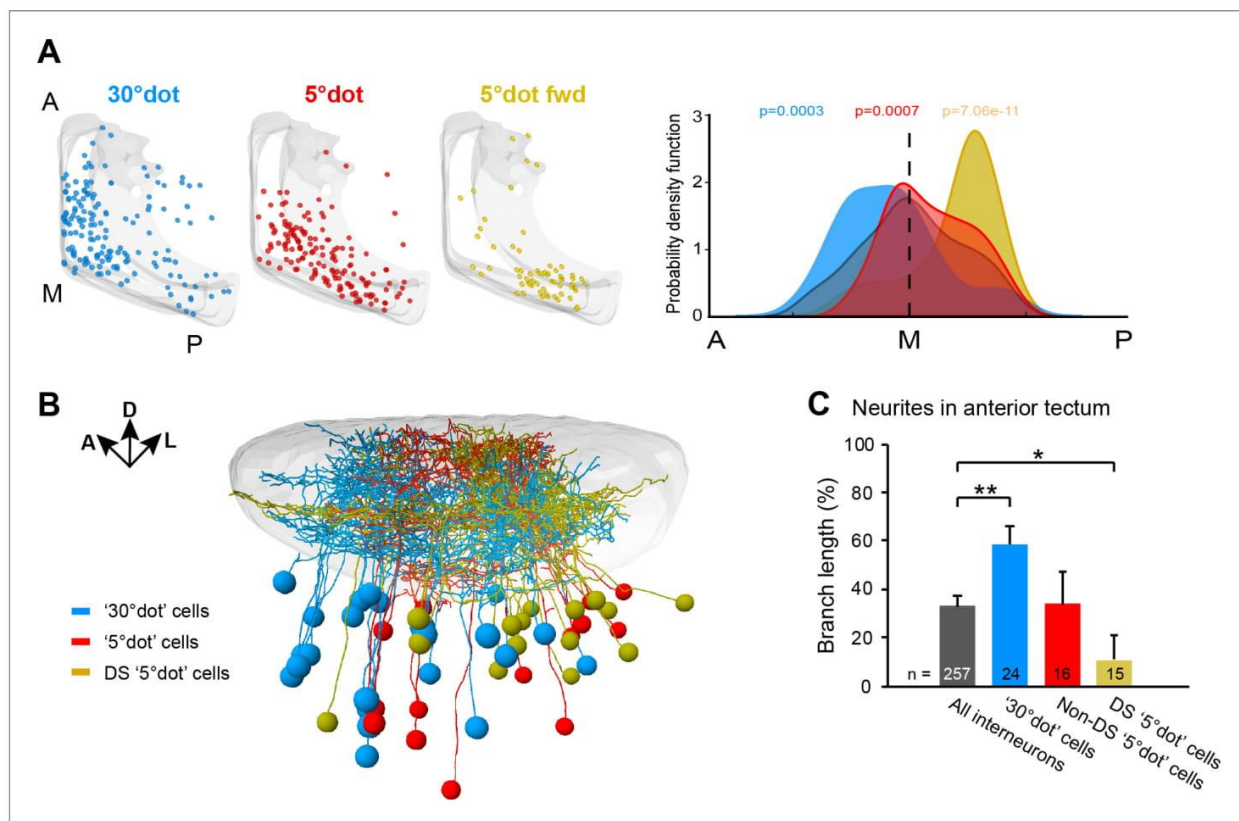


Figure 6. Functional compartmentalization of the tectum along the anterior-posterior axis. (A) Distribution of tectal cell bodies from 30°-dot (blue), 5°-dot (red) and 5°-dot-forward (yellow) response clusters. Anterior (A), medial (M) and posterior (P) positions of the tectum are indicated. Graph shows probability density function for cell body distribution. Integrals are colored according to their functional cluster with p-values characterizing the difference from the distribution of all sampled cells (gray integral). (B) Tectal sideview of registered FuGIMA neurons showing the distribution of 30°-dot (blue), 5°-dot non-DS (red) and 5°-dot-DS (yellow) cells. (C) Quantification of proportional neurite branch length of tectal cells in the anterior tectum. N equals number of cells. **: $p = 0.006$; *: $p = 0.014$.

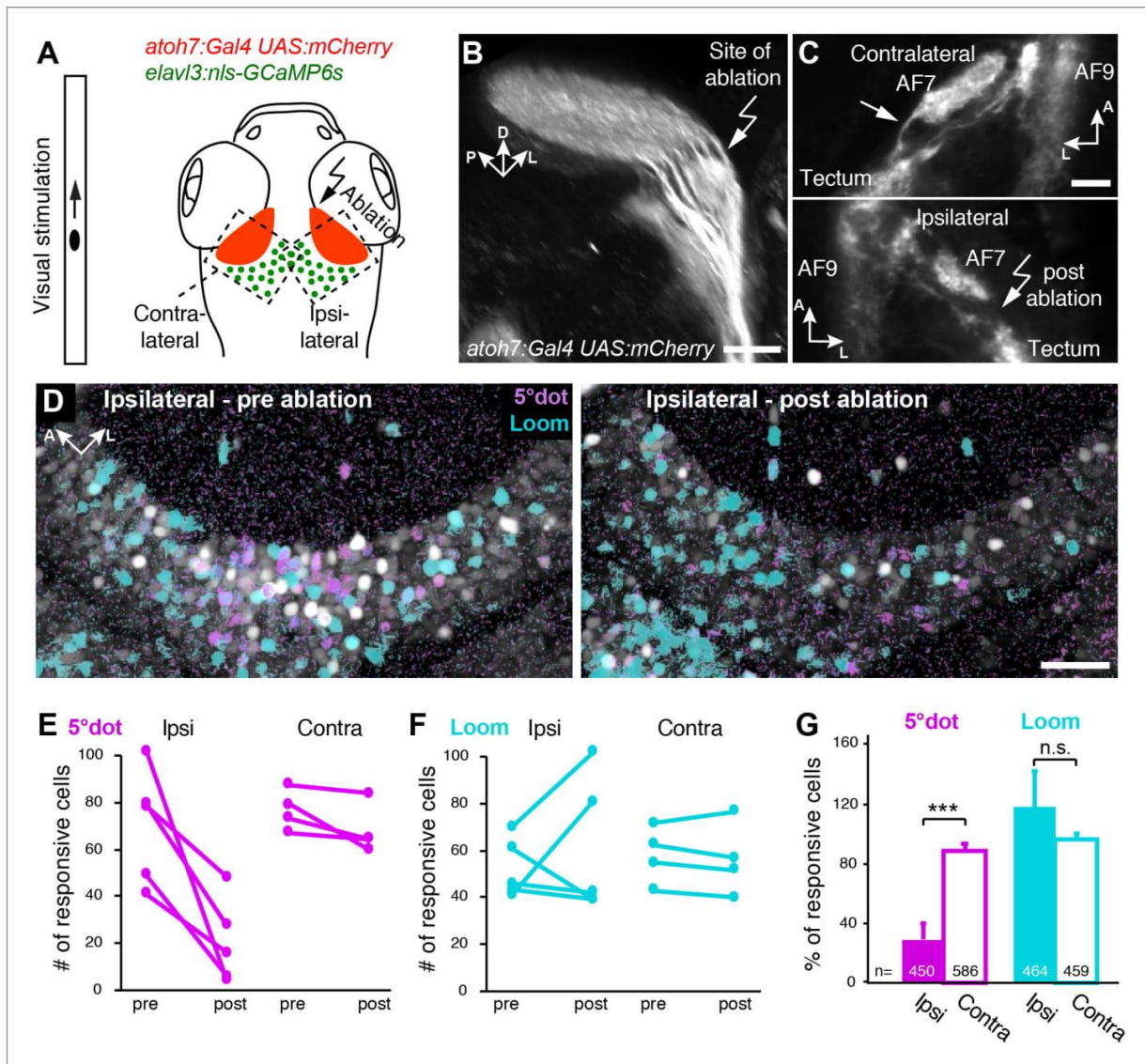


Figure 7. Small size-tuned RGC inputs are essential for small-object processing in the tectum. (A) Experimental setup for RGC axon ablations. Larvae are expressing mCherry in RGCs and nuclear GCaMP6s panneuronally. The eye contralateral to the ablation site is visually stimulated and the ipsilateral tectal cells are functionally imaged before and after the ablations. As a control, the eye ipsilateral to the ablation site is stimulated and the contralateral tectal cells are imaged in the same fish. (B) Sideview of mCherry expression in RGCs at 6 dpf shows the most lateral axon bundle, which leaves AF7 for the SO layer (arrow). (C) Dorsal view of single image planes showing the axon fibers of interest in the contralateral (control, upper panel) and ipsilateral (ablated, lower panel) pretectum of the same fish. (D) Single functional image planes, projected over time, showing nuclear GCaMP6s expression in the ipsilateral tectum, before (6 dpf, left) and after (7 dpf, right) ablation. Pixels are color-coded by preference for 5° dot (magenta) or looming (cyan) stimuli. (E) Number of cells per image plane (out of two fish), which are responsive to a 5° dot stimulus, before and after ablations in the ipsilateral and the contralateral tectum. (F) Same as (E), showing the number of cells responsive to a looming stimulus. (G) Fraction of 5°-dot- and looming-responsive cells after ablations in the ipsilateral and contralateral tectum. Error bars are SEM. ***: $p = 0.0006$; n.s.: $p = 0.46$. N equals number of cells from two independent fish. Scale bars in (B): 30 μm , (C): 20 μm , and (D): 50 μm .

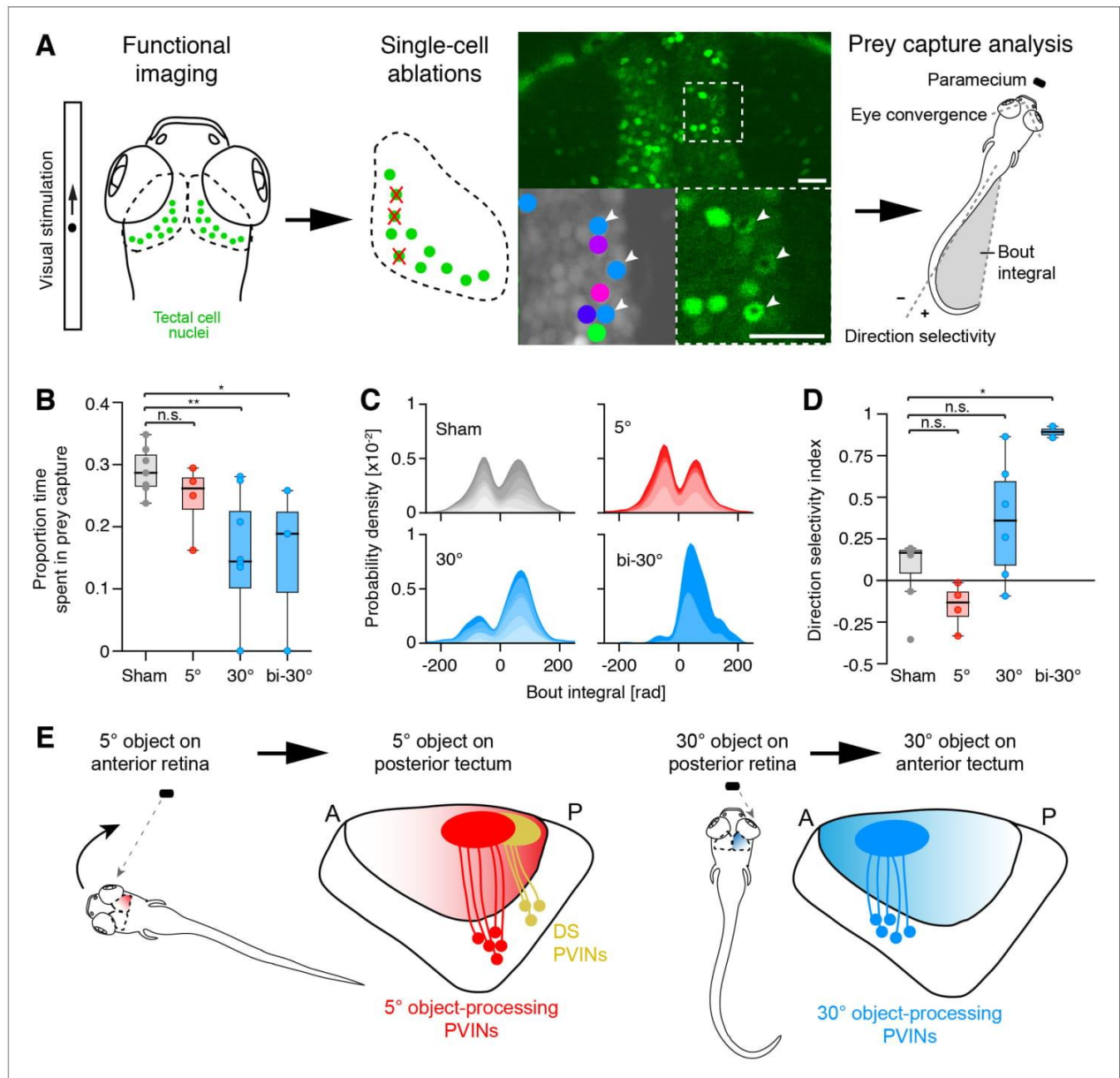


Figure 8. Large-object processing cells are required for hunting behavior. (A) 7 dpf old fish panneuronally expressing nuclear-localized GCaMP6s (green) were visually stimulated and imaged. Tectal cells were functionally identified (cluster-colored circles) and selected for ablations (arrowheads). At dpf, hunting behavior was analyzed in free-swimming larvae. (B) Proportion of time larvae spent engaged in hunting behavior, having their eyes converged. Single data points represent individual fish. ‘Sham’ (gray): control larvae with ablations of non-responsive cells, ‘5°’ (red): unilateral ablations of 5°-dot-responsive cells in the right tectum, ‘30°’ (blue): unilateral ablations of 30°-dot-responsive cells in the right tectum, ‘bi-30°’: bilateral ablations of 30°-dot-responsive cells. *: $p = 0.02$, **: $p = 0.006$, n.s.: $p = 0.15$. (C) Probability density plots of bout integrals for the initial J-turns, with positive values indicating a rightward and negative values indicating a leftward turn. Color shading indicates accumulated data for individual fish. (D) Direction selectivity index for initial J-turns of individual fish. *: $p = 0.029$, n.s.: $p > 0.05$. (E) Ethological relevance for A-P distribution of functionally distinct tectal cells. Before initiation of prey capture behavior, small moving objects are likely spotted in the temporal, monocular visual field. Precise recognition and processing of object movement by posterior DS cells avoids losing the object and enables adapted orientation turns towards the object. During prey pursuit, prey size seemingly increases and is detected by large-dot-responsive cells in the anterior tectum. Eye convergence allows binocular processing of object size and movement.

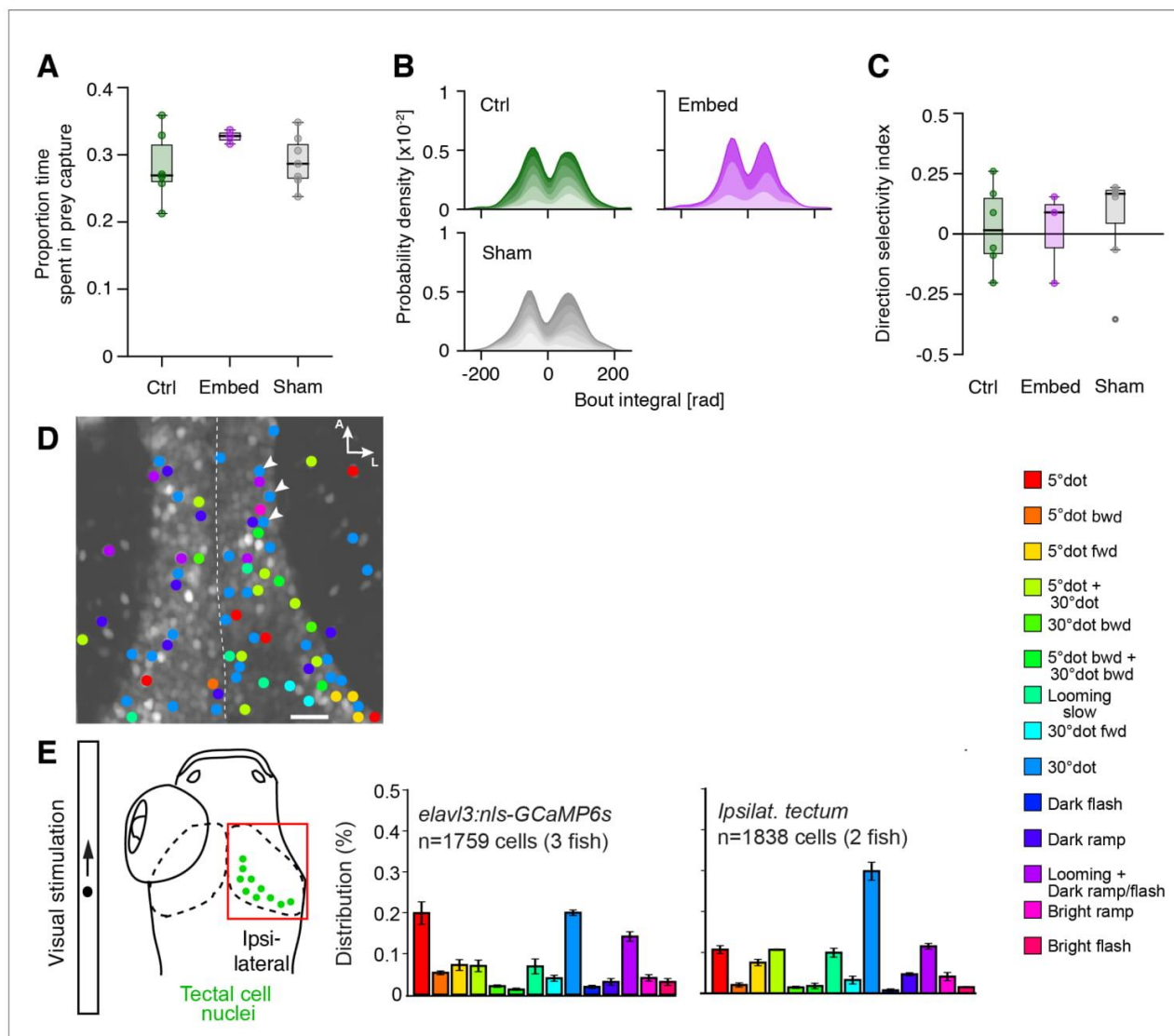


Figure 8—figure supplement 1. Tectal cell ablation controls and enucleation experiments. (A–C) In our free-swimming prey capture assay, ‘sham’ ablated larvae (gray), in which non-responsive tectal cells have been removed, did not behave differently from untreated (‘ctrl’, green), or agarose-embedded and released (‘embed’, purple) larvae, in terms of time spent in prey capture (A), initial J-turn kinematics (B), or direction selectivity index (C). (D) Cluster color-coded functional cell responses in both anterior tecta for the experiment shown in **Figure 8A** (arrow heads highlighting cells selected for ablations). Midline is indicated by a dashed white line. Note the tectal cell responses in the left, non-stimulated tectum. (E) Enucleated larvae expressing *elavl3:nls-GCaMP6s* were functionally imaged as described, and the functional cluster distribution of tectal cells was compared to untreated fish. Error bars are SEM. Functional cluster colors are described on the right. Scale bar in (D): 20 μ m.

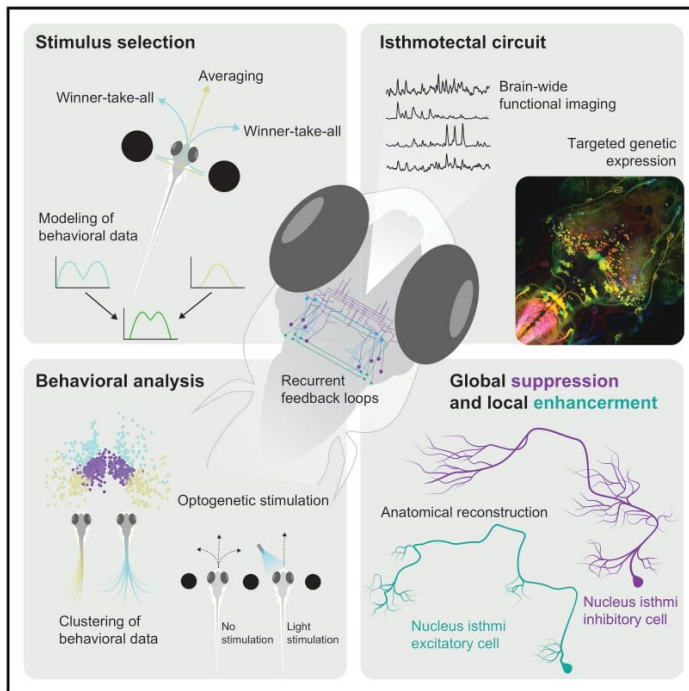
2.3 Neural circuitry for stimulus selection in the zebrafish visual system

António M. Fernandes, **Duncan S. Mearns**, Joseph C. Donovan, Johannes Larsch, Thomas O. Helmbrecht, Yvonne Kölsch, Eva Laurell, Koichi Kawakami, Marco dal Maschio, and Herwig Baier

This article was published in *Neuron* in March 2021 (Fernandes et al., 2021).

Neural circuitry for stimulus selection in the zebrafish visual system

Graphical Abstract



Authors

António M. Fernandes,
Duncan S. Mearns,
Joseph C. Donovan, ...,
Koichi Kawakami, Marco dal Maschio,
Herwig Baier

Correspondence

hbaier@neuro.mpg.de

In Brief

Fernandes et al. investigate how zebrafish larvae respond selectively to one of two stimuli competing for the animal's attention. Two strategies for stimulus selection are used: winner-take-all or averaging. The corresponding neuronal computations are implemented in an intricate system of feedback loops between tectum and nucleus isthmi.

Highlights

- Zebrafish respond to competing stimuli using winner-take-all and averaging strategies
- Retinotectal and isthmotectal circuits enable context-dependent stimulus selection
- Perturbing nucleus isthmi function disrupts behavioral action selection
- Isthmotectal circuit layout is consistent with local enhancement and global suppression

Fernandes et al., 2021, *Neuron* 109, 1–18
March 3, 2021 © 2020 Published by Elsevier Inc.
<https://doi.org/10.1016/j.neuron.2020.12.002>



Article

Neural circuitry for stimulus selection in the zebrafish visual system

António M. Fernandes,¹ Duncan S. Mearns,^{1,2} Joseph C. Donovan,¹ Johannes Larsch,¹ Thomas O. Helmbrecht,^{1,2} Yvonne Kölsch,^{1,2} Eva Laurell,¹ Koichi Kawakami,³ Marco dal Maschio,^{1,4} and Herwig Baier^{1,5,*}

¹Department Genes-Circuits-Behavior, Max Planck Institute of Neurobiology, 82152 Martinsried, Germany

²Graduate School of Systemic Neurosciences, LMU BioCenter, Grosshaderner Strasse 2, 82152 Martinsried, Germany

³Laboratory of Molecular and Developmental Biology, National Institute of Genetics, Department of Genetics, SOKENDAI (The Graduate University for Advanced Studies), Mishima, Shizuoka 411-8540, Japan

⁴Present address: Department of Biomedical Sciences, Padua Neuroscience Center, University of Padua, via Ugo Bassi 58B, 35131 Padua, Italy

⁵Lead contact

*Correspondence: hbaier@neuro.mpg.de

<https://doi.org/10.1016/j.neuron.2020.12.002>

SUMMARY

When navigating the environment, animals need to prioritize responses to the most relevant stimuli. Although a theoretical framework for selective visual attention exists, its circuit implementation has remained obscure. Here we investigated how larval zebrafish select between simultaneously presented visual stimuli. We found that a mix of winner-take-all (WTA) and averaging strategies best simulates behavioral responses. We identified two circuits whose activity patterns predict the relative salencies of competing visual objects. Stimuli presented to only one eye are selected by WTA computation in the inner retina. Binocularly presented stimuli, on the other hand, are processed by reciprocal, bilateral connections between the nucleus isthmi (NI) and the tectum. This interhemispheric computation leads to WTA or averaging responses. Optogenetic stimulation and laser ablation of NI neurons disrupt stimulus selection and behavioral action selection. Thus, depending on the relative locations of competing stimuli, a combination of retinotectal and isthmotectal circuits enables selective visual attention.

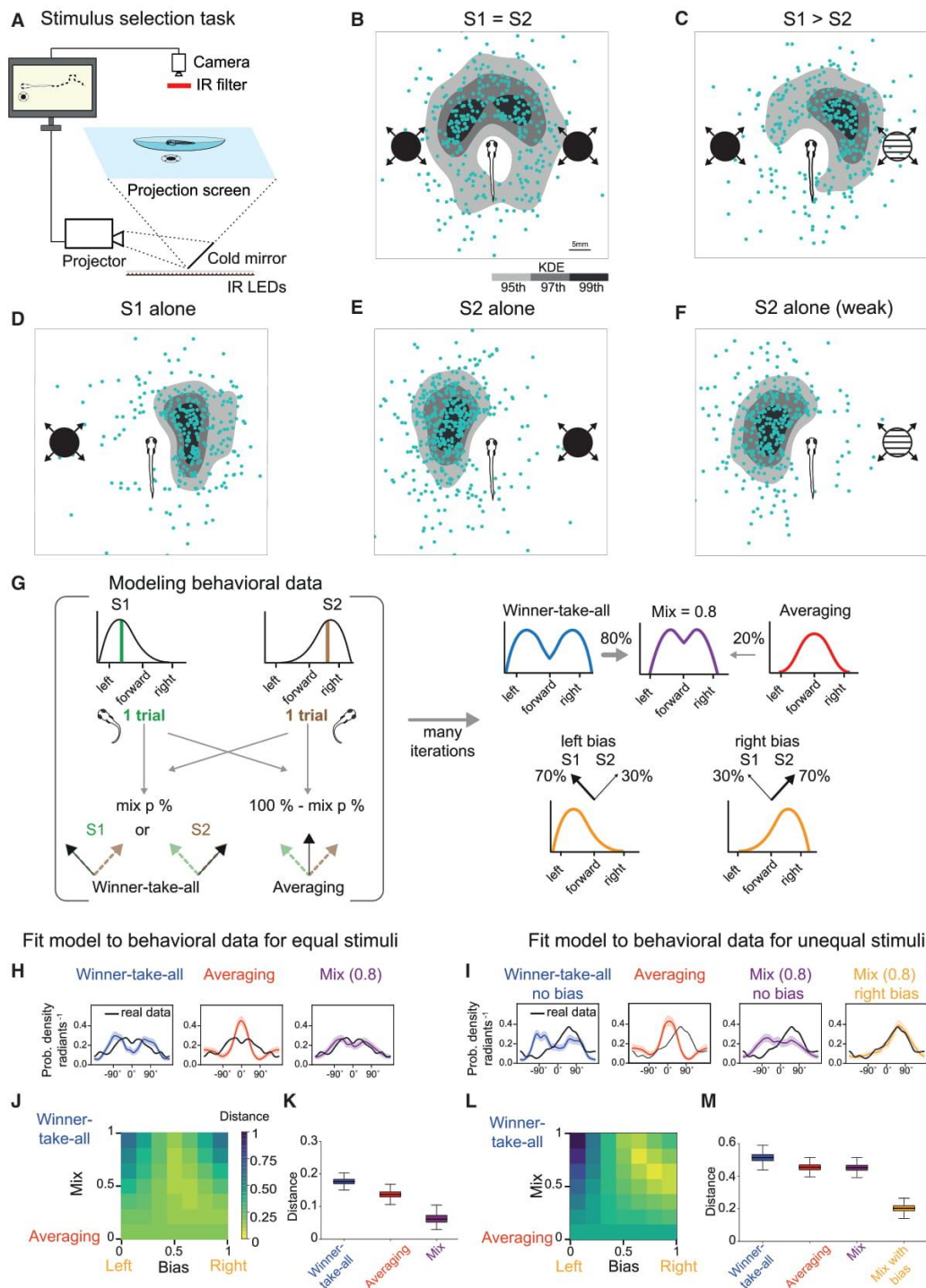
INTRODUCTION

When confronted with a crowded visual scene, animals often choose a single object for a behavioral response from multiple competing stimuli. Examples of such stimulus selection include escaping from the most imminent among several approaching threats or focusing on one individual prey item within a herd or shoal. Elementary forms of spatial attention exist in many species, including flies (Sareen et al., 2011), fish (Ben-Tov et al., 2015), and mice (Wang and Krauzlis, 2018). Winner-take-all (WTA) computations, in which an animal responds to a single target while disregarding others, are considered to be crucial during bottom-up, stimulus-driven attention (Itti and Koch, 2000). In addition to WTA mechanisms, evidence suggests that presentation of multiple visual targets in primates can also lead to gaze shifts toward their mean locations (Lisberger and Ferrera, 1997; Nummela and Krauzlis, 2011; Ottes et al., 1984). In contrast to the WTA strategy, this “averaging” mode suggests the existence of a neurocognitive process that integrates across competing sensory stimuli rather than selecting a single stimulus for a response.

It has been postulated that, during decision-making, multiple potential actions are represented in the brain and that these par-

allel representations compete against each other (e.g., Cisek, 2007). According to this view, the relative importance of targets across the visual field is represented in the brain through circuit mechanisms that focally enhance the response to the salient stimulus and globally suppress neuronal activity elsewhere (Ewert, 1997; Koch and Ullman, 1985; Lee et al., 1999). Such a “saliency map” appears to be implemented in the tectum/superior colliculus of vertebrates as distantly related as lampreys, goldfish, birds, and primates (e.g., Gruberg et al., 2006; Kardamakis et al., 2015; Knudsen, 2018; Krauzlis et al., 2018; Schellart et al., 1979; Zhaoping, 2016). Studies in the barn owl tectum suggest that stimulus competition could be supported by a neuronal circuit with reciprocal loops between the tectum and the nucleus isthmi (NI), a satellite nucleus, which is homologous to the parabigeminal nucleus of mammals and is located in the tegmentum (Knudsen, 2018). Evidence for this model has come mainly from single-cell electrophysiology and classical tract-tracing studies.

Here we investigated the behavioral decisions of zebrafish larvae when they are faced with two competing threatening stimuli. We found that escape direction is determined by WTA and averaging strategies, which are implemented to varying degrees by individual fish. Brain-wide two-photon functional imaging, targeted cell ablations, and optogenetic stimulation of identified



(legend on next page)

neuronal populations revealed two circuits impinging on the tectum that contribute to stimulus selection in a location-dependent manner. When both stimuli are presented to the same eye, the saliency computation is already detectable in the activity of retinal ganglion cell terminals in the tectum. When the two stimuli are presented to different eyes, an isthmotectal pathway, forming recurrent feedback loops between the NI and the tectum, weighs the relative stimulus strengths and is required for target selection across hemispheres. These results pinpoint neural circuitries for intra- and interhemispheric stimulus competition in a vertebrate visual system.

RESULTS

A WTA strategy predominates behavioral responses to competing stimuli

To identify the strategies adopted in response to competing stimuli, we established a stimulus selection paradigm for zebrafish larvae. We tracked individual larvae swimming freely in an arena using computer vision. Based on its location, visual stimuli were projected from below at defined positions relative to the animal's orientation (Figure 1A). The stimulus consisted of one or two looming disks of defined expansion rate and contrast. Dark expanding stimuli, mimicking an approaching predator or an object on a collision course, are strongly aversive for zebrafish and lead to a vigorous escape movement (Bhattacharyya et al., 2017; Dunn et al., 2016; Temizer et al., 2015). Single looming disks presented to one side of the fish were highly effective in driving an escape response to the opposite side (Figures 1D–1F and S1). Depending on the location and the strength of the stimulus, larvae adjusted the direction and magnitude of their response. Increasing the expansion rate or contrast of the stimulus resulted in a higher probability and greater vigor of escape responses (Figures S1A–S1E, S1I, and S1J). These observations confirm earlier studies that larval zebrafish adapt their behavior to the strength of a looming stimulus (Bhattacharyya et al., 2017).

Next we wanted to find out how larvae respond to two stimuli presented simultaneously at different locations. We dis-

played two looming stimuli to the same eye in non-overlapping parts of the visual field (Figure S2A), first alone and then in combination. A single looming disk positioned in the anterior visual field triggered a sideways escape ($82.5^\circ \pm 75$, mean \pm standard deviation [SD]) with respect to the heading direction; Figures S2B, S2E, and S2L), whereas a posteriorly located disk triggered a forward escape ($47^\circ \pm 41$ SD; Figures S2C, S2H, and S2L). For two identical stimuli, we expected either a stochastic choice or an escape trajectory corresponding to the average of the two locations. If the two stimuli differ, the more salient stimulus should dominate the response. In this case, the escape direction may still be a weighted average of the stimulus strengths. Both stimuli presented together yielded a distribution of escape angles that included the responses to single stimuli (Figures S2D and S2G). As expected by a WTA strategy, the faster of the two stimuli dominated the escape direction so that the mean response angle was similar to that triggered by a single stimulus presented at the same position (Figures S2F, S2I, and S2J–S2L).

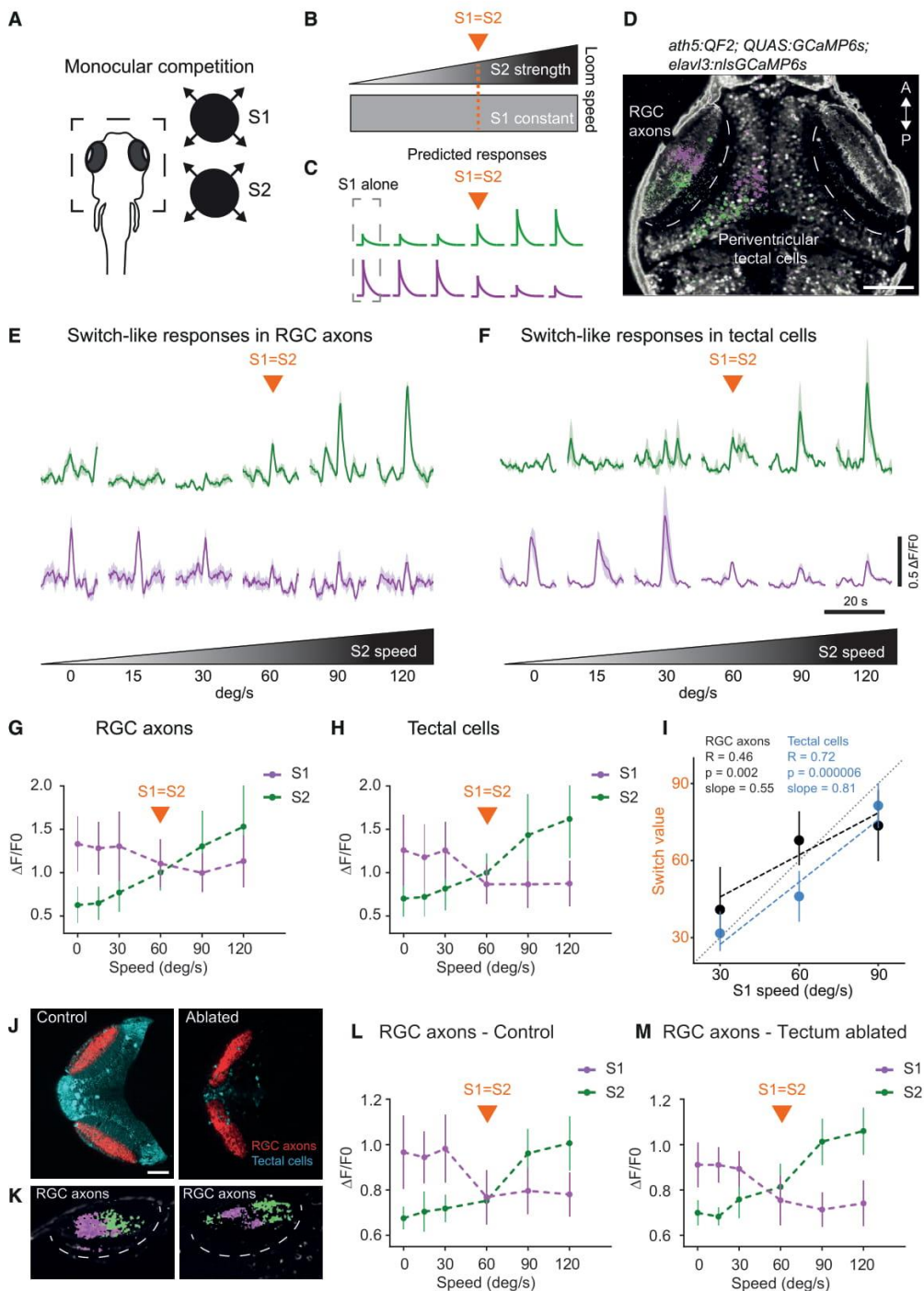
For two looming objects presented to opposite sides of the fish, we observed a bimodal distribution of escape trajectories. When the two disks expanded at identical rates, this distribution was largely symmetrical around the heading direction. Thus, larvae escaped in a direction away from one, apparently randomly chosen disk (Figures 1B and S1G). Modulating the expansion rate of one stimulus biased escapes away from the faster stimulus (Figures 1C and S1H). These observations indicate that larvae adapt the direction and magnitude of their behavioral response to the location and strength of the more salient stimulus.

Modeling reveals that fish larvae use a mixture of WTA and averaging strategies

Although WTA-mediated escapes comprise many responses (approximately 80%), a notable fraction of responses (approximately 20%) had a heading between the two stimuli, a behavior best explained by an averaging strategy. To estimate the relative contributions of each strategy, we fit the data with a model that

Figure 1. Zebrafish respond to competing stimuli according to their relative saliencies

- (A) Schematic of the stimulus selection task. The animal is tracked while updating, in real time, the positions of the looming disks projected from below.
- (B) Presentation of equal stimuli ($S1 = S2$, $90^\circ/s$). Blue dots are XY positions of fish after escape. In grayscale are kernel density estimation (KDE) isocontours of the same data. Fish schematics are enlarged for clarity.
- (C) Competition between unequal stimuli ($S1 > S2$, $90^\circ/s$ versus $60^\circ/s$).
- (D) Response to a single looming stimulus ($S1$ alone, $90^\circ/s$) presented on the left side of the fish.
- (E) Same stimulus presented to the right side of the fish.
- (F) Weaker stimulus ($S2$, $60^\circ/s$) presented on the right side.
- (G) Implementation of a WTA, averaging, and mixed strategy models to explain observed behavioral data. Mix adjusts the amount of WTA relative to averaging. Bias adjusts the probability of response for $S1$ versus $S2$ to accommodate unequal stimuli. A bias parameter equal to 0.5 corresponds to no bias left or right (50% chance of a fish selecting either of two looming stimuli).
- (H) Modeling of behavior for equal stimulus competition. Shaded areas are 95% confidence intervals (CIs).
- (I) Similar to (H) but for unequal stimuli.
- (J) Behavior reconstruction goodness of fit. Heatmap showing the normalized energy distance between model and real data (related to H) depending on the model parameters (bias and mix).
- (K) Boxplot quantification of model energy distance to the real data using resampling statistics. Permutation test p values that the mix model outperforms the simpler models are as follows: WTA, 0.0001; averaging, 0.008. For details, see STAR methods.
- (L) Similar to (J) but for unequal stimuli.
- (M) Similar to (K) but for unequal stimuli. Permutation test p values that the mix bias model outperforms the simpler models are $p < 0.001$ (WTA), $p < 0.001$ (averaging), and $p < 0.001$ (mix model).
- $n = 117$ fish.



(legend on next page)

mixed predictions from both behavioral strategies (Figure 1G). Models where WTA outweighed averaging provided a better fit for the behavioral data when stimuli had equal strengths (Figures 1H, 1J, 1K, S1K, and S1L). For unequal stimuli, we found that the fish responded more often to the faster looming disk. This asymmetry could be modeled by adding a bias term, where 0.5 is balanced and other values reflect asymmetry, to the WTA component of the model while keeping the same relative mixture of WTA and averaging (Figures 1L, 1M, S1M, and S1N).

Observing the responses of single animals revealed that individual larvae could switch between WTA and averaging strategies (Figure S1P). We conclude that both strategies are implemented in the same brain and are called up in a context-dependent manner. The exact conditions, experience, or internal states that bias the underlying circuits to choose the WTA over the averaging mode and vice versa are not known.

Tectal neurons exhibit WTA dynamics in response to competing stimuli

We next investigated the neural correlates of stimulus selection using brain-wide calcium imaging. First we determined which regions of the brain respond reliably to looming stimuli. Monocular presentation activated retinal ganglion cell (RGC) axons, the tectum, the pretectum, and a thalamic area near retinal arborization field 4 (AF4) (Heap et al., 2018; Temizer et al., 2015; Figure S3A). In addition, our recordings revealed a responsive area located at the midbrain-hindbrain boundary, a location that coincides with the expected position of the NI (Gruberg et al., 2006; Northmore, 1991; Northmore and Gallagher, 2003).

For implementation of a WTA strategy, at least two neuronal response types need to be present: (1) neurons whose activity scales with the strength of one stimulus and (2) neurons whose activity is suppressed by a more salient competitor (Knudsen, 2018). To search for these response signatures, we kept the expansion rate of one looming stimulus constant (S1) while systematically varying the expansion rate of a

competitor (S2) (Figures 2A–2C). We used transgenic fish expressing cytosolic genetically encoded calcium indicator GCaMP6s in RGCs and nucleus-localized GCaMP6s in all neurons. This approach enabled simultaneous recording and unambiguous separation of RGC axon activity in the tectal neuropil layers from tectal cell activity in the cell body layer. As expected, the activity elicited by monocular presentation of S1 and S2 was organized retinotopically, leading to non-overlapping response foci in the anterior or posterior tectal cells and neuropil, respectively (Figure 2D).

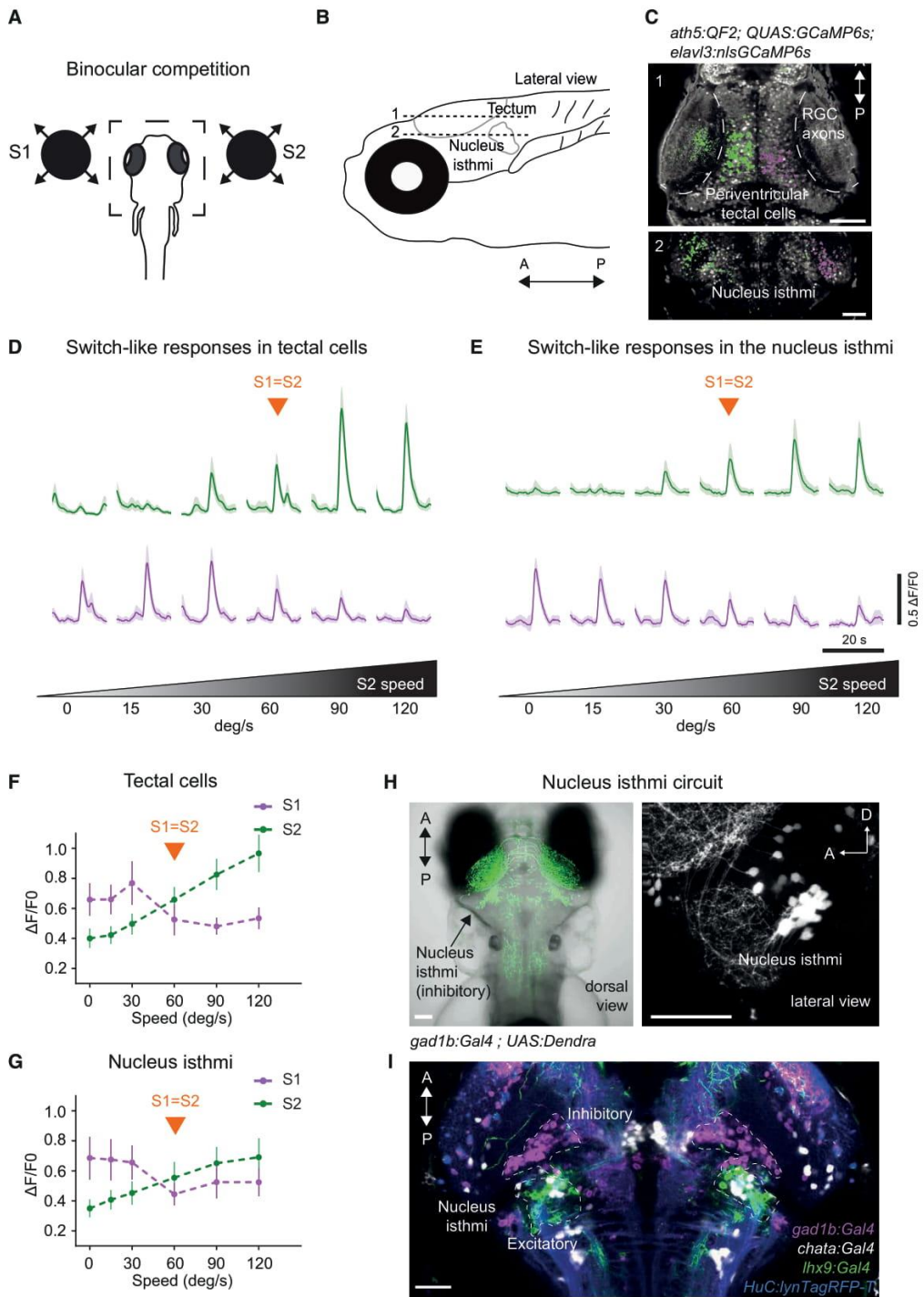
Presenting two competing stimuli to the same eye resulted in a variety of responses in the tectum. Some responses scaled with increasing S2 expansion rate (Figures 2F and 2H, green traces). On the other hand, a subset of S1-responsive tectal cells was suppressed when S2 was stronger or identical to S1 and enhanced when S2 was weaker than S1 (Figures 2F and 2H, magenta traces). This switch-like tuning is consistent with stimulus competition by reciprocal inhibition (Mysore and Knudsen, 2012). Thus, functional imaging revealed the presence of neurons in the tectum whose activity scales with the strength of one stimulus and neurons whose activity is suppressed by a salient competitor, consistent with the predictions of a WTA model.

Monocular WTA dynamics are implemented in the inner retina

For two looming stimuli visible to the same eye, we observed switch-like responses not only in tectal cells but already at the level of the RGC axonal projections to the tectum (Figures 2E and 2G). The switch transition for the population response was flexible and shifted systematically with the strength of S1 (Figures 2I and S3B–S3G). We noticed that tectal cells better predicted the switch value compared with RGCs (difference between correlations: Fisher's z -transformation $p = 0.039$; Figure 2I). We conclude that monocular stimulus competition manifests in reduced activity of RGC axons and is sharpened further in the tectum.

Figure 2. Activity of RGCs and tectal neurons exhibit switch-like responses during monocular competition

- (A) Schematic of the calcium imaging experiment. Right: monocular competition task. S1, stimulus 1; S2, stimulus 2.
- (B) Schematic of the competition protocol. The orange line represents the condition with presentation of equal stimuli (switch value).
- (C) Predicted responses following a strategy resembling WTA.
- (D) Pixel-wise regression analysis of the temporal series during a single imaging trial. The corresponding t -statistic for each pixel is calculated (only pixels that passed a threshold using the 90th percentile are shown). Map shows associated S1-responsive pixels suppressed by a stronger S2 (magenta) and pixels with enhanced responses as a function of S2 strength (green). Scale bar, 50 μ m.
- (E) Characteristic activity profiles for RGCs. Top traces, average of 10 RGC axon regions of interest (ROIs) enhanced by S2 (in green). Lower traces, average of 10 RGC axon ROIs suppressed by a stronger S2 (in magenta). The orange arrow represents the condition with presentation of equal stimuli (switch value).
- (F) Similar to (E) but for tectal cells.
- (G) Summary plot across all conditions for RGC axon pixels. Switch-like responses, showing RGC pixels suppressed by S2, are shown in magenta. RGC pixels enhanced by S2 are shown in green. The S1 expansion rate is 60°/s.
- (H) Similar to (G) but for tectal pixels.
- (I) Switch value increases with S1 strength for RGC axons and tectal cells. The R value is the correlation coefficient. The p value relates to testing whether the slope is zero. $n = 5$ fish.
- (J) Chemogenetic ablation of tectal cells does not affect suppression observed in RGC axons. The genotype used were *ath5:QF2*, *QUAS:GCaMP6s* (red), *SAGFF(LF)81C*, and *UAS:NTR-mCherry* (cyan). Left: control fish. Right: ablated fish. Scale bar: 100 μ m.
- (K) Pixel-wise regression analysis of the temporal series during a single imaging trial. The corresponding t -statistic for each pixel is calculated as in (D). The map shows associated S1-responsive pixels suppressed by a stronger S2 (magenta) and pixels that enhance their responses as a function of S2 strength (green). Left panel: control fish. Right panel: ablated fish.
- (L) Summary plot across all conditions for RGC axon pixels. Switch-like responses, showing RGC pixels suppressed by S2, are shown in magenta. RGC pixels enhanced by S2 are shown in green. The S1 expansion rate is 60°/s. Control fish. $n = 4$ fish.
- (M) Similar to (L) but for ablated fish. $n = 5$ fish. Error bars indicate SD.



(legend on next page)

To test whether RGC modulation was due to feedback from the tectum (Henley et al., 1986), we imaged GCaMP6s-labeled retinal axon terminals following chemogenetic ablation of nitroreductase-expressing tectal neurons (Figures 2J, 2K, and S4J). Treatment with the cell-death-inducing pro-toxin metronidazole led to severe impairments in behavioral responses to looming and prey stimuli (Figures S4D–S4G). Switch-like responses of RGCs, however, remained intact (Figure 2L and 2M; $p = 0.1797$, two-way Mann-Whitney test). These results indicate that stimulus competition already shapes neuronal responses in the inner retina and does not require retrograde modulation by tectal cells.

Retinotectal WTA is a general mechanism for stimulus selection independent of valence

Synthetic prey-like objects have been shown previously to evoke hunting behavior in zebrafish larvae (Bianco et al., 2011; Semmelhack et al., 2014). We tested whether the WTA dynamics observed in response to two looming disks extend to the response to two small, motile dots that simulate prey. As with looming stimuli, RGC axons and tectal responses showed suppression and enhancement driven by competing prey-like stimuli (Figures S4A–S4C). Such a mechanism might serve efficient target selection during hunting against a background of distractors. This finding indicates that stimulus competition in the retinotectal system is a global mechanism, not restricted to looming stimuli, and guides diverse natural behaviors.

Tectal and isthmic neurons show WTA responses to competing binocular stimuli

Based on previous work in birds, the NI is a prime candidate for shaping tectal responses to binocular competing stimuli (Figure 3A). Indeed, in response to concurrent stimuli presented to each eye, we observed WTA dynamics in both tectal hemispheres and the NI (Figures 3B and 3C). The activity patterns of left and right hemispheres were unbalanced; when one tectal hemisphere had high activity, the other hemisphere had low activity, mirroring the relative strengths of the stimuli (Figures 3C–3E). Similar to monocular competition, we found S1-responsive neurons that were inhibited by a stronger S2 and stimulus-selective neurons that enhanced their response as a function of either S1 or S2 intensity (Figures 3D–3G). This switch-like suppression

and enhancement matched our predicted WTA signature and thus identifies a neural correlate of interhemispheric spatial attention.

To characterize the cellular composition of the NI, we used transmitter-specific Gal4 lines, RNA *in situ* hybridization, and immunohistochemistry to label glutamatergic (*vglut2a* and *lhx9*), cholinergic (choline acetyltransferase, ChAT), and GABAergic neurons (Figures 3H, 3I, and S5). Co-registration of these lines and markers within a standard brain (Kunst et al., 2019) revealed that the glutamatergic and GABAergic populations form two spatially segregated clusters close to the midbrain-hindbrain boundary (Figure 3I). A small subset of *lhx9*-positive, glutamatergic neurons co-express ChAT (Figures S5F). NI cells express known marker genes for the isthmic region, e.g., Reelin (Figure S5; Volkman et al., 2010) and project mainly to the tectum (Figure 3H, right panel). The vast majority of GABAergic and glutamatergic NI neurons labeled in the lines used here respond to looming stimuli; only a small fraction to prey-like or dimming stimuli (Figures S6A and S6D). Functional imaging during binocular competition revealed that glutamatergic and GABAergic NI populations displayed switch-like activity (Figures S6B and S6E). However, only glutamatergic neuronal activity scaled significantly with the strength of the distractor S2 (Figures S6G–S6K). These data suggest that NI neurons show responses compatible with their function in generating a saliency map.

Inhibition of the NI reduces the number of WTA behavioral responses

Next we wanted to identify the functional role of the NI in generating behavioral responses to competing looming stimuli. To this end, we developed a restrained preparation that allowed us to selectively activate or inhibit the NI while presenting looming stimuli to both eyes (Figure 4A). In the absence of visual stimulation, we found that optogenetic activation of *lhx9*-positive NI neurons using ChR2 was more than twice as likely to induce swimming behavior compared with ChR2– controls (ChR2+, response probability = 0.44 ± 0.34 , $n = 21$ fish; control, response probability = 0.19 ± 0.17 , $n = 18$; mean \pm SD; $p = 0.0217$; Figure 4B). Inhibition of the same NI population using GtACR2 neither increased nor suppressed swimming responses to the light (response probability = 0.21 ± 0.14 , $n = 9$, $p = 0.189$

Figure 3. WTA dynamics in tectal and isthmic neurons in response to competing binocular stimuli

(A) Binocular competition task.
(B) Anatomical location of the tectum (plane 1) and the NI (plane 2).
(C) Pixel-wise regression analysis during a single imaging trial. The *t*-statistic for each pixel is calculated as in Figure 2D. Map 1 shows associated S1-responsive tectal pixels suppressed by a stronger S2 stimulus (in magenta). Pixels that enhance their response as a function of S2 intensity are shown in green. Map 2: similar to Map 1 but for the NI. Scale bars, 50 μ m.
(D) Characteristic activity profiles for tectal cells. Top traces, average of 10 tectal ROIs enhanced by S2 (green). Lower traces, average of 10 tectal ROIs suppressed by a stronger S2 stimulus (magenta).
(E) Similar to (D) but for NI.
(F) Summary plot across all conditions for tectal pixels. Switch-like responses, showing pixels suppressed by S2, are shown in magenta. Pixels enhanced by S2 are shown in green. $n = 5$ fish.
(G) Similar to (F) but for NI. $n = 4$ fish. Error bars indicate SD.
(H) Dorsal image of a double-transgenic *gad1b:Gal4VP16^{mpn155}; UAS:Dendra-kras^{s1998t}* fish, labeling GABAergic neurons in green. The arrow indicates the location of GABAergic NI neurons. Right panel, lateral view of *gad1b:Gal4VP16^{mpn155}; UAS:nfsb-mCherry^{c264}* fish, labeling GABAergic neurons in white.
(I) Alignment of several transgenic lines: *gad1b:Gal4VP16^{mpn155}* labeling GABAergic NI neurons (magenta), *lhx9:Gal4VP16^{mpn203}* labeling *lhx9*-positive NI neurons (green), and *chata:Gal4VP16^{mpn202}* labeling cholinergic NI neurons (white). *elav3:lyn-tagRFP^{mpn404}* is used as a reference channel (blue). Scale bars, 50 μ m.

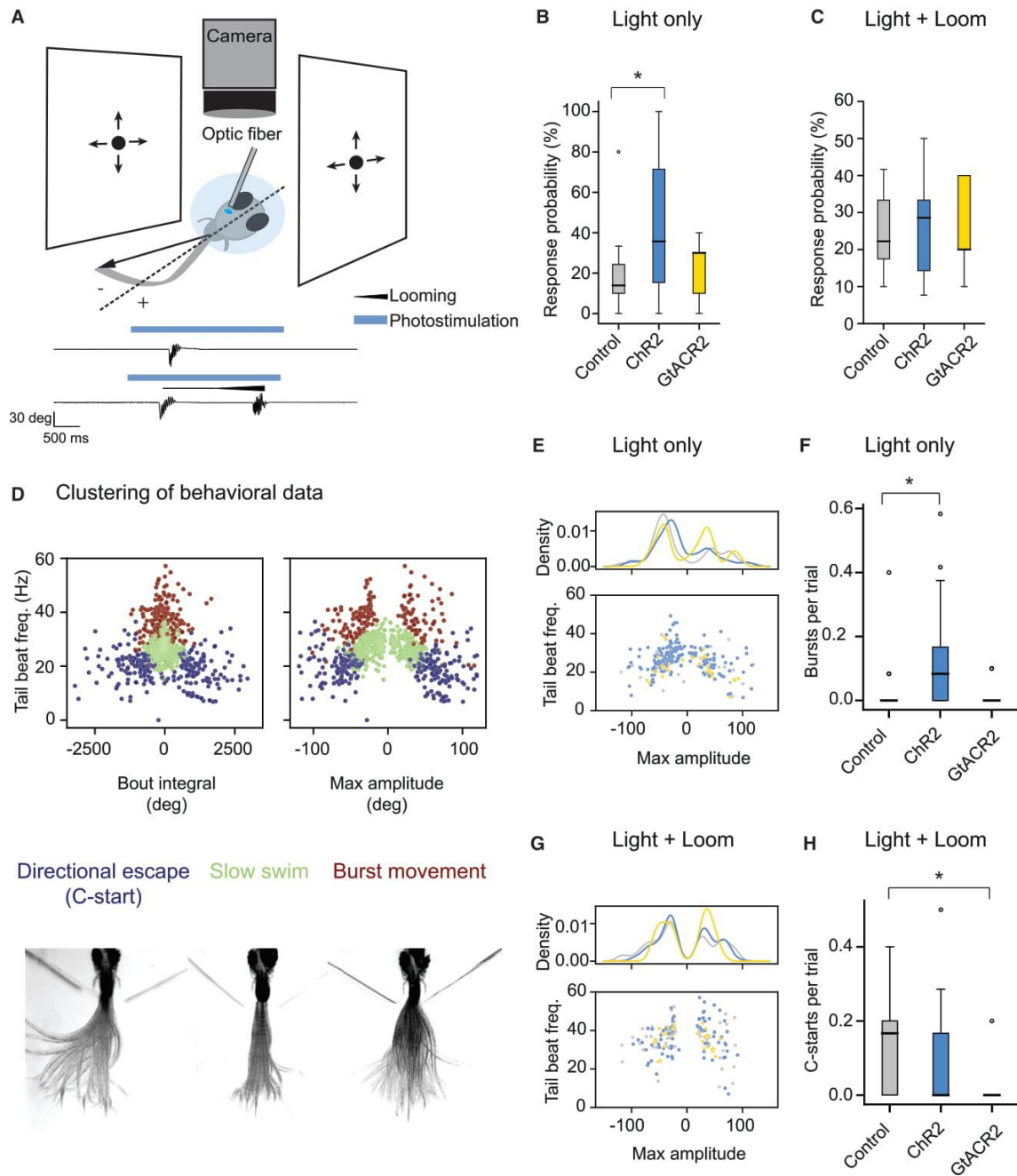


Figure 4. Optogenetic manipulation of the NI during presentation of competing binocular looming stimuli

(A) Schematic of the optogenetics setup. A fish is embedded in agarose with the tail free. The tail is recorded with a camera. Equal looming stimuli are presented to both eyes simultaneously. NI is stimulated unilaterally with an optical fiber. Negative angles represent tail deflections toward the stimulated side, and positive angles represent tail deflections away from the stimulated side. Bottom: example trials from a fish expressing Chr2 in the NI. Shown are photostimulation only (top) and photostimulation with looms (bottom). Black traces show tail angle over time. The blue bar represents time of optogenetic stimulation. The black line above the tail trace triangle represents the duration of loom.

(legend continued on next page)

compared with controls). Notably, we found that neither excitation nor inhibition of *lhx9*-positive cells in the NI affected the probability of responding to looming stimuli (response probabilities = 0.24 ± 0.10 , controls; 0.26 ± 0.12 , ChR2+; 0.27 ± 0.11 , GtACR2+) (Figure 4C). These results demonstrate that activity within the excitatory cells of the NI is sufficient to drive behavioral responses.

We next sought to identify what kinds of swim bouts larvae performed in response to optogenetic and visual stimulation. We identified all bouts in the dataset, including light-evoked, looming-evoked, and spontaneous bouts that occurred outside the stimulation period ($n = 881$ bouts total) and characterized each bout based on three kinematic parameters (bout integral, maximum tail amplitude, and tail beat frequency). We then performed hierarchical clustering in this kinematic space and identified three primary bout types (Figure 4D; STAR Methods). C-starts were characterized by a large maximum tail amplitude and large bout integral (Burgess and Granato, 2007; Figure 4D, blue cluster). Burst swims exhibited a high tail beat frequency and were symmetric across the midline (Budick and O'Malley, 2000; Figure 4D, red cluster). Slow swims exhibited relatively small values across all three parameters (Figure 4D, green cluster). These slow swims appeared to encompass routine turns and slow 1 and slow 2 swims described previously (Marques et al., 2018). We found that activation of the NI in the absence of visual stimuli predominantly drove slow swims that were biased ipsilaterally to the stimulation site (Figure 4E). Interestingly, we were also able to elicit a small but significant number of burst swims in multiple animals (ChR2+, number of swims = 0.13 ± 0.16 per trial; control, number of swims = 0.03 ± 0.09 ; mean \pm SD; $p = 0.0026$; Figure 4F). These results suggest that the NI is sufficient to release fast forward swimming as well as slow orientation behaviors.

Finally, we investigated the bouts fish performed in response to competing looming stimuli. In control animals not expressing any optogenetic effector, we found evidence of WTA (C-starts) and averaging (burst swims) behavioral dynamics, consistent with our observations from free-swimming larvae (Figure 1). In this restrained preparation, we found that an averaging response was more likely than WTA (0.44 ± 0.34 burst swims per loom, 0.12 ± 0.12 C-start per loom, mean \pm SD). Surprisingly, we found that, even though NI stimulation in isolation was sufficient to drive burst swims, we were unable to drive additional burst swims in response to competing looms upon ChR2 stimulation (0.50 ± 0.33 per loom, $p = 0.21$ compared with controls). This

may be a result of a ceiling effect, with averaging strategies already dominating in this behavioral paradigm, or due to optogenetic stimulation being insufficient to override innate responses to looming stimuli (Klapoetke et al., 2017). Inhibition of *lhx9*-positive NI cells during the presentation of looming stimuli, however, decreased the number of C-starts elicited by around 80% (0.02 ± 0.06 C-starts per trial, $p = 0.020$ compared with controls) (Figure 4H). Neither excitation nor inhibition of the NI biased the direction of elicited C-starts (Figure 4G), suggesting that the direction of an escape is not determined by the activity in one nucleus in isolation. These results suggest that the NI plays an instructive role in generation of behavior in response to competing looming stimuli, contributing to averaging and WTA strategies.

Optogenetic activation of excitatory NI cells leads to predominantly WTA dynamics in the tectum

We next wanted to find out how optogenetic manipulation of the NI affects tectal dynamics. We combined multiplane functional imaging and cell-resolution optogenetic perturbations with two-photon computer-generated holographic (2P-CGH) photostimulation (Dal Maschio et al., 2017; Figure 5A). In the absence of visual stimulation, optogenetic activation of ChR2-expressing *lhx9*-positive neurons in the NI induced activity in the tectum that resembled WTA (one tectum with more cells being active, opto-activation index less than -0.25 or more than 0.25) and averaging dynamics (both tecta with almost equal numbers of active cells, opto-activation index between -0.25 and 0.25) (Figures 5B–5E). Detectable calcium signals in tectal cells after unilateral stimulation of *lhx9*-positive NI cells were evident in 9% of the trials, with the majority of successful trials leading to WTA dynamics (Figure 5B). Notably, our stimulation protocol resulted in stochastic tectal activity, with different cells in the tectum activated each time and left or right tectal activity dominating each trial. Such a variable response mirrors the behavior and suggests that, although the NI directly influences tectal activity, the effect may be mediated by a heterogeneous population interacting with the ipsilateral and contralateral tectum.

Next we wanted to find out how the NI contributes to tectal processing of looming visual stimuli. To investigate involvement of the NI in looming-evoked responses, we imaged activity in the NI and tectum in response to a single looming stimulus while optogenetically activating small subsets (8–10 cells) of excitatory *lhx9*-positive neurons in the NI (Figure 5F). This pairing of visual stimulation with photostimulation of the NI resulted in the

(B) Probability that fish perform a swim bout in response to photostimulation under control (gray), ChR2+ (blue), and GtACR2+ (yellow) conditions. ChR2 and GtACR2 animals express ChR2-mCherry or GtACR2-YFP in excitatory *lhx9*-positive cells of the NI. Control animals express no optogenetic actuator.

(C) Probability that fish perform a swim bout when simultaneously presented with looming stimuli to each eye and the NI is stimulated unilaterally.

(D) Hierarchical clustering of swim bouts. Identified types are directional C-start escapes (blue), slow swims (green), and burst swims (red). Bottom: overlay of frames from representative bouts belonging to each of the three clusters.

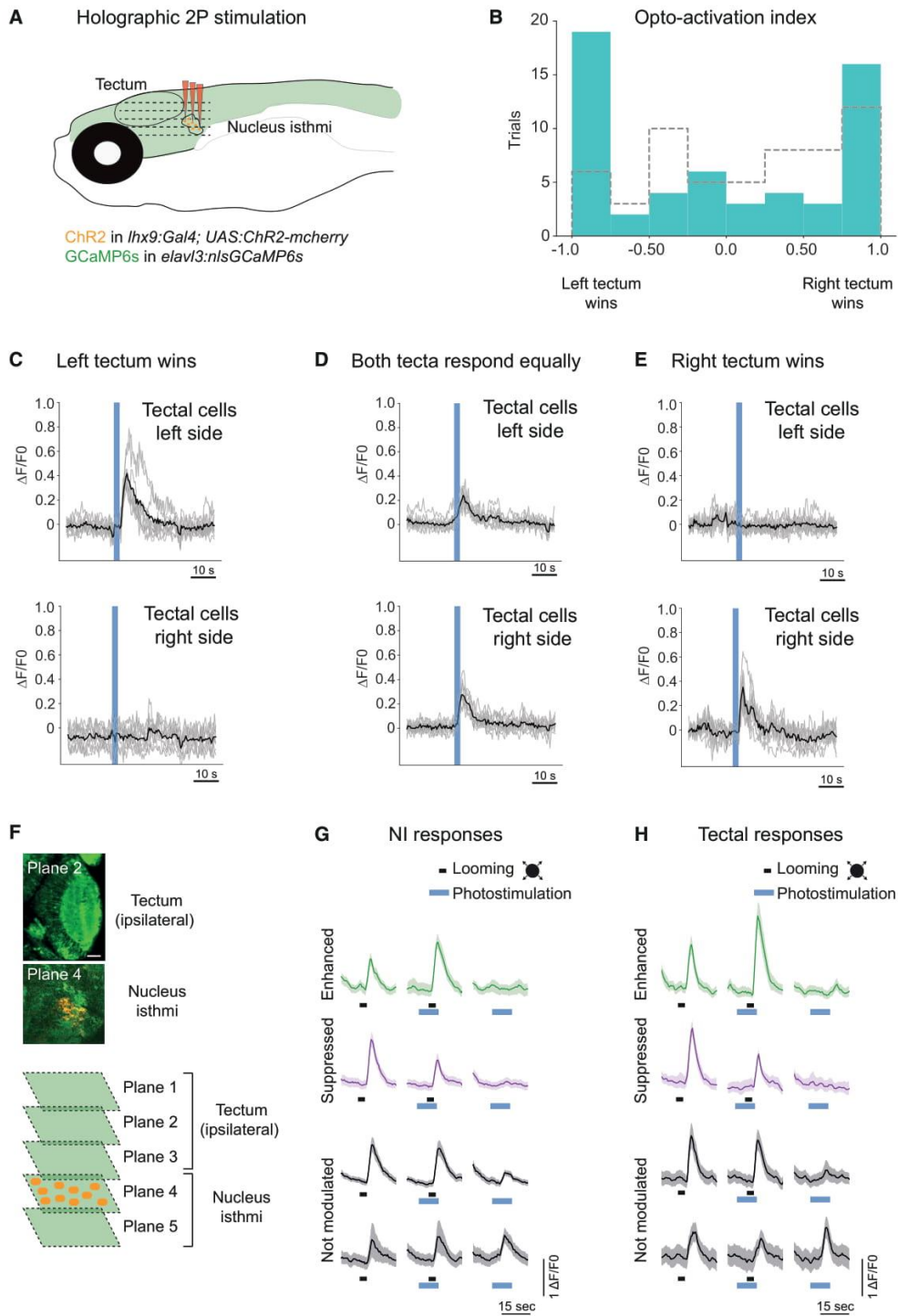
(E) Tail beat frequency plotted against maximum tail amplitude for light-evoked bouts across all conditions. Density indicates the KDE over the maximum amplitude. Bouts evoked in ChR2+ fish (blue) are of lower amplitude compared with controls ($p = 0.043$, Kolmogorov-Smirnov test).

(F) Average number of burst swims evoked per trial in response to light stimulation across fish.

(G) As in (E) except for bouts evoked by presentation of equal looms to the two eyes during optogenetic stimulation. Distributions are not significantly different between control and optogenetic conditions ($p > 0.05$, Kolmogorov-Smirnov test).

(H) Average number of C-starts (WTA responses) evoked per trial in response to equal looms presented to the two eyes during simultaneous stimulation of the NI across fish.

Control fish, $n = 18$; ChR2+, $n = 21$; GtACR2+, $n = 9$.



(legend on next page)

modulation of tectal and NI neurons (Figures 5G and 5H). Interestingly, individual cells in the ipsilateral tectum increased or decreased their stimulus-evoked activity upon activation of the NI (Figures 5G, 5H, and S7A–S7F). Thus, the nature of the excitatory modulation of looming stimuli can be facilitatory and suppressive, providing further evidence for heterogeneity within the *hmx9*-positive NI population.

Ablation of specific NI cells disrupts behavioral responses to looming stimuli to both sides

We next tested the effects of ablating the NI on neural activity and behavior. Our optogenetics results suggest that such an experiment should disrupt responses to looming stimuli to both sides. Supporting this hypothesis, we observed that unilateral two-photon ablation of the GABAergic NI population with ultrashort laser pulses (Figure 6A) caused a deficit in looming-evoked escape responses to either side (Figures 6B and 6C). Similarly, animals with unilateral ablation of excitatory *hmx9*-positive NI neurons showed a significant reduction in escape responses (Figures 6D and 6E) compared with sham ablated animals (Figures S8A–S8D). Such a bilateral effect on escape responses from unilateral ablation is consistent with our optogenetic manipulations, which were unable to bias the directions of escapes in an acute manipulation (Figure 4G) and provides further evidence of a binocular computation implemented within the NI.

Hunting behavior, as measured by eye convergence, bout rate, and prey detection rate, was only mildly affected in NI-ablated fish (Figures S8G–S8L). J-turns, which fish use to orient toward prey that are lateral in the visual field, were intact after ablation of NI cells (Figures S8M–S8R). Optomotor response was intact by ablation of glutamatergic or GABAergic NI cells (Figures S8E and S8F). These controls indicate the specificity of the manipulation and suggest the existence of dedicated circuits for selecting stimuli of different valence.

NI cells are required to specifically activate looming responses in both tectal hemispheres

Next we imaged tectal cell activity (periventricular neurons) following ablation of NI cells. First we wanted to find out whether such treatment generally affected the processing of visual stimuli across tectal hemispheres. We stimulated one eye with a looming stimulus as well as with control stimuli, including prey and

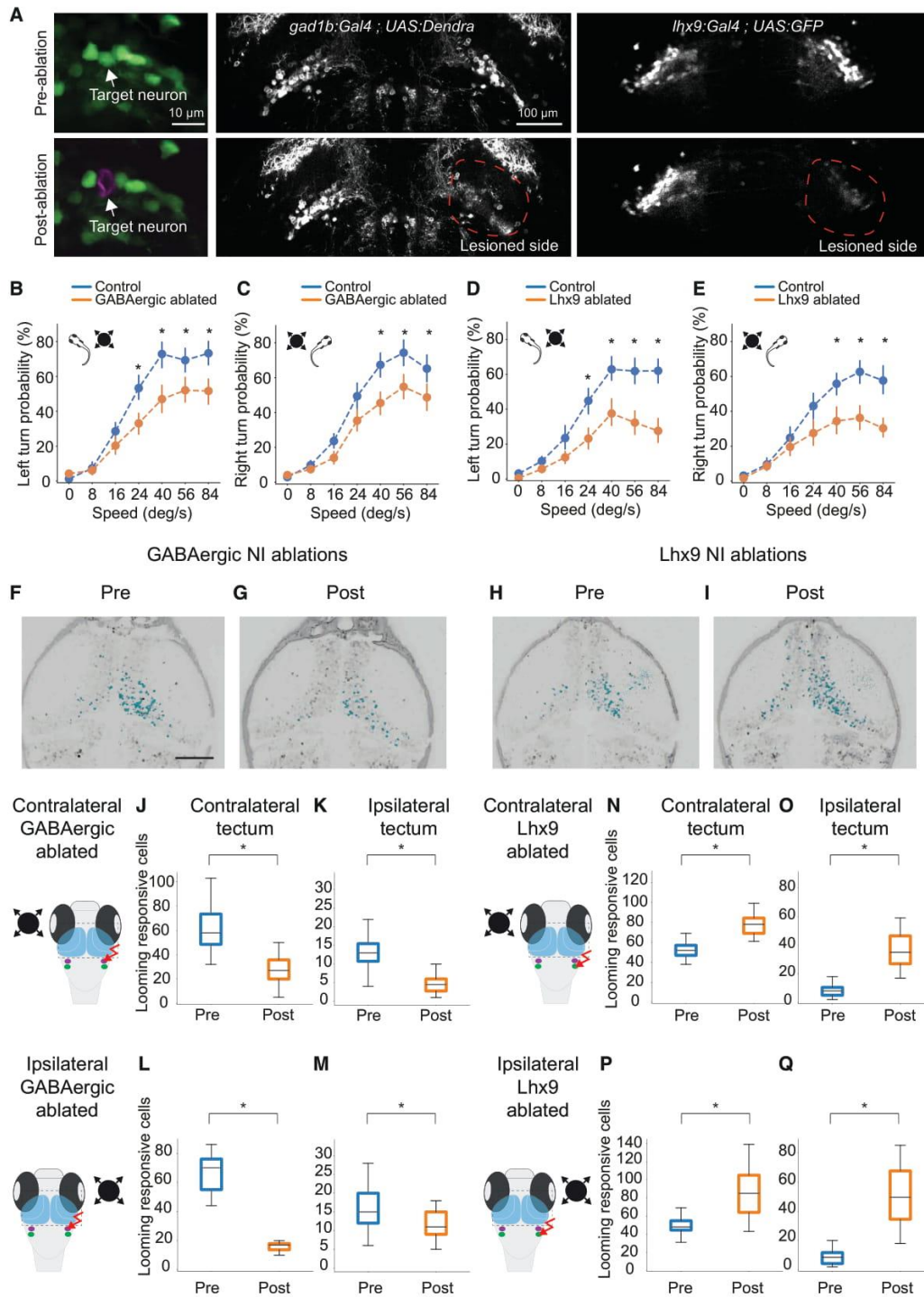
dimming. Unilateral ablation of GABAergic NI cells decreased looming responses in both tecta (Figures 6F, 6G, 6J, 6K, S9D, and S9E), whereas prey-like and dimming responses were unaffected (Figures S9L and S9M). These results match our observation that 90% of GABAergic-positive cells in the NI respond to looming stimuli and only a small percentage to prey-like (1%) and dimming (9%) stimuli (Figure S6D). We also observed a general decrease in the number of looming-responsive cells in both tecta during stimulation of the eye ipsilateral to the ablated NI (Figures 6L, 6M, S9H, and S9I). In contrast, ablation of *hmx9*-positive glutamatergic NI neurons bilaterally increased responses to looming (Figures 6H, 6I, 6N, 6O, S9F, and S9G) but not prey-like and dimming stimuli (Figures S9N and S9O), again matching the distribution of responsive cells (Figure S6A). Visual stimulation of the eye ipsilateral to the *hmx9* ablation also increased looming responsive cells in both tecta (Figures 6P, 6Q, S9J, and S9K). These results match the behavioral phenotypes we observed; unilateral ablation of excitatory or inhibitory NI neurons leads to bilateral and loom-specific deficits in neuronal responses, altering the weighted integration of visual stimuli across hemispheres, with concomitant bilateral effects on behavioral output. This modulation supports a role of the NI in binocular stimulus competition. Our data demonstrate involvement of NI cells in WTA and averaging dynamics and context-dependent functional connectivity between the NI and tectum.

Tecto-isthmical and isthmotectal projections form interhemispheric loops

To identify the neural circuit architecture underlying NI-mediated interhemispheric stimulus selection, we acquired a dataset of stochastically labeled, single-cell morphologies and co-registered these neurons in a standard brain atlas (Kunst et al., 2019). Co-alignment of tectal projection neurons (Helmbrecht et al., 2018) revealed that the axons of intertectal and tectobulbar neurons frequently innervate the neuropil regions of the NI (Figures 7A–7D and S10A–S10C). We noticed that, although tectobulbar axon collaterals appear to span the excitatory and inhibitory neuropil regions of the ipsilateral NI, intertectal neurons preferentially innervate the excitatory NI neuropil on both sides of the brain (Figures S10A–S10C). Thus, in the tecto-isthmical direction, there are neurons that project only ipsilaterally to the NI and extend to the hindbrain reticular formation

Figure 5. Optogenetic activation leads to WTA and averaging activity dynamics and modulates tectal responses to looming stimuli

- (A) Schematic of the holographic optogenetics experiment.
- (B) Opto-activation index. Unilateral optogenetic activation of *hmx9*-positive isthmical neurons (right side) leads to WTA and averaging activity in the tectum (in blue). The opto-activation index is calculated as follows: $(\text{responsive cells right tectum} - \text{responsive cells left tectum}) / (\text{responsive cells right tectum} + \text{responsive cells left tectum})$. Opto-index distribution for the control condition (ChR2 negative fish) is shown in gray. Distributions are significantly different ($p = 0.038$, two-sided Kolmogorov-Smirnov test).
- (C) Example of 10 cells from each tectum in a trial where the left tectum “won” (WTA). The black line shows mean response for all cells. Gray traces show individual cell activity.
- (D) Similar to (C) but for a trial where both tecta were equally active (averaging).
- (E) Similar to (C) and (D) but a trial where the right tectum “won” (WTA).
- (F) Activation of specific *hmx9*-positive isthmical neurons expressing Channelrhodopsin (ChR2; orange), combined with volumetric imaging of ipsilateral tectal responses (GCaMP6s, green). Up to five planes, including the tectum and NI region, were recorded simultaneously.
- (G) Photostimulation of *hmx9*-positive isthmical neurons. Some of the isthmical looming-evoked responses are unaffected by optogenetic stimulation (in gray), whereas others are either suppressed (magenta) or enhanced (green). Examples of averages of 10 cells are shown for each response type. Shaded areas represent SD.
- (H) Similar to (G) but for tectal cells.



(legend on next page)

as well as neurons that project bilaterally to the NI in both hemispheres.

To survey isthmotectal connections, we reconstructed single NI cells and traced their projections (Figures 7E–7H and S10E). We found bilateral projections from individual NI cells to both tecta. We identified three classes of glutamatergic neuronal projection types (Lhx9 classes I, II, and III). Excitatory neurons project to the ipsilateral and/or contralateral tectum and connect the two hemispheres via the postoptic commissure (Figures 7E and 7F). Lhx9 class I cells project first from the NI to the ipsilateral and then to the contralateral tectum (Figures 7E). We found class I cells that arborize mainly either in the ipsilateral or the contralateral side (Figure 7I). Lhx9 class II cells project first to the contralateral glutamatergic NI neuropil, with arborizations reaching the pretectum, thalamus, and a neuropil region close to the contralateral semicircular torus and tectum. These neurons then re-cross the midline and innervate the other hemisphere (Figures 7F and 7J). Lhx9 class III cells target only the ipsilateral thalamic region (Figure S10D).

We also identified two classes of GABAergic NI neurons (GABAergic classes I and II). GABAergic class I cells project to ipsilateral and contralateral tecta, crossing the midline via a dorsal commissure near the skin (Figure 7G). GABAergic class II cells project to the ipsilateral tectum only (Figure 7H). Our single-cell reconstructions reveal an intricate system of excitatory and inhibitory feedback loops that support interhemispheric computations.

Isthmotectal axon arborization patterns support focal excitation and broad inhibition

A common model of stimulus selection implementing WTA selection postulates the existence of localized enhancement of responses to a salient stimulus and widespread suppression of responses to background distractors. Consistent with this hypothesis, we found that glutamatergic NI neurons arborize

focally in the tectum (Figure S10F); their mean axonal innervation length in the tectum is 196 μm , with an average of 6 branches per arbor. GABAergic class II NI neuron arborization length in the tectum is also limited, with a mean length of 319 μm and on average of 18 branches per arbor. In contrast, arborizations of GABAergic class I NI neurons projecting to both tecta are, on average, five times larger than excitatory NI neurons: 969 μm in length and 39 branches per arbor ($p = 9.64 \times 10^{-4}$ for length and $p = 3.08 \times 10^{-3}$ for number of branches; Figure S10G). The layout of the isthmotectal system thus fulfills the predictions of the local enhancement/global suppression model of WTA dynamics across both hemispheres.

DISCUSSION

An animal's ability to respond to a single stimulus in a crowded visual scene is an ancestral form of selective attention (Krauzlis et al., 2018). In bottom-up, stimulus-driven attention, the saliency of a stimulus is compared with that of other stimuli in the scene, producing targeted behavioral responses. Determining the behavioral strategies, neurophysiological dynamics, as well as circuit motifs that mediate stimulus selection is key to understanding how animals allocate attentional resources and make behavioral decisions. Here we find evidence of stimulus selection in retinotectal and isthmotectal circuits. Our results support a model in which retinotectal circuits underlie monocular stimulus selection, whereas a newly discovered isthmotectal loop mediates binocular competition. Our findings are summarized schematically in Figure 8.

Stimulus selection is already evident from behavioral observations. When freely swimming fish encounter two looming disks, each able to trigger an escape response on its own, they escape from one randomly chosen stimulus in the majority of cases. In the remaining trials, the fish appear to average the locations of

Figure 6. Unilateral ablation of NI cells modulates looming-evoked responses bilaterally

(A) 2P laser ablation of isthmic neurons. Shown is an example of single cell ablation (left panels). After ablation of a cell, red fluorescence (magenta) is visible in the target spot. The center panels show representative images of unilateral 2P laser ablation of GABAergic-positive isthmic neurons in *gad1b:Gal4VP16^{mpn155}; UAS:Dendra-kras^{S199R}* pre-ablation and post-ablation. Right panels: ablation of glutamatergic isthmic neurons in *lhx9:Gal4VP16^{mpn203}; UAS:EGFP* pre-ablation and post-ablation.

(B) Probability of left escapes in control (blue) and GABAergic NI-ablated fish (orange).

(C) Similar to (B) but for right escapes.

(D) Probability of left escapes in control (blue) and *lhx9* NI-ablated fish (orange).

(E) Similar to (D) but for right escapes. For all looming-evoked escape panels, error bars represent SD. $n = 12$ for control fish (blue). $n = 15$ for ablated fish (orange). * $p < 0.05$, Tukey's honestly significant difference (HSD) test.

(F and G) Example of the effect of unilateral ablation of the GABAergic-positive NI on the right hemisphere. (F) is before ablation and (G) is after ablation. The corresponding t -statistic for each pixel is calculated for looming-responsive cells and labeled in cyan.

(H and I) Example of the effect of unilateral ablation of the *lhx9*-positive NI on the right hemisphere before (H) and after (I) ablation.

(J) Number of looming-responsive cells in the contralateral (relative to looming stimulus) tectum before and after ablation of GABAergic-positive NI cells in the right hemisphere. $n = 4$.

(K) Number of looming-responsive cells in the ipsilateral (relative to looming stimulus) tectum.

(L) Number of looming responsive cells in the contralateral tectum (relative to looming stimulus) for the intact hemisphere before and after ablation of GABAergic-positive NI cells in the right hemisphere. $N = 2$.

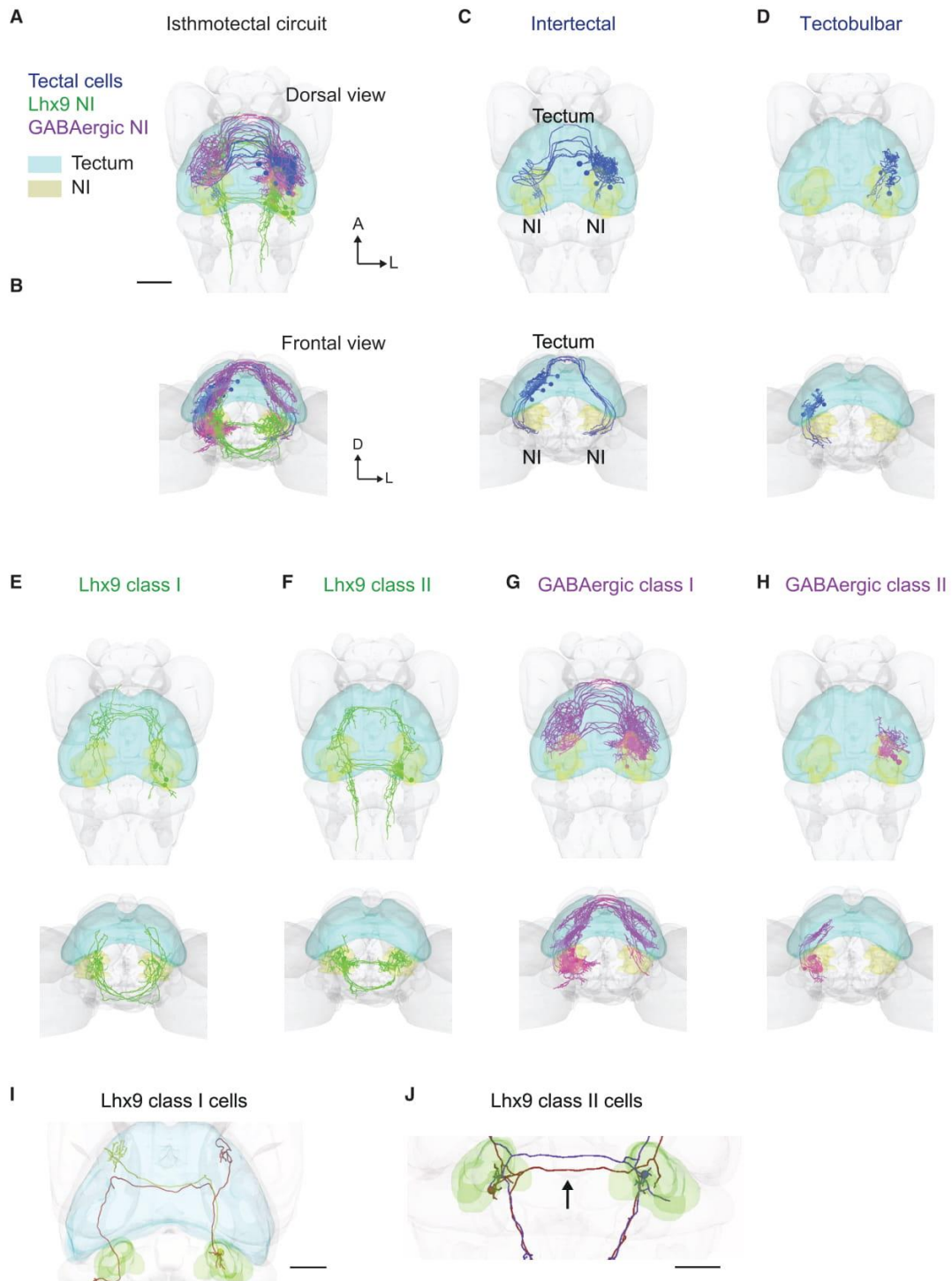
(M) Number of looming-responsive cells in the ipsilateral tectum (relative to looming stimulus) for the intact hemisphere after ablation of the GABAergic-positive NI.

(N) Number of looming-responsive cells in the contralateral (relative to looming stimulus) tectum before and after ablation of *lhx9*-positive NI cells in the right hemisphere. $n = 3$ fish.

(O) Number of looming-responsive cells in the ipsilateral (relative to looming stimulus) tectum.

(P) Number of looming-responsive cells in the contralateral tectum (relative to looming stimulus) for the intact hemisphere before and after ablation of *lhx9*-positive NI cells in the right hemisphere. $n = 2$ fish.

(Q) Number of looming-responsive cells in the ipsilateral tectum (relative to looming stimulus) for the intact hemisphere after ablation of *lhx9*-positive NI cells. For all panels, * $p < 0.05$, Mann-Whitney U test.



the two stimuli and swim between them. Individual animals employ either strategy in successive trials, suggesting that WTA and averaging can occur in the same brain. Their respective engagement presumably depends on stimulus history and internal state. When the two stimuli are unequal in expansion rate, the escape responses are biased to the stronger stimulus, indicating that zebrafish larvae weigh the relative salencies of competing stimuli. This behavioral choice exhibited by larval zebrafish thus shows the hallmarks of selective spatial attention.

Neural signatures of WTA first emerge in the early stages of visual processing: the retina and the tectum. Interestingly, we found that a salient stimulus suppresses the response to the weaker stimulus presented to the same eye already at the level of the RGCs (Figures 2 and 8A). By chemogenetic ablation of the tectum, we ruled out that this effect is the result of feedback modulation of RGC presynaptic axon terminals by tectal cells. Presentation of two prey-like objects produced the same WTA dynamics in the retinotectal system, suggesting that such dynamics are part of a global mechanism involved in stimulus selection in diverse behavioral contexts (escape and hunting) and independent of stimulus valence. Monocular stimulus competition is likely the result of antagonistic mechanisms within the inner retina, apparently operating outside of the classical receptive field (Deny et al., 2017; McIlwain, 1964).

Retinal mechanisms cannot, in principle, account for competition across the hemispheres. We discovered that the NI, together with the tectum, integrates information from both eyes. A reciprocal loop between these two structures may enhance responses to the stronger stimulus and suppress responses to the weaker stimulus. As a result, the two tecta show unbalanced activity patterns in response to looming disks presented to opposite sides (Figures 3 and 8B). Inter-hemispheric inhibition has been demonstrated in other species and contexts. In *Drosophila*, cats, barn owls, and monkeys, for example, a strong stimulus located anywhere outside of the receptive field, including in the opposite hemisphere, can suppress responses to an otherwise effective stimulus (Herman et al., 2018; Mysore and Knudsen, 2012; Rizzolatti et al., 1979; Sun et al., 2017).

Our data support a mechanism where neuronal projection patterns and transmitter identities of recurrent isthmotectal connections lead to focal enhancement of the most salient stimulus combined with global suppression elsewhere (Brandt and Wessel, 2007; Cisek, 2019; Jovanic et al., 2016; Koyama and Pujala,

2018; Mysore and Knudsen, 2012). This neural circuit possesses four key properties. First, the relative levels of tectal and isthmic activity in the right and left hemispheres can discriminate the stronger stimulus. Depending on which side of the brain “wins,” neurons exhibit switch-like behavior, as expected from a WTA mechanism across hemispheres. Second, by virtue of their bilateral projections, NI neurons can enhance or suppress tectal cell activity in response to looming stimuli across both hemispheres. Third, excitatory NI cells arborize focally, whereas inhibitory NI cells arborize broadly. Fourth, unilateral manipulation of the NI causes bilateral effects in tectal neural dynamics and behavior. These results suggest that WTA dynamics emerge from a tightly coordinated inter-hemispheric computation. We argue that salient stimuli are detected based on the relative levels of activity in the right and left tectum, similar to a pooling model (Herman et al., 2018). We postulate that Lhx9 class I cells may implement WTA (directed escapes) by driving more activity in the ipsilateral or contralateral tectum together with global inhibition of the “losing” side provided by GABAergic NI cells. Lhx9 class II cells are potential candidates for involvement in implementation of an averaging strategy (leading to burst forward movements), with direct contralateral projections to the other NI leading to a balancing of activity across hemispheres, preventing one side from “winning” during stimulus competition.

The isthmotectal system is at least as old as the osteichthyan lineage, which includes bony fish, amphibians, mammals, and sauropsids. The NI’s possible behavioral functions have been debated over the years and may not be restricted to prioritization of threats. We show here that unilateral manipulation of NI cells causes bilateral behavioral impairments in response to looming stimuli and deficits in visual processing on both sides of the brain. In contrast, ablation of cholinergic NI neurons in zebrafish causes deficits in hunting but only mild effects in loom avoidance (Henriques et al., 2019). Moreover, a population of GABAergic neurons, ventral to the tectum and in close apposition to the NI, projects to both tecta and is involved in interhemispheric coordination for prey capture (Gebhardt et al., 2019). We propose that the NI, perhaps in concert with other tegmental and peristhmic nuclei, has multiple region-specific functions. Accordingly, our work here and the aforementioned studies may have investigated distinct subpopulations of isthmic neurons. There is precedent for such functional segregation by stimulus valence. Processing of prey versus looming information, for example, is confined to separate layers of the tectum (Semmelhack et al.,

Figure 7. Cellular architecture of isthmotectal circuitry

- (A) Cellular-resolution atlas of isthmotectal circuitry showing single-cell reconstructions. Shown are tectal cells in blue, *lhx9*-positive NI cells in green, and GABAergic-positive NI cells in magenta, dorsal view, and masks for the tectum and NI (light blue and yellow, respectively).
- (B) Same as (A) but frontal view.
- (C) Intertectal cells with a bifurcated axon, terminating in the vicinity of the NI on both sides.
- (D) Tectobulbar neurons targeting the ipsilateral NI.
- (E) Lhx9-positive NI cells (class I) projecting first to the ipsilateral tectum and then to the contralateral tectum.
- (F) Lhx9-positive NI cells (class II) projecting first to the contralateral NI, close to the contralateral tectum, and then to the ipsilateral tectum.
- (G) GABAergic-positive NI cells (class I) projecting first to the ipsilateral tectum and then to the contralateral tectum.
- (H) GABAergic-positive NI cells (class II) projecting only to the ipsilateral tectum. For each morphological type, dorsal and frontal views are shown.
- (I) Example of two Lhx9 class I cells with projections to the tectum. Both cell bodies are on the right. The brown cell shows terminations mainly in the ipsilateral tectum, whereas the green cell shows termination mainly in the contralateral tectum.
- (J) Example of reciprocal projections of two Lhx9 class II NI cells. The red cell has its soma in the left NI and terminations in the right NI. The purple cell has its soma in the right NI and terminations in the left NI. Both cells have descending projections to the hindbrain. Scale bars, 50 μ m.

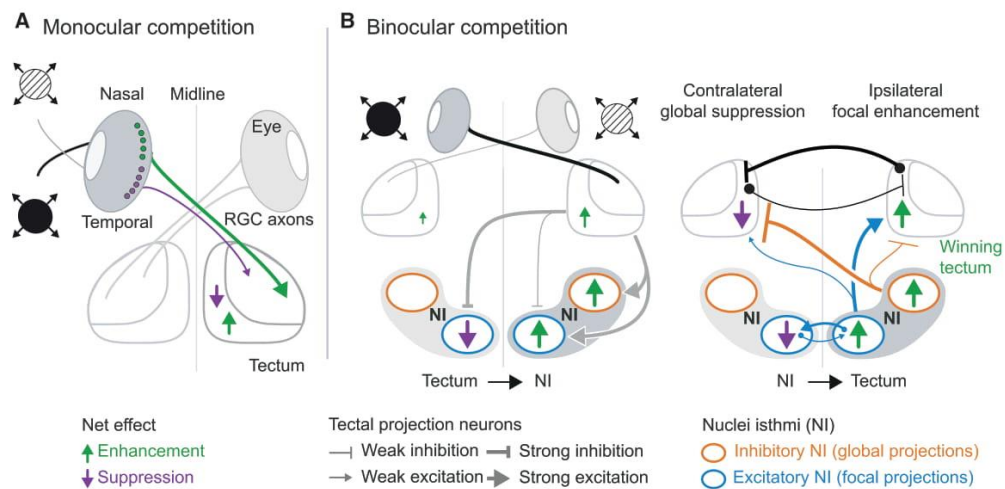


Figure 8. Schematic summary of findings

(A) Schematized summary of findings for monocular competition. The most salient stimulus “wins” in the retina through reciprocal inhibition, possibly mediated by amacrine cells. Saliency tuning is sharpened by a tectum-intrinsic circuit.

(B) Circuit model for binocular competition. Each tectum drives activity in the ipsilateral NI (putative excitatory tectobulbar neurons) and suppresses activity in the contralateral NI (putative inhibitory intertectal neurons). Focal enhancement, mediated by excitatory NI cells, is stronger on the “winning” stimulus side (green arrows). Suppression, mediated by globally projecting inhibitory NI neurons, is stronger on the “losing” stimulus side (magenta arrows). Reciprocal isthmotectal loops ensure focal enhancement of responses to a stronger stimulus and suppression of responses to a weaker stimulus, implementing a WTA computation. Black connections across both tecta represent putative inhibitory commissural neurons projecting to the contralateral side. Equal activity in both NIs may result in neither tectum winning and an averaging strategy being implemented instead.

2014; Temizer et al., 2015) and transmitted by separate output pathways to the tegmentum and reticular formation (Helmbrecht et al., 2018).

We conclude that a feedforward retinotectal and a recurrent isthmotectal circuit implement context-dependent target selection and may form the basis of an evolutionarily conserved, bottom-up attention mechanism. It will be important to examine how the choice between escape, other defensive actions (e.g., freezing), and prey capture is computed as a function of the type of stimuli and their combination. Future work will help clarify interactions between different subpopulations of NI neurons. Further dissection of these interconnected circuits, especially under the top-down influence of the animal’s internal state, such as experience, hunger, or stress, will reveal elementary principles underlying selective spatial attention in vertebrates.

STAR★METHODS

Detailed methods are provided in the online version of this paper and include the following:

- KEY RESOURCES TABLE
- RESOURCE AVAILABILITY
 - Lead contact
 - Materials availability
 - Data and code availability
- EXPERIMENTAL MODEL AND SUBJECT DETAILS
 - Zebrafish lines

- Q-system transgenics
- METHOD DETAILS
 - Visual competition behavioral assay
 - Data analysis for behavioral experiments with competing looming stimuli
 - Modeling
 - Prey capture experiments
 - Calcium imaging
 - Two-photon computer generated holographic (2P-CGH) optogenetics
 - Genetic ablation of neurons
 - Imaging analysis
 - Optogenetic stimulation during presentation of looming stimuli
 - Analysis of optogenetic experiments
 - Two-photon ablation of neurons
 - Single-cell reconstructions
 - Confocal imaging and anatomical reconstruction of neurons
 - *In situ* hybridization and immunohistochemistry
- QUANTIFICATION AND STATISTICAL ANALYSIS
 - Quantification of arbor length and number of arborizations of NI cells

SUPPLEMENTAL INFORMATION

Supplemental Information can be found online at <https://doi.org/10.1016/j.neuron.2020.12.002>.

ACKNOWLEDGMENTS

We thank Yunmin Wu, Aristides Arrenberg, and Ruben Portugues for advice. Anna Kramer helped with drawing Figure 8. Enrico Kühn, Styliani Koutsouli, Krasimir Slanchev, and Irene Arnold-Ammer provided expert technical support. Vilim Stih and Andreas Kist shared scripts used in the analysis of imaging data. Wolfgang Driever provided the riboprobes for detection of *gad1b* and *trh*. Michael Kunst and Nawwar Mokayes assisted with experiments and analysis of anatomical reconstruction data. We thank all members of the Baier lab for discussions. Funding was provided by the Max Planck Society and the DFG (SFB 870 "Assembly and Function of Neural Circuits" and the Priority Program SPP 1926 "Next Generation Optogenetics" to H.B.). K.K. received support from NIG-JOINT (2014-A) and the Japan Agency for Medical Research and Development (JP20km0210087 and JP20km0210168).

AUTHOR CONTRIBUTIONS

Conceptualization, A.M.F. and H.B.; Methodology, A.M.F., J.L., J.C.D., T.O.H., D.S.M., Y.K., E.L., K.K., and M.D.M.; Software, A.M.F., J.L., J.C.D., T.O.H., D.S.M., and M.D.M.; Formal Analysis, A.M.F., J.L., J.C.D., T.O.H., D.S.M., and M.D.M.; Investigation, A.M.F., D.S.M., E.L., and M.D.M.; Writing – Original Draft, A.M.F. and H.B.; Writing – Review & Editing, all authors; Funding Acquisition, H.B.; Supervision, H.B.

DECLARATION OF INTERESTS

The authors declare no competing interests.

Received: June 15, 2020

Revised: November 9, 2020

Accepted: December 2, 2020

Published: December 22, 2020

REFERENCES

Arrenberg, A.B., Del Bene, F., and Baier, H. (2009). Optical control of zebrafish behavior with halorhodopsin. *Proc. Natl. Acad. Sci. USA* *106*, 17968–17973.

Asakawa, K., Suster, M.L., Mizusawa, K., Nagayoshi, S., Kotani, T., Urasaki, A., Kishimoto, Y., Hibi, M., and Kawakami, K. (2008). Genetic dissection of neural circuits by Tol2 transposon-mediated Gal4 gene and enhancer trapping in zebrafish. *Proc. Natl. Acad. Sci. USA* *105*, 1255–1260.

Ben-Tov, M., Donchin, O., Ben-Shahar, O., and Segev, R. (2015). Pop-out in visual search of moving targets in the archer fish. *Nat. Commun.* *6*, 6476.

Berens, P. (2009). CircStat: A MATLAB Toolbox for Circular Statistics. *Journal of Statistical Software* *31*, 1–21.

Bhattacharyya, K., McLean, D.L., and MacIver, M.A. (2017). Visual Threat Assessment and Reticulospinal Encoding of Calibrated Responses in Larval Zebrafish. *Curr. Biol.* *27*, 2751–2762.e6.

Bianco, I.H., Kampff, A.R., and Engert, F. (2011). Prey capture behavior evoked by simple visual stimuli in larval zebrafish. *Front. Syst. Neurosci.* *5*, 101.

Brandt, S.F., and Wessel, R. (2007). Winner-take-all selection in a neural system with delayed feedback. *Biol. Cybern.* *97*, 221–228.

Budick, S.A., and O'Malley, D.M. (2000). Locomotor repertoire of the larval zebrafish: swimming, turning and prey capture. *J. Exp. Biol.* *203*, 2565–2579.

Burgess, H.A., and Granato, M. (2007). Modulation of locomotor activity in larval zebrafish during light adaptation. *J. Exp. Biol.* *210*, 2526–2539.

Cisek, P. (2007). Cortical mechanisms of action selection: the affordance competition hypothesis. *Philos. Trans. R. Soc. Lond. B Biol. Sci.* *362*, 1585–1599.

Cisek, P. (2019). Resynthesizing behavior through phylogenetic refinement. *Atten. Percept. Psychophys.* *81*, 2265–2287.

Dal Maschio, M., Donovan, J.C., Helmbrecht, T.O., and Baier, H. (2017). Linking Neurons to Network Function and Behavior by Two-Photon Holographic Optogenetics and Volumetric Imaging. *Neuron* *94*, 774–789.e5.

Davison, J.M., Akitake, C.M., Goll, M.G., Rhee, J.M., Gosse, N., Baier, H., Halpern, M.E., Leach, S.D., and Parsons, M.J. (2007). Transactivation from Gal4-VP16 transgenic insertions for tissue-specific cell labeling and ablation in zebrafish. *Dev. Biol.* *304*, 811–824.

Del Bene, F., Wyart, C., Robles, E., Tran, A., Looger, L., Scott, E.K., Isacoff, E.Y., and Baier, H. (2010). Filtering of visual information in the tectum by an identified neural circuit. *Science* *330*, 669–673.

Deny, S., Ferrari, U., Macé, E., Yger, P., Caplette, R., Picaud, S., Tkačik, G., and Marre, O. (2017). Multiplexed computations in retinal ganglion cells of a single type. *Nat. Commun.* *8*, 1964.

Dunn, T.W., Gebhardt, C., Naumann, E.A., Riegler, C., Ahrens, M.B., Engert, F., and Del Bene, F. (2016). Neural Circuits Underlying Visually Evoked Escapes in Larval Zebrafish. *Neuron* *89*, 613–628.

Ewert, J.-P. (1997). Neural correlates of key stimulus and releasing mechanism: a case study and two concepts. *Trends Neurosci.* *8*, 332–339.

Feng, L., Zhao, T., and Kim, J. (2015). NeuTube 1.0: A New Design for Efficient Neuron Reconstruction Software Based on the SWC Format. *eNeuro* *2*.

Fernandes, A.M., Fero, K., Arrenberg, A.B., Bergeron, S.A., Driever, W., and Burgess, H.A. (2012). Deep brain photoreceptors control light seeking behavior in zebrafish larvae. *Curr Biol* *22*, 2042–2047.

Förster, D., Arnold-Ammer, I., Laurell, E., Barker, A.J., Fernandes, A.M., Finger-Baier, K., Filosa, A., Helmbrecht, T.O., Kölsch, Y., Kühn, E., et al. (2017). Genetic targeting and anatomical registration of neuronal populations in the zebrafish brain with a new set of BAC transgenic tools. *Sci. Rep.* *7*, 5230.

Gebhardt, C., Auer, T.O., Henriques, P.M., Rajan, G., Duroure, K., Bianco, I.H., and Del Bene, F. (2019). An interhemispheric neural circuit allowing binocular integration in the optic tectum. *Nat. Commun.* *10*, 5471.

Gruberg, E., Dudkin, E., Wang, Y., Marín, G., Salas, C., Sentis, E., Letelier, J., Mpodozis, J., Malpeli, J., Cui, H., et al. (2006). Influencing and interpreting visual input: the role of a visual feedback system. *J. Neurosci.* *26*, 10368–10371.

Heap, L.A.L., Vanwalleghem, G., Thompson, A.W., Favre-Bulle, I.A., and Scott, E.K. (2018). Luminance Changes Drive Directional Startle through a Thalamic Pathway. *Neuron* *99*, 293–301.e4.

Helmbrecht, T.O., Dal Maschio, M., Donovan, J.C., Koutsouli, S., and Baier, H. (2018). Topography of a Visuomotor Transformation. *Neuron* *100*, 1429–1445.e4.

Henley, J.M., Lindstrom, J.M., and Oswald, R.E. (1986). Acetylcholine receptor synthesis in retina and transport to optic tectum in goldfish. *Science* *232*, 1627–1629.

Henriques, P.M., Rahman, N., Jackson, S.E., and Bianco, I.H. (2019). Nucleus Isthmi Is Required to Sustain Target Pursuit during Visually Guided Prey-Catching. *Curr. Biol.* *29*, 1771–1786.e5.

Herman, J.P., Katz, L.N., and Krauzlis, R.J. (2018). Midbrain activity can explain perceptual decisions during an attention task. *Nat. Neurosci.* *21*, 1651–1655.

Itti, L., and Koch, C. (2000). A saliency-based search mechanism for overt and covert shifts of visual attention. *Vision Res.* *40*, 1489–1506.

Jovanic, T., Schneider-Mizell, C.M., Shao, M., Masson, J.-B., Denisov, G., Fetter, R.D., Mensh, B.D., Truman, J.W., Cardona, A., and Zlatić, M. (2016). Competitive Disinhibition Mediates Behavioral Choice and Sequences in *Drosophila*. *Cell* *167*, 858–870.e19.

Kardamakis, A.A., Saitoh, K., and Grillner, S. (2015). Tectal microcircuit generating visual selection commands on gaze-controlling neurons. *Proc. Natl. Acad. Sci. USA* *112*, E1956–E1965.

Klapoetke, N.C., Nern, A., Peek, M.Y., Rogers, E.M., Breads, P., Rubin, G.M., Reiser, M.B., and Card, G.M. (2017). Ultra-selective looming detection from radial motion opponency. *Nature* *551*, 237–241.

Knudsen, E.I. (2018). Neural Circuits That Mediate Selective Attention: A Comparative Perspective. *Trends Neurosci.* *41*, 789–805.

Koch, C., and Ullman, S. (1985). Shifts in selective visual attention: towards the underlying neural circuitry. *Hum. Neurobiol.* *4*, 219–227.

- Koyama, M., and Pujala, A. (2018). Mutual inhibition of lateral inhibition: a network motif for an elementary computation in the brain. *Curr. Opin. Neurobiol.* *49*, 69–74.
- Krauzlis, R.J., Bogadhi, A.R., Herman, J.P., and Bollimunta, A. (2018). Selective attention without a neocortex. *Cortex* *102*, 161–175.
- Kunst, M., Laurell, E., Mokayes, N., Kramer, A., Kubo, F., Fernandes, A.M., Förster, D., Dal Maschio, M., and Baier, H. (2019). A Cellular-Resolution Atlas of the Larval Zebrafish Brain. *Neuron* *103*, 21–38.e5.
- Larsch, J., and Baier, H. (2018). Biological Motion as an Innate Perceptual Mechanism Driving Social Affiliation. *Curr. Biol.* *28*, 3523–3532.e4.
- Lee, D.K., Itti, L., Koch, C., and Braun, J. (1999). Attention activates winner-take-all competition among visual filters. *Nat. Neurosci.* *2*, 375–381.
- Lisberger, S.G., and Ferrera, V.P. (1997). Vector averaging for smooth pursuit eye movements initiated by two moving targets in monkeys. *J. Neurosci.* *17*, 7490–7502.
- Löhr, H., Ryu, S., and Driever, W. (2009). Zebrafish diencephalic A11-related dopaminergic neurons share a conserved transcriptional network with neuroendocrine cell lineages. *Development* *136*, 1007–1017.
- Lopes, G., Bonacchi, N., Frazão, J., Neto, J.P., Atallah, B.V., Soares, S., Moreira, L., Matias, S., Itskov, P.M., Correia, P.A., et al. (2015). Bonsai: an event-based framework for processing and controlling data streams. *Front. Neuroinform.* *9*, 7.
- Marques, J.C., Lackner, S., Félix, R., and Orger, M.B. (2018). Structure of the Zebrafish Locomotor Repertoire Revealed with Unsupervised Behavioral Clustering. *Curr. Biol.* *28*, 181–195.e5.
- McIlwain, J.T. (1964). Receptive fields of optic tract axons and lateral geniculate cells: peripheral extent and barbiturate sensitivity. *J. Neurophysiol.* *27*, 1154–1173.
- Mearns, D.S., Donovan, J.C., Fernandes, A.M., Semmelhack, J.L., and Baier, H. (2020). Deconstructing Hunting Behavior Reveals a Tightly Coupled Stimulus-Response Loop. *Curr. Biol.* *30*, 54–69.e9.
- Miri, A., Daie, K., Burdine, R.D., Aksay, E., and Tank, D.W. (2011). Regression-Based Identification of Behavior-Encoding Neurons During Large-Scale Optical Imaging of Neural Activity at Cellular Resolution. *J. Neurophysiol.* *105*, 964–980.
- Mohamed, G.A., Cheng, R.-K., Ho, J., Krishnan, S., Mohammad, F., Claridge-Chang, A., and Jesuthasan, S. (2017). Optical inhibition of larval zebrafish behaviour with anion channelrhodopsins. *BMC Biol.* *15*, 103.
- Mysore, S.P., and Knudsen, E.I. (2012). Reciprocal inhibition of inhibition: a circuit motif for flexible categorization in stimulus selection. *Neuron* *73*, 193–205.
- Northmore, D.P. (1991). Visual responses of nucleus isthmi in a teleost fish (*Lepomis macrochirus*). *Vision Res.* *31*, 525–535.
- Northmore, D.P.M., and Gallagher, S.P. (2003). Functional relationship between nucleus isthmi and tectum in teleosts: synchrony but no topography. *Vis. Neurosci.* *20*, 335–348.
- Nummela, S.U., and Krauzlis, R.J. (2011). Superior colliculus inactivation alters the weighted integration of visual stimuli. *J. Neurosci.* *31*, 8059–8066.
- Ottes, F.P., Van Gisbergen, J.A., and Eggermont, J.J. (1984). Metrics of saccade responses to visual double stimuli: two different modes. *Vision Res.* *24*, 1169–1179.
- Peirce, J., Gray, J.R., Simpson, S., MacAskill, M., Höchenberger, R., Sogo, H., Kastman, E., and Lindeløv, J.K. (2019). PsychoPy2: Experiments in behavior made easy. *Behav. Res. Methods* *51*, 195–203.
- Potter, C.J., Tasic, B., Russler, E.V., Liang, L., and Luo, L. (2010). The Q System: A Repressible Binary System for Transgene Expression, Lineage Tracing and Mosaic Analysis. *Cell* *141*, 536–548.
- Riabinina, O., Luginbuhl, D., Marr, E., Liu, S., Wu, M.N., Luo, L., and Potter, C.J. (2015). Improved and expanded Q-system reagents for genetic manipulations. *Nat. Methods* *12*, 219–222, 5 p following 222.
- Rizzolatti, G., Bertoloni, G., and Buchtel, H.A. (1979). Interference of concomitant motor and verbal tasks on simple reaction time: a hemispheric difference. *Neuropsychologia* *17*, 323–330.
- Robles, E., Filosa, A., and Baier, H. (2013). Precise Lamination of Retinal Axons Generates Multiple Parallel Input Pathways in the Tectum. *J. Neurosci.* *33*, 5027–5039.
- Rohlfing, T., and Maurer, C.R. (2003). Nonrigid image registration in shared-memory multiprocessor environments with application to brains, breasts, and bees. *IEEE Trans. Inf. Technol. Biomed.* *7*, 16–25.
- Sareen, P., Wolf, R., and Heisenberg, M. (2011). Attracting the attention of a fly. *Proc. Natl. Acad. Sci. USA* *108*, 7230–7235.
- Sato, T., Sato, F., Kamezaki, A., Sakaguchi, K., Tanigome, R., Kawakami, K., and Sehara-Fujisawa, A. (2015). Neuregulin 1 Type II-ErbB Signaling Promotes Cell Divisions Generating Neurons from Neural Progenitor Cells in the Developing Zebrafish Brain. *PLoS ONE* *10*, e0127360.
- Satou, C., Kimura, Y., Hirata, H., Suster, M.L., Kawakami, K., and Higashijima, S. (2013). Transgenic tools to characterize neuronal properties of discrete populations of zebrafish neurons. *Development* *140*, 3927–3931.
- Schellart, N.A.M., Riemsdijk, F.C.C., and Sperkrijse, H. (1979). Center-surround organisation and interactions in receptive fields of goldfish tectal units. *Vision Res.* *19*, 459–467.
- Semmelhack, J.L., Donovan, J.C., Thiele, T.R., Kuehn, E., Laurell, E., and Baier, H. (2014). A dedicated visual pathway for prey detection in larval zebrafish. *eLife* *3*, 3.
- Sun, Y., Nern, A., Franconville, R., Dana, H., Schreiter, E.R., Looger, L.L., Svoboda, K., Kim, D.S., Hermundstad, A.M., and Jayaraman, V. (2017). Neural signatures of dynamic stimulus selection in *Drosophila*. *Nat. Neurosci.* *20*, 1104–1113.
- Tabor, K.M., Bergeron, S.A., Horstick, E.J., Jordan, D.C., Aho, V., Porkka-Heiskanen, T., Haspel, G., and Burgess, H.A. (2014). Direct activation of the Mauthner cell by electric field pulses drives ultrarapid escape responses. *J. Neurophysiol.* *112*, 834–844.
- Temizer, I., Donovan, J.C., Baier, H., and Semmelhack, J.L. (2015). A Visual Pathway for Looming-Evoked Escape in Larval Zebrafish. *Curr. Biol.* *25*, 1823–1834.
- Thiele, T.R., Donovan, J.C., and Baier, H. (2014). Descending control of swim posture by a midbrain nucleus in zebrafish. *Neuron* *83*, 679–691.
- Volkman, K., Chen, Y.-Y., Harris, M.P., Wullmann, M.F., and Köster, R.W. (2010). The zebrafish cerebellar upper rhombic lip generates tegmental hindbrain nuclei by long-distance migration in an evolutionary conserved manner. *J. Comp. Neurol.* *518*, 2794–2817.
- Wang, L., and Krauzlis, R.J. (2018). Visual Selective Attention in Mice. *Curr. Biol.* *28*, 676–685.e4.
- Zhaoping, L. (2016). From the optic tectum to the primary visual cortex: migration through evolution of the saliency map for exogenous attentional guidance. *Curr. Opin. Neurobiol.* *40*, 94–102.

STAR★METHODS

KEY RESOURCES TABLE

REAGENT or RESOURCE	SOURCE	IDENTIFIER
Antibodies		
Mouse anti-TH	Merck Millipore	RRID:AB_2201528
Mouse anti-REELIN	Millipore	RRID:AB_10682217
Mouse anti-GFP	Takara Bio Clontech	RRID:AB_10013427
Chicken anti-GFP	Thermo Fisher Scientific	RRID:AB_2534023
Goat anti-CHAT	Merck Millipore	RRID:AB_2079751
Chemicals, Peptides, and Recombinant Proteins		
DAPI	Sigma-Aldrich	28718-90-3
Metronidazole	Sigma-Aldrich	M3761
Experimental Models: Organisms/Strains		
Tg(ath5:QF2)mpn405	This manuscript	N/A
Tg(QUAS:GFPcaax)mpn163	This manuscript	N/A
Tg(QUAS:GCaMP6s)mpn164	This manuscript	N/A
Tg(QUAS:epNTR-tagRFP)mpn165	This manuscript	N/A
Tg(UAS:HaloTagCAAX)mpn170	This manuscript	N/A
Tg(elavl3:lyn-tagRFP)mpn404	Dal Maschio et al., 2017	ZDB-ALT-170731-38
Tg(UAS:ChR2(H134R)-mCherry)mpn134	Dal Maschio et al., 2017	ZDB-ALT-170731-36
Tg(UAS:GtACR2-eYFP)sq212	Mohamed et al., 2017	ZDB-ALT-170913-6
Tg(elavl3:nlsGCaMP6s)mpn400	Dal Maschio et al., 2017	ZDB-ALT-170731-37
Tg(gad1b:Gal4VP16)mpn155	Förster et al., 2017	ZDB-ALT-160726-5
Tg(lhx9:Gal4VP16)mpn203	Förster et al., 2017	ZDB-ALT-170908-16
Tg(chata:Gal4VP16)mpn202	Förster et al., 2017	ZDB-ALT-170908-4
Tg(nkSAGFFL81C)	Sato et al., 2015	ZDB-ALT-151006-4
Tg(UAS:nfsb-mCherry)c264	Davison et al., 2007	ZDB-ALT-070316-1
Tg(-7atoh7:GAL4-VP16)s1992tTg	Del Bene et al., 2010	ZDB-ALT-110912-2
Tg(gad1b:loxP-DsRed-loxP-GFP)	Satou et al., 2013	ZDB-TGCONSTRUCT-131127-7
Tg(vglut2a:loxP-DsRedloxP-GFP)	Satou et al., 2013	ZDB-TGCONSTRUCT-110413-4
Tg(UAS:GCaMP6s)mpn101	Thiele et al., 2014	ZDB-ALT-140811-3
Tg(UAS:Dendra-kras)s1998t	Arrenberg et al., 2009	ZDB-ALT-110808-3
Tg(elavl3:GCaMP6s)a13203	Dunn et al., 2016	ZDB-ALT-180502-2
Tg(UAS:Dendra-kras)s1998t	Arrenberg et al., 2009	ZDB-ALT-110808-3
Tg(5xUAS:EGFP)zf82	Asakawa et al., 2008	ZDB-ALT-080528-1
Tg(UAS-E1b:Kaede)s1999t	Davison et al., 2007	ZDB-TGCONSTRUCT-070314-1
Software and Algorithms		
Python 2.7	Python	https://www.python.org/
Python 3.7	Python	https://www.python.org/
CMTK	Rohlfing and Maurer, 2003	https://www.nitrc.org/projects/cmtk/
Fiji (ImageJ)	NIH	http://fiji.sc/
Psychopy2	Peirce et al., 2019	https://www.psychopy.org/
neuTube	Feng et al., 2015	https://www.neutracing.com/

RESOURCE AVAILABILITY

Lead contact

Further information and requests for reagents should be directed to and will be fulfilled by the Lead Contact, Herwig Baier (hbaier@neuro.mpg.de).

Materials availability

Unique materials such as plasmids generated in this study will be available upon request without any restrictions.

Data and code availability

The datasets and custom software that support the findings of this study will be made available upon request.

EXPERIMENTAL MODEL AND SUBJECT DETAILS

All animal procedures conformed to the institutional guidelines set by the Max Planck Society and were approved under licenses from the regional government of Upper Bavaria (Regierung von Oberbayern).

Zebrafish lines

For the experiments in this study, we used 5–9 days post fertilization (d.p.f.) larvae carrying mutations in the *mitfa* allele (nacre). Sex is not determined at larval stage. Fish were raised on a 14h light/ 10h dark cycle at 28°C. Transgenic lines used in this study are shown in the Key Resources Table. For making the *Tg(UAS:HaloTagCAAX)mpn170* line, the pFC14A HaloTag CMV Flexi Vector was purchased from Promega and the HaloTag was inserted with an N-terminal CAAX domain into a pTol2 UAS vector with bleeding heart marker at the EcoRI site. This construct was pressure-injected together with Tol2 mRNA (concentration for both: 25 ng/l) into one- to two-cell-stage embryos. Positive carriers of the construct were raised until adulthood and crossed to the *Tg(gad1b:Gal4VP16)mpn155* line. 1 μM of Halotag ligand (JF549, kind gift of Luke Levis, Janelia) and 1:500 dilution of lysotracker (deep red, Invitrogen, L12492) in DMSO (final concentration 1%), were added to the water of 4 dpf larvae. The larvae were kept in this solution for 36 h. Dyes were washed out prior to imaging at 6 dpf.

Q-system transgenics

A pTol2-(5x)QUAS-e1b:EcoRV-polyA;cmlc2:mCherry vector was generated using oligo synthesized QUAS promoter sequences (Potter et al., 2010). A GCaMP6s fragment (Thiele et al., 2014) was inserted into the EcoRV-linearized vector using traditional restriction-ligation cloning. The same approach was used to generate an epNTR-TagRFP (Tabor et al., 2014) and GFPcaax (Förster et al., 2017) version. To generate the *Tg(QUAS)* reporter lines, transposase mRNA (50 ng/μl) and the construct (25 ng/μl) were co-injected into TL/nacre zebrafish eggs. Injected fish were sorted based on heart expression of the transgenesis marker *cmlc2:mCherry* and raised into adulthood. Founders were obtained by outcrosses to TL/nacre. The QF2 coding sequence was obtained from Addgene Plasmid #61312 (Riabinina et al., 2015). To establish the driver line *Tg(ath5:QF2)*, a QF2-polyA; FRT-KAN-FRT;cmlc2:Cerulean fragment was PCR amplified and inserted into the *ath5* BAC clone DKEY-111E19 using BAC recombineering as described previously (Förster et al., 2017). The resulting Tol2-*ath5:QF2* BAC (100 ng/μl) was co-injected with transposase mRNA (50ng/μl) into TL/nacre zebrafish eggs. *Cmlc2:Cerulean* expressing larvae were raised and identified as founders by an outcross by an outcross to *Tg(QUAS:GFPcaax)* fish. Stable *ath5:QF2* transgenes could then be crossed to *Tg(QUAS:GCaMP6s)* or *Tg(QUAS:epNTR-TagRFP)* fish.

METHOD DETAILS

Visual competition behavioral assay

We designed a setup to project looming stimuli to 9 individual zebrafish larvae simultaneously via a screen below the animals. We adapted a previously described virtual reality setup which allows real-time tracking and presentation of arbitrary visual stimuli at animal-centric positions (Larsch and Baier, 2018). Animals were monitored individually in shallow glass dishes of 10 cm diameter separated by opaque walls to prevent visual contact. The dishes rested on a projection film for visual stimulation, confining the animals' distance to the screen to approximately between 3 mm and 13 mm by the rounded bottom of the dish and the surface of the water. To minimize stimulus distortion due to refraction at the air-glass-water interfaces, we submerged the projection film and glass dishes in water. Animals were recorded at 30 fps with cameras using the CMV4000 sCMOS chip (IDS UI-3370CP-NIR or PointGrey Grasshopper GS3-U3-41C6NIR-C) at a resolution of 2048x2048 pixels. We used a 25 mm lens (Edmund Optics Nr. 86-572) at a distance of 800 mm resulting in an image resolution of 150 μm/pixel. Visual stimuli were projected onto the projection film from underneath via a cold mirror. Diffuse Infrared illumination for imaging was provided from below. Visible light stimuli (peaks around 450 nm, 525 nm and 625 nm) were provided to the fish via the projector (Optoma ML750ST, RGB values (255,255,255) for white) but blocked before the camera by an NIR band-pass filter.

Real-time processing of images and stimulus generation were performed on a Desktop PC running Bonsai (Lopes et al., 2015). Briefly, each camera frame was background subtracted and an empirically determined threshold was applied to isolate animals against the background. Next, contours were extracted to compute the center of mass and orientation of each animal. Based on animal positions and a stimulus property file, we generated animal-centric visual stimuli using custom Python scripts in Bonsai to control OpenGL drawing routines. Stimuli were dots (for black, RGB value (0,0,0)) on white background (RGB value (255,255,255)) unless noted otherwise. Dot size was a multiple of projected pixel size (1 pixel was 0.47 mm side length). Looming stimuli were presented as stationary dots expanding for 500 ms (15 frames) with a linear increase in diameter. Stimuli were presented 1 cm from the

fish at angles of 45°, 90°, 135°, 180°, 225°, 270°, or 315° relative to the animals' center of mass and orientation at the beginning of the stimulus. Loom stimuli were presented once per minute. A moving grating was presented for 20 s ending 10 s before the presentation of the next loom stimulus to drive larvae toward the center of the dishes. At each frame, animal and stimulus parameters were streamed to a text file for offline analysis. The program also stored the video data after background subtraction into an xVid compressed .avi file via FFmpeg (ffmpeg.org) for later inspection. Camera and projector were aligned using a separate Bonsai routine before every experimental day as described previously (Larsch and Baier, 2018). Animals were tested at 5–8 dpf in fish water at room temperature (22–25°C). Before behavior testing, animals were kept in a Petri dish floating above a fully lit portion of the projection screen to allow habituation to light and temperature conditions of the experiment. Animals were analyzed for 60 to 300 minutes. The order of different stimuli was randomized for each group of 9 animals.

Data analysis for behavioral experiments with competing looming stimuli

Exported text files containing behavioral data and stimulus parameters were analyzed offline using custom-written Python scripts. We classified responses as escapes if the distance to the original position at the end of the expansion time of the stimuli (500 ms, after 15 frames) was at least 5 mm (approximately one fish body length). Distance from the initial position was defined as the Euclidean distance from the origin to a point in the x-y plane after 500 ms (end of stimuli expansion). The distance modulation of escape behaviors is in agreement with a previous study (Bhattacharyya et al., 2017) and was used as an indication of stimulus strength. Circular behavioral data statistics were performed with the python version of pycircstat (Berens, 2009); <https://github.com/circstat/pycircstat>.

Modeling

All models were implemented in Python, using NumPy and SciPy libraries. All models are based on repeated random sampling, where one stimulus response from an S1 trial and one stimulus response from an S2 trial are combined. The repetition of this sampling procedure generates a distribution of combined responses. The averaging model combines the pair of responses by taking the vector average of the response angle. In agreement with the reduced amount of backward responses, we implemented a mechanism to reduce the prevalence of such escapes in our model by redistributing backward swims to other headings. The winner-take-all model chooses randomly between the S1 response and the S2 response (effectively adding the S1 and S2 response distribution). The mixture model implements a random assortment between the winner-take-all model (with mix probability p) and the averaging model (with probability $p-1$). Distributions are plotted using a kernel density estimate (KDE) plot, with a von Mises (circularized) distribution. The mix model with bias was optimized using cross-validation and a grid search over parameter space. To compare the similarity of distributions, a circularized version of the energy distance metric was used. The plot in 1K and 1M quantifies the energy distance between models and real data, using many repeated generations of each model (which is stochastic, since the models themselves are based on random sampling from the real data). To generate a p value comparing model performance, we used a permutation test on the difference in energy distance to real data.

Prey capture experiments

Prey capture experiments were performed as described previously (Mearns et al., 2020). Briefly, we made a square chamber (15 × 15 mm, 5 mm deep) with walls made from 2% agarose. Individual larvae were introduced to the chamber with a drop of dense paramecia culture (*Paramecium multimicronucleatum*, Carolina Biological Supply Company, Burlington, NC). The setup was lit from below with an IR LED light source, and larvae were filmed for 20 minutes at 500 fps with a high-speed camera (Photonfocus MV1-D1312-160-CL, Switzerland). The analysis was performed offline with custom-written Python code. We extracted the outline of the fish from each frame by finding the largest contour following background subtraction and thresholding. A second threshold was then set to extract contours of the eyes and swim bladder. We used the image moments of these contours to calculate the angle of each eye. Eye convergence in each frame was calculated as the difference between the eye angles, with positive values corresponding to eye convergence, zero corresponding to eyes parallel, and negative angles corresponding to eye divergence. For each animal, we defined the threshold for prey engagement as the local minimum of the bimodal distribution of eye convergence angles across all frames and defined the prey capture score as the proportion of time the fish spent engaged in prey capture.

Swim bouts were segmented automatically using a change point algorithm on the derivative of the tail angle with respect to time. J-turns were defined as any bout where the eyes were unconverged prior to the bout onset and converged by the end of the bout (i.e., the first bout in any hunting episode when the prey are first detected). Bout integrals were calculated by summing the tail angle values over the duration of a bout.

Calcium imaging

Zebrafish larvae were embedded in 2.5% low melting point agarose (Invitrogen). Visual stimuli were generated using custom Psychopy2/Psychopy3 scripts (Peirce et al., 2019) and consisted of black looming stimuli. For prey competition (Figures S4A–S4C) movies from recordings of real paramecia were binarized and scaled, keeping important parameters such as kinetics and size in agreement with previous work (Semmelhack et al., 2014). For quantification of the number of neurons before and after two-photon ablation of neurons the stimuli consisted of six presentations (three times in nasalward direction and three times in temporalward direction, alternating order) of a prey-like (8° dot, kinetics extracted from the same real paramecia movie described above, red on

black), followed by three presentations of a black looming stimulus (expanding 60 deg/s for 2 s) and three presentation of a dimming stimulus (red to black, 2 s).

The minimum distance between competing stimuli resulting in non-overlapping receptive fields was determined in pilot experiments to be at least 30 degrees in visual space. The centers of the two looming stimuli are 60 degrees apart, and at full expansion, the stimuli are 45 degrees, 30 degrees, or 15 degrees apart (for conditions where both stimuli are equal and expansion rate is, respectively, 30 deg/s, 60 deg/s, and 90 deg/s). Visual stimuli were projected onto a white diffusive screen using the red channel of a LED projector (LG, Model No. PA72G) from the side (animal distance to the screen was approximately 4cm) and a DLP® LightCrafter 4500 development module from the bottom (animal distance to the screen was approximately 1 cm). For full emission spectrum of projectors see:

https://github.com/amgfernandes/Imaging_analysis/tree/master/Projector_measurements.

Size of the stimuli (in degrees of visual angle) was adjusted taking into account the size of the projection and distance to the fish using PsychoPy2/Psychopy3 Monitor Center. For monocular stimulation, we presented both from the side and bottom. Results were similar for both conditions. The 2P microscope used for imaging and holographic optogenetics is based on a modified Femtonics 3DRC (Femtonics, Hungary) driven by a Ti:Sapphire laser source (Chameleon Ultra II, Coherent) (see Dal Maschio et al., 2017). An electrically tunable lens placed just before the galvo scanner (ETL, Optotune, EL-10-30-Ci-IR-LD-MV) was used to enable fast remote refocusing. For Figure S3A we used a remote-Z-scanning module with a resonant 2P microscope. The module consists of a second objective and a piezo-modulated mirror, which allows us to shift between conjugated focal planes in the fish brain with high frequency.

Two-photon computer generated holographic (2P-CGH) optogenetics

For more details of the holographic approach see Dal Maschio et al. (2017). For experiments in the absence of visual stimuli, we stimulated Lhx9 NI cells with 920 nm excitation for 1000 ms, while recording the activity of tectal neurons with GCaMP6s at 1,020 nm (both cytosolic and nuclear version of GCaMP6s were used). Only cells that showed an increased activity of at least 15% when compared to baseline mean activity were considered for the analysis. This analysis also selects cells with strong spontaneous activity (this was very common for ChR2 negative control fish). For experiments with visual stimuli, optogenetic stimulation of ChR2 positive neurons was performed with 920 nm excitation with a total duration of 1000 ms (photostimulation started 500 ms before the visual stimulation and ended 500 ms later at the end of visual stimulation). Visual stimulation consisted of a single looming stimulus presented from the side (total duration of expansion of 500 ms, 60°/s expansion rate). Imaging was performed simultaneously with GCaMP6s at 1020 nm.

Genetic ablation of neurons

Larvae expressing *Tg(UAS:nfsb-mCherry)c264*, were treated with 7.5mM metronidazole (MTZ, Sigma Aldrich) in fish water containing 0.2% DMSO, typically for at a minimum of 8h. MTZ solution was washed three times and larvae were allowed to recover for at least 12h before imaging or behavioral experiments were performed.

Imaging analysis

Imaging analysis was performed with custom-written Python scripts. A regressor-based pixel-wise analysis of the imaging data was performed similarly to (Miri et al., 2011). Briefly, regressors are generated with time series that are set to zero for all time points except the time points of stimulation (visual stimuli), which are set to one. The regressors are then convolved with a kernel describing the GCaMP response function (GCaMP6s, tau-off = 1.8 s). *T*-scores for each pixel were calculated as in (Miri et al., 2011) and only pixels that passed an empirically determined threshold (using the 90th percentile) were used for further analysis. For Figure 21 a linear regression was used (Python `scipy.stats.linregress`). For ROI analysis, a linear regression approach was used (Python `scikit-learn`) similarly to Helmbrecht et al. (2018). We used the ordinary least-squares linear regression, $y = a + b_0x_0 + b_1x_1 + e...$ (*y* representing the functional response, *a* representing the Y-intercept, *b* the coefficients (slope), *x* the regressors (independent variables) and *e* the random error term) to select ROIs. The coefficients of determination (*R*²), were calculated using the `sklearn.linear_model.LinearRegression` method. *R*² was used to set a threshold removing ROIs with activity not locked to stimulus presentation (spontaneously active). The estimated coefficients for the linear regression problem were used to set a second threshold that selects ROIs fitting to the regressors used (time series set to zero for all time points except the time points of visual stimulation).

For quantification of holographic optogenetic activation effects, we generated a control distribution by shuffling the labels of trials with visual alone and trials with visual combined with optogenetic stimulation. This approach led to a normal distribution with a strong peak at around zero, used to set thresholds considered for quantification of enhanced and suppressed ROIs.

For quantification of the number of ROIs in both tecta before and after two-photon ablation of NI neurons, we used a method consisting of steps to identify functionally distinct cells, and then distinguishing prey-like, looming, and dimming-evoked responses. Extracted ROIs (see above) were clustered using hierarchical clustering (agglomerative approach with Python `scipy.cluster.hierarchy.linkage`) for visualization of response types. Regressors were created for each stimulus and convolved with a GCaMP6s kernel (see above) and a multiple linear regression (Python `sklearn.linear_model.LinearRegression`) was used to calculate *R*² scores of the regressors to the functional responses of each ROI. *R*² values were then used to set a threshold removing spontaneously active

ROIs. Afterward, the maximum score of either the prey-like stimuli (nasalward and temporalward), looming or dimming stimuli was used to assign ROIs to specific response types.

Optogenetic stimulation during presentation of looming stimuli

To perform optogenetic stimulation of the NI during the bilateral presentation of looming stimuli we used either *Tg(lhx9:Gal4VP16)mpn203*; *Tg(UAS:ChR2(H134R)-mCherry)mpn134* or *Tg(lhx9:Gal4VP16)mpn203*; *Tg(UAS:GtACR2-eYFP)sq212* double transgenic larvae. Controls were either sibling *lhx9:Gal4* larvae not expressing an optogenetic effector or *Tg(lhx9:Gal4VP16)mpn203*; *Tg(5xUAS:EGFP)zf82* larvae. In some experiments we used *Tg(lhx9:Gal4VP16)mpn203*; *Tg(UAS:ChR2(H134R)-mCherry)mpn134*; *Tg(UAS-E1b:Kaede)s1999t* larvae to photoconvert the stimulated region and confirm we were correctly targeting the NI.

We embedded 5–7 dpf larvae in 2% low-melting point agarose. After the agarose solidified, the dish was filled with Danieau's solution and agarose around the tail below the swim bladder was cut away using a scalpel, leaving the tail free to move and tested them the following day (6–8 dpf). Larvae were positioned between two LCD screens (LCD35VGAN, Accelelevision) displaying a white background. A 50 μ m light fiber (M24L05, Thorlabs), connected to a laser beam combiner (Lighthub, Omicron) to either stimulate (473 nm, LuxX 80 mW, Omicron) or photoconvert (405 nm, LuxX 60 mW, Omicron) neurons, was positioned over the NI via a microcontroller (MC1000e, Siskiyou). For stimulation, we used 0.5–2 mW power as measured at the fiber tip, pulsed at 30 Hz with a 50% duty cycle. We recorded tail movements at 350 fps with a Pike F032B camera (Allied Vision Technologies) positioned above the fish and backlit from below using a custom-built IR LED array.

We performed 6–14 trials per fish, with at least three minutes between trials. Every trial consisted of a 10 s pre-stimulation phase, followed by 3 s of light stimulation, and then a 10 s post-stimulation phase. In half of the trials for each animal, we presented looming stimuli to both eyes simultaneously during the stimulation phase. In these "looming trials" a stationary black dot (5° visual angle) appeared on each screen 0.5 s after the onset of the optogenetic stimulation. After one second, the dots expanded at a constant linear rate (20–40°/s) for one second and then disappeared. Stimuli were controlled using the PsychoPy2 python library (Peirce, 2007). In photoconversion experiments, we switched to the UV laser and stimulated for 5 minutes (0.5 mW, 30 Hz, 50% duty cycle) after all experimental trials had concluded.

Analysis of optogenetic experiments

We excluded any animal that did not respond at least once to the looming stimuli. We tracked the tail of the fish using computer vision algorithms written in Python 3 (Helmbrecht et al., 2018). The tail angle was defined as the angular deviation of the tail tip from the midline of the fish, with negative angles signifying deflections toward the stimulated side. Individual swim bouts were identified using a custom-written bout detection algorithm as described previously (Mearns et al., 2020) ($n = 916$ from 48 fish). We defined light-evoked bouts as any bout whose onset occurred while the laser light was on, and prior to the onset of the expansion of the dots for looming trials. Loom-evoked bouts were defined as any bout that occurred during the expansion phase of the visual stimulus. Fish also performed spontaneous bouts outside the stimulation phase of the experiment, which were included to generate the bout space but not subject to further analysis. To generate the bout space we first excluded any bout whose standard deviation was greater than 50° and maximum absolute tail angle greater than 120° ($n = 35$), as these represented struggling behaviors that likely occur as a result of the fish being embedded rather than in response to optogenetic or visual stimulation. We computed three features for each bout: the bout integral (sum of all tail angles over the duration of a bout), the maximum tail amplitude (signed maximum value of the absolute tail angle), and the tail beat frequency (bout peaks were identified using the `scipy.signal.find_peaks` Python function). To identify bout types, we applied hierarchical clustering over these three features and identified a maximum in the silhouette score at three clusters (sklearn Python library). Note that, to ensure consistent boundaries between bout types for ipsilateral and contralateral swims, we ignored the signs of the bout features. We assigned the labels C-start, burst swim and slow swim to the clusters following post hoc inspection of the bouts belonging to each cluster.

Statistical comparisons were always between the control group and either ChR2(+) or GtACR2(+) animals and were performed using the `scipy.stats` Python library. Probabilities of evoking swims under different stimulation conditions (light only or light + loom) were compared using Mann-Whitney U tests. The number of C-starts and burst swims elicited under different stimulation conditions were compared using Mann-Whitney U tests. Differences in the distributions of maximum tail amplitudes were compared using a Kolmogorov-Smirnov test.

Two-photon ablation of neurons

We targeted inhibitory (GABAergic-positive) and excitatory (*lhx9*-positive) NI neurons for ablation based on their position and fluorescence (GFP, Dendra or mCherry) using a two-photon microscope. A line scan spanning each cell was performed for a total of three times (800 nm, for 10 ms each round with 1 s delay in between). The power used was dependent on the dorsal-ventral position of the cells (250 mW was used for dorsal areas and 330mW was used for more ventral areas). To validate that this approach led to specific ablation of single cells with minimal off-target damage we recorded the same neurons before and after the ablation protocol. The appearance of red autofluorescence after ablation in the target neuron but not in the neighboring neurons verified that this protocol was highly specific (see Figure 6A; compare pre-ablation and post-ablation). Sham ablations consisted of ablating cerebellum neurons labeled by the *Tg(lhx9:Gal4)mpn203* line. We targeted approximately 30–40 cells for each line used (same number of cells as for real ablation experiments). Control not ablated fish were embedded in the same dish together with ablated animals and follow the same protocol, except for the ablation part. For behavior experiments, after ablation fish were unmounted from agarose and allowed to recover for at least 12

hours before behavior testing. For imaging experiments, the same tectal plane was recorded before ablation and one hour after ablation.

Single-cell reconstructions

For some single neuron labeling, the transgenic fish line *Tg(brn3c:GAL4, UAS:gap43-GFP)s318t* (BGUG) was crossed to the *Tg(lhx9:Gal4)mpn203* line similar to (Helmbrecht et al., 2018). This approach could not be used with other lines (e.g., *Tg(gad1b:Gal4VP16)mpn155*) possibly due to low expression level. To overcome this problem, we devised another method to achieve sparse labeling by co-injecting a plasmid with a heat shock promoter expressing Cre (*hsp70l:cre*) together with a *UAS:Brainbow* plasmid (*UAS:Brb1.0L*; Robles et al., 2013). These constructs were co-injected with Tol2 mRNA into *Tg(lhx9:Gal4)mpn203* or *Tg(gad1b:Gal4VP16)mpn155*; *Tg(UAS:nfsb-mCherry)c264* embryos. By calibrating the heat shock duration (heat shock in a water bath at 37°C for 5–45 min), the EYFP fluorescence from the *UAS:Brainbow* construct could be used to label single cells. Constructs were pressure injected at a concentration of 25–50 ng/μL into 1–4 cell-stage embryos. Larvae were screened using a confocal microscope for single labeled projection neurons and positive larvae were used to record a high-resolution (1024 × 1024 pixels) confocal stack. Labeling of some individual GABAergic neurons was also achieved by crossing the *Tg(gad1b:Gal4VP16)mpn155* line to a *UAS:HaloTag* line that expresses in a highly variegated fashion. Due to the highly variegated expression of the *UAS-HaloTag*, single neurons in the *Gad1b* pattern could be imaged and reconstructed. This approach is part of the mapzebrain project (<https://fishatlas.neuro.mpg.de/>; Kunst et al., 2019).

Confocal imaging and anatomical reconstruction of neurons

Before acquiring confocal stacks, fish were anesthetized with 0.02% tricaine. For single-cell reconstructions and generation of the brain atlas imaging was performed as described previously (Helmbrecht et al., 2018). The collected neurons were then traced using the software neuTube (Build1.0z) and confirmed by at least two independent tracers. For live-imaging rainbow experiments, no reference channel was available. However, in the YFP-channel the signal was strong not only for the single neurons but also for the auto-fluorescence of the skin. We took advantage of this and registered the whole-brain YFP-stacks to a standard brain of the skin auto-fluorescence using the Computational Morphometry toolkit (CMTK; <https://www.nitrc.org/projects/cmtk/>;) with the following settings: -awr 01 -T30 -X52 -C8 -G120 -R3 -A'-accuracy 0.8' -W'-accuracy 0.8'. This standard brain was generated by registering the red and green channel of 150 fish expressing *Tg(elavl3:lyn-tagRFP)mpn404* to the standard brain as described in Helmbrecht et al. (2018). The registered green channel of these fish was then averaged to obtain a standard brain of the skin auto-fluorescence. In experiments using fixed animals, fish were stained against GFP for single neurons and synapsin as a whole brain marker and registered to the fixed synapsin standard brain as described in Kunst et al. (2019). The skin-registered neurons were then bridged to the synapsin standard brain using the *Tg(elavl3:lyn-tagRFP)mpn404* channel. All reconstructed neurons were visualized in their common coordinate system (synapsin) using mapzebrain (<https://fishatlas.neuro.mpg.de/neurons/>; Kunst et al., 2019; Figure 7) or the single-neurite tracer ImageJ plugin (Figures S10A–S10D). Standard brain *s1020t* used in Figure S10D is part of the mapzebrain project.

In situ hybridization and immunohistochemistry

Stainings were performed according to published protocols (Fernandes et al., 2012). For antibodies used see Key Resources Table. Riboprobes for *adcypap1a*, *nnos1* and *lhx9*, were generated from cDNA and subcloned into the TOPO vector (pCR2.1-TOPO, Invitrogen). Sense probes were used as a negative control for newly cloned probes. Riboprobes for *gad1b* and *trh* (Löhr et al., 2009) were a kind gift of Wolfgang Driever. For Figures S4K–S4M, DAPI (28718-90-3, Sigma) was used to label nuclear DNA of cells.

QUANTIFICATION AND STATISTICAL ANALYSIS

For statistical tests, we used the Python SciPy, Numpy, Matplotlib, Seaborn libraries and GraphPad Prism version 7 for Windows. For imaging experiments, we preferentially selected fish with strong expression. All error bars used are mentioned in figure legends.

Quantification of arbor length and number of arborizations of NI cells

To measure the total length and number of arborizations of NI cells projections in the tectum we used a mask for the tectum part of the mapzebrain (<https://fishatlas.neuro.mpg.de/neurons/>) project and extracted the axonal part occupied by the axon terminals. Values were averaged for each population (inhibitory and excitatory) and analyzed with Python. Plots were made using the Seaborn library. Pairwise multiple comparisons were performed with Kruskal-Wallis H-test from the SciPy library, followed by post hoc tests (Conover's test) with the scikit-posthocs library (<https://scikit-posthocs.readthedocs.io/en/latest/>; related to Figures S10F and S10G).

Neuron, Volume 109

Supplemental Information

**Neural circuitry for stimulus selection
in the zebrafish visual system**

António M. Fernandes, Duncan S. Mearns, Joseph C. Donovan, Johannes Larsch, Thomas O. Helmbrecht, Yvonne Kölsch, Eva Laurell, Koichi Kawakami, Marco dal Maschio, and Herwig Baier

Suppl. Fig. S1 (Fig. 1)

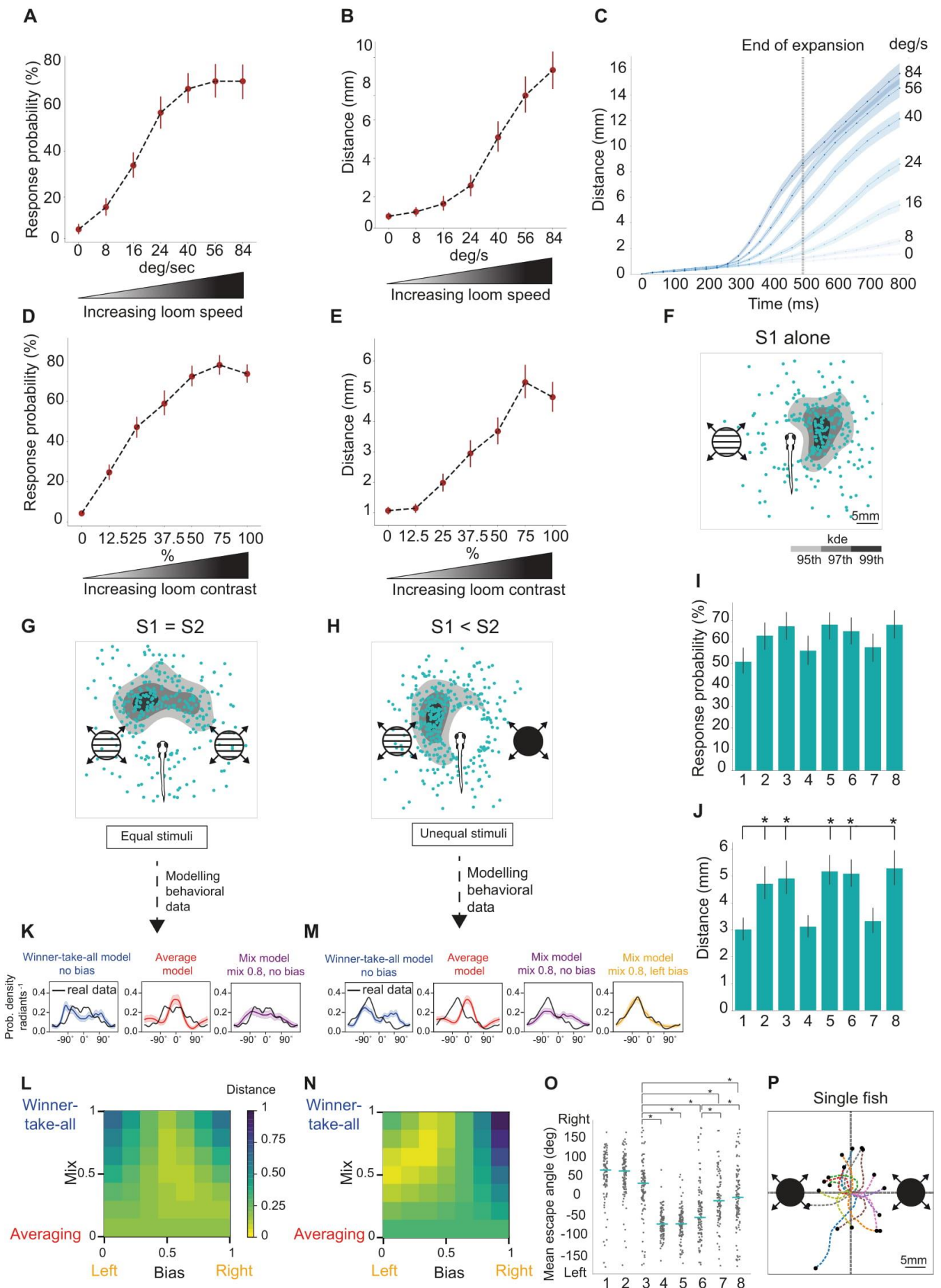


Figure S1. Zebrafish modulate their escape behavior in response to differences in expansion rate and contrast of looming stimuli. Related to Figure 1.

(A, B) Probability of escape (A) and distance traveled (B) increase with looming expansion rate.

(C) Time course plot of distances traveled under different looming expansion rate conditions. Vertical line marks the end of the expansion (500 ms) for stimuli.

(D, E) Probability of escape (D) and distance traveled (E) increase with stimulus contrast.

(F) Response to a single looming stimulus (S1 alone, 60°/s) presented on the left side of the fish. Blue dots are the XY positions of the fish following their escape at the end of the expansion period of the stimulus (500 ms, 60°/s). In grayscale are the kernel density estimation (KDE) isocontours of the same data.

(G) Competition (S1 = S2) of equal stimuli (60°/s).

(H) Competition (S1 < S2) of unequal stimuli (60°/s vs. 90°/s).

(I, J) Escape probability (I) and distance traveled (J) for all binocular competition conditions. Conditions: 1) S1 alone, 60°/s; 2) S1 alone, 90°/s; 3) S1 and S2, 90°/s vs 60°/s; 4) S2 alone, 60°/s; 5) S2 alone, 90°/s; 6) S1 and S2 alone, 60°/s vs 90°/s; 7) S1 and S2, 90°/s vs 90°/s

(K) Modeling of behavior outcome for equal stimuli competition (60°/s). Shaded areas are 95% confidence intervals (CI).

(L) Heatmap showing the normalized energy distance from panel (K) depending on the model parameters (Bias and Mix). Bias: represents the probability of response left vs right; Mix: represents the mixing factor between 'winner-take-all' and 'averaging' models.

(M) Modeling of behavior outcome for unequal stimuli competition (60°/s vs. 90°/s). Shaded areas are 95% CI.

(N) Heatmap showing the normalized energy distance from panel (L) depending on the model parameters (Bias and Mix).

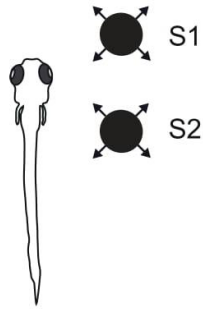
(O) Summary plot showing mean escape angle for all conditions during binocular competition.

(P) Competition (S1 = S2) of equal stimuli (90°/s) for a single animal (18 trials shown). Different colors represent the different trials. Errors are SEM.

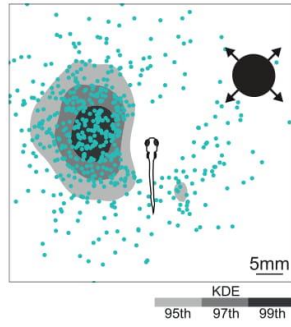
* marks significant comparisons (p-value < 0.05, Tukey's HSD pairwise test) except for panel (O), where a circular data statistics approach was used (p-value < 0.05, Watson-Williams test, see methods). N=117 fish for all panels. Conditions similar to panel (I).

Suppl. Fig. S2 (Fig. 2)

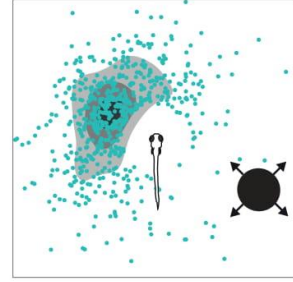
A Monocular competition



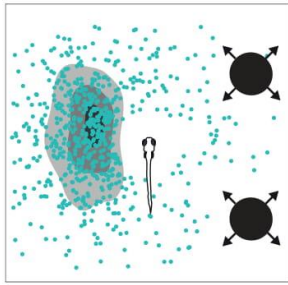
B S1 alone



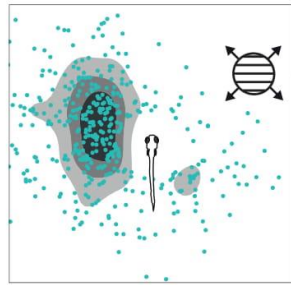
C S2 alone



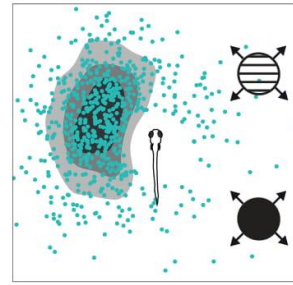
D S1 = S2



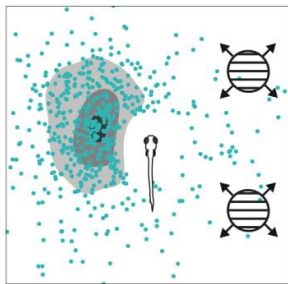
E S1 alone



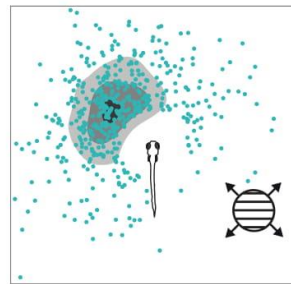
F S1 < S2



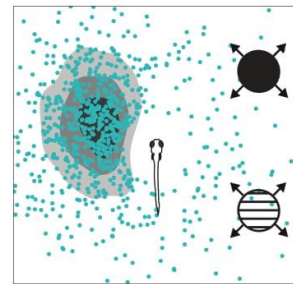
G S1 = S2



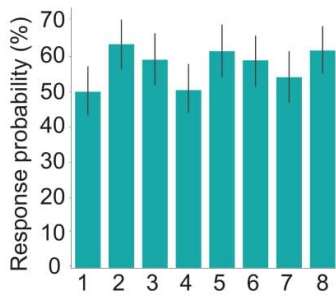
H S2 alone



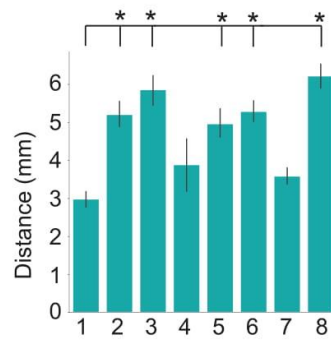
I S1 > S2



J



K



L

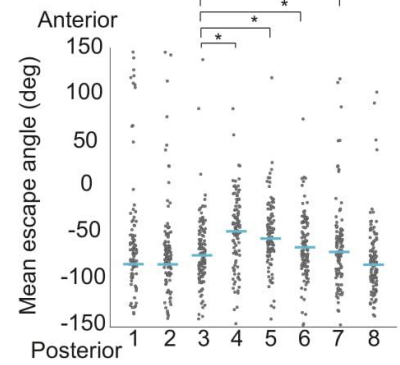


Figure S2. Monocular stimulus competition. Related to Figure 2.

(A) Schematic of monocular competition paradigm. Two stimuli are presented in the visual field of the same eye, anteriorly and posteriorly at 45° or 135°, relative to the fish center of mass, respectively, with 0 being the fish's initial heading direction.

(B) Response to looming stimulus (S1 alone, 90°/s) presented in the anterior visual field. Blue dots are the XY positions of the fish after escape at the end of the expansion period of the stimulus. In grayscale are the kernel density estimation (KDE), isocontours of the same data. Fish schematic enlarged for clarity.

(C) Response to looming stimulus (S2 alone, 90°/s) presented posteriorly.

(D) Competition (S1 = S2) of equal strength stimuli (90°/s).

(E) Weak stimuli (S1, 60°/s) presented on the anterior part of the visual field.

(F) Competition (S1 < S2) of unequal stimuli (60°/s vs. 90°/s).

(G) Competition (S1 = S2) of equal strength stimuli (60°/s).

(H) Weak stimuli (S2, 60°/s) presented on the posterior part of the visual field.

(I) Competition (S1 > S2) of unequal stimuli (90°/s vs. 60°/s).

(J) Response probability plot for all monocular competition conditions. Conditions: 1) S1 alone, 60°/s; 2) S1 alone, 90°/s; 3) S1 and S2, 90°/s vs 60°/s; 4) S2 alone, 60°/s; 5) S2 alone, 90°/s; 6) S1 and S2 alone, 60°/s vs 90°/s; 7) S1 and S2, 60°/s vs 60°/s; 8) S1 and S2, 90°/s vs 90°/s

(K) Distance travelled by the fish for all monocular competition conditions. Conditions similar to panel (J).

(L) Summary plot showing mean escape angles for all conditions during monocular competition.

* marks significant comparisons (p-value < 0.05, Tukey's HSD pairwise test) except for panel (L), where a circular data statistics approach was used (p-value < 0.05, Watson-Williams test, see methods). N=126 fish for all panels. Errors are SEM. Conditions similar to panel (J).

Suppl. Fig. S3 (Fig. 2)

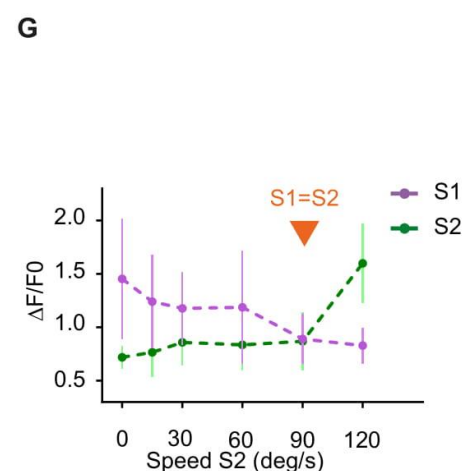
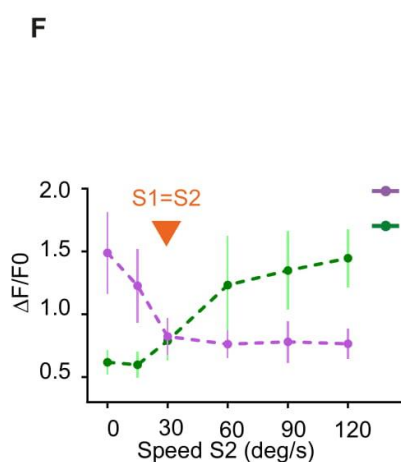
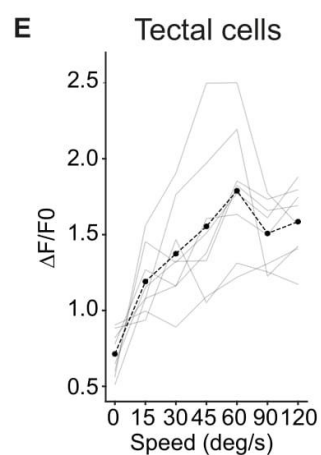
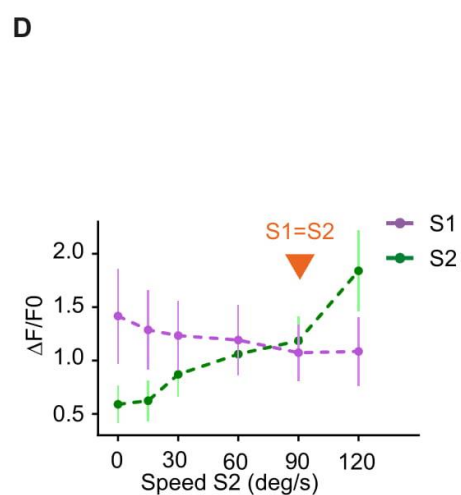
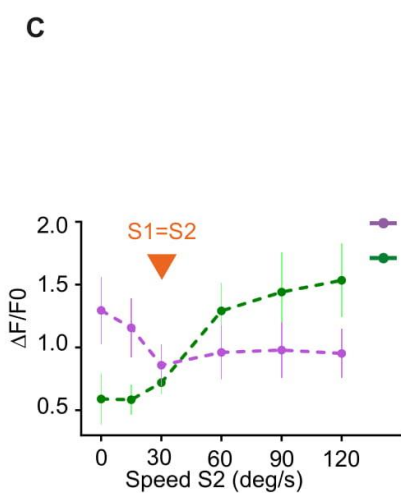
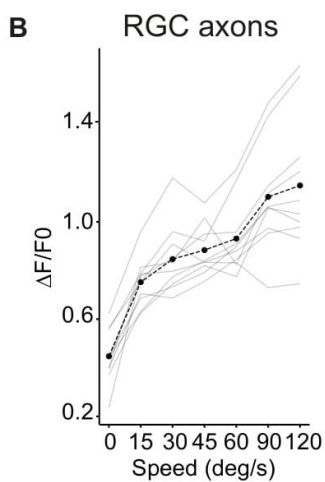
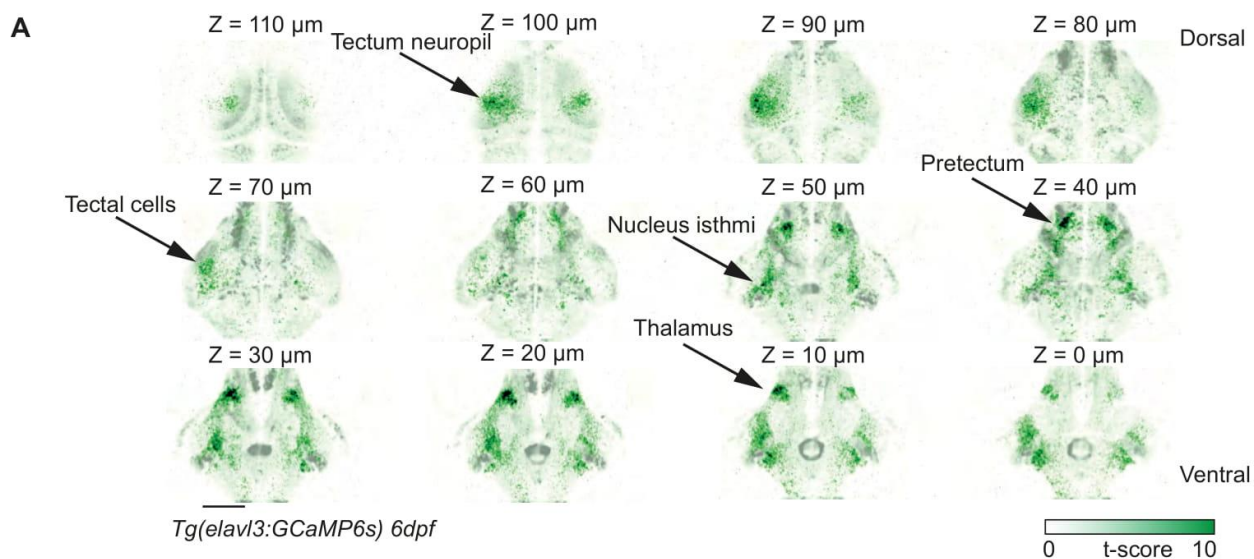


**Figure S3. Whole-brain imaging identifies regions active during stimulus competition.
Related to Figure 2.**

(A) Whole-brain imaging of regions that respond reliably to looming stimuli (dark green). Scale bar is 100 μm . In this example, the stimulus was presented to the right side of the animal.

(B) RGC axon activity increases with faster looming expansion rate. Strong stimuli drive RGC axons to saturation. N=3 fish.

(C) Summary plot across all conditions for RGC axon pixels. Suppressed RGC pixels are shown in magenta. Enhanced RGC pixels are shown in green. S1 expansion rate is $30^\circ/\text{s}$.

(D) Similar to (C), but S1 expansion rate is $90^\circ/\text{s}$. N=5 fish.

(E) Tectal cell activity increases with faster looming expansion rate. Strong stimuli drive tectal cells to saturation. N=2 fish.

(F) Summary plot across all conditions for tectal pixels. Suppressed tectal pixels are shown in magenta. Enhanced tectal pixels are shown in green. S1 expansion rate is $30^\circ/\text{s}$.

(G) Similar to (F), but S1 expansion rate is $90^\circ/\text{s}$. N=5 fish. Errors are SD.

Suppl. Fig. S4 (Fig. 2)

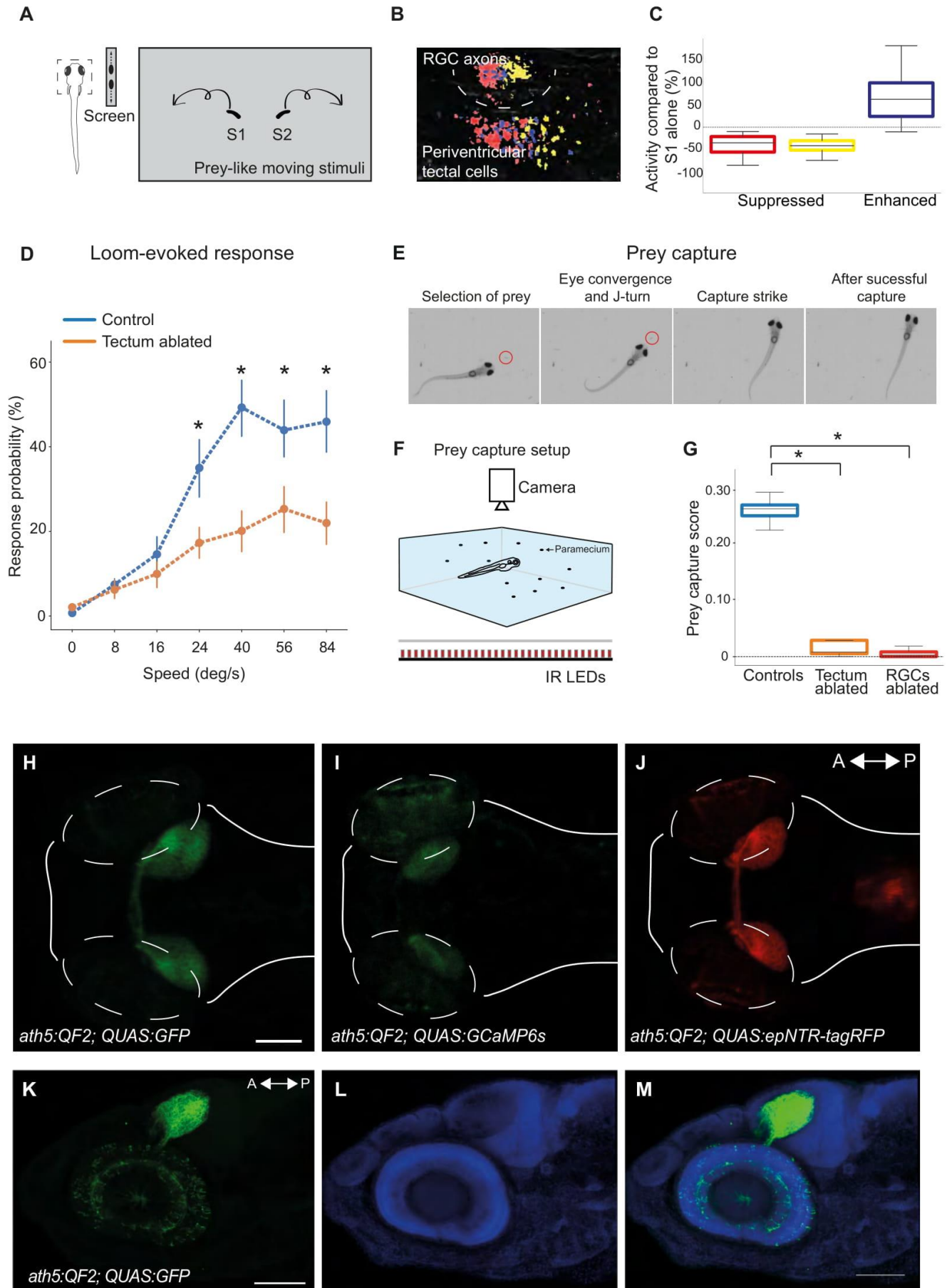
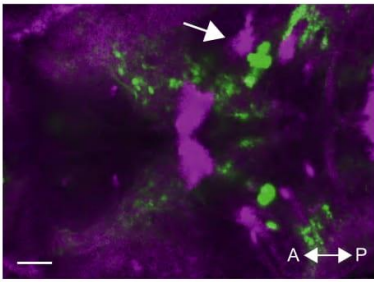


Figure S4. Suppression of activity by competitor stimulus is detectable in RGC axons and tectal cells. Related to Figure 2.

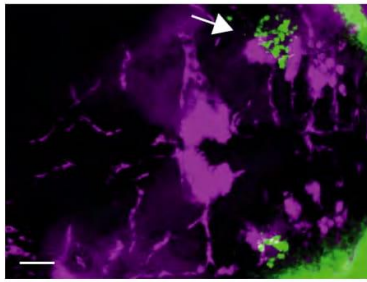
- (A) Monocular competition paradigm for prey-like moving stimuli.
- (B) Presentation of competing prey-like stimuli in the monocular visual field leads to suppression (red pixels responding to S1 and yellow pixels responding to S2) and enhancement of responses (blue pixels respond to both stimuli, with overlapping receptive fields for S1 and S2) in RGC axons and tectal cells.
- (C) Quantification of responses to competing prey-like stimuli. Same colors as in B. Activity was normalized to activity in response to a single stimulus. N=5 fish.
- (D) Ablation of tectal cells leads to impaired responses to looming stimuli (control in blue, ablated fish in orange). N=45 fish. * marks significant comparisons Mann-Whitney-U followed by Bonferroni's correction. * marks significant comparisons (p -value < 0.05).
- (E) Example of hunting sequence leading to the successful capture of a paramecium (red circle).
- (F) Schematic of the setup used to record prey capture events in larval zebrafish.
- (G) Ablation of tectal cells leads to impaired responses to prey items (paramecia). Shown is prey capture score for control fish (non-expressors treated with MTZ, n=9 fish), tectum ablated fish (*SAGFF(LF)81C; UAS:NTR-mCherry*, treated with MTZ, n=4 fish) and RGC-ablated fish (*ath5:Gal4; UAS:NTR-mCherry*, treated with MTZ, n=4 fish). Control vs. RGC ablation: $p < 0.05$, control vs. tectum ablation: $p < 0.05$, RGC ablation vs. tectum ablation: $p = 0.689$, Mann-Whitney-U followed by Bonferroni's correction. * marks significant comparisons (p -value < 0.05).
- (H) Newly developed QF2 transgenic lines to label retinal circuits. QF2 (*ath5:QF2*) activation of QUAS:GFP (in green) in RGCs in a live zebrafish larvae.
- (I) QF2 (*ath5:QF2*) activation of QUAS:GCaMP6s (in green) in RGCs in a live zebrafish larvae.
- (J) QF2 (*ath5:QF2*) activation of QUAS:epNTR-tagRFP (in red) in RGCs in a live zebrafish larvae.
- (K-M) Immunohistochemistry anti-GFP (in green) showing expression of GFP in RGC axons. DAPI staining is shown in blue. Lateral view. Scale bars represent 100 μ m.

Suppl. Fig. S5 (Fig. 3)

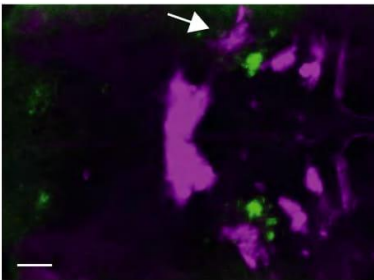
A anti-TH anti-CHAT



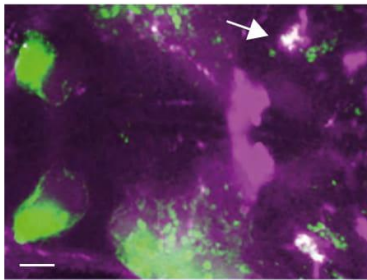
B *adcyap1a* anti-CHAT



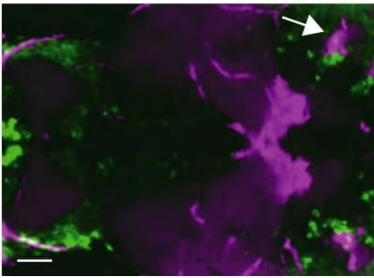
C *trh* anti-CHAT



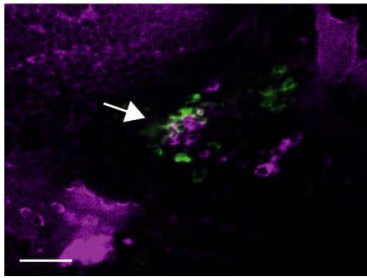
D anti-REELIN anti-CHAT



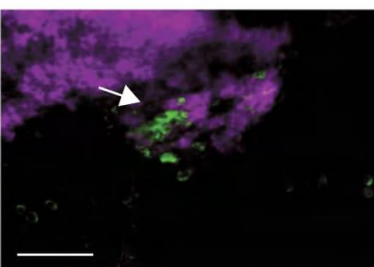
E *nnos1* anti-CHAT



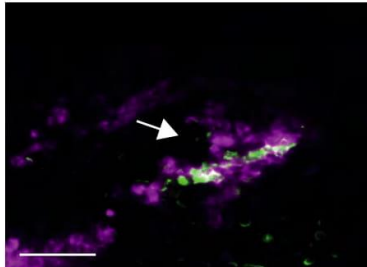
F *lhx9:Gal4* anti-CHAT



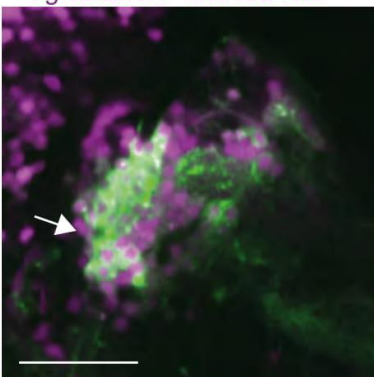
G *lhx9:Gal4* *lhx9*



H *gad1b:Gal4* *gad1b*



I *lhx9:Gal4; UAS:Dendra*
vglut2a:loxP-DsRed-loxP



J *gad1b:Gal4; UAS:Dendra*
gad1b:loxP-DsRed-loxP

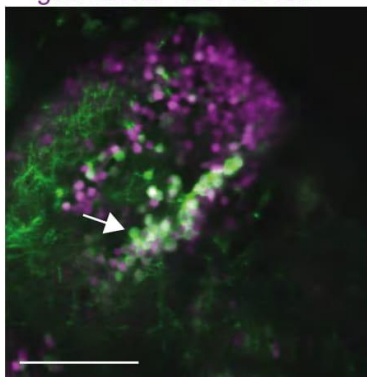


Figure S5. Nucleus isthmi is evolutionarily conserved in larval zebrafish. Related to Figure 3.

(A) Tyrosine hydroxylase (TH) immunohistochemistry labeling (in green) showing Locus Coeruleus (LC) in the vicinity of cholinergic nucleus isthmi cells (arrow points to nucleus isthmi, anti-ChAT in magenta).

(B) *adcyap1a* expression (in green) in the vicinity of cholinergic nucleus isthmi cells (in magenta, white arrow).

(C) *thyrotropin-releasing hormone (trh)* (in green) in the vicinity of cholinergic nucleus isthmi cells (in magenta, white arrow).

(D) REELIN immunohistochemistry labeling (in green) showing colocalization with cholinergic nucleus isthmi cells (in magenta, white arrow).

(E) *nitric oxide synthase (nnos1)* expression (in green) in the vicinity of cholinergic nucleus isthmi cells (in magenta, white arrow).

(F) *lhx9:Gal4* line expression (in green) showing colocalization with cholinergic nucleus isthmi cells (in magenta, white arrow).

(G) *lhx9:Gal4* line expression (in green) showing colocalization with *lhx9* expression in the nucleus isthmi (in magenta, white arrow).

(H) *gad1b:Gal4* line expression pattern (in green) showing colocalization with *gad67* mRNA expression in the nucleus isthmi (in magenta, white arrow).

(I) *lhx9:Gal4; UAS:Dendra* live expression (in green) showing colocalization with *vglut2a* neurons in *vglut2a:loxP-DsRed-loxP* line in the nucleus isthmi (in magenta, white arrow).

(J) *gad1b:Gal4; UAS:Dendra* live expression (in green) showing colocalization with GABAergic neurons in *gad1b:loxP-DsRed-loxP* line in the nucleus isthmi (in magenta, white arrow). Scale bars represent 25 μ m.

Suppl. Fig. S6 (Fig. 3)

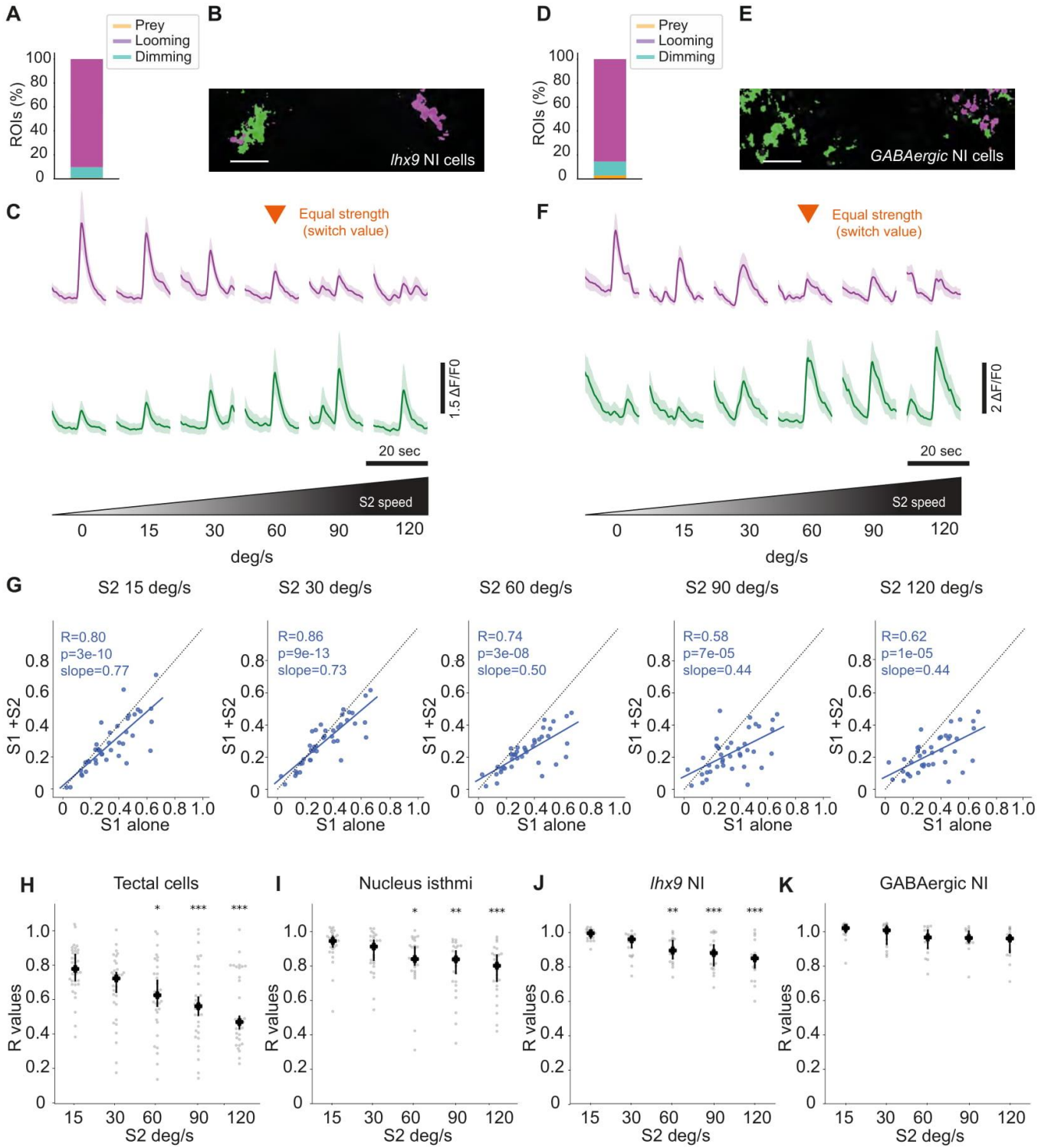


Figure S6. Glutamatergic but not GABAergic nucleus isthmi cells show significant suppression by a competing stimulus across the hemispheres. Related to Figure 3.

(A) Percentage of prey-like (orange), looming (cyan), and dimming (magenta) *lhx9*-positive responsive NI cells. N=3 fish.

(B) Map shows associated S1 responsive glutamatergic (*lhx9:Gal4; UAS:GCaMP6s* positive) nucleus isthmi pixels, suppressed by a stronger S2 stimulus (in magenta). Pixels that enhance their response as a function of S2 intensity are shown in green.

(C) Average of 10 selected glutamatergic nucleus isthmi ROIs suppressed by a stronger S2 stimulus (in magenta). Lower traces, average of 10 selected NI ROIs enhanced by S2 strength (in green). Below is shown schematically S2 strength. Orange arrow shows the condition where both stimuli have equal strength.

(D) Percentage of prey-like (orange), looming (cyan) and dimming (magenta) GABAergic-positive responsive NI cells. N=3 fish.

(E) Map shows associated S1 responsive GABAergic (*gad1b:Gal4; UAS:GCaMP6s* positive) nucleus isthmi pixels, suppressed by a stronger S2 stimulus (in magenta). Pixels that enhance their response as a function of S2 intensity are shown in green. Scale bars represent 25 μm .

(F) Average of 10 selected GABAergic nucleus isthmi ROIs suppressed by a stronger S2 stimulus (in magenta). Lower traces, average of 10 selected GABAergic nucleus isthmi ROIs enhanced by S2 strength (in green). Below is shown schematically S2 strength. Orange arrow shows the condition where both stimuli have equal strength.

(G) Single-trial example of correlation of activity of nucleus isthmi ROIs (*elavl3:nlsGCaMP6s* positive cells in the NI) between trials with single stimuli and competition trials. X-axis shows stimulus alone (S1, 60°/s) and Y-axis shows the activity of ROIs during different competition conditions (from left to right, S2 competitor stimulus with 15, 30, 60, 90 and 120 deg/s expansion rate).

(H) Summary plot for correlation (R-values for each trial is shown in grey and mean + 95% CI is shown in cyan) across multiple conditions for tectal ROIs (*elavl3:nlsGCaMP6s* tectal positive cells). N=5 fish.

(I) Summary plot for correlation (R-values for each trial is shown in grey and mean + 95% CI is shown in cyan) across multiple conditions for nucleus isthmi ROIs (*elavl3:nlsGCaMP6s* NI positive cells). N=4 fish.

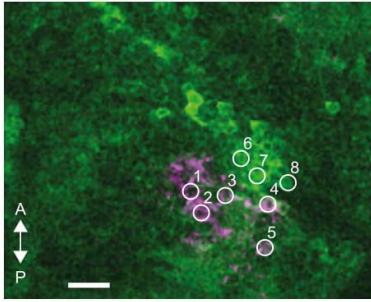
(J) Summary plot for correlation (R-values for each trial is shown in grey and mean + 95% CI is shown in cyan) across multiple conditions for glutamatergic nucleus isthmi ROIs (*lhx9:Gal4; UAS:GCaMP6s* positive cells). N=2 fish.

(K) Summary plot for correlation (R-values for each trial is shown in grey and mean + 95% CI is shown in cyan) across multiple conditions for GABAergic nucleus isthmi ROIs (*gad1b:Gal4;*

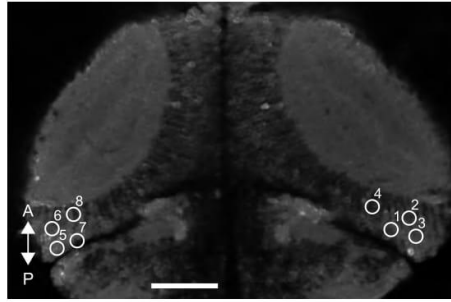
UAS:GCaMP6s positive cells). N=2 fish. Asterisks mark significant comparisons (* p-value < 0.05, ** p-value < 0.01, *** p-value < 0.001).

Suppl. Fig. S7 (Fig.5)

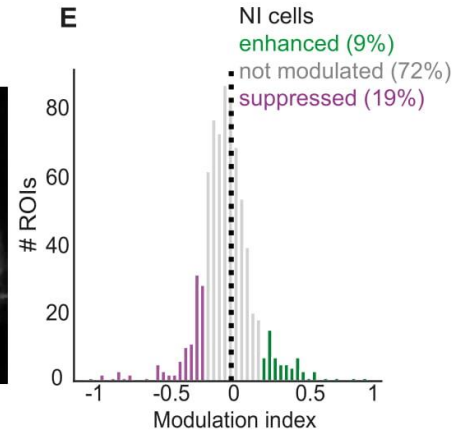
A *lhx9:Gal4VP16;*
UAS:ChR2-mCherry;
elav13:GCaMP6s



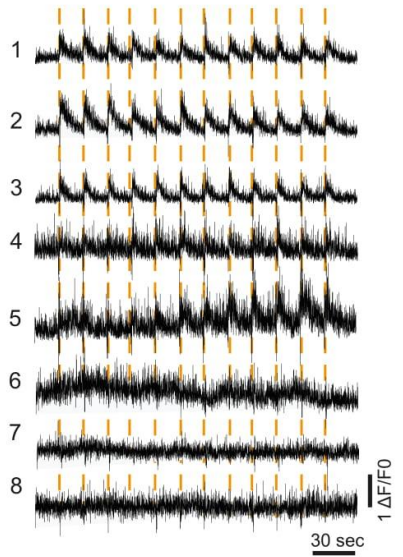
B



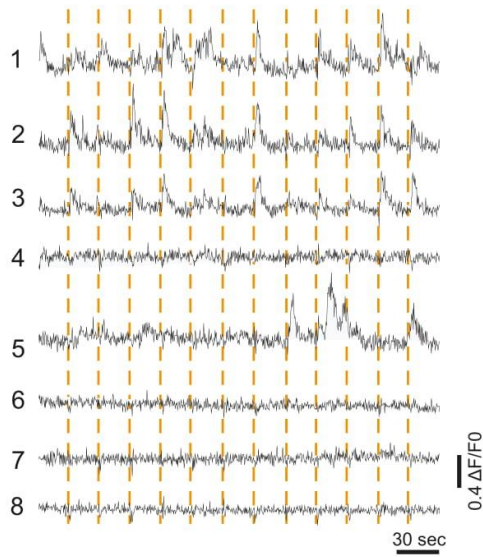
E



C



D



F

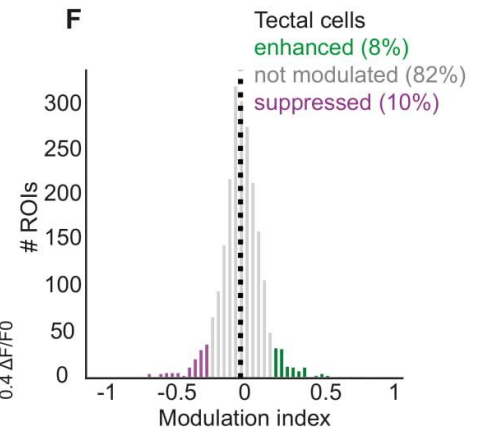


Figure S7. Optogenetic stimulation of the NI modulates tectal responses to looming stimuli. Related to Figure 5.

(A) Expression of pan-neuronal cytosolic calcium indicator (GCaMP6s, in green) and ChR2-mCherry in *lhx9*-positive nucleus isthmi cells (in magenta). Scale bar represents 15 μm .

(B) Expression of pan-neuronal cytosolic calcium indicator (GCaMP6s, in grey) in both tecta. Selected ROIs are shown. Scale bar represents 50 μm .

(C) Optogenetic activation of *lhx9*-positive nucleus isthmi neurons in (F) induced by 1000 ms photostimulation at 920 nm while imaging at 1,020 nm.

(D) Activity of ROIs in (G) driven by optogenetic stimulation of glutamatergic nucleus isthmi neurons.

(E) Histogram showing quantification of modulation of isthmic responses. N=4. Modulation index is defined as $((\text{visual alone}) - (\text{visual combined with optogenetic stimulation})) / ((\text{visual alone}) + (\text{visual combined with optogenetic stimulation}))$.

(F) Histogram showing quantification of tectal response modulation. N=4.

Suppl. Fig. S8 (Fig.6)

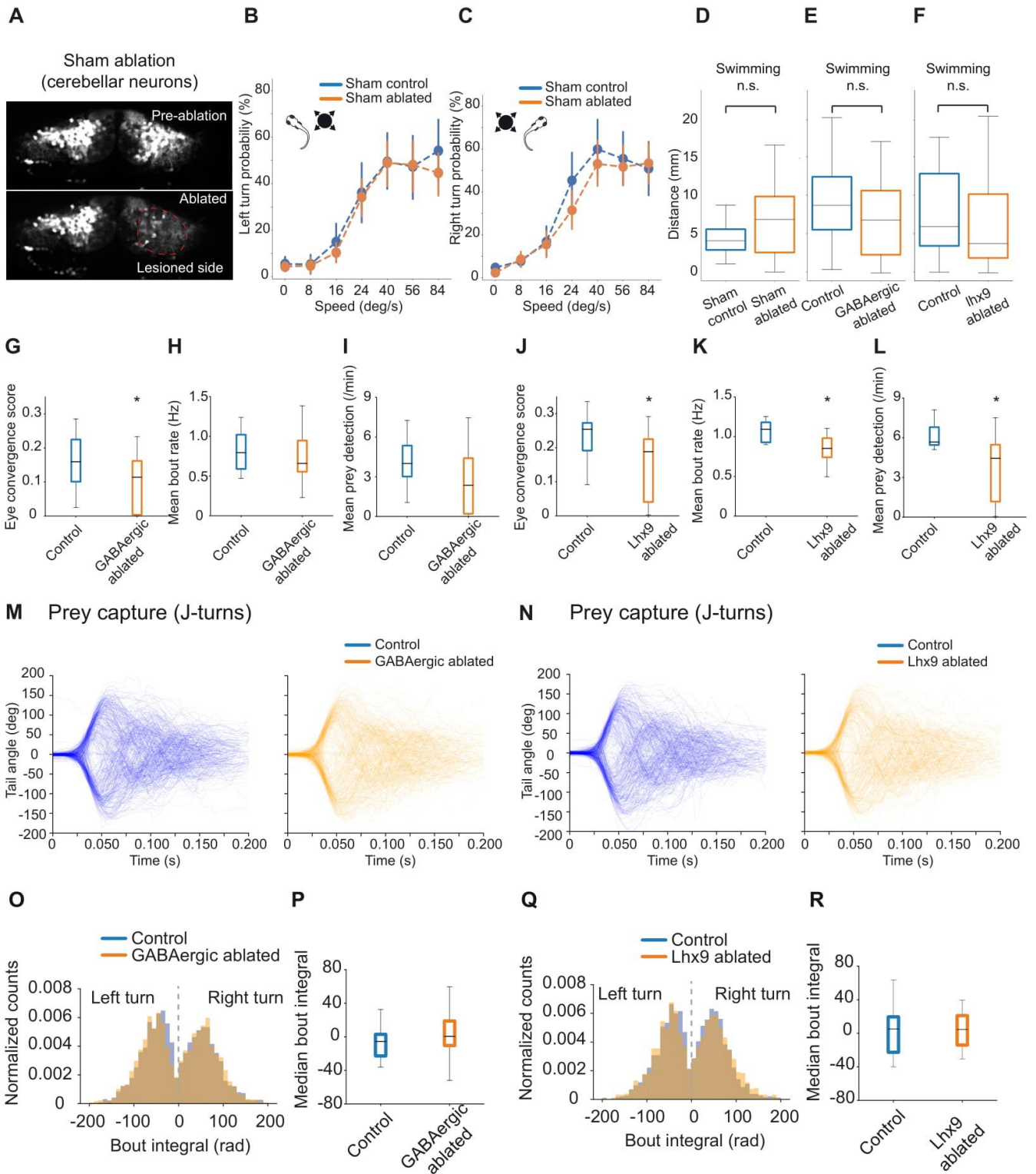


Figure S8. Two-photon ablation of cerebellar and NI neurons. Related to Figure 6.

(A) Targeted 2P laser ablation of cerebellar neurons in zebrafish larvae (sham ablation). Representative images of unilateral 2P laser ablation of *lhx9*-positive cerebellar neurons in *lhx9: Gal4VP16; UAS:GFP* (pre-ablation) and (post-ablation).

(B) Probability of left escapes in controls and sham ablated fish.

(C) Probability of right escapes in controls and sham ablated fish.

(D) Optomotor response in controls and sham ablated fish.

(E) Optomotor response in controls and GABAergic-NI ablated fish.

(F) Optomotor response in controls and *lhx9*-NI ablated fish.

For all looming and optomotor panels, error bars represent standard deviation. Sham ablation panels: N= 8 for control fish (in blue) and N=10 for ablated fish (in orange). All NI ablation panels: N= 10 for control fish (in blue) and N=11 for ablated fish (in orange).

(G) Eye convergence scores in controls and in GABAergic-NI ablated fish.

(H) Mean bout rate in controls and in GABAergic-NI ablated fish.

(I) Mean prey detection rate in controls and in GABAergic-NI ablated fish.

(J) Eye convergence scores in controls and in *lhx9*-NI ablated fish.

(K) Mean bout rate in controls and in *lhx9*-NI ablated fish.

(L) Mean prey detection rate in controls and in *lhx9*-NI ablated fish.

For all prey capture panels: N= 10 for control fish (in blue). N=11 for ablated fish (in orange).

* $p < 0.05$, Mann–Whitney U test.

(M) Tail-angle during J-turns in response to paramecia in control fish (blue) and GABAergic-NI ablated fish (orange).

(N) Tail-angle during J-turns in response to paramecia in control fish (blue) and *lhx9*-NI ablated fish (orange).

(O) Histogram showing normalized counts of bout integral (in radians) during J-turns in response to paramecia in control fish (blue) and GABAergic-NI ablated fish (orange).

(P) Median bout integral plot related to (F).

(Q) Histogram showing normalized counts of bout integral (in radians) during J-turns in response to paramecia in control fish (blue) and *lhx9*-NI ablated fish (orange).

(R) Median bout integral plot related to (H). For all prey capture panels: N= 10 for control fish (in blue). N=11 for ablated fish (in orange). For all prey capture panels, * $p < 0.05$, Mann–Whitney U test.

Suppl. Fig. S9 (Fig.6)

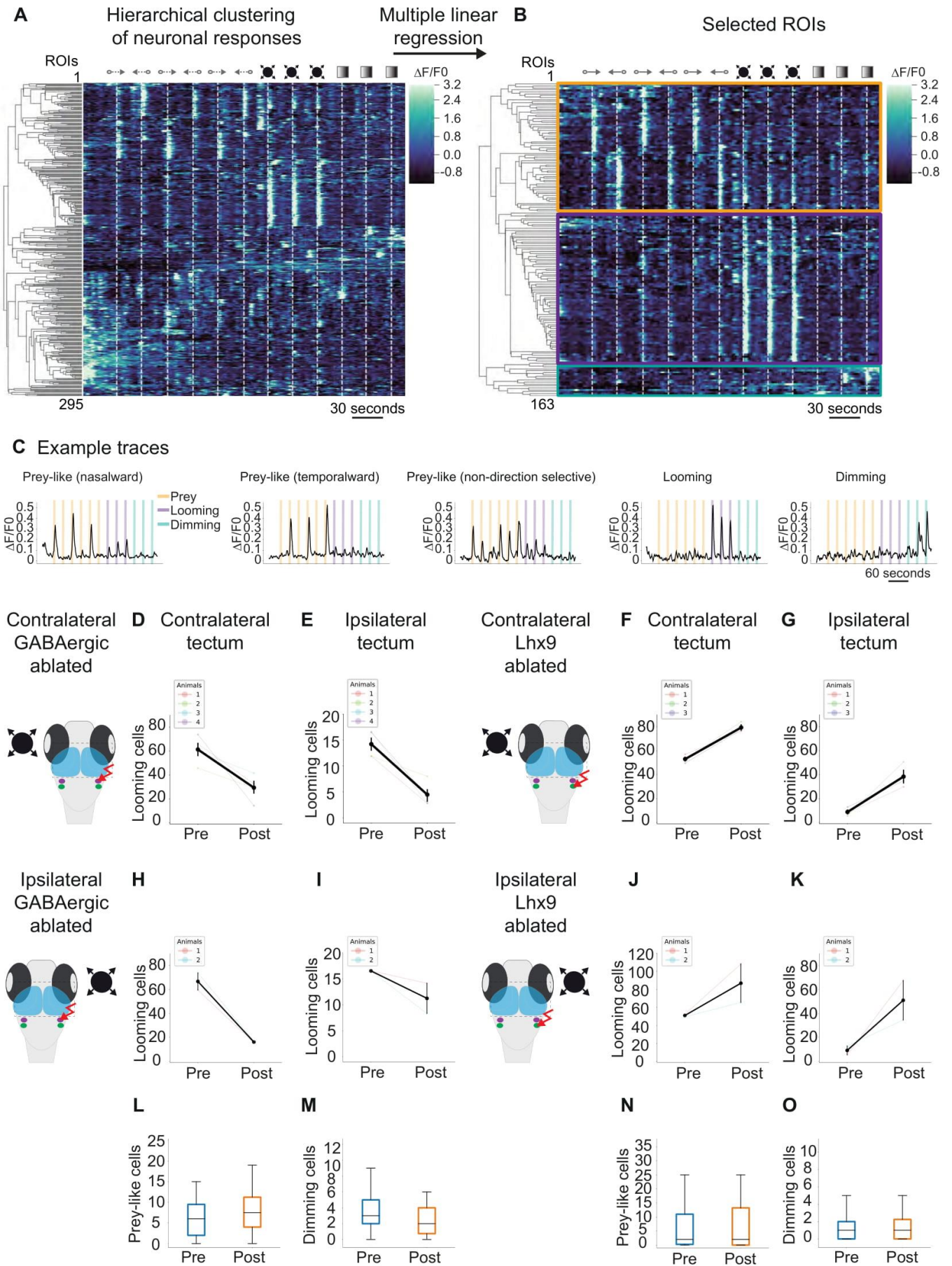


Figure S9. Unilateral ablation of NI cells modulates tectal responses to looming stimuli but not to prey-like or dimming stimuli. Related to Figure 6

(A) Example of hierarchical clustering of neuronal responses to monocular presentation of prey-like stimuli (nasalward and temporalward direction), looming stimuli and dimming stimuli (295 cells).

(B) Example of multiple linear regression analysis of neuronal responses. This approach selects stimulus-locked responses from spontaneously active neurons (163 cells).

(C) Example traces of selected neuronal responses to prey-like, looming and dimming stimuli.

(D) Mean results across animals related to Figure 6J.

(E) Mean results across animals related to Figure 6K.

(F) Mean results across animals related to Figure 6N.

(G) Mean results across animals related to Figure 6O.

(H) Mean results across animals related to Figure 6L.

(I) Mean results across animals related to Figure 6M.

(J) Mean results across animals related to Figure 6P.

(K) Mean results across animals related to Figure 6Q. For panels D-K, error bars represent 95% CI.

(L) Number of prey responsive cells in the contralateral (relative to looming stimulus) tectum. Before ablation in blue and after ablation of GABAergic-positive NI cells in the right hemisphere in orange. N=4.

(M) Number of dimming responsive cells in the contralateral (relative to looming stimulus) tectum. Before ablation in blue and after ablation of GABAergic-positive NI cells in the right hemisphere in orange. N=4.

(N) Number of prey responsive cells in the contralateral (relative to looming stimulus) tectum. Before ablation in blue and after ablation of Ihx9-positive NI cells in the right hemisphere in orange. N=3.

(O) Number of dimming responsive cells in the contralateral (relative to looming stimulus) tectum. Before ablation in blue and after ablation of Ihx9-positive NI cells in the right hemisphere in orange. N=3.

Suppl. Fig. S10 (Fig.7)

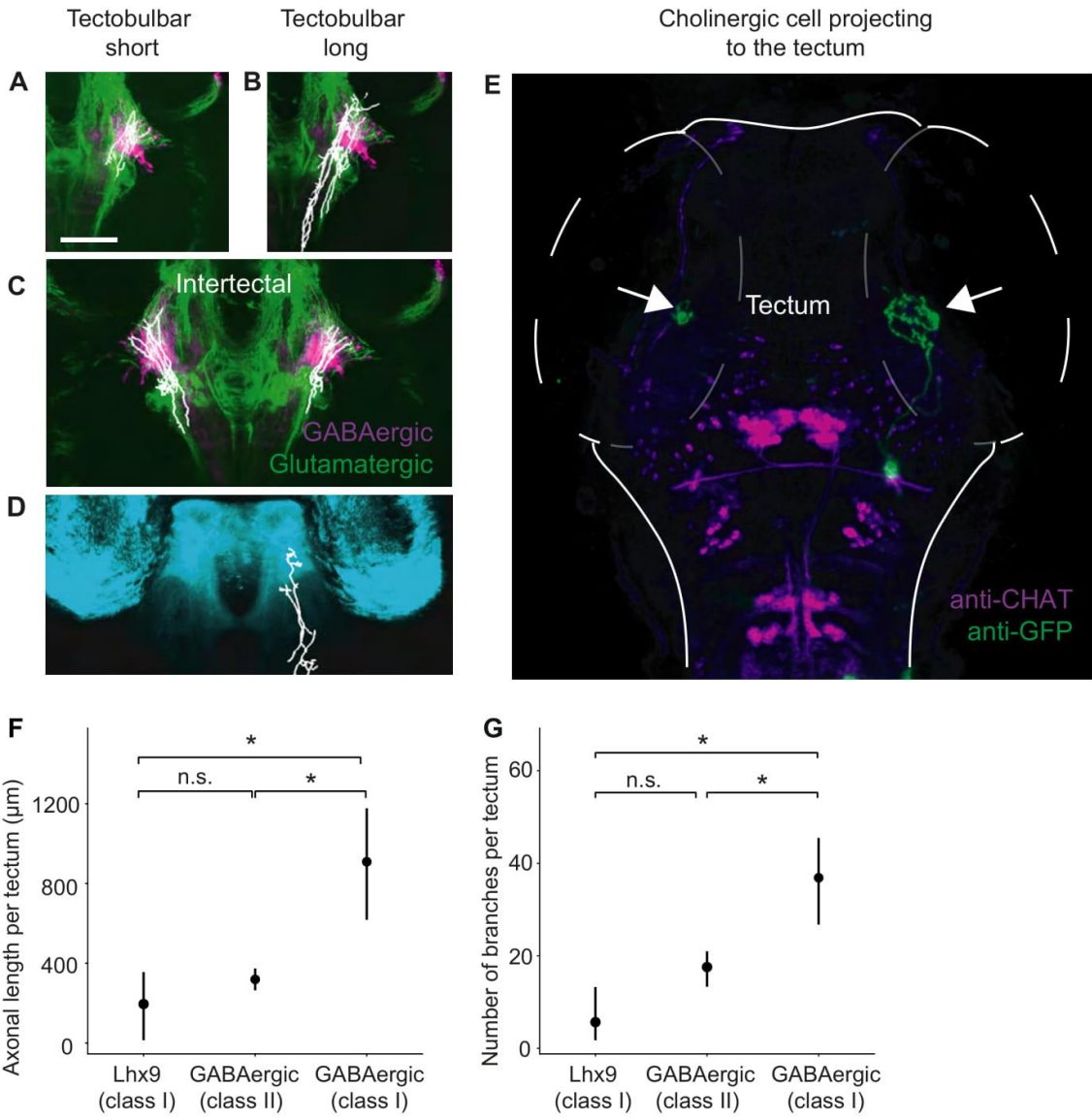


Figure S10. Nucleus isthmi forms a feedback loop with the tectum. Related to Figure 7.

- (A) Tectobulbar cells (with short axons) projections to the ipsilateral nucleus isthmi region. GABAergic nucleus isthmi in magenta and glutamatergic nucleus isthmi in green.
- (B) Tectobulbar cells (with long axons) projections to the ipsilateral nucleus isthmi region.
- (C) Intertectal neurons projections to ipsilateral and contralateral nucleus isthmi region.
- (D) *Lhx9* class III cells projecting to the ipsilateral thalamus (in blue, *s1020t* line expression).
- (E) Example of sparse labeling of a cholinergic nucleus isthmi cell. Immunohistochemistry against GFP (in green) and against ChAT (in magenta) is shown. Arrows indicate projections to both tecta.
- (F) Quantification of arbor length of NI cells in the tectum (N=3 for *Lhx9*-positive cells, N=7 for GABAergic-positive ipsilateral projecting only cells and N=20 for GABAergic-positive ipsilateral and contralateral projecting cells). Error bars represent 99% confidence interval.
- (G) Quantification of number of branches of NI cells in the tectum (N=3 for *Lhx9*-positive cells, N=7 for GABAergic-positive ipsilateral projecting only cells and N=20 for GABAergic-positive ipsilateral and contralateral projecting cells). Error bars represent 99% confidence interval. * $p < 0.05$, Kruskal-Wallis H-test followed by Conover's post hoc test.

3. DISCUSSION

With the nervous system intact the reactions of the various parts of that system, the 'simple reflexes', are ever combined into great unitary harmonies, actions which in their sequence one upon another constitute in their continuity what may be termed the 'behaviour'.

Charles Scott Sherrington

Animals do not live in the real world, but in the “inner world” of their *Umwelt*. What do animals see in that *Umwelt*, and how do they influence it through their behaviour?

For the zebrafish larva, the *Umwelt* is a reflection of the pools and streams, tributaries of the Ganges, in the foothills of the Himalayas (Parichy, 2015). Small and defenceless, all the week-old larva can do is eat as much as possible while staying out of harm's way. Small, shiny zooplankton likely feature heavily in the zebrafish larva *Umwelt*. As do the bigger fish in the pond, lurking in the depths, which can quickly turn the hunter into the hunted.

Thus, there exists a balance of needs in the brain of the zebrafish larva, as in all brains. Grabbing a quick meal is a priority; best not to linger too long; but to be overly cautious is to risk starvation. These competing drives do not paralyse the animal. Rather, its movements are structured, ordered, and tailored towards selected goals. Perhaps a few simple stereotyped movements are sufficient to navigate the *Umwelt*, easy for the brain to produce and replicate with consistent results; or perhaps a continuum of movements is best, allowing for more variable but less reliable behaviour. What does a “goal” even look like to a fish; what features of prey and predators filter through to its *Umwelt*? How does its brain build these representations? Then, out of all the clutter, how does it select one representation as the current “goal” most in need of a response? How does that goal persist in the brain – is it a static representation or a dynamically shifting mirage as the animal moves through its environment? Finally, how does the perceptual field of the *Umwelt* wire to the releasers of behaviour, allowing the animal to fulfil these goals in the first place?

Here, I will discuss tools for investigating the structure of animals' movements and their temporal coordination. Next, I will consider the movements and stimuli that allow zebrafish larvae to capture their prey. I will discuss how neural circuits might build representations of salient objects in the visual field, select one for a response, and then generate appropriate targeted movements. Finally, I will propose how future work might seek to expand our understanding of the zebrafish larva's *Umwelt*, and consider more generally how new *Umwelten* might emerge over evolution.

3.1 Mapping behaviour

Identifying the building blocks of behaviour

Tinbergen's hierarchical organisation of behaviour is intrinsically modular: animals have numerous instincts that drive them towards distinct survival and reproductive goals; these goals are achieved through distinct activities; and these activities are composed of discrete actions, released by specific stimuli. While differences between high-level behaviours (e.g. courtship vs. feeding) might be readily apparent to human observers (although, occasionally, these go hand-in-hand; (Thornhill, 1976)), at lower levels of the hierarchy, identifying boundaries between distinct actions becomes non-trivial, especially if the movements of an animal are fused into a continuum. Identifying elementary building blocks can provide a useful framework for discussing behaviour (Egnor and Branson, 2016), reveal how the brain encodes movement (Bizzi and Cheung, 2013), and serve as plausible substrates for behavioural evolution (Brown and Bivort, 2018; Hernández et al., 2020).

In my research, I have treated the bout as the elementary unit of zebrafish behaviour, in concordance with previous analyses (Mirat et al., 2013). Whether the bout is the lowest meaningful level to study zebrafish behaviour, however, is not clear. For example, while the initial tail beats of a bout appear to be truly ballistic movements, later tail beats are subject to modulation by sensory feedback (Portugues and Engert, 2011; Trivedi and Bollmann, 2013). Furthermore, analysis of bout sub-structure has revealed stereotyped tail half beats that combine to produce distinct bout types (Marques et al., 2018). Nonetheless, studies of the reticular formation of zebrafish larvae suggest that, at least at this level, neural correlates of bout types such as C-starts, slow and fast swims, and routine turns exist (Huang et al., 2013; Kimmel et al., 1980; O'Malley et al., 1996; Orger et al., 2008; Severi et al., 2014; Wang and McLean, 2014). Therefore, one could hypothesise that characterising the variation and stereotypy in zebrafish bouts could reveal the encoding of behaviour at the level of the hindbrain, which, in mammals, similarly represents complete actions (Capelli et al., 2017; Esposito et al., 2014).

Mapping the structure of behaviour

After determining what level of behaviour to study, we can seek informative representations that reveal its structure and how this relates to underlying neural mechanisms. Numerous strategies have emerged as starting points for characterising the kinematics of behaviour, most of which fall under two broad categories: feature-based approaches and postural dynamics. Either of these approaches can produce behavioural maps: quantitative,

visual representations of the movements of an animal that reveal something informative about its structure (see **Figure 6**).

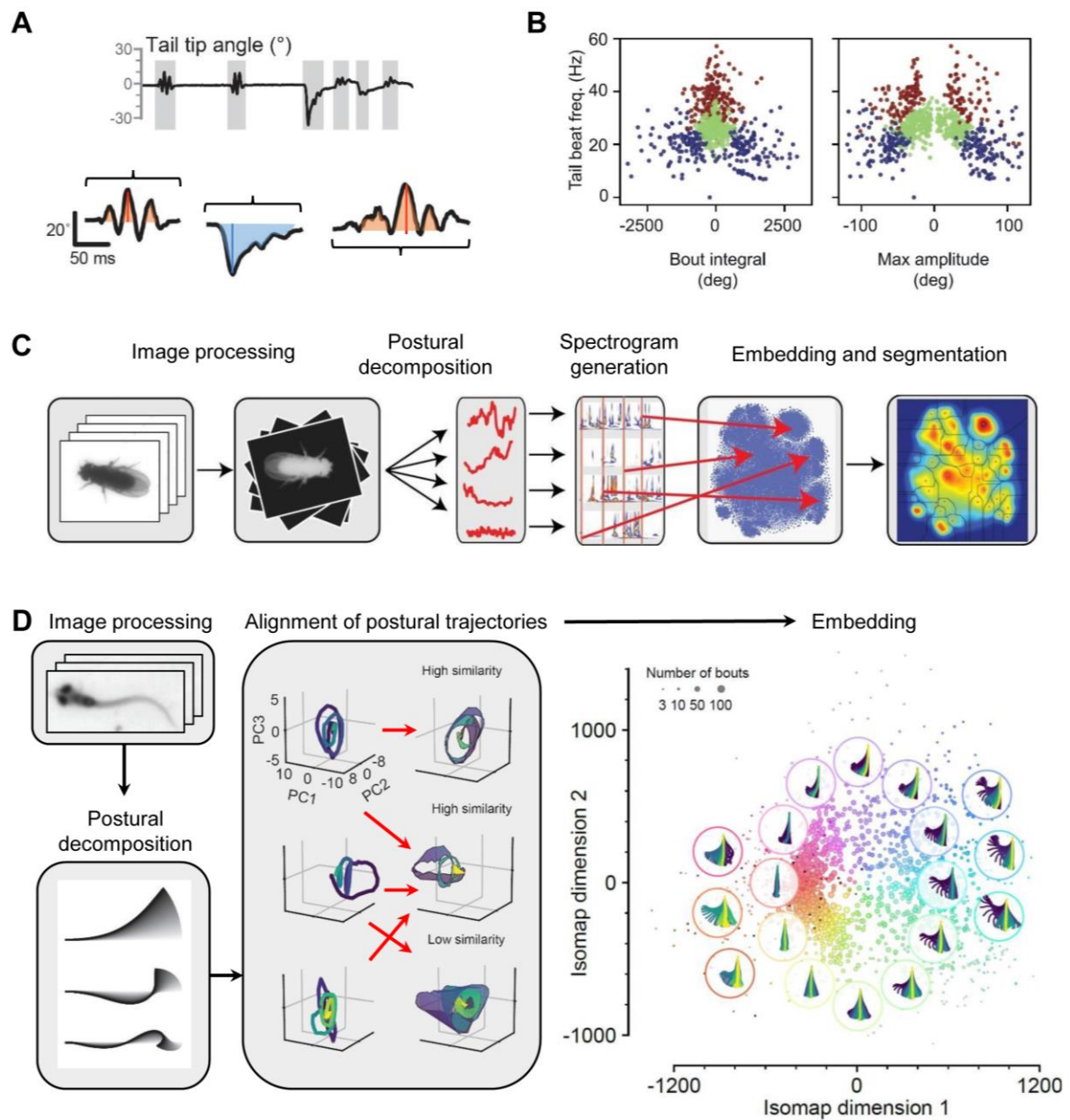


Figure 6. Mapping the structure of behaviour

(A) Extracting bout features from segmented behavioural traces.

(B) Behavioural map of bout features. Adapted from Fernandes et al. (2021).

(C) MotionMapper pipeline for generating maps of behaviour. Adapted from Berman et al. (2014).

(D) Generating behaviour maps from postural dynamics. Adapted from Mearns et al. (2020).

In Fernandes et al., (2021), my colleagues and I showed that threatening stimuli that compete for visual attention elicit one of two behavioural strategies: select one stimulus for a response and ignore the other (winner-take-all); or integrate the stimuli to produce a response intermediate to what would be elicited by each stimulus alone (averaging). Both of these strategies are implemented in the same brain, suggesting that internal states might tip the balance between one strategy and the other. I applied a feature-based approach to characterising swim bouts in embedded larvae responding to looming disks, which revealed that these two strategies are realised by different kinds of swim bout: C-starts for winner-take-all, and burst swims for averaging (see **Figure 6B**, blue and red points, respectively). Feature-based approaches are appealing since they start with intuitive descriptions of an animal's movement ("how fast?", "how large?"), and have been used to categorise bouts of free-swimming larvae into robust categories (Marques et al., 2018; Mirat et al., 2013).

One drawback of feature-based approaches, however, is that it is less clear how neural circuits could take such representations and convert them into a coherent sequence of muscle contractions. Ultimately, distinct behaviours emerge via the differential contraction of muscle groups and the resulting forces acting mechanically on the body parts of an animal (and additional counteracting forces provided by the environment). Such comprehensive physical models are, however, challenging to obtain. The study of postural dynamics, describing how the shape of an animal changes over time, has emerged as a more accessible approximation of this complex physical interplay (Berman et al., 2014; Brown and Bivort, 2018; Girdhar et al., 2015; Stephens et al., 2008; Wiltchko et al., 2015) (see **Figure 6C,D**).

In Mearns et al. (2020), I mapped the structure of free-swimming zebrafish behaviour by studying postural dynamics. Applying a dimensionality reducing method (PCA) to a "skeletonised" representation of the tail revealed that relatively few simple shapes, known as "eigenmodes", explained the majority (>85%) of the variation in tail posture over time. Girdhar et al. (2015) found a similar, limited set of "eigenmodes" when they studied the spontaneous swimming of zebrafish larvae, and low-dimensional representations of tail posture have also been found in nematodes (Stephens et al., 2008). In organisms with more complex body plans, such as fruit flies and mice, more "eigenmodes" are required to explain the same variance in body posture (ten for mice (Wiltchko et al., 2015), and as many as 50 for flies (Berman et al., 2014)). Notably, however, tail shape alone does not sufficiently describe the complete posture of a zebrafish larva. The jaws, pectoral fins, and eyes all further contribute to the movements of the fish, and likely add to the dimensionality of their postural space. Moreover, principal components do not necessarily capture neural representations of body posture. In the case of the zebrafish tail, principal components are reminiscent of a harmonic series, and so these components reflect an efficient representation of an oscillating string; and in worms, "eigenmodes" do not map directly to observed neural activity (Kato et al., 2015).

Behaviour is dynamic: animal motion is continuous, and we can represent that motion as trajectories in postural space. Postural dynamics also provides a handle on questions of discreteness and stereotypy in behaviour (see **Figure 2**). What kinds of trajectories through this space do animals make, and how precisely do they repeat? These questions, however, pose the new challenge of sufficiently capturing time information in our behavioural maps. In Mearns et al. (2020), I used dynamic time warping (DTW), which provides a measure of similarity between time series (Sakoe and Chiba, 1978). An alternative approach, adopted by Berman et al. (2014), is to convert postural time series to a spectrogram, capturing variation in frequency. Yet another approach has used autoregression to identify timescales that best captured modularity in behaviour (Wiltschko et al., 2015). Notably, these approaches were applied in vastly different species, yet all revealed repeating kinematic motifs lasting hundreds of milliseconds, suggesting that these sub-second timescales are deeply ingrained into motor representations of the brain across taxa.

While the postural space of an animal may be inherently low dimensional, the myriad behaviours that can emerge from these postures over time may not (Bialek, 2020). This poses a final problem for the generation of behavioural maps from postural dynamics – depicting high-dimensional behavioural data in an informative way. Here, non-linear embedding algorithms have emerged as a promising solution. In Mearns et al. (2020), I favoured isomap (Tenenbaum et al., 2000) as a method to uncover the structure of the zebrafish behavioural space. Isomap “unwraps” the distances between points in a high-dimensional space, identifying new axes that preserve the global structure of the data. MotionMapper (Berman et al., 2014) uses t-SNE, which preserves local clusters of nearby points in the embedding, but disrupts the structure of the data on a larger scale. This t-SNE-based approach reveals discrete behaviours with direct neural correlates in the brain in flies (Cande et al., 2018). However, obvious discreteness does not emerge when embedding zebrafish swim bouts using t-SNE (Johnson et al., 2020; Jouary and Sumbre, 2016; Mearns et al., 2020), unless multiple additional clustering steps are applied (Marques et al., 2018). The more continuous representations of behaviour revealed by isomap might also have neural correlates in the brain, as discussed below, and might better reflect the encoding of behaviour in spinal-projecting neurons in fish.

Mapping behavioural sequences

Behaviour is not random, but rather structured by both internal and external factors. After characterising the diversity of zebrafish larval bouts in Mearns et al. (2020), I next addressed how bouts of different kinds are chained together to produce goal-directed behaviours. In doing so, I hoped to reveal a kind of “behavioural grammar”, identifying rules that govern

transitions between bouts in different parts of the behavioural map. Such transition rules might reveal “sticky” regions of the space, where animals perform a group of behaviours repeatedly; or, alternatively, bouts from different regions of the space that larvae chain into stereotyped sequences.

To this end, I deployed singular-value decomposition (SVD) to illuminate common sequence motifs that recur during behaviour. An intermediate clustering step facilitated embedding, and grouped bouts into a few hundred elementary “syllables” that tiled the behavioural map. These “microclusters” likely significantly over-estimate the true diversity of bout types, allowing transition rules to be revealed within the behavioural continuum without forcing kinematically different bouts into the same behavioural category. Computing the pairwise transition frequencies between these microclusters generates a matrix that describes how animals transitioned between different regions of the map. Importantly, this matrix is not necessarily symmetric, i.e. some behavioural transitions might be directional, preferentially occurring in one direction over the other. Such sequences were analysed separately from the bidirectional transitions within the space, producing two “flavours” of transition rules, labelled “symmetric” and “antisymmetric” to reflect the nature of the underlying matrices. The relative likelihood of a behavioural transition obeying a given transition rule is captured by a number called the *singular value*. Many moderate singular values in the decomposition might suggest intricate and finely structured temporal sequences, while a few dominating singular values could emerge from a handful of broader transition rules. For zebrafish behaviour, I found the latter to be the case.

The SVD breakdown of zebrafish behavioural sequences is depicted in **Figure 7**. Symmetric transition modes (S-modes) capture transition rules that, in words, say, “If an animal performed a bout from one of *these* places in the behaviour map, the next bout is likely to come from another one of these same places, but *not* from one of *those* other places.” The first such transition rule to come from the SVD reflects how often bouts from different places in the behavioural map were used (“common bouts are most likely to follow common bouts”). The next transition rule almost perfectly delineated hunting swims and spontaneous swims (“if fish are doing prey capture, the next bout is also likely to be a prey capture bout; and if fish are exploring the environment, the next bout is likely to be another exploratory bout”). This finding is non-trivial, since SVD was able to identify the difference between spontaneous and hunting swims based on sequence structure alone. In cases where independent readouts of behavioural states might not be available, SVD has the potential to identify “sticky” regions of a behavioural map, hinting towards underlying states that might be restricting an animal’s behaviour. Moreover, the SVD provides a metric to quantify transition structure within a dataset. For example, when I compared the SVD of transition matrices obtained from healthy fish and genetic mutants, I found that bout usage over the space was different, and prey

capture sequences were less “sticky” in mutants, being more likely to terminate prematurely and resort back to exploratory swimming behaviour.

Antisymmetric transition modes (A-modes) capture transition rules that, in words, say, “Transitions from *these* places in the behavioural map to *those* places in the behavioural map are more likely than transitions from *those* places to *these* places.” Mathematically, they represent a 90° rotation of a hyperplane in a high dimensional “bout space”, and consequently each A-mode is able to represent up to four kinds of transitions. In healthy fish, but not visually impaired mutants, a single A-mode dominated, and represented progressive bout chains during prey capture sequences: exploratory swimming → orienting → approach → capture or abort → exploratory swimming. Thus, this approach has the potential to reveal stereotyped behavioural chains, including within continuous maps that might otherwise preclude clustering into discrete actions.

The SVD approach I applied in Mearns et al. (2020) bears similarities to the approach used by Berman et al. (2016). Berman et al. used the eigendecomposition of transition probability matrices to map behavioural hierarchies in the spontaneous behaviours of fruit flies. These approaches reveal that, for both zebrafish larvae and fruit flies, transitions are most common between nearby regions of their respective behavioural spaces. Berman et al. focus on the “stickiness” of these states over longer timescales, considering probability matrices after multiples behavioural transitions. Their approach showed that fruit fly behaviour displays “non-Markovian” dynamics, meaning that behaviours in the past (sometimes up to hundreds of transitions prior) contain information about the ongoing behaviour of the animal. Contrasting this, my analysis in Mearns et al. (2020) showed that for zebrafish larvae the current behaviour is a strong predictor of the next, and that knowing additional past behaviours generally does not improve predictions for future ones. Mouse and fly behaviour have also been modelled using a hidden Markov model (HMM), whose “hidden” states influence behaviour in ways that cannot sufficiently be predicted with a first-order Markov process (Katsov et al., 2017; Wiltschko et al., 2015). The different timescales and behavioural contexts used in these studies might explain the differences observed in the temporal structuring of behaviour in flies and mice on the one hand, and zebrafish larvae on the other. Prey capture depends strongly on visual cues, which patterns behaviour in a predictable way, and over relatively short timescales (i.e. seconds); whereas the aforementioned studies in other model systems focused on spontaneously generated behaviours, where longer-lasting persistent states might prevail.

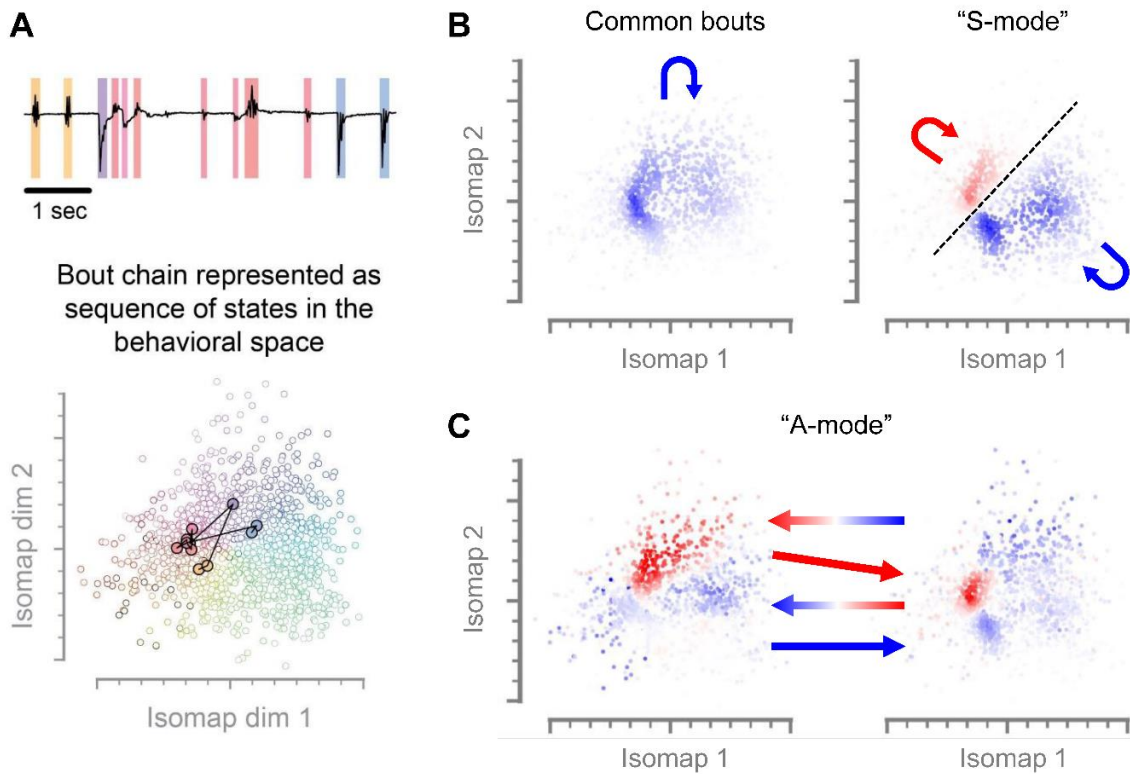


Figure 7. Analysis of behavioural sequences

(A) Sequences of bouts within a behavioural map. Tail angle trace (top) with individual bouts colour-coded based on their position in the behavioural map (below).

(B) & (C) Transition rules identified through SVD. Intensity of the colour indicates how many transitions each position in the behaviour map contributes to the transition mode.

(B) Symmetric transition modes. For each transition mode, bouts with the same colour are more likely to transition to each other, while bouts with different colours are less likely to transition to each other. The black dotted line through the space on the right indicates the approximate boundary between prey capture and spontaneous swims.

(C) An antisymmetric transition mode encoding cyclical behavioural transitions, representing stereotyped bout chaining during prey capture. Points on the left transition to points on the right with the *same* colour. Points on the right transition to points on the left with the *opposing* colour. Red regions on the left predominantly represent J-turns, and blue regions predominantly represent capture strikes and routine turns. The red region on the right encodes slow forward swims.

Adapted from Mearns et al. (2020).

In mammals and birds, the sequencing of behaviour is believed to be coordinated in “executive” centres of the forebrain (Arber and Costa, 2018; Long et al., 2010); however, imaging studies in fish reveal hindbrain oscillators that appear to structure behaviour on these intermediate timescales (Dunn et al., 2016a; Marques et al., 2020). One exciting future prospect would be to try to link neural activity within these “higher-order” and “executive” brain regions to the rules that underlie behavioural sequencing.

3.2 Prey capture behaviour of the zebrafish larva

During prey capture, zebrafish larvae perform a sequence of bouts whose goal is to bring prey items into a “strike zone” located 0.5-1 mm away, centred, and approximately 20° elevated in the visual field (Bolton et al., 2019; Mearns et al., 2020; Patterson et al., 2013). Once prey fall within the strike zone, larvae use distance cues to select an appropriate strike response: suction for nearer prey, attack swim for prey at an intermediate distance, or an energetic S-strike for the most distant prey. I have shown that binocular cues allow for optimal action selection during the strike, corroborating previous hypotheses (Bianco et al., 2011; Patterson et al., 2013), but not for initiation of the strike itself. The critical decision points in the behaviour, along with putative associated releasing stimuli, are summarised in **Figure 8**, and framed as a hierarchical model after Tinbergen.

In Mearns et al. (2020), I have argued that consistent bout chaining in prey capture emerges from a stimulus-response loop. The location of prey in the visual field triggers a bout that moves the prey to a new location in the visual field, which triggers the next bout, etc. Under such a model, the previous bout should be a strong predictor of the next in a hunting sequence, as it should consistently set up a new releasing stimulus. In this study, I used a Markov modelling strategy to demonstrate that this is indeed the case. Moreover, I demonstrated that visual cues pattern the behaviour on short timescales using a closed-loop free-swimming virtual prey capture assay. The sudden removal of a stimulus after initiation of a hunting sequence causes larvae to abort the behaviour almost immediately, showing that persistent visual cues are necessary to pattern the behaviour. Going forward, this behavioural paradigm could be used to test more specific models of prey capture behaviour, e.g. by jumping the stimulus to the strike zone immediately after it is detected to test whether a consistent stimulus history is necessary for the initiation of the strike.

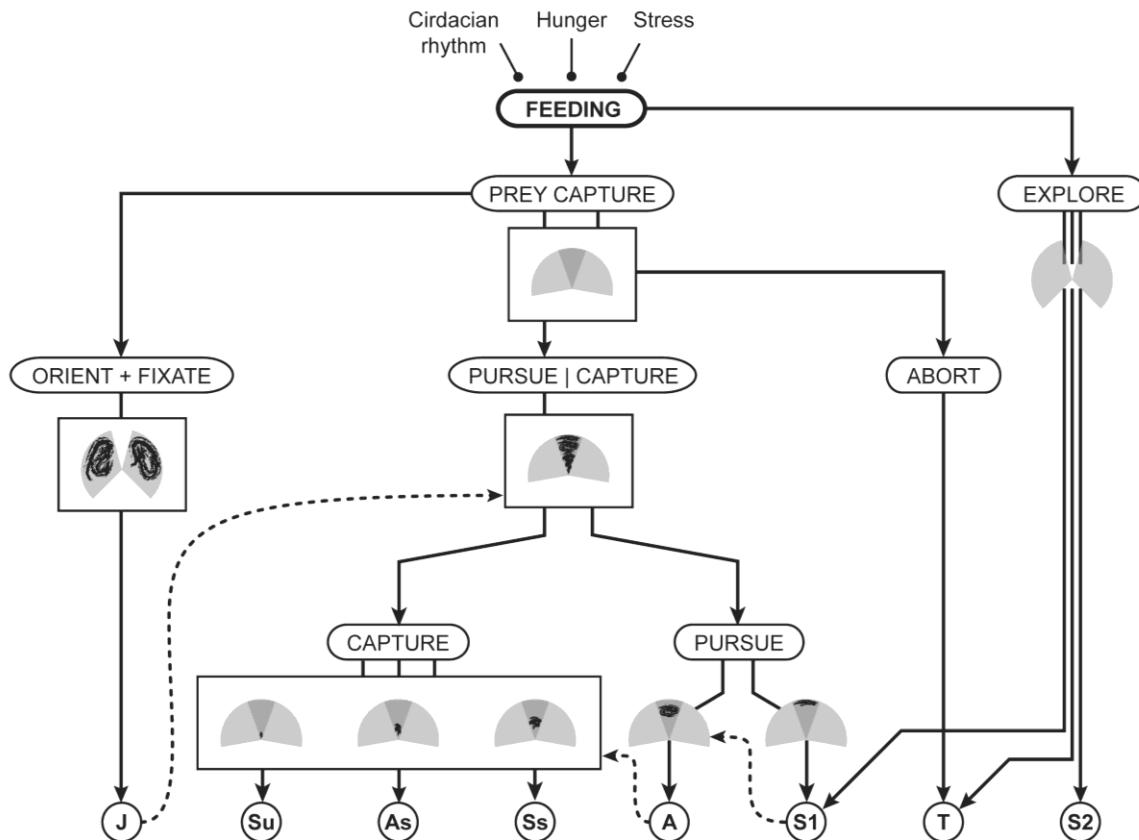


Figure 8. Hierarchical model for prey capture behaviour in zebrafish larvae

Behaviours, named inside bubbles, are organised into a hierarchy, with the instinct (feeding) at the top. Bout types are shown at the lowest level of the hierarchy. Solid arrows show the flow of impulses from higher levels to lower levels. Boxes represent blocks that prevent impulses from flowing. Pictograms inside blocks indicate a “sign stimulus” needed to release downstream behaviours. Other pictograms represent “directing” stimuli that guide appetitive behaviours in the absence of sign stimuli. Grey shaded areas represent the visual fields of the two eyes. Black shading indicates the presence of a prey item in this part of the visual field. Dashed arrows represent the transformation of one stimulus into another by the release of a behaviour. J: J-turn; Su: suction; As: attack swim; Ss: S-strike; A: approach; S1: slow 1; T: routine turn; S2: slow 2.

Johnson et al. (2020) modelled the hunting behaviour of zebrafish larvae using a marked renewal process, considering additional aspects of the behaviour, including the interval between bouts, the number of preceding bouts in the hunting sequence, and the length of time fish had spent in the behavioural arena. They similarly found that the preceding bout was the best predictor of the next one in the sequence. This model was particularly good at predicting bouts within a hunting sequence, but generally poorer at determining when the first hunting bout would occur (i.e. when prey items are detected). Thus, the two papers are largely in agreement in their assessment of prey capture in zebrafish larvae; larvae have a repertoire of bouts specifically deployed to orient towards, pursue and capture prey, with the temporal

organisation of bouts predominantly structured by the immediate visual scene and preceding bout in the sequence.

In contrast to the classical idea of an invariant fixed action pattern, in Mearns et al. (2020) I showed that there is significant variation in the kinematics of bouts deployed during hunting behaviour in zebrafish larvae (see **Figure 6D**). Previously, studies have shown that the distance and angular position of prey affects the kinematics of hunting bouts (Patterson et al., 2013; Trivedi and Bollmann, 2013). Bolton et al. (2019) showed that each successive bout in the sequence serves to approximately halve the visual angle and distance between the current position of the prey and the strike zone. Interestingly, stochasticity in their model improves performance, decreasing the total number of bouts required to bring prey to the strike zone. Thus, variability in bout kinematics appears to be a feature of zebrafish prey capture that improves efficiency by decreasing the time engaged in hunting activity.

3.3 Neural circuits for prey capture

With a thorough understanding of the behavioural rules that underlie prey capture, we can now consider how these rules might be realised in neural circuits. Visually guided prey capture starts in the retina, which transmits parallelised feature representations of the outside world to forebrain and midbrain structures. Thereafter, salient objects are detected across the visual field, a single object is selected for a response, and a sensorimotor transformation occurs that computes a movement that would best achieve the current goal of the animal (i.e., to bring prey to the strike zone, initiate a capture strike, or abort the behaviour). This movement is ultimately realised by the patterned activity of motor neuron pools, which generate muscle contractions and change the posture of the animal.

From the brain's perspective, the goal of prey capture appears to be to position prey bilaterally on the strike zone, which maps to the anterior tectum (see **Figure 9**). Prey is almost always detected unilaterally, since the eyes create minimal binocular overlap in the visual field when unconverged. The stimulus becomes binocular, however, after the initial J-turn and saccadic convergence of the contralateral eye. It is possible that the appearance of prey on the temporal retina of the contralateral eye provides a termination signal for the initial J-turn (see **Figure 9**). Thereafter, the brain would need to compute movements that maintain the position of prey on the strike zone of one eye, while incrementally moving it closer to the strike zone of the other. While this model is speculative, it is arguably consistent with behavioural observations, and provides constraints on the sensorimotor transformations of prey capture by limiting the degrees of freedom, thereby simplifying the necessary computations in the brain. Interestingly, when predatory insects pursue prey, they also appear to position targets within a restricted "visual window" (Fabian et al., 2018; Lin and Leonardo, 2017), possibly

reminiscent of the “strike zone” in fish. Such a system might have evolved repeatedly to solve the challenges of catching prey in three-dimensional environments.

Retina

The retina does not contain uniform maps of space, but rather processes features differentially across the visual field (Baden et al., 2020). In zebrafish larvae, prey-responsive retinal ganglion cells (RGCs) project to a pretectal arborisation field, AF7, and the superficial SO layer of the tectum (Semmelhack et al., 2014). Both of these arborisation sites have an over-representation of the temporal retina (Robles et al., 2014), which contains notable specialisations in the zebrafish larva. In particular, the temporal-ventral retina contains a high-acuity zone (Schmitt and Dowling, 1999), where larvae position prey prior to the strike (the aforementioned “strike zone”). Under naturalistic sunlit conditions, protozoa such as paramecia appear as UV-bright spots when viewed against the backdrop of the water surface (Zimmermann et al., 2018). Both photoreceptors and RGCs are specialised for detecting UV in the strike zone (Yoshimatsu et al., 2020; Zhou et al., 2020). Interestingly, molecularly defined RGCs expressing the transcription factor, *mafaa*, are enriched in the temporal retina, and project to AF7 and the SO (Kölsch et al., 2021), hinting towards genetically encoded circuitry specialised for prey detection in this region.

Pretectum

Neurons neighbouring AF7, putatively receiving prey feature maps from the retina, project to the superficial layers of the tectum (Semmelhack et al., 2014), or to the tectum and hindbrain (Antinucci et al., 2019; Semmelhack et al., 2014). Other cells in the vicinity, which respond to prey but may not necessarily be directly retinorecipient, project to the hypothalamus, an important centre for appetite control (Muto et al., 2017). The Semmelhack-Antinucci cells preferentially respond to prey-like stimuli and optogenetically stimulating them can drive entire hunting sequences, even in the absence of prey (Antinucci et al., 2019). These cells are certainly integral to prey capture, seemingly constituting a command-like element for the behaviour.

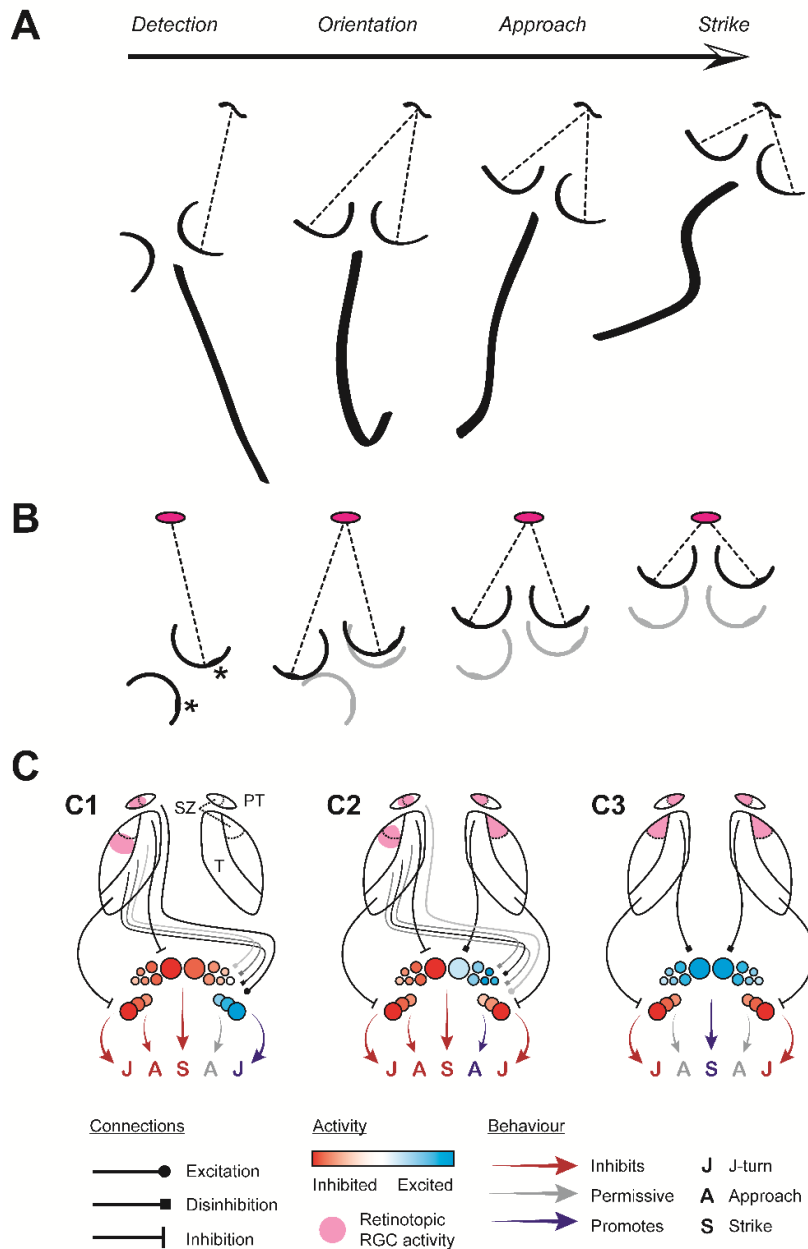


Figure 9. Circuit model for the descending control of prey capture behaviour

(A) Schematic of the stages of a zebrafish larva hunting sequence.

(B) Schematic for the binocular representation of prey over time during hunting. The paramecium (pink) is the reference point. Black semicircles represent the position of the eyes relative to the prey; grey semicircles show the location of the eyes at the previous stage of the behaviour. Enlarged regions (highlighted by asterisks in the first panel) represent the strike zone on the retina.

(C) Hypothetical feed-forward circuit for action selection during hunting, showing activity at three intermediate stages of the behaviour. Two bilaterally symmetric neuronal populations control bouts, representing a hypothesised role for the nMLF and vSPNs. Presence of prey in one tectum inhibits ipsilateral vSPNs, and the nMLF. Prey in the anterior tectum disinhibits the nMLF. Pretectum activates downstream neurons directly via crossed excitatory projections. Tectum shapes activity indirectly via disinhibition, mediated by pools of inhibitory interneurons (omitted for clarity). In this model, strong symmetric activity in the nMLF releases strikes. (C1) Release of the initial J-turn. (C2) Release of an approach swim. (C3) Release of the capture strike. PT: pretectal arborisation field AF7; T: tectum; SZ: strike zone.

Tectum

In Förster et al. (2020), my colleagues and I showed that cells in the tectum selectively respond to prey-like stimuli, corroborating previous findings (Bianco and Engert, 2015). Removing superficial visual input to the tectum substantially decreased tectal cell responses to prey-like stimuli, suggesting such responses are inherited from RGCs and not computed *de novo*. Moreover, this tuning likely depends on accurate and restricted retinotopic mapping of the RGC inputs, since disruption of this topography in *blumenkohl* mutants, where the RGC axons over-branch in the tectum, reduces visual acuity during prey capture (Mearns et al., 2020).

Notably, however, a linear summation of RGC response profiles does not fully explain the observed tuning of prey-responsive tectal cells (Förster et al., 2020). This suggests that the tectum sharpens tuning to prey-like stimuli, possibly via non-linear integration of RGC inputs or via tectum-intrinsic circuitry. Furthermore, behavioural studies show that larvae adjust their orienting swims based on direction of prey motion, producing complex backward-directed J-turns when prey moves backwards in the visual field (Bolton et al., 2019; Patterson et al., 2013). The tectum appears to compute this backward motion of prey-like stimuli *de novo*, rather than inheriting such responses from RGCs (Förster et al., 2020). On the retina, such a stimulus represents nasalward motion, away from the high-acuity strike zone. Perhaps this specialisation of the retina forces a trade-off, whereby prey-detecting cells in the nasal retina are too distantly spaced to accurately compute motion (or motion at the speeds used in the present study), offloading the computation downstream to the tectum.

Moreover, recent studies suggest that the prey capture circuitry is not entirely hardwired. Experienced larvae have improved prey detection and better-targeted orienting swims (Lagogiannis et al., 2020; Oldfield et al., 2020), possibly via the refinement of tectal microcircuits (Avitan et al., 2020).

In Förster et al. (2020), we showed a spatial map of size tuning over the anterior-posterior axis of the tectum. Such a change in size preference might be relevant for prey capture. As the behaviour progresses, and the prey moves closer to the near anterior visual field, it would grow on the retina of the fish, filling the strike zone. Curiously, we found that targeted ablation of neurons that respond to larger prey sizes decreased engagement in prey capture behaviour.

To maintain hunting sequences, we might hypothesise that larvae keep track of the prey as it shifts in the visual field between bouts. How they would achieve this is unknown, although we do know that a motor map overlays the retinotopic map in the tectum such that the magnitude of orienting swims released by the tectum increases from anterior to posterior (Helmbrecht et al., 2018). I would suggest that such a signal could emerge by the computation

of an “error vector” between the current location of a target in the visual field and the “strike zone” in the anterior tectum (see **Figure 10**). Such a vector could be transmitted to the hindbrain via a space code in the ipsilateral tectobulbar tract (Helmbrecht et al., 2018), but exist as an “activity code” in the tectum, whereby a local predictive enhancement of activity in the anterior tectum “catches” the prey as it shifts forward in the visual map. Disrupting circuitry in the anterior tectum could disrupt the computation of this error vector, preventing the release of the motor command.

Binocular integration

As noted above, prey capture becomes a binocular behaviour after the initial eye convergence and J-turn. Thus, the two tecta and pretecta must work in tandem to generate coherent goal-directed motion towards a prey stimulus in the visual field. This immediately creates a four way correspondence problem in the zebrafish larva brain: how do larvae “know” that neural activity in the pretectum and tectum correspond to the same prey object in the visual field, and how is this same object matched across hemispheres? The best guess answer to the former question is that recurrent loops between tectum and pretectum coordinate neural activity between these two regions. Neurons neighbouring AF7 project to the tectum (Semmelhack et al., 2014), and PVPNs in the tectum project back to the pretectum (Helmbrecht et al., 2018). Whether such projection neurons connect, and whether projections follow topographic rules, remains to be determined.

Experimental evidence sheds a little more light on how activity is coordinated between hemispheres. In Förster et al. (2020), we showed that the “ipsilateral” tectum (i.e. the “wrong” side given the fully crossed of RGC projection in fish) responds to unilaterally presented visual stimuli. These responses remained even after enucleation of the contralateral eye, demonstrating that such responses arise from within the brain and not an artefact caused, e.g., by a reflection of the stimulus. Ablation of these cells also impaired the release of prey capture behaviour. This demonstrates the importance of interhemispheric circuitry at all stages of the behaviour. As discussed above, during the initial J-turn, a prey stimulus will suddenly appear in this ipsilateral tectum. If a kind of “predictive” feed-forward circuit is required to release the behaviour, disrupted or incoherent network activity in this other tectum could block that release. Alternatively, ablation of these neurons could disrupt the saccade-generating assemblies in the tectum (Bianco and Engert, 2015), preventing eye convergence and thus also blocking the behaviour.

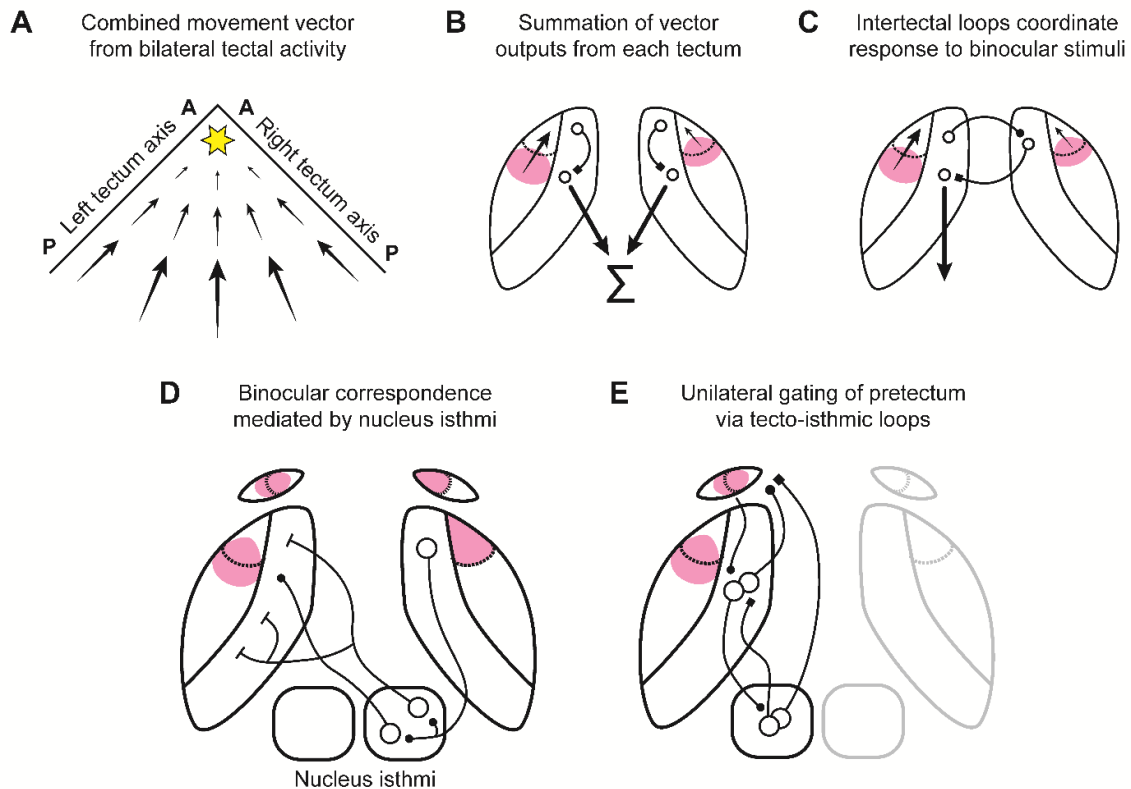


Figure 10. Hypotheses for the binocular coordination of prey capture behaviour

(A) Vector summation model for action selection during prey capture. Arrows indicate a movement vector that brings prey closer to the strike zone (star, representing bilateral activity in the anterior tecta).

(B) Hypothetical implementation of the vector summation model by the integration of tectal outputs.

(C) Hypothetical model for the binocular coordination of behaviour. Motor commands from one tectum would induce a predicted change in prey position in the other tectum. Intertectal loops ensure prey tracking across hemispheres.

(D) Hypothetical model for correspondence of objects in the visual field mediated by the nucleus isthmi. Winner-take-all computations consists of global suppression and local enhancement. A similar circuit might be able to “match” activity across hemispheres for bilaterally represented stimuli.

(E) Hypothetical model for pretecto-tecto-isthmic loop that release behaviour. Tecto-pretectal loops match activity to the same stimulus between the two regions. Tecto-isthmic loops serve as an attentional mechanism to keep track of prey. Synchronous activity might allow for disinhibition of pretectal command neurons by the nucleus isthmi. The shown projections exist, but whether they are excitatory or inhibitory is unknown. Schematic conventions the same as Figure 9.

Interhemispheric coordination also appears to be necessary for correct targeting of the prey to the strike zone. In Mearns et al. (2020), I tested the prey capture behaviour of fish that I had blinded in one eye. These animals still initiated prey capture towards prey on their intact side, converged their eyes as normal, and were able to maintain the behaviour despite missing half the normal visual inputs. However, these larvae were approximately half as likely to initiate strikes, and, when they did, prey were not correctly positioned within the usual “strike zone”. I would propose that each tectum has the ability to “veto” the initiation of a strike if a target is

not properly positioned in the anterior tectum. However, such a veto requires activity in that tectum in the first place, which would be absent in half-blinded fish. Moreover, feed-forward signals from the “sighted” tectum mentioned previously could erroneously alert the “blind” tectum to the presence of prey in the strike zone, causing premature release of the behaviour. A class of inhibitory crossed intertectal neurons appear to be important for the initiation of strikes, and could form part of the interhemispheric circuitry coordinating the behaviour (Gebhardt et al., 2019).

Why does the fish brain distribute neural circuits for prey capture between the tectum and pretectum, when either would appear sufficient to drive the behaviour? In *The Study of Instinct*, Tinbergen distinguishes between “sign stimuli” that release a behaviour and “directing stimuli” that guide the movements of the animal. Herein might lie the answer. Stimulation of Semmelhack-Antinucci cells drives “undirected” prey capture sequences, suggesting that these neurons might provide a classical “releasing mechanism” for the behaviour, perhaps in conjunction with the tectum. The tectum provides a finely graded topographic map of the visual field, and converts this map into fine-tuned movements that allow the animal to orient towards a specific point in space. Both tectum and pretectum project to the hindbrain, where the outputs of the two may be reconciled within premotor circuitry to generate the graded, target-directed swims observed in prey capture behaviour. Supporting this model, unilateral lesions to tectal outputs causes misguided orienting movements during prey capture in frogs, but removing one tectum blocks the orienting behaviour altogether (Kostyk and Grobstein, 1987).

Reticular formation

The discovery of neurons that could drive behaviour in crayfish led to the development of the “command neuron concept” (Wiersma and Ikeda, 1964), which posits that complete actions might be encoded in single neurons in the brain. The concept was refined in the following decades, resulting in a stricter definition, but also extended to encompass “command systems” of neurons that control specific behaviours (Kupfermann and Weiss, 1978). The command neuron concept provides a plausible hypothesis for how kinematically distinct modular behaviours could be encoded in the brain. For example, stimulation of single descending neurons in the fly brain can elicit specific movements (Cande et al., 2018; Robie et al., 2017).

In zebrafish larvae, approximately 100 reticulospinal neurons on each side of the brain descend to the spinal cord (Kimmel et al., 1982). Within this system, the Mauthner cell and its segmental homologues might reasonably constitute a “command system” for the C-start escape behaviour (Liu and Fetcho, 1999). On the other hand, imaging studies of the reticular formation during the behaviour has revealed a broad escape network encompassing a large

number of neurons (Gahtan et al., 2002), and commands for long-latency visual escapes reach the spinal cord via a Mauthner-independent pathway (Bhattacharyya et al., 2017). In Fernandes et al. (2021), I showed that excitatory feedbacks to the tectum from the nucleus isthmi (NI) could be involved in guiding the directionality of this behaviour. Curiously, I found that stimulation of the NI could drive burst swims directly, suggesting that this nucleus itself might also target premotor centres via descending projections to the hindbrain.

The ventral spinal projection neurons (vSPNs) constitute another possible command system, involved in turning behaviours (Bhattacharyya et al., 2017; Huang et al., 2013). It is unlikely, however, that there is a simple one-to-one mapping between all reticulospinal neurons and bout types. For example, the nucleus of the medial longitudinal fasciculus (nMLF) has been implicated in controlling both swimming speed (Severi et al., 2014; Wang and McLean, 2014) and turning (Thiele et al., 2014), including during prey capture (Gahtan et al., 2005). Thiele et al. suggest that this nucleus is controlling something more fundamental entirely, namely postural adjustments of the tail, which is essential in controlling a range of different behaviours.

The behaviour map I generated in Mearns et al. (2020) shows that pursuit bouts in prey capture do not separate into kinematically distinct modules, but rather form a continuum. Other studies of prey capture support this view (Bolton et al., 2019; Borla et al., 2002; Johnson et al., 2020; Patterson et al., 2013; Trivedi and Bollmann, 2013). This finding invites us to consider these more nuanced hypotheses for how the reticular formation might encode behaviour. The timing and magnitude of a “turning” component in a bout vary strongly along the first dimension of the space, and this could reflect activity of vSPNs. This would suggest that vSPNs should be active over a range of behaviours, including prey capture. The second dimension of the space appears to separate bouts based on a combination of swimming speed (with faster burst swims at the bottom of the space) and bout symmetry (with asymmetric J-turns at the top). Notably, the nMLF is implicated in both of these aspects of swimming. Moreover, some reticulospinal neurons may not be specifically involved in bout production at all, but in stopping ongoing movement (Bouvier et al., 2015; Grätsch et al., 2019), or coordinating eye, fin and jaw movements with swimming.

Neurons in both the tectum and pretectum project to the hindbrain and can drive hunting bouts (Antinucci et al., 2019; Helmbrecht et al., 2018). While their targets are unknown, axons of Semmelhack-Antinucci cells terminate near to the nMLF and vSPNs. Possible targets of ipsilaterally descending tectobulbar neurons, however, are less certain. One complicating factor is that motor commands from the tectum must cross back to the other hemisphere to guide swims towards a target. I think that direct feed-forward excitatory drive to reticulospinal neurons, which might also receive strong descending excitation from the pretectum, represents a poor system for guiding such swims. Rather, I would propose ipsilaterally

descending tectobulbar neurons might shift activity in reticulospinal pools via crossed disinhibition, mediated through a relay of, as of yet unidentified, inhibitory interneuron pools (see **Figure 9**).

Furthermore, orienting towards prey requires an animal to know both the location of prey in the visual field and the current eye position. The integration of retina-centric and body-centric reference frames happens downstream of the tectum (probably in the hindbrain) (Helmbrecht et al., 2018), which also contains the oculomotor integrator encoding eye position (Lee et al., 2015; Miri et al., 2011). Further research is required to determine how and where all these inputs – descending commands from tectum and pretectum, and eye position – are integrated.

Circuits for the capture strike

Contrasting pursuit swims, in Mearns et al. (2020) I showed that capture strikes separate into two kinematically distinct clusters. The explosive S-strike is reminiscent of the S-start escape response (Liu et al., 2012) and, plausibly, could be Mauthner-mediated. Although Borla et al. (2002) found that ablation of the Mauthner cells did not affect the production strikes, the presence of a secondary attack swim might provide redundant backup to ensure robust triggering of the behaviour. Such a system exists for the escape response, where long-latency escapes via a Mauthner-independent pathway serve as a redundant mechanism for triggering the behaviour (Burgess and Granato, 2007b). The neuronal substrate of the attack swim is also unknown, but such a circuit could involve the large cells of the nMLF, which can drive fast forward swims (Severi et al., 2014; Wang and McLean, 2014).

Interestingly, as larvae gain hunting experience, S-strikes become more common and more accurate (Lagogiannis et al., 2020). By the time they reach the juvenile stage, discrete hunting bouts have fused into a single “homing strike” (Westphal and O’Malley, 2013). While these shifts in the behaviour could represent differential recruitment of premotor command systems, alternatively both S-strikes and attack swims could be generated within the same neural population. The production of different motor patterns within a single circuit is well-established in other systems (Marder and Bucher, 2007).

We do not know where the command or decision to strike originates in the brain. It is very likely that the anterior tectum is involved, since prey would induce bilateral activity here immediately prior to the strike. Similarly, the tectum is believed to be the source of the snapping command in toads (Ewert et al., 1994). In mice, however, the signal to capture prey appears to come from the central amygdala (Han et al., 2017). Yet another possibility is the nucleus isthmi (NI), which is implicated in maintaining prey capture sequences (Henriques et al., 2019), as well as coordinating binocular responses to predators (Fernandes et al., 2021).

Thus, it likely implements attentional gating of a wide range of behaviours, possibly including the capture strike.

In Mearns et al. (2020) I showed that zebrafish larvae capture prey with a stereotyped jaw movement involving coordinated extension of the mandible, depression of the hyoid and dorsal flexion of the cranium. Hernández et al. (2002) argue that such a movement requires simultaneous contraction of multiple muscle groups throughout the lower jaw and trunk. Thus, this behaviour must emerge from the coordinated activity of no fewer than five motor neuron pools distributed between trigeminal and facial motor nuclei and the anterior spinal cord, timed perfectly within the capture bout. Premotor circuitry controlling orofacial movements is poorly characterised, but may also exist within the reticular formation.

4. OUTLOOK

Modulation of prey capture behaviour

While feeding is obviously essential for animal survival, it is also potentially a very costly behaviour. Lingering at the water surface in broad daylight makes zebrafish larvae easy targets for predators from both above and below. Prey capture behaviour consumes neural resources, such as attention, that could otherwise be focussed on recognising and responding to these potential threats. Explosive strike manoeuvres are energetically demanding and cannot be wasted on nutrient-poor or out of reach targets. Thus, all levels of the behaviour – from determining the best time to feed, to selecting the best targets for a response, to determining whether and when to strike – must be carefully balanced with other needs of the animal. Recent advances are starting to shed light on the neural mechanisms that modulate prey capture behaviour.

Hunger is clearly a strong motivator of prey capture behaviour, and zebrafish larvae are more voracious hunters when starved (Johnson et al., 2020). The hypothalamus, a well-known appetite control centre in mammals, is modulated by food cues and feeding state in zebrafish larvae (Wee et al., 2019). Information about prey in the visual field reaches the hypothalamus via the pretectum (Muto et al., 2017). However, it is unknown how hunger and satiety states encoded in the hypothalamus might feedback to gate the visuomotor circuits of prey capture.

Another neural correlate of hunting motivation is found in the dorsal raphe nucleus. Activity in this nucleus oscillates as fish switch between exploratory and exploitative behavioural states, during which larvae are less or more likely to engage in prey capture, respectively (Marques et al., 2020). Serotonin released by dorsal raphe neurons modulates the tuning of tectal neurons to visual stimuli (Filosa et al., 2016), and thus could provide a mechanism for how the internal motivational state of the larva gates prey capture behaviour. Further work might seek to uncover the morphology and function of tectal neurons that are subject to neuromodulation, as well as investigate whether this system also modulates other prey capture-related brain regions.

Multimodal integration

While vision is the dominant sensory modality underlying zebrafish larval prey capture, they are occasionally able to capture prey in the dark (Gahtan et al., 2005; Patterson et al., 2013). Some other species depend heavily on the lateral line for prey capture (Lloyd et al., 2018; Schwalbe et al., 2012). Integration of lateral line and visual inputs probably occurs during the behaviour, especially when the prey is close to the fish prior to the onset of a strike

(New, 2002). Second-order lateral line neurons in the hindbrain project predominantly to the torus semicircularis, but also to the tectum (Bleckmann, 2008; Fame et al., 2006). Thus, multimodal integration of visual and lateral line information could occur in the tectum (Thompson et al., 2016), and influence from the latter may be the more important for prey catching in some species.

Olfaction represents another important sensory modality for feeding. Certain amino acids provide an appetitive signal for fish (Vitebsky et al., 2005), and thus may provide cues that direct exploratory swimming towards potential food sources. In some fish species, the mere presence of some amino acids is sufficient to release prey capture-like behaviours (Mearns, 1989). While the terminal nerve provides a direct connection between the olfactory system and the retina (Whitlock, 2004), descending projections from the telencephalon to the diencephalon, midbrain, and hindbrain represent more likely candidates for multimodal integration between vision and olfaction during prey capture. The neural circuits through which olfaction influences this behaviour, however, remain comparatively unexplored.

Evolution of behaviour

The evolution of jaws more than 400 million years ago allowed for the diversification of feeding strategies and radiation of gnathostomes, representing all extant vertebrates except hagfish and lampreys. Distinct behavioural modules for the pursuit and capture of prey, with correspondingly distinct neural pathways, appears to be a shared feature of hunting across taxa, from fish (discussed here) to frogs (Ewert, 1987) to mice (Han et al., 2017). These similarities are probably not a coincidence, since all vertebrates share a common neural *bauplan*, and the ancestral circuitry that drove active predation in our last common ancestor must surely have left a mark on its descendants. There is remarkable conservation of the gene regulatory networks that guide the development of motor and premotor circuits in vertebrates, their connectivity, and their function (Grillner and El Manira, 2019).

But while the effectors of the *Umwelt* remain invariant – *eat* this; *avoid* that –, the receptors for *this* and *that* are forever changing as predators and prey try to outpace each other in an evolutionary arms race. Thus, behaviour could evolve as new and repurposed sensory representations are rewired to the primordial circuits that pattern motion. These motor circuits, in contrast, need only be fine-tuned to the specifics of the environment and biomechanics of the animal. Comparative studies of prey capture in vertebrates could yield great insights into the genetic and neural substrates of behavioural evolution.

References

- Akerboom, J., Chen, T.-W., Wardill, T.J., Tian, L., Marvin, J.S., Mutlu, S., Calderón, N.C., Esposti, F., Borghuis, B.G., Sun, X.R., et al. (2012). Optimization of a GCaMP Calcium Indicator for Neural Activity Imaging. *J. Neurosci.* *32*, 13819–13840.
- Anderson, D.J., and Perona, P. (2014). Toward a Science of Computational Ethology. *Neuron* *84*, 18–31.
- Antinucci, P., Folgueira, M., and Bianco, I.H. (2019). Pretectal neurons control hunting behaviour. *ELife* *8*, e48114.
- Antinucci, P., Dumitrescu, A., Deleuze, C., Morley, H.J., Leung, K., Hagley, T., Kubo, F., Baier, H., Bianco, I.H., and Wyart, C. (2020). A calibrated optogenetic toolbox of stable zebrafish opsin lines. *ELife* *9*, e54937.
- Arber, S., and Costa, R.M. (2018). Connecting neuronal circuits for movement. *Science* *360*, 1403–1404.
- Arrenberg, A.B., Bene, F.D., and Baier, H. (2009). Optical control of zebrafish behavior with halorhodopsin. *Proc. Natl. Acad. Sci.* *106*, 17968–17973.
- Avitan, L., Pujic, Z., Mölter, J., McCullough, M., Zhu, S., Sun, B., Myhre, A.-E., and Goodhill, G.J. (2020). Behavioral Signatures of a Developing Neural Code. *Curr. Biol.* *30*, 3352-3363.e5.
- Baden, T., Euler, T., and Berens, P. (2020). Understanding the retinal basis of vision across species. *Nat. Rev. Neurosci.* *21*, 5–20.
- Baier, H., and Scott, E.K. (2009). Genetic and optical targeting of neural circuits and behavior—zebrafish in the spotlight. *Curr. Opin. Neurobiol.* *19*, 553–560.
- Barker, A.J., and Baier, H. (2015). Sensorimotor Decision Making in the Zebrafish Tectum. *Curr. Biol.* *25*, 2804–2814.
- Barlow, H.B., Blakemore, C., and Pettigrew, J.D. (1967). The neural mechanism of binocular depth discrimination. *J. Physiol.* *193*, 327–342.
- Ben-Tov, M., Donchin, O., Ben-Shahar, O., and Segev, R. (2015). Pop-out in visual search of moving targets in the archer fish. *Nat. Commun.* *6*, 6476.
- Berman, G.J. (2018). Measuring behavior across scales. *BMC Biol.* *16*, 23.
- Berman, G.J., Choi, D.M., Bialek, W., and Shaevitz, J.W. (2014). Mapping the stereotyped behaviour of freely moving fruit flies. *J. R. Soc. Interface* *11*, 20140672.
- Berman, G.J., Bialek, W., and Shaevitz, J.W. (2016). Predictability and hierarchy in *Drosophila* behavior. *Proc. Natl. Acad. Sci.* *113*, 11943–11948.
- Bhattacharyya, K., McLean, D.L., and MacIver, M.A. (2017). Visual Threat Assessment and Reticulospinal Encoding of Calibrated Responses in Larval Zebrafish. *Curr. Biol.* *27*, 2751-2762.e6.

- Bialek, W. (2020). What do we mean by the dimensionality of behavior? ArXiv200809574 Cond-Mat Q-Bio.
- Bianco, I.H., and Engert, F. (2015). Visuomotor Transformations Underlying Hunting Behavior in Zebrafish. *Curr. Biol.* 25, 831–846.
- Bianco, I.H., Kampff, A.R., and Engert, F. (2011). Prey Capture Behavior Evoked by Simple Visual Stimuli in Larval Zebrafish. *Front. Syst. Neurosci.* 5.
- Bilotta, J., Saszik, S., and Sutherland, S.E. (2001). Rod contributions to the electroretinogram of the dark-adapted developing zebrafish. *Dev. Dyn.* 222, 564–570.
- Bizzi, E., and Cheung, V.C. (2013). The neural origin of muscle synergies. *Front. Comput. Neurosci.* 7.
- Bleckmann, H. (2008). Peripheral and central processing of lateral line information. *J. Comp. Physiol. A* 194, 145–158.
- Bolton, A.D., Haesemeyer, M., Jordi, J., Schaechtle, U., Saad, F.A., Mansinghka, V.K., Tenenbaum, J.B., and Engert, F. (2019). Elements of a stochastic 3D prediction engine in larval zebrafish prey capture. *ELife* 8, e51975.
- Borla, M.A., Palecek, B., Budick, S., and O'Malley, D.M. (2002). Prey Capture by Larval Zebrafish: Evidence for Fine Axial Motor Control. *Brain. Behav. Evol.* 60, 207–229.
- Bouvier, J., Caggiano, V., Leiras, R., Caldeira, V., Bellardita, C., Balueva, K., Fuchs, A., and Kiehn, O. (2015). Descending Command Neurons in the Brainstem that Halt Locomotion. *Cell* 163, 1191–1203.
- Boyden, E.S., Zhang, F., Bamberg, E., Nagel, G., and Deisseroth, K. (2005). Millisecond-timescale, genetically targeted optical control of neural activity. *Nat. Neurosci.* 8, 1263–1268.
- Brown, A.E.X., and Bivort, B. de (2018). Ethology as a physical science. *Nat. Phys.* 1.
- Brown, A.E.X., Yemini, E.I., Grundy, L.J., Jucikas, T., and Schafer, W.R. (2013). A dictionary of behavioral motifs reveals clusters of genes affecting *Caenorhabditis elegans* locomotion. *Proc. Natl. Acad. Sci.* 110, 791–796.
- Budick, S.A., and O'Malley, D.M. (2000). Locomotor repertoire of the larval zebrafish: swimming, turning and prey capture. *J. Exp. Biol.* 203, 2565–2579.
- Burgess, H.A., and Granato, M. (2007a). Modulation of locomotor activity in larval zebrafish during light adaptation. *J. Exp. Biol.* 210, 2526–2539.
- Burgess, H.A., and Granato, M. (2007b). Sensorimotor Gating in Larval Zebrafish. *J. Neurosci.* 27, 4984–4994.
- Burrill, J.D., and Easter, S.S. (1994). Development of the retinofugal projections in the embryonic and larval zebrafish (*Brachydanio rerio*). *J. Comp. Neurol.* 346, 583–600.
- Cande, J., Namiki, S., Qiu, J., Korff, W., Card, G.M., Shaevitz, J.W., Stern, D.L., and Berman, G.J. (2018). Optogenetic dissection of descending behavioral control in *Drosophila*. *ELife* 7, e34275.

- Capelli, P., Pivetta, C., Soledad Esposito, M., and Arber, S. (2017). Locomotor speed control circuits in the caudal brainstem. *Nature* 551, 373–377.
- Coen, P., Clemens, J., Weinstein, A.J., Pacheco, D.A., Deng, Y., and Murthy, M. (2014). Dynamic sensory cues shape song structure in *Drosophila*. *Nature* 507, 233–237.
- Collett, T. (1977). Stereopsis in toads. *Nature* 267, 349–351.
- Comoli, E., Ribeiro-Barbosa, E.R., and Canteras, N.S. (2003). Predatory hunting and exposure to a live predator induce opposite patterns of Fos immunoreactivity in the PAG. *Behav. Brain Res.* 138, 17–28.
- Del Vecchio, D., Murray, R.M., and Perona, P. (2003). Decomposition of human motion into dynamics-based primitives with application to drawing tasks. *Automatica* 39, 2085–2098.
- Denk, W., Strickler, J.H., and Webb, W.W. (1990). Two-photon laser scanning fluorescence microscopy. *Science* 248, 73–76.
- Dunn, T.W., Mu, Y., Narayan, S., Randlett, O., Naumann, E.A., Yang, C.-T., Schier, A.F., Freeman, J., Engert, F., and Ahrens, M.B. (2016a). Brain-wide mapping of neural activity controlling zebrafish exploratory locomotion. *ELife* 5, e12741.
- Dunn, T.W., Gebhardt, C., Naumann, E.A., Riegler, C., Ahrens, M.B., Engert, F., and Del Bene, F. (2016b). Neural Circuits Underlying Visually Evoked Escapes in Larval Zebrafish. *Neuron* 89, 613–628.
- Egnor, S.E.R., and Branson, K. (2016). Computational Analysis of Behavior.
- Esposito, M.S., Capelli, P., and Arber, S. (2014). Brainstem nucleus MdV mediates skilled forelimb motor tasks. *Nature* 508, 351–356.
- Ewert, J.-P. (1987). Neuroethology of releasing mechanisms: Prey-catching in toads. *Behav. Brain Sci.* 10, 337–368.
- Ewert, J.-P., Beneke, T.W., Schürg-Pfeiffer, E., Schwippert, W.W., and Weerasuriya, A. (1994). Sensorimotor Processes That Underlie Feeding Behavior in Tetrapods. In *Biomechanics of Feeding in Vertebrates*, V.L. Bels, M. Chardon, and P. Vandewalle, eds. (Berlin, Heidelberg: Springer Berlin Heidelberg), pp. 119–162.
- Ewert, J.-P., Buxbaum-Conradi, H., Dreisvogt, F., Glagow, M., Merkel-Harff, C., Röttgen, A., Schürg-Pfeiffer, E., and Schwippert, W.W. (2001). Neural modulation of visuomotor functions underlying prey-catching behaviour in anurans: perception, attention, motor performance, learning. *Comp. Biochem. Physiol. A. Mol. Integr. Physiol.* 128, 417–460.
- Fabian, S.T., Sumner, M.E., Wardill, T.J., Rossoni, S., and Gonzalez-Bellido, P.T. (2018). Interception by two predatory fly species is explained by a proportional navigation feedback controller. *J. R. Soc. Interface* 15, 20180466.
- Fadok, J.P., Markovic, M., Tovote, P., and Lüthi, A. (2018). New perspectives on central amygdala function. *Curr. Opin. Neurobiol.* 49, 141–147.
- Fame, R.M., Brajon, C., and Ghysen, A. (2006). Second-order projection from the posterior lateral line in the early zebrafish brain. *Neural Develop.* 1, 4.

- Fernandes, A.M., Mearns, D.S., Donovan, J.C., Larsch, J., Helmbrecht, T.O., Kölsch, Y., Laurell, E., Kawakami, K., dal Maschio, M., and Baier, H. (2021). Neural circuitry for stimulus selection in the zebrafish visual system. *Neuron* 109, 805-822.e6.
- Fero, K., Yokogawa, T., and Burgess, H.A. (2011). The Behavioral Repertoire of Larval Zebrafish. In *Zebrafish Models in Neurobehavioral Research*, (Humana Press, Totowa, NJ), pp. 249–291.
- Filosa, A., Barker, A.J., Dal Maschio, M., and Baier, H. (2016). Feeding State Modulates Behavioral Choice and Processing of Prey Stimuli in the Zebrafish Tectum. *Neuron* 90, 596–608.
- Flash, T., and Hochner, B. (2005). Motor primitives in vertebrates and invertebrates. *Curr. Opin. Neurobiol.* 15, 660–666.
- Förster, D., Dal Maschio, M., Laurell, E., and Baier, H. (2017). An optogenetic toolbox for unbiased discovery of functionally connected cells in neural circuits. *Nat. Commun.* 8, 116.
- Förster, D., Kramer, A., Baier, H., and Kubo, F. (2018). Optogenetic precision toolkit to reveal form, function and connectivity of single neurons. *Methods* 150, 42–48.
- Förster, D., Helmbrecht, T.O., Mearns, D.S., Jordan, L., Mokayes, N., and Baier, H. (2020). Retinotectal circuitry of larval zebrafish is adapted to detection and pursuit of prey. *ELife* 9, e58596.
- Gahtan, E., Sankrithi, N., Campos, J.B., and O'Malley, D.M. (2002). Evidence for a Widespread Brain Stem Escape Network in Larval Zebrafish. *J. Neurophysiol.* 87, 608–614.
- Gahtan, E., Tanger, P., and Baier, H. (2005). Visual Prey Capture in Larval Zebrafish Is Controlled by Identified Reticulospinal Neurons Downstream of the Tectum. *J. Neurosci.* 25, 9294–9303.
- Gebhardt, C., Auer, T.O., Henriques, P.M., Rajan, G., Durore, K., Bianco, I.H., and Del Bene, F. (2019). An interhemispheric neural circuit allowing binocular integration in the optic tectum. *Nat. Commun.* 10, 5471.
- Girdhar, K., Gruebele, M., and Chemla, Y.R. (2015). The Behavioral Space of Zebrafish Locomotion and Its Neural Network Analog. *PLOS ONE* 10, e0128668.
- Gomez-Marin, A., Stephens, G.J., and Brown, A.E.X. (2016). Hierarchical compression of *Caenorhabditis elegans* locomotion reveals phenotypic differences in the organization of behaviour. *J. R. Soc. Interface* 13, 20160466.
- Govorunova, E.G., Sineshchekov, O.A., Janz, R., Liu, X., and Spudich, J.L. (2015). Natural light-gated anion channels: A family of microbial rhodopsins for advanced optogenetics. *Science* 349, 647–650.
- Grätsch, S., Auclair, F., Demers, O., Auguste, E., Hanna, A., Büschges, A., and Dubuc, R. (2019). A Brainstem Neural Substrate for Stopping Locomotion. *J. Neurosci.* 39, 1044–1057.
- Grienberger, C., and Konnerth, A. (2012). Imaging Calcium in Neurons. *Neuron* 73, 862–885.

- Grillner, S., and El Manira, A. (2019). Current Principles of Motor Control, with Special Reference to Vertebrate Locomotion. *Physiol. Rev.* 100, 271–320.
- Han, W., Tellez, L.A., Rangel, M.J., Motta, S.C., Zhang, X., Perez, I.O., Canteras, N.S., Shammah-Lagnado, S.J., Pol, A.N. van den, and Araujo, I.E. de (2017). Integrated Control of Predatory Hunting by the Central Nucleus of the Amygdala. *Cell* 168, 311-324.e18.
- Helmbrecht, T.O., dal Maschio, M., Donovan, J.C., Koutsouli, S., and Baier, H. (2018). Topography of a Visuomotor Transformation. *Neuron* 100, 1429-1445.e4.
- Henriques, P.M., Rahman, N., Jackson, S.E., and Bianco, I.H. (2019). Nucleus Isthmi Is Required to Sustain Target Pursuit during Visually Guided Prey-Catching. *Curr. Biol.* 0.
- Hernández, D.G., Rivera, C., Cande, J., Zhou, B., Stern, D.L., and Berman, G.J. (2020). A framework for studying behavioral evolution by reconstructing ancestral repertoires. *BioRxiv* 2020.07.17.209361.
- Hernández, L.P., Barresi, M.J.F., and Devoto, S.H. (2002). Functional Morphology and Developmental Biology of Zebrafish: Reciprocal Illumination from an Unlikely Couple. *Integr. Comp. Biol.* 42, 222–231.
- Higashijima, S., Hotta, Y., and Okamoto, H. (2000). Visualization of Cranial Motor Neurons in Live Transgenic Zebrafish Expressing Green Fluorescent Protein Under the Control of the *Islet-1* Promoter/Enhancer. *J. Neurosci.* 20, 206–218.
- Hinz, R.C., and Polavieja, G.G. de (2017). Ontogeny of collective behavior reveals a simple attraction rule. *Proc. Natl. Acad. Sci.* 114, 2295–2300.
- Huang, K.-H., Ahrens, M.B., Dunn, T.W., and Engert, F. (2013). Spinal Projection Neurons Control Turning Behaviors in Zebrafish. *Curr. Biol.* 23, 1566–1573.
- Hubel, D.H., and Wiesel, T.N. (1970). Stereoscopic Vision in Macaque Monkey: Cells sensitive to Binocular Depth in Area 18 of the Macaque Monkey Cortex. *Nature* 225, 41–42.
- Jin, L., Joest, E.F., Li, W., Gao, S., Offenhäusser, A., and Maybeck, V. (2017). High current optogenetic channels for stimulation and inhibition of primary rat cortical neurons. *BioRxiv* 145441.
- Johnson, R.E., Linderman, S., Panier, T., Wee, C.L., Song, E., Herrera, K.J., Miller, A., and Engert, F. (2020). Probabilistic Models of Larval Zebrafish Behavior Reveal Structure on Many Scales. *Curr. Biol.* 30, 70-82.e4.
- Jouary, A., and Sumbre, G. (2016). Automatic classification of behavior in zebrafish larvae. *BioRxiv* 052324.
- Kardamakis, A.A., Saitoh, K., and Grillner, S. (2015). Tectal microcircuit generating visual selection commands on gaze-controlling neurons. *Proc. Natl. Acad. Sci.* 112, E1956–E1965.
- Kato, S., Kaplan, H.S., Schrödel, T., Skora, S., Lindsay, T.H., Yemini, E., Lockery, S., and Zimmer, M. (2015). Global Brain Dynamics Embed the Motor Command Sequence of *Caenorhabditis elegans*. *Cell* 163, 656–669.
- Katsov, A.Y., Freifeld, L., Horowitz, M., Kuehn, S., and Clandinin, T.R. (2017). Dynamic structure of locomotor behavior in walking fruit flies. *ELife* 6, e26410.

- Kimmel, C.B., Eaton, R.C., and Powell, S.L. (1980). Decreased fast-start performance of zebrafish larvae lacking mauthner neurons. *J. Comp. Physiol.* *140*, 343–350.
- Kimmel, C.B., Powell, S.L., and Metcalfe, W.K. (1982). Brain neurons which project to the spinal cord in young larvae of the zebrafish. *J. Comp. Neurol.* *205*, 112–127.
- Klapoetke, N.C., Nern, A., Peek, M.Y., Rogers, E.M., Breads, P., Rubin, G.M., Reiser, M.B., and Card, G.M. (2017). Ultra-selective looming detection from radial motion opponency. *Nature* *551*, 237–241.
- Knudsen, E.I. (2018). Neural Circuits That Mediate Selective Attention: A Comparative Perspective. *Trends Neurosci.* *41*, 789–805.
- Koch, C., and Ullman, S. (1987). Shifts in Selective Visual Attention: Towards the Underlying Neural Circuitry. In *Matters of Intelligence: Conceptual Structures in Cognitive Neuroscience*, L.M. Vaina, ed. (Dordrecht: Springer Netherlands), pp. 115–141.
- Kölsch, Y., Hahn, J., Sappington, A., Stemmer, M., Fernandes, A.M., Helmbrecht, T.O., Lele, S., Butrus, S., Laurell, E., Arnold-Ammer, I., et al. (2021). Molecular classification of zebrafish retinal ganglion cells links genes to cell types to behavior. *Neuron* *109*, 645-662.e9.
- Korn, H., and Faber, D.S. (2005). The Mauthner Cell Half a Century Later: A Neurobiological Model for Decision-Making? *Neuron* *47*, 13–28.
- Kostyk, S.K., and Grobstein, P. (1987). Neuronal organization underlying visually elicited prey orienting in the frog—I. Effects of various unilateral lesions. *Neuroscience* *21*, 41–55.
- Krakauer, J.W., Ghazanfar, A.A., Gomez-Marin, A., MacIver, M.A., and Poeppel, D. (2017). Neuroscience Needs Behavior: Correcting a Reductionist Bias. *Neuron* *93*, 480–490.
- Kubo, F., Hablitzel, B., Dal Maschio, M., Driever, W., Baier, H., and Arrenberg, A.B. (2014). Functional Architecture of an Optic Flow-Responsive Area that Drives Horizontal Eye Movements in Zebrafish. *Neuron* *81*, 1344–1359.
- Kupfermann, I., and Weiss, K.R. (1978). The command neuron concept. *Behav. Brain Sci.* *1*, 3–10.
- Lagogiannis, K., Diana, G., and Meyer, M.P. (2020). Learning steers the ontogeny of an efficient hunting sequence in zebrafish larvae. *ELife* *9*, e55119.
- Lee, D.K., Itti, L., Koch, C., and Braun, J. (1999). Attention activates winner-take-all competition among visual filters. *Nat. Neurosci.* *2*, 375–381.
- Lee, M.M., Arrenberg, A.B., and Aksay, E.R.F. (2015). A Structural and Genotypic Scaffold Underlying Temporal Integration. *J. Neurosci.* *35*, 7903–7920.
- Levitis, D.A., Lidicker, W.Z., and Freund, G. (2009). Behavioural biologists do not agree on what constitutes behaviour. *Anim. Behav.* *78*, 103–110.
- Lin, H.-T., and Leonardo, A. (2017). Heuristic Rules Underlying Dragonfly Prey Selection and Interception. *Curr. Biol.* *27*, 1124–1137.
- Lisberger, S.G., and Ferrera, V.P. (1997). Vector Averaging for Smooth Pursuit Eye Movements Initiated by Two Moving Targets in Monkeys. *J. Neurosci.* *17*, 7490–7502.

- Liu, K.S., and Fetcho, J.R. (1999). Laser Ablations Reveal Functional Relationships of Segmental Hindbrain Neurons in Zebrafish. *Neuron* 23, 325–335.
- Liu, Y.-C., Bailey, I., and Hale, M.E. (2012). Alternative startle motor patterns and behaviors in the larval zebrafish (*Danio rerio*). *J. Comp. Physiol. A* 198, 11–24.
- Lloyd, E., Olive, C., Stahl, B.A., Jaggard, J.B., Amaral, P., Duboué, E.R., and Keene, A.C. (2018). Evolutionary shift towards lateral line dependent prey capture behavior in the blind Mexican cavefish. *Dev. Biol.* 441, 328–337.
- Long, M.A., Jin, D.Z., and Fee, M.S. (2010). Support for a synaptic chain model of neuronal sequence generation. *Nature* 468, 394–399.
- Mahn, M., Gibor, L., Patil, P., Cohen-Kashi Malina, K., Oring, S., Printz, Y., Levy, R., Lampl, I., and Yizhar, O. (2018). High-efficiency optogenetic silencing with soma-targeted anion-conducting channelrhodopsins. *Nat. Commun.* 9, 4125.
- Marder, E., and Bucher, D. (2007). Understanding Circuit Dynamics Using the Stomatogastric Nervous System of Lobsters and Crabs. *Annu. Rev. Physiol.* 69, 291–316.
- Marques, J.C., Lackner, S., Félix, R., and Orger, M.B. (2018). Structure of the Zebrafish Locomotor Repertoire Revealed with Unsupervised Behavioral Clustering. *Curr. Biol.* 28, 181-195.e5.
- Marques, J.C., Li, M., Schaak, D., Robson, D.N., and Li, J.M. (2020). Internal state dynamics shape brainwide activity and foraging behaviour. *Nature* 577, 239–243.
- dal Maschio, M., Donovan, J.C., Helmbrecht, T.O., and Baier, H. (2017). Linking Neurons to Network Function and Behavior by Two-Photon Holographic Optogenetics and Volumetric Imaging. *Neuron* 94, 774-789.e5.
- McClenahan, P., Troup, M., and Scott, E.K. (2012). Fin-Tail Coordination during Escape and Predatory Behavior in Larval Zebrafish. *PLOS ONE* 7, e32295.
- McElligott, M.B., and O'Malley, D.M. (2005). Prey Tracking by Larval Zebrafish: Axial Kinematics and Visual Control. *Brain. Behav. Evol.* 66, 177–196.
- McLean, D.L., Fan, J., Higashijima, S., Hale, M.E., and Fetcho, J.R. (2007). A topographic map of recruitment in spinal cord. *Nature* 446, 71–75.
- Mearns, K.J. (1989). Behavioural responses of salmonid fry to low amino acid concentrations. *J. Fish Biol.* 34, 223–232.
- Mearns, D.S., Donovan, J.C., Fernandes, A.M., Semmelhack, J.L., and Baier, H. (2020). Deconstructing Hunting Behavior Reveals a Tightly Coupled Stimulus-Response Loop. *Curr. Biol.* 30, 54-69.e9.
- Metcalfe, W.K., Mendelson, B., and Kimmel, C.B. (1986). Segmental homologies among reticulospinal neurons in the hindbrain of the zebrafish larva. *J. Comp. Neurol.* 251, 147–159.
- Mirat, O., Sternberg, J.R., Severi, K.E., and Wyart, C. (2013). ZebraZoom: an automated program for high-throughput behavioral analysis and categorization. *Front. Neural Circuits* 7.

- Miri, A., Daie, K., Burdine, R.D., Aksay, E., and Tank, D.W. (2011). Regression-Based Identification of Behavior-Encoding Neurons During Large-Scale Optical Imaging of Neural Activity at Cellular Resolution. *J. Neurophysiol.* *105*, 964–980.
- Mohamed, G.A., Cheng, R.-K., Ho, J., Krishnan, S., Mohammad, F., Claridge-Chang, A., and Jesuthasan, S. (2017). Optical inhibition of larval zebrafish behaviour with anion channelrhodopsins. *BMC Biol.* *15*, 103.
- Müller, U.K., and van Leeuwen, J.L. (2004). Swimming of larval zebrafish: ontogeny of body waves and implications for locomotory development. *J. Exp. Biol.* *207*, 853–868.
- Muto, A., and Kawakami, K. (2018). Ablation of a Neuronal Population Using a Two-photon Laser and Its Assessment Using Calcium Imaging and Behavioral Recording in Zebrafish Larvae. *JoVE J. Vis. Exp.* e57485.
- Muto, A., Ohkura, M., Abe, G., Nakai, J., and Kawakami, K. (2013). Real-Time Visualization of Neuronal Activity during Perception. *Curr. Biol.* *23*, 307–311.
- Muto, A., Lal, P., Ailani, D., Abe, G., Itoh, M., and Kawakami, K. (2017). Activation of the hypothalamic feeding centre upon visual prey detection. *Nat. Commun.* *8*, 15029.
- Nagel, G., Szellas, T., Huhn, W., Kateriya, S., Adeishvili, N., Berthold, P., Ollig, D., Hegemann, P., and Bamberg, E. (2003). Channelrhodopsin-2, a directly light-gated cation-selective membrane channel. *Proc. Natl. Acad. Sci.* *100*, 13940–13945.
- Nakagawa, H., and Hongjian, K. (2010). Collision-Sensitive Neurons in the Optic Tectum of the Bullfrog, *Rana catesbeiana*. *J. Neurophysiol.* *104*, 2487–2499.
- Nakai, J., Ohkura, M., and Imoto, K. (2001). A high signal-to-noise Ca²⁺ probe composed of a single green fluorescent protein. *Nat. Biotechnol.* *19*, 137–141.
- Neuhauss, S.C.F., Biehlmaier, O., Seeliger, M.W., Das, T., Kohler, K., Harris, W.A., and Baier, H. (1999). Genetic Disorders of Vision Revealed by a Behavioral Screen of 400 Essential Loci in Zebrafish. *J. Neurosci.* *19*, 8603–8615.
- Nevin, L.M., Robles, E., Baier, H., and Scott, E.K. (2010). Focusing on optic tectum circuitry through the lens of genetics. *BMC Biol.* *8*, 126.
- New, J.G. (2002). Multimodal Integration in the Feeding Behaviors of Predatory Teleost Fishes. *Brain. Behav. Evol.* *59*, 177–189.
- Nityananda, V., Tarawneh, G., Rosner, R., Nicolas, J., Crichton, S., and Read, J. (2016). Insect stereopsis demonstrated using a 3D insect cinema. *Sci. Rep.* *6*, 18718.
- Nityananda, V., Tarawneh, G., Henriksen, S., Umeton, D., Simmons, A., and Read, J.C.A. (2018). A Novel Form of Stereo Vision in the Praying Mantis. *Curr. Biol.* *28*, 588-593.e4.
- Niv, Y. (2020). The primacy of behavioral research for understanding the brain.
- Nummela, S.U., and Krauzlis, R.J. (2011). Superior Colliculus Inactivation Alters the Weighted Integration of Visual Stimuli. *J. Neurosci.* *31*, 8059–8066.
- Nüsslein-Volhard, C. (2012). The zebrafish issue of *Development*. *Development* *139*, 4099–4103.

- Ohzawa, I., DeAngelis, G.C., and Freeman, R.D. (1990). Stereoscopic depth discrimination in the visual cortex: neurons ideally suited as disparity detectors. *Science* 249, 1037–1041.
- Oldfield, C.S., Grossrubatscher, I., Chávez, M., Hoagland, A., Huth, A.R., Carroll, E.C., Prendergast, A., Qu, T., Gallant, J.L., Wyart, C., et al. (2020). Experience, circuit dynamics, and forebrain recruitment in larval zebrafish prey capture. *ELife* 9, e56619.
- O'Malley, D.M., Kao, Y.-H., and Fetcho, J.R. (1996). Imaging the Functional Organization of Zebrafish Hindbrain Segments during Escape Behaviors. *Neuron* 17, 1145–1155.
- Orger, M.B., and de Polavieja, G.G. (2017). Zebrafish Behavior: Opportunities and Challenges. *Annu. Rev. Neurosci.* 40, 125–147.
- Orger, M.B., Kampff, A.R., Severi, K.E., Bollmann, J.H., and Engert, F. (2008). Control of visually guided behavior by distinct populations of spinal projection neurons. *Nat. Neurosci.* 11, 327–333.
- Parichy, D.M. (2015). Advancing biology through a deeper understanding of zebrafish ecology and evolution. *ELife* 4, e05635.
- Patterson, B.W., Abraham, A.O., MacIver, M.A., and McLean, D.L. (2013). Visually guided gradation of prey capture movements in larval zebrafish. *J. Exp. Biol.* 216, 3071–3083.
- Portugues, R., and Engert, F. (2011). Adaptive Locomotor Behavior in Larval Zebrafish. *Front. Syst. Neurosci.* 5.
- Preuss, S.J., Trivedi, C.A., vom Berg-Maurer, C.M., Ryu, S., and Bollmann, J.H. (2014). Classification of Object Size in Retinotectal Microcircuits. *Curr. Biol.* 24, 2376–2385.
- Robie, A.A., Hirokawa, J., Edwards, A.W., Umayam, L.A., Lee, A., Phillips, M.L., Card, G.M., Korff, W., Rubin, G.M., Simpson, J.H., et al. (2017). Mapping the Neural Substrates of Behavior. *Cell* 170, 393-406.e28.
- Robles, E., Smith, S.J., and Baier, H. (2011). Characterization of Genetically Targeted Neuron Types in the Zebrafish Optic Tectum. *Front. Neural Circuits* 5.
- Robles, E., Laurell, E., and Baier, H. (2014). The Retinal Projectome Reveals Brain-Area-Specific Visual Representations Generated by Ganglion Cell Diversity. *Curr. Biol.* 24, 2085–2096.
- Sahibzada, N., Dean, P., and Redgrave, P. (1986). Movements resembling orientation or avoidance elicited by electrical stimulation of the superior colliculus in rats. *J. Neurosci.* 6, 723–733.
- Sakoe, H., and Chiba, S. (1978). Dynamic programming algorithm optimization for spoken word recognition. *IEEE Trans. Acoust. Speech Signal Process.* 26, 43–49.
- Schmitt, E.A., and Dowling, J.E. (1999). Early retinal development in the zebrafish, *Danio rerio*: Light and electron microscopic analyses. *J. Comp. Neurol.* 404, 515–536.
- Schwalbe, M.A.B., Bassett, D.K., and Webb, J.F. (2012). Feeding in the dark: lateral-line-mediated prey detection in the peacock cichlid *Aulonocara stuartgranti*. *J. Exp. Biol.* 215, 2060–2071.

- Seeds, A.M., Ravbar, P., Chung, P., Hampel, S., Jr, F.M.M., Mensh, B.D., and Simpson, J.H. (2014). A suppression hierarchy among competing motor programs drives sequential grooming in *Drosophila*. *ELife* 3, e02951.
- Semmelhack, J.L., Donovan, J.C., Thiele, T.R., Kuehn, E., Laurell, E., and Baier, H. (2014). A dedicated visual pathway for prey detection in larval zebrafish. *ELife* 3, e04878.
- Severi, K.E., Portugues, R., Marques, J.C., O'Malley, D.M., Orger, M.B., and Engert, F. (2014). Neural Control and Modulation of Swimming Speed in the Larval Zebrafish. *Neuron* 83, 692–707.
- Simmons, P.J., Rind, F.C., and Santer, R.D. (2010). Escapes with and without preparation: The neuroethology of visual startle in locusts. *J. Insect Physiol.* 56, 876–883.
- Stephens, G.J., Johnson-Kerner, B., Bialek, W., and Ryu, W.S. (2008). Dimensionality and Dynamics in the Behavior of *C. elegans*. *PLOS Comput. Biol.* 4, e1000028.
- Stephens, G.J., Mesquita, M.B. de, Ryu, W.S., and Bialek, W. (2011). Emergence of long timescales and stereotyped behaviors in *Caenorhabditis elegans*. *Proc. Natl. Acad. Sci.* 108, 7286–7289.
- Streisinger, G., Walker, C., Dower, N., Knauber, D., and Singer, F. (1981). Production of clones of homozygous diploid zebra fish (*Brachydanio rerio*). *Nature* 291, 293–296.
- Stuermer, C.A. (1988). Retinotopic organization of the developing retinotectal projection in the zebrafish embryo. *J. Neurosci.* 8, 4513–4530.
- Sugano, Y., and Neuhauss, S.C.F. (2013). Reverse genetics tools in zebrafish: A forward dive into endocrinology. *Gen. Comp. Endocrinol.* 188, 303–308.
- Tao, L., Ozarkar, S., Beck, J.M., and Bhandawat, V. (2019). Statistical structure of locomotion and its modulation by odors. *ELife* 8, e41235.
- Temizer, I., Donovan, J.C., Baier, H., and Semmelhack, J.L. (2015). A Visual Pathway for Looming-Evoked Escape in Larval Zebrafish. *Curr. Biol.* 25, 1823–1834.
- Tenenbaum, J.B., Silva, V. de, and Langford, J.C. (2000). A Global Geometric Framework for Nonlinear Dimensionality Reduction. *Science* 290, 2319–2323.
- Thiele, T.R., Donovan, J.C., and Baier, H. (2014). Descending Control of Swim Posture by a Midbrain Nucleus in Zebrafish. *Neuron* 83, 679–691.
- Thompson, A.W., Vanwalleghem, G.C., Heap, L.A., and Scott, E.K. (2016). Functional Profiles of Visual-, Auditory-, and Water Flow-Responsive Neurons in the Zebrafish Tectum. *Curr. Biol.* 26, 743–754.
- Thornhill, R. (1976). Sexual Selection and Paternal Investment in Insects. *Am. Nat.* 110, 153–163.
- Thyme, S.B., Pieper, L.M., Li, E.H., Pandey, S., Wang, Y., Morris, N.S., Sha, C., Choi, J.W., Herrera, K.J., Soucy, E.R., et al. (2019). Phenotypic Landscape of Schizophrenia-Associated Genes Defines Candidates and Their Shared Functions. *Cell* 177, 478–491.e20.
- Tian, L., Hires, S.A., and Looger, L.L. (2012). Imaging Neuronal Activity with Genetically Encoded Calcium Indicators. *Cold Spring Harb. Protoc.* 2012, pdb.top069609.

- Tinbergen, N. (1951). *The Study of Instinct* (Oxford: Oxford University Press).
- Trivedi, C.A., and Bollmann, J.H. (2013). Visually driven chaining of elementary swim patterns into a goal-directed motor sequence: a virtual reality study of zebrafish prey capture. *Front. Neural Circuits* 7.
- Tsien, R.Y. (1980). New calcium indicators and buffers with high selectivity against magnesium and protons: design, synthesis, and properties of prototype structures. *Biochemistry* 19, 2396–2404.
- Uexküll, J.V. (1992). A stroll through the worlds of animals and men: A picture book of invisible worlds. 89, 319–391.
- Vitebsky, A., Reyes, R., Sanderson, M.J., Michel, W.C., and Whitlock, K.E. (2005). Isolation and characterization of the laure olfactory behavioral mutant in the zebrafish, *Danio rerio*. *Dev. Dyn.* 234, 229–242.
- Vladimirov, N., Wang, C., Höckendorf, B., Pujala, A., Tanimoto, M., Mu, Y., Yang, C.-T., Wittenbach, J.D., Freeman, J., Preibisch, S., et al. (2018). Brain-wide circuit interrogation at the cellular level guided by online analysis of neuronal function. *Nat. Methods* 15, 1117–1125.
- Wang, W.-C., and McLean, D.L. (2014). Selective Responses to Tonic Descending Commands by Temporal Summation in a Spinal Motor Pool. *Neuron* 83, 708–721.
- Wee, C.L., Song, E.Y., Johnson, R.E., Ailani, D., Randlett, O., Kim, J.-Y., Nikitchenko, M., Bahl, A., Yang, C.-T., Ahrens, M.B., et al. (2019). A bidirectional network for appetite control in larval zebrafish. *ELife* 8, e43775.
- Westphal, R.E., and O'Malley, D.M. (2013). Fusion of locomotor maneuvers, and improving sensory capabilities, give rise to the flexible homing strikes of juvenile zebrafish. *Front. Neural Circuits* 7.
- White, B.J., Berg, D.J., Kan, J.Y., Marino, R.A., Itti, L., and Munoz, D.P. (2017). Superior colliculus neurons encode a visual saliency map during free viewing of natural dynamic video. *Nat. Commun.* 8, 14263.
- Whitlock, K.E. (2004). Development of the nervus terminalis: Origin and migration. *Microsc. Res. Tech.* 65, 2–12.
- Wiersma, C.A.G., and Ikeda, K. (1964). Interneurons commanding swimmeret movements in the crayfish, *Procambarus clarki* (girard). *Comp. Biochem. Physiol.* 12, 509–525.
- Willigen, R.F. van der (2011). Owls see in stereo much like humans do. *J. Vis.* 11, 10–10.
- Wilson, D.M. (1959). Function of Giant Mauthner's Neurons in the Lungfish. *Science* 129, 841–842.
- Wiltschko, A.B., Johnson, M.J., Iurilli, G., Peterson, R.E., Katon, J.M., Pashkovski, S.L., Abaira, V.E., Adams, R.P., and Datta, S.R. (2015). Mapping Sub-Second Structure in Mouse Behavior. *Neuron* 88, 1121–1135.

Wöhl, S., and Schuster, S. (2007). The predictive start of hunting archer fish: a flexible and precise motor pattern performed with the kinematics of an escape C-start. *J. Exp. Biol.* *210*, 311–324.

Wu, Y., Maschio, M. dal, Kubo, F., and Baier, H. (2020). An Optical Illusion Pinpoints an Essential Circuit Node for Global Motion Processing. *Neuron* *108*, 722-734.e5.

Yilmaz, M., and Meister, M. (2013). Rapid Innate Defensive Responses of Mice to Looming Visual Stimuli. *Curr. Biol.* *23*, 2011–2015.

Yoshimatsu, T., Schröder, C., Nevala, N.E., Berens, P., and Baden, T. (2020). Fovea-like Photoreceptor Specializations Underlie Single UV Cone Driven Prey-Capture Behavior in Zebrafish. *Neuron* *107*, 320-337.e6.

Zhang, F., Wang, L.-P., Brauner, M., Liewald, J.F., Kay, K., Watzke, N., Wood, P.G., Bamberg, E., Nagel, G., Gottschalk, A., et al. (2007). Multimodal fast optical interrogation of neural circuitry. *Nature* *446*, 633–639.

Zhang, M., Liu, Y., Wang, S., Zhong, W., Liu, B., and Tao, H.W. (2011). Functional Elimination of Excitatory Feedforward Inputs Underlies Developmental Refinement of Visual Receptive Fields in Zebrafish. *J. Neurosci.* *31*, 5460–5469.

Zhou, M., Bear, J., Roberts, P.A., Janiak, F.K., Semmelhack, J., Yoshimatsu, T., and Baden, T. (2020). Zebrafish Retinal Ganglion Cells Asymmetrically Encode Spectral and Temporal Information across Visual Space. *Curr. Biol.* *30*, 2927-2942.e7.

Zimmermann, M.J.Y., Nevala, N.E., Yoshimatsu, T., Osorio, D., Nilsson, D.-E., Berens, P., and Baden, T. (2018). Zebrafish Differentially Process Color across Visual Space to Match Natural Scenes. *Curr. Biol.* *28*, 2018-2032.e5.

ACKNOWLEDGEMENTS

When I moved to Munich at the beginning of 2014, I thought I would not stay longer than a year. But after my first six months in the Baier lab, I knew that I had to stay; and now, seven years later, I am so glad that I did. Countless people have helped and supported me on this journey.

Thank you, Herwig. You have given me the intellectual freedom to pursue my own ideas in the lab, and nurtured an environment full of great experimentalists and thinkers from around the world, who have helped me bring those ideas to fruition. You have taught me how to think, taught me how to write, taught me how to present my work. You have mentored and supported me for so many years, and I am enormously grateful.

Thank you, Tod and Julie. Tod, for your teaching and mentorship in that first year, which set me on the path to pursuing my doctoral research in zebrafish. Julie, for showing me the importance of behavioural research in neuroscience, introducing me to the prey capture field, and teaching me how to be a better scientist: you continue to be a valued mentor to this day.

Thank you, my coauthors. Joe, for your technical and computational expertise that have pushed the horizons of my thinking into new, higher-dimensional spaces. Miguel, for giving me support during those critical experiments when I needed it most, and teaching me how to be a principled scientist. Thomas, for the brilliant ideas, great banter, and awesome research that has so deeply influenced my own. Dominique, for showing me the power of collaborative research.

Thank you, all members of the Baier lab, past and present, for critical and insightful feedback, and fruitful discussions. In particular, thank you, Marco, Estuardo, Johannes, Alison, Yvonne, Ksenia, and Yunmin, for feedback and support over the years. Thank you, Martin, for feedback on this dissertation. Thank you, Irene and Enrico, for technical support. Thank you Krasimir, Karin, and the animal caretakers, without whom I would not have had animals for experiments. Thank you, Anne, for administrative support.

Thank you, friends and colleagues at the institute and beyond, who have provided such a wonderful research environment over the years. In particular, thank you, Axel and Ruben, for critical feedback on my project. Thank you, Nejc, for the coffee breaks. Thank you, Sonja, for the tea breaks.

Finally, thank you, family, to whom I have dedicated this dissertation. You, more than anyone, have sculpted my thinking and supported me through the years.

APPENDICES

APPENDIX 1: CURRICULUM VITAE

EDUCATION

Fast-Track PhD program Graduate School of System Neurosciences, **Munich, Germany**
Ludwig-Maximilians-Universität **2015-2021**

- GPA 1.42 (preparatory year)
- Subjects: Systems Neurobiology, Methods in Neuroscience, Sensory Physiology, Computational Neuroscience, Molecular Neurobiology, Neurophilosophy

BA (Hons) Natural Sciences Pembroke College, University of **Cambridge, UK**
Cambridge **2010-2013**

- Final grade: Class II, division 1
- Subjects: Neuroscience, Developmental Biology, Physiology, Cell Biology, Biochemistry, Chemistry, Mathematics

RESEARCH

Doctoral Research Max Planck Institute of Neurobiology **Munich, Germany**
2016-present

- Thesis title: *Neural organisation of behaviour in zebrafish larvae*
- Supervisor: Prof. Dr. Herwig Baier

Research Assistant Max Planck Institute of Neurobiology **Munich, Germany**
2014-2015

- Project: *Neural circuits governing swim posture in larval zebrafish*
- Supervisors: Prof. Dr. Herwig Baier, Dr. Tod Thiele

Honours Thesis Project University of Cambridge **Cambridge, UK**
2012-2013

- Thesis title: *The effects of nutrition on progenitor cell proliferation in explanted *Xenopus laevis* retinas*
- Supervisor: Prof. William Harris

Wellcome Trust Biomedical Vacation Scholarship University of **Cambridge, UK**
Cambridge **Jun-Aug 2012**

- Project: *Characterisation of cholinergic interneurons in the ventral nerve cord of the *Drosophila melanogaster* larva*
- Supervisor: Dr. Matthias Landgraf

PUBLICATIONS

Duncan S. Mearns, Joseph C. Donovan, António M. Fernandes, Julia L. Semmelhack, Herwig Baier. Deconstructing Hunting Behavior Reveals a Tightly Coupled Stimulus-Response Loop. *Current Biology*, Volume 30, Issue 1, 6 January 2020, Pages 54-69.e9
Biorxiv preprint: <https://doi.org/10.1101/656959>

Dominique Förster, Thomas O. Helmbrecht, **Duncan S. Mearns**, Linda Jordan, Nouwar Mokayes, Herwig Baier. Retinotectal circuitry of larval zebrafish is adapted to detection and pursuit of prey. *eLife* 2020;9:e58596 DOI: [10.7554/eLife.58596](https://doi.org/10.7554/eLife.58596)

António M. Fernandes, **Duncan S. Mearns**, Joseph C. Donovan, Johannes Larsch, Thomas O. Helmbrecht, Yvonne Kölsch, Eva Laurell, Koichi Kawakami, Marco Dal Maschio, Herwig Baier. Neuronal circuitry for stimulus selection in the visual system. *Neuron*, 3 March 2021; Pages 805-822.e6, doi: [10.1016/j.neuron.2020.12.002](https://doi.org/10.1016/j.neuron.2020.12.002)

CONFERENCES AND INVITED TALKS

- 2019 GRS & GRC Neuroethology, Mount Snow, VT (*Poster*)
Department of Molecular and Cellular Biology, Harvard University (*Invited Talk*)
WireUp, Max Planck Neuroscience PhD symposium (*Vice Chair*)
- 2018 International Congress on Neuroethology, Brisbane (*Poster, Talk*)
Queensland Brain Institute (*Invited Talk*)
- 2017 GRS & GRC Neuroethology, Les Diablerets, Switzerland (*Poster*)
LMU-Harvard Young Scientists' Forum, Munich, Germany (*Invited Talk*)
- 2016 Imaging Structure and Function in the Zebrafish Brain, Munich, Germany (*Poster*)

SUPERVISION AND TEACHING

Supervised Amgen Student Jacopo Razzauti (Summer 2019)
Course Organizer: Molecular Neurobiology in the Zebrafish Larva (2017-2018)

PRIZES AND AWARDS

First place in the Munich Science Slam (2018, 2019)
College Scholar (2011) for obtaining a first class grade at university that year
Dux (2010) for best academic performance in Aberdeen Grammar School
Edinburgh Mathematical Society Award (2010) for outstanding performance in Advanced Higher mathematics
Alex Watters Memorial Award (2008) for most promising young pianist in the Aberdeen Music Festival

APPENDIX 2: LIST OF PUBLICATIONS

Duncan S. Mearns, Joseph C. Donovan, António M. Fernandes, Julia L. Semmelhack, Herwig Baier. Deconstructing Hunting Behavior Reveals a Tightly Coupled Stimulus-Response Loop. *Current Biology*, Volume 30, Issue 1, 6 January 2020, Pages 54-69.e9, DOI: 10.1016/j.cub.2019.11.022.

BioRxiv preprint: <https://doi.org/10.1101/656959>

Dominique Förster, Thomas O. Helmbrecht, **Duncan S. Mearns**, Linda Jordan, Nouwar Mokayes, Herwig Baier. Retinotectal circuitry of larval zebrafish is adapted to detection and pursuit of prey. *eLife* 2020;9:e58596 DOI: 10.7554/eLife.58596

António M. Fernandes, **Duncan S. Mearns**, Joseph C. Donovan, Johannes Larsch, Thomas O. Helmbrecht, Yvonne Kölsch, Eva Laurell, Koichi Kawakami, Marco dal Maschio, Herwig Baier,

Neural circuitry for stimulus selection in the zebrafish visual system. *Neuron*, Volume 109, Issue 5, 3 March 2021, Pages 805-822.e6, DOI: 10.1016/j.neuron.2020.12.002.

APPENDIX 3: PERMISSIONS

All figures are reproduced with permission.

APPENDIX 4: AFFIDAVIT

Eidesstattliche Versicherung/Affidavit Hiermit versichere ich an Eides statt, dass ich die vorliegende Dissertation **Neural Organisation of Innate Behaviour in Zebrafish Larvae** selbstständig angefertigt habe, mich außer der angegebenen keiner weiteren Hilfsmittel bedient und alle Erkenntnisse, die aus dem Schrifttum ganz oder annähernd übernommen sind, als solche kenntlich gemacht und nach ihrer Herkunft unter Bezeichnung der Fundstelle einzeln nachgewiesen habe.

I hereby confirm that the dissertation **Neural Organisation of Innate Behaviour in Zebrafish Larvae** is the result of my own work and that I have only used sources or materials listed and specified in the dissertation.

Munich, 3rd May, 2021

Duncan Mearns

APPENDIX 5: DECLARATION OF AUTHOR CONTRIBUTIONS

Deconstructing Hunting Behaviour Reveals a Tightly Coupled Stimulus-Response Loop

Duncan S. Mearns, Joseph C. Donovan, António M. Fernandes, Julia L. Semmelhack, and Herwig Baier

Conceptualization, D.S.M., J.L.S., and H.B.; Methodology, D.S.M., J.C.D., A.M.F., and H.B.; Investigation, D.S.M.; Software, D.S.M. and J.C.D.; Formal Analysis, D.S.M.; Visualization, D.S.M.; Writing – Original Draft, D.S.M.; Writing – Review & Editing, J.C.D., A.M.F., J.L.S., and H.B.; Supervision, J.L.S. and H.B.; Funding Acquisition, H.B.

Retinotectal Circuitry of Larval Zebrafish is Adapted to Detection and Pursuit of Prey

Dominique Förster[†], Thomas O. Helmbrecht[†], **Duncan S. Mearns**, Linda Jordan, Nouwar Mokayes, and Herwig Baier

[†]These authors contributed equally to this work.

Dominique Förster, Conceptualization, Data curation, Formal analysis, Methodology, Writing - original draft, Project administration, Designed the experiments. Performed the experiments with support from LJ

Thomas O Helmbrecht, Conceptualization, Data curation, Software, Formal analysis, Writing - review and editing, Designed the experiments, Analyzed the data

Duncan S Mearns, Data curation, Software, Methodology, Writing - review and editing, Performed and analyzed prey capture experiments

Linda Jordan, Data curation, Methodology

Nouwar Mokayes, Data curation, Software, Wrote the code for morphological quantifications

Herwig Baier, Conceptualization, Supervision, Funding acquisition, Writing - review and editing

Neural Circuitry for Stimulus Selection in the Zebrafish Visual System

António M. Fernandes, **Duncan S. Mearns**, Joseph C. Donovan, Johannes Larsch, Thomas O. Helmbrecht, Yvonne Kölsch, Eva Laurell, Koichi Kawakami, Marco dal Maschio, and Herwig Baier

Conceptualization, A.M.F. and H.B.; Methodology, A.M.F., J.L., J.C.D., T.O.H., D.S.M., Y.K., E.L., K.K., and M.D.M.; Software, A.M.F., J.L., J.C.D., T.O.H., D.S.M., and M.D.M.; Formal Analysis, A.M.F., J.L., J.C.D., T.O.H., D.S.M., and M.D.M.; Investigation, A.M.F., D.S.M., E.L., and M.D.M.; Writing – Original Draft, A.M.F. and H.B.; Writing – Review & Editing, all authors; Funding Acquisition, H.B.; Supervision, H.B.

Duncan Mearns

Herwig Baier